High Energy and Soft-Collinear Resummation in QCD for Jet Production at Hadron Colliders

HASSAN, HITHAM,THABIT

High Energy and Soft-Collinear Resummation in QCD for Jet Production at Hadron Colliders

Hitham Thabit Hassan

A Thesis presented for the degree of
Doctor of Philosophy

Institute for Particle Physics Phenomenology
Department of Physics
Durham University
United Kingdom

October 2023

High Energy and Soft-Collinear Resummation in QCD for Jet Production at Hadron Colliders

Hitham Thabit Hassan

Submitted for the degree of Doctor of Philosophy

October 2023

Abstract: In this thesis a detailed discussion of resummation in QCD for high energy perturbative effects (with *High Energy Jets* or HEJ) and in the soft-collinear regime (with the PYTHIA parton shower) for processes involving the production of jets at hadron collider experiments. We develop and validate a sophisticated novel prescription (HEJ+PYTHIA) for merging high energy with soft-collinear resummation, which preserves the logarithmic accuracy of each resummation. Predictions produced by merging the resummation schemes in this way are compared to experimental data for inclusive $pp \to jj$ production at the *Large Hadron Collider* (LHC). Future experimental analyses to disentangle high-energy and soft-collinear effects are suggested.

We also extend the HEJ framework and present significant developments in the description of Higgs production, particularly in describing inclusive $pp \to H + 1j$ production at hadron colliders, and compare predictions within this framework to LHC data. This presents the first leading-logarithmically accurate HEJ-resummed prediction for an inclusive single-jet process, and represents a significant development in precision descriptions of strong physics in the Higgs sector at large energies.

Contents

List of Figures **9**

List of Tables **17**

Declaration **19**

Acknowledgements **21**

1 Introduction **25**

1.1 The Quantum Chromodynamics Lagrangian 27

1.2 The Standard Model and Spontaneous Symmetry Breaking . . . 31

1.3 QCD at Hadron Colliders 37

1.3.1 Perturbative QCD 37

1.3.2 Higher Orders and Divergences 44

1.3.3 Factorisation in QCD 55

1.4 Experimental Observables at Hadron Colliders 61

1.5 Monte Carlo Event Generation 66

1.5.1 The Monte Carlo Method 67

1.5.2 General Purpose Monte Carlo Event Generators 71

2 Frameworks for Perturbative Calculations in QCD **79**

2.1 Regge Scaling and the High Energy Limit 80

2.1.1 Multi-Regge Kinematics 81

2.1.2 Regge Scaling of Amplitudes 83

2.2 The *High Energy Jets* Framework 87
2.2.1 Currents and $2 \to 2$ Amplitudes in HEJ 87
2.2.2 Effective Emission Vertices in HEJ 90
2.2.3 All-Orders with HEJ — The Lipatov Ansatz 93
2.2.4 Event Generation in HEJ 96
2.3 Parton Showers and Soft-Collinear Logarithms 101
2.3.1 The Sudakov Veto Algorithm 104
2.3.2 Modern Parton Showers 107
2.3.3 Matching and Merging Hard Processes to Parton Showers . 111

3 Merging High Energy and Soft Collinear Resummation 117
3.1 The HEJ+Pythia All-Orders Merging Scheme 119
3.1.1 The All-Orders Subtracted Trial Shower 120
3.1.2 Constructing Subtracted Trial Showers for HEJ Event Histories 126
3.1.3 Full Subtraction in the Pythia Shower 133
3.1.4 Classification of HEJ-Resummable States 134
3.2 Predictions and Comparisons to Data 141
3.2.1 Differential and Integrated Jet Profiles 141
3.2.2 Multi-Jet Cross Sections 146
3.2.3 Predictions for the Average Number of Jets 156
3.3 Conclusions and Future Work 160
3.3.1 Future Work in HEJ and HEJ+Pythia 161
3.3.2 Final Comments 165

4 Inclusive Production of a Higgs Boson with at Least One Jet in *High Energy Jets* 167
4.1 Higgs Boson plus Jets Production in the High Energy Limit . . . 169
4.1.1 $H+ \geq 2j$ Processes within HEJ 169
4.1.2 Scaling of $H+ \geq 1j$ Amplitudes 174
4.1.3 New Components for $H+ \geq 1j$ and an Outer Higgs Boson . 175

4.2 Predictions and Comparison to Data 179
4.2.1 Predictions for $\sqrt{s} = 13$ TeV and Comparison to Data . . . 181
4.2.2 Predictions for $\sqrt{s} = 8$ TeV and Comparison to Data . . . 185
4.3 Conclusions 193

5 Conclusions and Outlook **195**

A The Higgs-Gluon-Gluon Coupling **199**

Bibliography **201**

List of Figures

1.1 Field content of the Standard Model with fermions arranged in their generations. The masses, spins and electric charges of each (as fractions of e) particle are also shown. Figure from ref. [1]. 35

1.2 Three Feynman diagrams contributing at LO to $gg \to gg$ scattering for momenta $p_a p_b \to p_1 p_2$. The top-left, top-right, and bottom diagrams are mediated by gluon exchange in the s-, t-, and u-channels respectively. 42

1.3 The gluon-quark-antiquark ($gq\overline{q}$) vertex in QCD at LO (a) and an example of a virtual loop correction (b). The momentum $p_1 + p_2$ of the gluon is incoming while p_1 and p_2 are both outgoing. 46

1.4 The running of α_s as compiled from several different experimental results. The figure is from the proceedings of the 2015 workshop *High precision measurements of α_s: From LHC to FCC-ee* at CERN [2] . 51

1.5 A real emission correction to the QCD gluon-quark-antiquark vertex of Fig. 1.3(a) 52

1.6 Schematic of the splitting $q \to gq$ with opening angle ϑ at LO in QCD. 58

1.7 Transverse slice of the CMS detector with the z-axis pointing out of the page and the sequenced calorimeters in the plane of the page. Figure from ref. [3]. 63

1.8 Schematic of the evolution of a scattering event at a hadron-hadron collider. See text for discussion. Figure from ref. [4]. 72

1.9 Schematic of the evolution of a hard $gg \to gg$ scattering under a parton shower with evolution variable t. As t decreases (to the right) further radiation is added to the matrix element configuration. At each stage the additional emissions enter the final state and thus can themselves undergo splitting. Both initial state and final state splittings are shown. 75

2.1 The form of the LO matrix elements for $ud \to ud$ (left) and $ug \to us\bar{s}$ (right) against half the rapidity separation between the forward and backward parton, evaluated for the phase space slices described in the text. LO matrix elements provided by MadGraph5_aMC@NLO [5]. 84

2.2 A colour flow contributing to the limit of widely-separated (in rapidity) hard radiation (left) and one not contributing in the same limit (right). The outgoing particles are ordered in rapidity. Reproduced from ref. [6]. 86

2.3 The LO scattering of distinct quarks $qQ \to qQ$. 88

2.4 All possible LO $qQ \to qgQ$ diagrams with the emitted final state gluon with momentum p_2 highlighted in blue from each available vertex. 90

2.5 Schematic of a `HEJ` amplitude, showing the scattering of currents as mediated by t-channel *reggeised*-gluon exchanges. Emissions from `HEJ`-generalised effective vertices are ordered in rapidity on the right. From ref. [7]. 95

2.6 The two possible colour flows (up to direction swaps) for scattering of gluons at LO. The left colour flow can be summarised as $(a1b2a)$ and the right as $(a12ba)$. The colour flow is highlighted in blue and orange to not mix the pattern in the left diagram for a crossing. . . 108

2.7 Schematic representation of terms featuring in the perturbative expansion for fixed-order frameworks and for parton shower resummation. The vertical axis plots orders in α_s while the horizontal plots powers of the shower logarithms L. Matrix element corrections are depicted in (a), full NLO matching in (b), and CKKW-L-style multi-jet merging in (c). See text for details. Figure reproduced from ref. [8]. . . . 112

3.1 Schematic overview of the HEJ+Pythia merging algorithm for each input HEJ configuration. The blocks are colour-coded for ease of reference. 125

3.2 All stages of the subtracted trial shower in the HEJ event history. For concision, we may refer to this also as the "merging" stage despite that the full procedure in Fig. 3.1 is the all-orders merging procedure. 127

3.3 Flow diagram charting the full subtraction in the shower evolution on the HEJ-resummed input states, after constructing the histories. . . 133

3.4 Schematic diagrams for the possible shower evolution for a (e.g.) $2 \to 2$ HEJ state (indicated by the black lines) showered with Pythia. Orange (solid, double-barred) lines represent shower emissions for which HEJ could produce a splitting kernel, while blue (dotted, double-barred) lines represent non-HEJ splittings. The shower emissions are ordered in decreasing evolution scale t. 135

3.5 An example schematic three-jet event from HEJ, displayed in the $y-p_\perp$ plane with the hard Born jet transverse momentum cut $p_{\perp j}$ indicated. The Born partons (forming the Born jets) are indicated by the black lines. As in Fig. 3.4, orange (solid, double-barred) lines represent emissions for which HEJ could produce a splitting kernel, in this case added by HEJ. 139

3.6 A possible configuration for the shower evolution of the schematic three-jet event from HEJ shown in Fig. 3.5. The partons at the centres of the extremal jets are coloured black to draw the connection with the Born partons. As in Fig. 3.4, orange (solid, double-barred) lines represent emissions for which HEJ could produce a splitting kernel, and blue (dashed, double-barred) lines indicate Pythia emissions for which HEJ can not produce a splitting kernel. 140

3.7 The evolution shown in Fig. 3.6 interpreted with a lower extremal transverse momentum cut for the jets, with the same colour/texture coding of emissions. By allowing the extremal jets to be counted above a softer transverse momentum cut, the HEJ-exclusive phase space is widened. 140

3.8 Visualisation of the differential (left) and integrated (right) jet profiles, showing the distribution of transverse momentum inside the jet cone. 143

3.9 HEJ+Pythia, CKKW-L-merged, and Pythia predictions for the differential jet profile $\rho(r)$, split into $p_{\perp j}$ bins, and the ratio of these predictions to data from ATLAS [9]. All showered predictions use the Monash 2013 tune [10]. Analysis cuts displayed on the figure. . . . 144

3.10 HEJ+Pythia, CKKW-L-merged, and Pythia predictions for the integrated jet profile $\Psi(r)$, split into $p_{\perp j}$ bins, and the ratio of these predictions to data from ATLAS [9]. All showered predictions use the Monash 2013 tune [10]. Analysis cuts displayed on the figure. . . . 145

3.11 HEJ+Pythia and HEJ predictions for the inclusive jet cross sections (left) and the distribution of the transverse momentum of the hardest jet for inclusive dijet events (right). The analysis matches the described cuts from ATLAS [11], which are displayed on the figures. 148

3.12 The decomposition of HEJ+Pythia into the full prediction, the resummable part merged with the algorithm we present in this chapter, and the CKKW-L-merged complement, for the hardest-jet transverse momentum distribution. In (a) this decomposition is plotted for the "LL" prediction, while (b) plots the decomposition for the "LL+subl." prediction. The relative difference — calculated as described in the text — is plotted in (c). Analysis cuts from ATLAS [11] are displayed on the figures. 150

3.13 The decomposition of HEJ+Pythia into the full prediction, the resummable part merged with the algorithm we present in this chapter, and the CKKW-L-merged complement, for the H_T distribution for inclusive $pp \to 4j$ events. In (a) this decomposition is plotted for the "LL" prediction, while (b) plots the decomposition for the "LL+subl." prediction. The relative difference — calculated as described in the text — is plotted in (c). Analysis cuts from ATLAS [11] are displayed on the figures. 152

3.14 HEJ, HEJ+Pythia, and CKKW-L predictions for the inclusive jet cross sections (left) and the distribution of the transverse momentum of the hardest jet for inclusive dijet events (right). Data and analysis cuts from ATLAS [11], which are displayed on the figures. 154

3.15 HEJ, HEJ+Pythia, and CKKW-L predictions for the distribution of the transverse momentum of the second-hardest (left) and third-hardest jet (right) for inclusive dijet and three-jet events respectively. Data and analysis cuts from ATLAS [11], which are displayed on the figures. 155

3.16 HEJ, HEJ+Pythia, and CKKW-L predictions for the distribution of the inclusive three-jet (left) and inclusive four-jet (right) cross sections in H_T. Data and analysis cuts from ATLAS [11], which are displayed on the figures. 155

3.17 HEJ, HEJ+Pythia, and CKKW-L predictions for the average number of jets in the rapidity interval between the two hardest jets, distributed in the size of this interval $\Delta y_{j_1,j_2}$. Data and analysis cuts from ATLAS [12], which are displayed on the figures. 157

3.18 HEJ and HEJ+Pythia predictions for average number of jets against the rapidity difference of the forward and backward jets $\Delta y_{j_f,j_b}$ (left), and against H_T (right). Analysis cuts match those of ref. [13], and are displayed on the figures. 159

4.1 Structure of the matrix element for the process $f_a f_b \to f_a \cdots H \cdots f_b$, as obtained in the HEJ framework. This diagram is a representation of the calculation in Eq. (4.1.1). 171

4.2 The GF interaction producing a Higgs boson as mediated by a massive quark loop (a) at high energies. At low energies/large distances, the assumption of infinite quark mass can be taken which produces the simpler effective vertex in (b). 172

4.3 Verifying the Regge scaling of the squared LO matrix elements, as in Eq. (2.1.7), for four different processes, indicated in the subcaptions for each figure. The MRK limit is approached as Δy becomes large. Final states are understood to be ordered in rapidity as listed. The phase space configurations used in each plot are shown in Table 4.1. 175

4.4 The tree-level diagram for the process $gq \to Hq$. The straight solid line denotes an arbitrary light quark or antiquark. 176

4.5 The eight LO diagrams which contribute to the process in Eq. (4.1.12). 177

4.6 The integrated cross section distributed against exclusive jet count (left), compared to CMS data from ref. [14], and the distribution of leading jet transverse momentum (right), compared to CMS data [15]. Both analyses apply the cuts described in Table 4.3. The "HX" component is extracted from those publications. 183

4.7 Distributions sensitive to high energy effects. In the left plot is plotted the minimum rapidity separation between any two outgoing particles (Higgs boson or jets) and in the right plot the maximum invariant mass between any two outgoing particles (Higgs or jets). Since these are inclusive single-jet observables, HEJ results are rescaled by the inclusive cross section ratio $\sigma_{\text{NLO},1j}/\sigma_{\texttt{HEJ@NLO},1j}$. 184

4.8 Distributions sensitive to high energy effects. In the left plot is plotted the maximum rapidity separation between any two outgoing particles (Higgs boson or jets) and in the right plot the maximum rapidity difference between the Higgs boson and any jet. Since these are inclusive single-jet observables, HEJ results are rescaled by the inclusive cross section ratio $\sigma_{\text{NLO},1j}/\sigma_{\texttt{HEJ@NLO},1j}$. 185

4.9 Integrated and differential cross sections against single- and multi-jet observables. The 1-jet HEJ predictions are rescaled by the inclusive cross section ratio $\sigma_{\text{NLO},1j}/\sigma_{\texttt{HEJ@NLO},1j}$ while the HEJ predictions of the 2- and 3-jet bins of (a) are rescaled by $\sigma_{\text{NLO},2j}/\sigma_{\texttt{HEJ@NLO},2j}$. In (a) and (b), the "HX" component is extracted from ref. [16]. The "HX" component was not available for (c) and (d). 188

4.10 High energy-sensitive 1-jet distributions. (a): minimum rapidity separation between any two outgoing particles (Higgs boson or jets). (b): maximum invariant mass between any two outgoing particles (Higgs boson or jets). HEJ results are rescaled by the inclusive cross section ratio $\sigma_{\text{NLO},1j}/\sigma_{\texttt{HEJ@NLO},1j}$. 189

4.11 Differential cross sections against inclusive $H+ \geq 2j$ observables. All 2-jet HEJ predictions are rescaled by the inclusive cross section ratio $\sigma_{\text{NLO,2J}}/\sigma_{\texttt{HEJ,2J}}$. The "HX" component is extracted from ref. [16] and added to the GF predictions. 190

4.12 Differential cross sections against inclusive $H+ \geq 2j$ observables and inclusive $H+ \geq 3j$ observables. All 2- and 3-jet HEJ predictions are rescaled by the inclusive cross section ratio $\sigma_{\text{NLO},2j}/\sigma_{\texttt{HEJ@NLO},2j}$. In (a) and (d), the "HX" component was extracted from ref. [16]; this was not available for (b) and (c). 191

4.13 Distributions sensitive to high energy effects. In the left plot is plotted the maximum rapidity separation between any two outgoing particles (Higgs boson or jets) and in the right plot the maximum rapidity difference between the Higgs boson and any jet. Since these are inclusive single-jet observables, HEJ results are rescaled by the inclusive cross section ratio $\sigma_{\text{NLO},1j}/\sigma_{\texttt{HEJ@NLO},1j}$. 192

List of Tables

4.1 The momentum configurations used to generate the phase space explorer plots in Fig. 4.3. 176

4.2 HEJ NLO Reweighting factors with $\mu_F = \mu_R = \max(m_{12}, m_H)$, calculated as given by Eq. (4.2.3). 181

4.3 Baseline photon and jet cuts of the 13 TeV analysis, following the CMS analysis of [14, 15]. $\text{Iso}^{\gamma}_{\text{gen}}$ denotes the sum of transverse energies of stable particles in a cone of radius $\Delta R = 0.3$ around each photon. 182

4.4 Pseudorapidity jet cuts used for the 13 TeV analysis observables presented in this section, following the CMS analysis of [14, 15]. . . 182

4.5 Baseline cuts of the 8 TeV inclusive Higgs production analysis, following the ATLAS cuts in ref. [16]. $\text{Iso}^{\gamma}_{\text{gen}}$ denotes the sum of transverse energies of stable particles in a cone of radius $\Delta R = 0.4$ around each photon. 186

Declaration

The work in this thesis is based on research carried out in the Department of Physics at Durham University. No part of this thesis has been submitted elsewhere for any degree or qualification. This thesis is based on joint research:

- Chapter 3 is based on ongoing work undertaken in collaboration with J. R. Andersen, M. Heil, L. Lönnblad, and S. Jaskiewicz.
- Chapter 4 is based on work undertaken in collaboration with J. R. Andersen, A. Maier, J. Paltrinieri, A. Papaefstathiou, and J. M. Smillie, entitled "*High energy resummed predictions for the production of a Higgs boson with at least one jet*", and published in *JHEP* **03** (2023) 001 `[2210.10671]`, ref. [17].

Acknowledgements

Firstly, I would like to thank my supervisor, Jeppe Andersen, for his guidance and encouragement. I would also like to thank all fellow members of the HEJ collaboration for the discussions and support, especially Marian Heil, Jenni Smillie, Sebastian Jaskiewicz, Malina Rosca, Jérémy Paltrinieri, and Conor Elrick. Thanks also to the students and researchers at the IPPP for curating an engaging, supportive, and friendly working environment which I have been privileged to be a part of. Many thanks to Joanne and Trudy, and Adam and Paul, for always being there to help and for keeping the institute ticking; nothing we do here would be possible without your efforts.

I would also like to thank Oscar Braun-White, Henry Truong, Lois Flower, Peter Meinzinger, Ryan Moodie, Sofie Nordahl Erner, Tom Stone, Sebastian Jaskiewicz, Mia West, Lucy Budge, Dan Milne, Jack Shergold, Conor Elrick, Jérémy Paltrinieri, and Jeppe Andersen for proof-reading parts of this thesis. Your insights and comments were an invaluable part of the writing process and are very much appreciated.

Finally, but by no means least, I would like to thank my Mum and brother, and my friends from before starting my postgraduate studies — particularly Charlotte and Alice — for your unwavering support across the years this undertaking has spanned.

I gratefully acknowledge funding from the UK Research and Innovation Science and Technology Facilities Council, under grant number ST/T506047/1.

In memory of

Thabit Ahmed Hassan

Father, mentor, friend

Chapter 1

Introduction

The Standard Model (SM) of particle physics is one of the most rigorously tested theories in physics, with high-precision measurements constraining physics beyond the Standard Model (BSM) at energy scales observable at collider experiments such as those undertaken at the LHC. Following the discovery of the Higgs boson in 2012 [18, 19], the full particle content of the Standard Model has now been experimentally tested to high levels of accuracy with different experiments corroborating results[2]. This theory includes a description of three of the four fundamental forces observed in nature: the strong nuclear force, the weak force, and electromagnetism, which are described by the (spontaneous breaking of the) composite gauge group:

$$\mathrm{SU}(3)_c \times \mathrm{SU}(2)_L \times \mathrm{U}(1)_Y, \tag{1.0.1}$$

whose ingredients we explore in greater detail in Sec. 1.2. This model is far from a complete theory of Nature, notably excluding a description of gravity, dark matter, and of neutrino masses. Several theoretical problems remain unaddressed to consensus, including the hierarchy problem arising from the discrepancy between the bare and renormalised Higgs boson masses [21], and the strong CP problem where experimental results constrain CP-violating extensions to the strong sector of the

[2]There have been measurements claiming to contradict those of other experiments, notably the CDF measurement of the W boson mass [20] yielding a value in larger than 5σ tension with the accepted value. At the time of writing this thesis, this result is still under discussion in the scientific community.

SM to be very close to zero [22]. These and more may be explained by new physics beyond the Standard Model. However, to adequately explore physics in this regime, a solid and precise understanding of the Standard Model contribution to scattering processes involving fundamental particles is required.

In this thesis we concern ourselves with developing the theoretical description of the strong sector, the quarks and gluons transforming under the unbroken $\mathrm{SU}(3)_c$ symmetry in the gauge group. We propose, test, and display predictions from methods for resumming perturbative corrections to the production of *jets* — collimated sprays of particles charged under the strong force — at hadron collider experiments. We show that we are able to stably model higher-order perturbative corrections to processes in high energy physics (HEP) mediated by the strong force — quantum chromodynamics (QCD). We apply these methods to the description of Higgs production for which the corrections to the strong-initiated process are large to all orders in perturbation theory [23].

In Ch. 2 we examine methods for producing resummed predictions in QCD with the *High Energy Jets* (`HEJ`) framework for high-energy effects, and with parton showers for soft-collinear effects. In Ch. 3 we present a sophisticated procedure for merging the high-energy resummation of *High Energy Jets* with the soft-collinear parton shower resummation of Pythia. We present developments to the *High Energy Jets* framework in describing the inclusive production of a Higgs boson with one jet at the LHC in Ch. 4. Finally, we present our conclusions and reflect on the outlook in Ch. 5.

Throughout this thesis we will use the natural system of units wherein $\hbar = c = 1$ and work with the mostly-minus metric of flat $3 + 1$-dimensional space-time in Special Relativity $g^{\mu\nu} = \mathrm{diag}(1, -1, -1, -1)$ unless stated otherwise. The Einstein summation convention, wherein repeated indices implies a sum over all values, is used unless stated otherwise.

1.1 The Quantum Chromodynamics Lagrangian

Quantum chromodynamics is the quantum field theory (QFT) describing the strong force in the Standard Model, governed by the $\mathrm{SU}(3)_c$ symmetry in the SM gauge group of Eq. (1.0.1). The *charge* associated to QCD is *colour*, and in the $\mathrm{SU}(3)_c$ theory there are $N_c = 3$ colours. In our discussion, we discuss QCD with N colours and show the Lagrangian for a $\mathrm{SU}(N)$ symmetry. This allows us to keep the dependence on N arbitrary and use simplifying approximations in calculations (such as the leading colour approximation which takes the large N limit).

The fundamental fermions (spin-$\frac{1}{2}$) charged under the strong interaction are the *quarks*. The gauge bosons (spin-1) that mediate the strong interaction are the *gluons*. Together, these particles are referred to as partons. The Lagrangian governing QCD is invariant under *local* transformations in $\mathrm{SU}(N)$. The quarks (represented by Dirac fields ψ) transform in the fundamental representation of $\mathrm{SU}(N)$, meaning we can write:

$$\psi^j(x) \to U^{jk}(x)\,\psi^k(x), \qquad U(x) = \exp(i\lambda^a(x)t^a) \in \mathrm{SU}(N), \tag{1.1.1}$$

where t^a are the *generators* of $\mathrm{SU}(N)$ in the *fundamental* representation, $a \in \left\{1, ..., N^2 - 1\right\}$. The locality of the transformation is encoded in the dependence on the four-position x. The functions $\lambda^a(x)$ contain all of the x-dependence in the matrices $U(x)$. The generators t^a are members of the Lie algebra $\mathbf{su}(N)$ of the group, defined via:

$$\left[t^a, t^b\right] = if^{abc}t^c, \tag{1.1.2}$$

where the Lie bracket associated to the Lie algebra $\mathbf{su}(N)$ is the regular commutator $[\hat{A}, \hat{B}] = \hat{A}\hat{B} - \hat{B}\hat{A}$ of operator-valued arguments. The constants f^{abc} are the *structure constants* of $\mathrm{SU}(N)$. By convention, the fundamental generators satisfy the normalisation [24]:

$$\mathrm{Tr}[t^a t^b] = T_R\delta^{ab} \equiv \frac{1}{2}\delta^{ab}. \tag{1.1.3}$$

This relation allows us to derive the *quadratic Casimir* operators C_R for any irreducible representation R of $\mathrm{SU}(N)$. These are given by $t^a_{(R)}t^a_{(R)} = C_R\mathbf{1}$, where $\mathbf{1}$ is the

identity operator. In SU(N), the quadratic Casimir operators for the fundamental and adjoint[1] representations are given respectively by:

$$C_F = \frac{N^2-1}{2N}, \qquad C_A = N. \tag{1.1.4}$$

These quantities, along with T_R, appear frequently in QCD calculations and highlight why working with the theory for general N can be useful. For $N = 3$, $C_F = \frac{4}{3}$ and $C_A = 3$.

The Lagrangian density (henceforth referred to just as the Lagrangian) for QCD with N colours and n_f distinct fermions (i.e. n_f *flavours* of fermion) is given by:

$$\mathcal{L}_{\rm YM} = \sum_{n=1}^{n_f} \overline{\psi}_n^j (i\gamma^\mu D_\mu^{jk} - m_n \delta^{jk})\psi_n^k - \frac{1}{4} F_{\mu\nu}^a F^{a,\mu\nu}. \tag{1.1.5}$$

The YM subscript denotes that this is a *Yang-Mills* Lagrangian. The invariance of the Lagrangian under local transformations in SU(N) is referred to as a SU(N) *gauge symmetry* of the theory [25]. Various quantities in Eq. (1.1.5) require introduction. The matrices γ^μ arise in the free Dirac Lagrangian for spin-$\frac{1}{2}$ particles, and satisfy the *Clifford algebra*, given by the anticommutation relations:

$$\{\gamma^\mu, \gamma^\nu\} \equiv \gamma^\mu\gamma^\nu + \gamma^\nu\gamma^\mu = 2g^{\mu\nu}\mathbf{1}. \tag{1.1.6}$$

The Dirac conjugate spinor is defined by $\overline{\psi}_n \equiv \psi_n^\dagger \gamma^0$. Each fermion has mass m_n and the mass term $-m_n\overline{\psi}_n\psi_n$ in the Lagrangian allows us to deduce this. The *helicity* of a particle is defined as the projection of the spin onto the momentum of the particle. As such fermions can have either positive or negative helicity. Fermions are left-(right-)handed if they have negative (positive) helicity. In the Standard Model, masses are not introduced in this way since left- and right-handed spinors are mixed in a mass term of the form $-m_n\overline{\psi}_n\psi_n$. Instead, the *Higgs mechanism* assigns masses to the massive SM particles. We discuss the Higgs mechanism in Sec. 1.2.

Free fermions would satisfy the *Dirac equation*, shown below for a single fermion

[1] For a matrix U in the fundamental representation, a matrix F transforms in the adjoint representation if the change of gauge maps $F \to UFU^\dagger$.

flavour:

$$(i\gamma^\mu \partial_\mu - m)\psi = 0. \tag{1.1.7}$$

This admits solutions for ψ and $\overline{\psi}$ of the form (with p the four-momentum):

$$\psi(x) = u(p)\exp(-ip^\mu x_\mu), \qquad \overline{\psi}(x) = v(p)\exp(ip^\mu x_\mu). \tag{1.1.8}$$

Here, u and v are *Dirac spinors* and *anti-spinors*. The solutions in Eq. (1.1.8) are two wave-like modes, one which propagates *forwards* through time (i.e. in the direction of increasing time), and the other *backwards* in time. We refer to the former as the *particle* solution and to the latter as the *antiparticle* solution.

The remaining quantities in Eq. (1.1.5) are related to the gluons. The covariant (understood to mean gauge-covariant) derivative D_μ is defined by:

$$D_\mu \equiv \partial_\mu - ig_s A^a_\mu t^a, \tag{1.1.9}$$

where A^a_μ are the gluon vector fields and g_s is the strong coupling. The gluons are massless and the remaining piece of the Lagrangian is given in terms of the gluon *field strength tensor* $F^a_{\mu\nu}$:

$$F^a_{\mu\nu} = 2\partial_{[\mu}A^a_{\nu]} + g_s f^{abc} A^b_\mu A^c_\nu \equiv \partial_\mu A^a_\nu - \partial_\nu A^a_\mu + g_s f^{abc} A^b_\mu A^c_\nu, \tag{1.1.10}$$

where the square brackets around Lorentz indices denote antisymmetrisation as shown explicitly by the identity in Eq. (1.1.10). The gauge bosons A^a_μ are the particles responsible for mediating the *interaction* that arises from the local SU(N) symmetry. The coupling g_s parametrises the strength of this interaction. In the basic Yang-Mills Lagrangian we note that there are terms present schematically of the form (dropping the γ matrices and the generators t^a, and not invoking the Einstein summation convention):

$$g_s \overline{\psi}_n A \psi_n, \qquad g_s AAA \qquad g_s^2 AAAA. \tag{1.1.11}$$

This exposes the interactions introduced to our theory by requiring local SU(N) invariance of the Lagrangian. The gluons couple fermions to their antiparticles with

strength g_s as showcased by the first term of Eq. (1.1.11). For the non-abelian theory, the gauge bosons self-interact, with the possibility of three bosons coupling (with strength g_s) or four (with strength g_s^2), shown by the latter two terms. We discuss a diagrammatic interpretation of these interactions in Sec. 1.3.

Before continuing our discussion of QCD, we briefly discuss the abelian U(1) theory governing quantum electrodynamics (QED), which is comparatively more simple. The symmetry group of QED has one generator and thus one gauge boson — the photon A_μ. The Lagrangian for QED is given by:

$$\mathcal{L}_{\text{QED}} = \sum_{n=1}^{n_f} \overline{\psi}_n^j (i\gamma^\mu D_\mu^{jk} - m_n \delta^{jk}) \psi_n^k - \frac{1}{4} F_{\mu\nu} F^{\mu\nu}. \tag{1.1.12}$$

Here the QED field strength and covariant derivative are given by:

$$\begin{aligned} F_{\mu\nu} &= 2\partial_{[\mu} A^a_{\nu]} \equiv \partial_\mu A^a_\nu - \partial_\nu A^a_\mu, \\ D_\mu &= \partial_\mu - ieA_\mu, \end{aligned} \tag{1.1.13}$$

where we have labelled the coupling e (which is equal to the absolute electron charge) in QED. This is the same as the Lagrangian for the Yang-Mills theory, except that the abelian nature of QED means the field strength and covariant derivative are simpler as there is only one generator. There is only one coupling in QED, between the photon and a fermion and anti-fermion of the same flavour.

Returning to QCD, the Lagrangian of the Yang-Mills theory is written in an unspecified gauge, meaning that we are unable to derive *correlation functions* (including *propagators* — see Sec. 1.3) for the non-abelian theory. The gauge is required to be fixed as the additional degrees of freedom introduced by the gauge symmetry are superfluous and unphysical[1]. A common method of fixing the gauge is by choosing a *covariant* gauge. This involves adding a term:

$$\mathcal{L}_\xi = -\frac{1}{2\xi} (\partial^\mu A^a_\mu)(\partial^\nu A^a_\nu), \tag{1.1.14}$$

to the Lagrangian of Eq. (1.1.5). The parameter $\xi \in \mathbb{R} \setminus \{0\}$ controls the gauge

[1]The reasoning for this becomes clearer in the path integral formulation of QFT which we do not discuss in this thesis.

choice. Taking $\xi \to 0$ gives the *Landau* gauge and $\xi \to 1$ the *Feynman* gauge. Other widely-used methods of fixing the gauge exist, including non-covariant gauges such as the axial gauge. In some gauges, anti-commuting scalar (spin-0) *ghost* fields c^a, transforming in the adjoint representation of SU(N), must be introduced to cancel the unphysical degrees of freedom [24]. This method of fixing the gauge is the Faddeev-Popov procedure. For fully detailed discussion of this procedure, including the treatment of ghosts, consult Ch. 71, 72 of ref. [24] and Sec. 16.2-16.4 of ref. [25].

The subject matter of this thesis focuses on developments in the formalism for making calculations in QCD as formulated in this section. In the next section we examine the theory in context, as part of the Standard Model.

1.2 The Standard Model and Spontaneous Symmetry Breaking

As we have discussed earlier, the Standard Model is the quantum field theory describing three of the four observed fundamental forces of nature. Interactions under the strong nuclear force, the weak force and the electromagnetic force are described by a Lagrangian invariant under the gauge group of Eq. (1.0.1) after spontaneous symmetry breaking (SSB), which we discuss in this chapter.

While we continue to chiefly concern ourselves with the sector of the theory governed by the $\mathrm{SU}(3)_c$ symmetry of QCD in this thesis, we connect our study of precision calculations in QCD to the other sectors of the SM, since one can not explore each sector in isolation at hadron collider experiments. The Higgs sector in particular is the least well-explored given relatively recent confirmation by experiment. The experimental community anticipates that data from the high-luminosity runs of the LHC (HL-LHC) will be able to constrain the Higgs self-couplings in coming years [26]. To bolster this, strong theoretical understanding of the SM is necessary in all sectors, since the interactions occurring at hadron collider experiments are not "chosen" to lie in a specific sector, i.e. if a Higgs boson is observed, one can

not *a priori* determine the mechanism by which it was produced.

We use this chapter to outline the Standard Model and provide context to the predictions we present later in the thesis. Notably this background is relevant for our description of inclusive $pp \to H + 1j$ production in Ch. 4 — where we focus on the QCD-initiated gluon-gluon fusion (GGF, also referred to as gluon fusion, GF) production mechanism, rather than the weak boson fusion (WBF, also referred to as vector boson fusion, VBF) mechanism in the electroweak sector.

In the SM, there are four vector bosons which mediate interactions. The gluons and photon of QCD and QED respectively are massless, as required by the unbroken gauge symmetries of the Lagrangian under each interaction. However, the W and Z bosons mediating weak interactions are observed to be massive, meaning they cannot arise from an unbroken gauge symmetry [25]. This implies that the Standard Model symmetry must be broken.

The composite symmetry $\mathrm{SU}(2)_L \times \mathrm{U}(1)_Y$ is *spontaneously broken* by the *Higgs mechanism* to leave only the abelian symmetry group of QED [24]:

$$\mathrm{SU}(2)_L \times \mathrm{U}(1)_Y \xrightarrow{\text{Higgs Mechanism}} \mathrm{U}(1)_e. \tag{1.2.1}$$

This occurs due to the presence of a complex scalar field $\mathbf{\Phi}$ transforming in the *doublet* representation of SU(2) — the Higgs doublet. This doublet enters in the Standard Model Lagrangian with the term:

$$\left(D_\mu \mathbf{\Phi}\right)^\dagger D^\mu \mathbf{\Phi} + \mu^2 \mathbf{\Phi}^\dagger \mathbf{\Phi} - \lambda \left(\mathbf{\Phi}^\dagger \mathbf{\Phi}\right)^2 =: \left(D_\mu \mathbf{\Phi}\right)^\dagger D^\mu \mathbf{\Phi} - \mathcal{V}_H(\mathbf{\Phi}), \tag{1.2.2}$$

with the *Higgs potential* $\mathcal{V}_H(\mathbf{\Phi})$ and the covariant derivative for the (non-strong) part of the Standard Model:

$$D_\mu = \partial_\mu - i g_L \tau^a W_\mu^a - \frac{1}{2} g_Y Y B_\mu. \tag{1.2.3}$$

Here, W^a are the three gauge bosons of $\mathrm{SU}(2)_L$, each attached to a generator τ^a of the same group, and B_μ the one gauge boson associated to the abelian symmetry $\mathrm{U}(1)_Y$ with generator Y. We may notice immediately that the potential $\mathcal{V}_H$ is

symmetric under SU(2) transformations (for fixed parameters μ, λ) and the locus of the vacua (i.e. the minima of the potential) is the curve defined by:

$$\mathbf{\Phi}^\dagger\mathbf{\Phi} = \frac{v^2}{2} \equiv \frac{1}{2}\frac{\mu^2}{\lambda}. \tag{1.2.4}$$

These vacua are infinitely degenerate. When the symmetry is spontaneously broken, Nature assigns to the physical Higgs doublet a vacuum expectation value (VEV) v, and a direction.

As a consequence of this symmetry breaking, the Hilbert spaces occupied by the Higgs doublet are built around the chosen vacuum. This reduces the degrees of freedom in the doublet from four to one, and only one real field manifests — the Higgs boson H. The other degrees of freedom are the scalar *Goldstone bosons*, however, a convenient choice of gauge can re-express these degrees of freedom as the longitudinal polarisations of the massive W and Z bosons — this is referred to as the *unitary* or sometimes the *unitarity* gauge [25]. Replacing $\mathbf{\Phi}$ in Eq. (1.2.2) by the doublet as composed in this unitary gauge gives:

$$\mathbf{\Phi} = \frac{1}{\sqrt{2}}\begin{pmatrix} 0 \\ v + H \end{pmatrix}. \tag{1.2.5}$$

Substituting this into the Higgs Lagrangian of Eq. (1.2.2) gives rise to gauge-invariant mass terms, dependent on the vacuum expectation value v, for the weak-mediating gauge bosons:

$$W_\mu^\pm = \frac{1}{\sqrt{2}}(W_\mu^1 \mp iW_\mu^2), \quad Z_\mu = \cos\theta_W W_\mu^3 - \sin\theta_W B_\mu, \quad A_\mu = \sin\theta_W W_\mu^3 + \cos\theta_W B_\mu, \tag{1.2.6}$$

where we have defined the *weak mixing* angle or *Weinberg* angle by:

$$\tan\theta_W = \frac{g_Y}{g_L}. \tag{1.2.7}$$

These are the $W^\pm$ bosons and the Z boson, respectively the first and second terms of Eq. (1.2.6). The masses of these bosons after SSB can be derived from the coefficient of the terms quadratic in $W^\pm$ and Z, from expanding the full expression

for the covariant derivative of Eq. (1.2.3) in Eq. (1.2.2). These masses, m_W (the two W bosons have equal masses) and m_Z, are related by $m_W = g_L v/2 \equiv m_Z \cos\theta_W$. Since these bosons manifest each with a mass following spontaneous symmetry breaking, they acquire also longitudinal polarisations (that would previously have been unphysical) which absorb the additional degrees of freedom that would have formed the Goldstone bosons of the theory [25]. The Higgs boson itself gains a mass of $m_H = \sqrt{2}\mu$.

The (massless) photon of QED is denoted by A_μ and represents the unbroken part of the symmetry, invariant under local $\mathrm{U}(1)_e$ transformations. Together with the gluons (which we here denote by G^a_μ to further distinguish them from the photon) of the unbroken $\mathrm{SU}(3)_c$ symmetry we can write a fully covariant derivative:

$$D_\mu = \partial_\mu - ig_L\tau^a W^a_\mu - \frac{1}{2}g_Y Y B_\mu - ig_s t^a G^a_\mu, \tag{1.2.8}$$

for the Standard Model gauge group.

Pre-SSB, the fermions in the theory observe symmetry under $\mathrm{SU}(2)_L$, thus there can be no terms in the Lagrangian that mix left- and right-handed fermion fields such as mass terms. However, post-SSB we can see that mass terms arise for the fermion fields in the theory via the Yukawa couplings:

$$\mathcal{L}_{\text{Yukawa}} = \overline{\psi}_i y_{ij} \mathbf{\Phi} \psi_j + \text{h.c.}, \tag{1.2.9}$$

where h.c. refers to the Hermitian conjugate. This means left- and right-handed fermions can be mixed to yield gauge-invariant mass terms as required. These couplings are proportional to the masses of the fermions meaning the Standard Model Higgs couples more strongly to heavier fermions.

Before concluding, we explore the transformation properties of the particle content of the Standard Model. In Fig. 1.1, we see the quarks and leptons of the theory as well as the force-carrying vector bosons and the Higgs. Charged under all three interactions of the Standard Model are the quarks of which there are the left-handed and right-handed forms. $\mathrm{SU}(3)_c$ does not differentiate between left- and right-handed

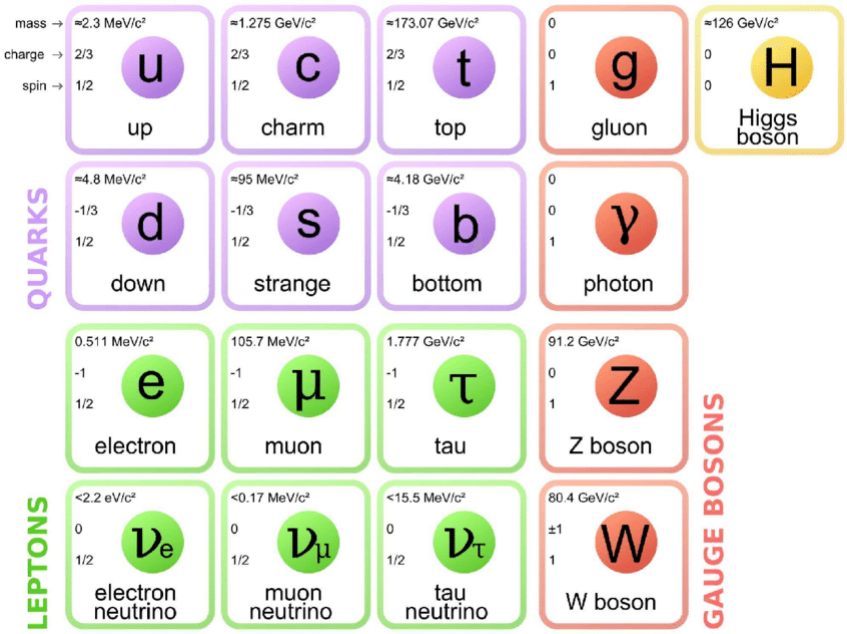

Figure 1.1: Field content of the Standard Model with fermions arranged in their generations. The masses, spins and electric charges of each (as fractions of e) particle are also shown. Figure from ref. [1].

quarks, as such they transform in the fundamental representation of $\mathrm{SU}(3)_c$, and antiquarks in the anti-fundamental. The left-handed quarks, however, form doublets in $\mathrm{SU}(2)_L$ which transform in the fundamental representation. In the Standard Model there are three such doublets of quarks — each referred to as a *generation*. In the fundamental representation of $\mathrm{SU}(2)_L$, we denote these by:

$$Q_L = (u_L, d_L), \tag{1.2.10}$$

where u_L is the up-type quark in each generation (i.e. the positively charged under QED) and d_L is the down-type (negatively charged under QED). The up-type quarks are (in order of increasing mass) the up u, charm c, and top/truth t quarks while the down-type quarks are the down d, the strange s, and the bottom/beauty b quarks (similarly ordered). The generations are shown in columns in Fig. 1.1.

The right-handed quarks manifest as singlets in $\mathrm{SU}(2)_L$, and are generally denoted by u_R (for the up-type quarks) and d_R (for the down-type). These transform trivially (i.e. are uncharged) under $\mathrm{SU}(2)_L$. There are three right-handed singlets for each of the up- and down-type quarks in the Standard Model.

The *leptons* also form generations as shown vertically again in Fig. 1.1. The left-handed leptons transform as doublets in the fundamental representation of $\mathrm{SU}(2)_L$ and are denoted by:

$$L_L = (\nu_{l,L}, l_L), \tag{1.2.11}$$

where ν_l is the *neutrino* corresponding to the lepton l. There are three leptons in the Standard Model, the electron e, muon μ and tau/tauon τ and each forms a generation with the corresponding neutrino. The left-handed leptons all transform trivially (i.e. are uncharged) under $\mathrm{SU}(3)_c$ and form doublets transforming in the fundamental representation of $\mathrm{SU}(2)_L$. The neutrinos are neutral under QED while the leptons all carry electric charge $-e$. In the Standard Model, no mechanisms give rise to neutrino masses. Thus the observation of neutrino masses must be explained by physics beyond the standard model, or by adding a Higgs-neutrino Yukawa coupling term to the SM. Adding such a coupling term is undesirable since the Higgs Yukawa couplings are proportional to the particle masses; for the neutrinos this term would hence be vanishingly small and pose a "fine-tuning" style problem similar to the hierarchy problem.

The right-handed leptons $\bar{l}_R$ similarly form singlets under both $\mathrm{SU}(3)_c$ and $\mathrm{SU}(2)_L$ and are necessary to give the leptons mass. There are three right-handed leptons, corresponding to each massive lepton observed in the Standard Model.

We re-emphasise in this section that the Standard Model, while certainly one of the most well-tested theories in physics, is incomplete. The Super-Kamiokande experiment demonstrated, for example, that neutrinos exhibit *oscillation* [27] i.e. their flavours change as they propagate. This effect is only possible if the neutrinos are massive — though experiments have constrained the neutrino masses to very small values. This means there must be three singlet right-handed neutrino $\overline{\nu}_{l,R}$ fields in an extension of the Standard Model with massive neutrinos.

Most visibly, the Standard Model excludes a description of gravity. It can be shown that the quantum field-theoretic description of gravity would require a *tensor* field to mediate the interaction [24] — the *graviton*. However this poses problems

for the ultraviolet-renormalisability (we discuss renormalisation in Sec. 1.3.2) of the theory [25].

The incompleteness of the SM is also readily apparent from cosmological observations. It has long-since been known that visible matter accounts for $\sim 5\%$ of the energy density of the observable universe, with the rest being comprised of dark matter and dark energy. Accounting for this discrepancy with QFTs requires introduction of new fields to the Standard Model Lagrangian [25].

For the remainder of this chapter, we draw the connection between this theoretical formalism and experiments by constructing theoretical equivalents to physical quantities and observables. We discuss perturbation theory in QCD in the larger picture of QCD at hadron colliders in the next section.

1.3 QCD at Hadron Colliders

The research presented in this thesis is centred around developments in perturbation theory, which is an indispensable framework that can be used to produce calculations in QCD at hadron colliders. In this section we discuss amplitudes at perturbative scales, where the quarks and gluons participate in hard interactions. Then we connect this to the physical picture of QCD as it manifests in nature and discuss how hadron collider experiments allow us to compare predictions to data.

1.3.1 Perturbative QCD

The fundamental quantity that can be directly extracted from particle collider experiments is the *cross section* which relates the particle collision events N per unit time to the *luminosity* L (the rate of change of the incoming particles over beam area with respect to time) by:

$$\sigma = \frac{1}{L}\frac{\mathrm{d}N}{\mathrm{d}t}. \tag{1.3.1}$$

One needs only connect this formula to the theory we have constructed in terms of the fields participating in the process.

In perturbation theory, particles are modelled as being free (i.e. not interacting) for early and late times, and interacting for short periods of time. Perturbation theory can be applied in the cases that the interaction terms of a theory (those coupling multiple particles in the Lagrangian) are much smaller than the free terms (the kinetic and mass terms of the Lagrangian). Thus, perturbative interactions occur only when particles are at short distances to each other.

We define *states* in our theory to be configurations of multiple excitations of our fields. The probability of scattering one configuration of particles (restricting ourselves for simplicity of notation to one type of field) with momenta k_i ($i \in \{1, ..., n\}$) at $t = -\infty$ to another set of particles with momenta p_j ($j \in \{1, ..., m\}$) at $t = +\infty$ is the square of the (absolute value of the) overlap:

$$P = \left| {}_{t=+\infty}\langle \{p_j\} | \{k_i\} \rangle_{t=-\infty} \right|^2 . \tag{1.3.2}$$

In the theories we presented in Sec. 1.1 there were interactions present that could make these processes possible. Assuming that these interactions are not present for very early or very late times we can reinterpret these states in the *interaction picture* [25], and define an according *time evolution operator* $S(t)$ which evolves the incoming to the outgoing states:

$${}_{t=+\infty}\langle \{p_j\} | \{k_i\} \rangle_{t=-\infty} = \lim_{t\to\infty} \langle \{p_j\} | S(t) | \{k_i\} \rangle . \tag{1.3.3}$$

The operator $S(t)$ is known as the *S-matrix* and is unitary to ensure conservation of probability [24]. It may be further decomposed to:

$$S = \mathbf{1} + iT, \tag{1.3.4}$$

which separates the overlap Eq. (1.3.3) to the identity $\mathbf{1}$ which will describe the *no-scattering* process, and the transfer operator T which describes the *scattering* processes where changes to the number of particles, and their momenta, may occur. From the unitarity of the S-matrix in Eq. (1.3.3), we may derive the following

relation for the transfer matrix:

$$T^\dagger T = -i(T - T^\dagger). \tag{1.3.5}$$

The *matrix element* (ME) or *amplitude* $\mathcal{M}$ for a process is a Lorentz-invariant quantity defined via:

$$\langle \{p_j\} | \, iT \, | \{k_i\} \rangle = (2\pi)^d \delta^{(d)} \left(\sum_{i=1}^{n} p_j - \sum_{j=1}^{m} k_i \right) \cdot i\mathcal{M}(\{k_i\} \to \{p_j\}), \tag{1.3.6}$$

in d-dimensional space-time.

QCD is not perturbative at macroscopic scales as we discuss in Sec. 1.3.3; the quarks and gluons are not accessible at low energies. Only *hadrons* — bound states of QCD — may be accessed at such scales. At high energy scales (or small distance scales) QCD is a perturbative theory, and the cross section for a partonic $2 \to n$ particle scattering process is defined by:

$$\hat{\sigma} = \int \mathrm{d}\mathbf{\Phi}_n \cdot \frac{1}{\mathcal{F}} \cdot \overline{|\mathcal{M}_{2\to n}(\mathbf{\Phi}_n)|^2}. \tag{1.3.7}$$

Here, the (squared) matrix elements have been summed and averaged over final and initial state (respectively) spins and colours and polarisations, as denoted by the bar. The quantity $\mathcal{F}$ is the *flux*, and depends only on the incoming particles, while $\mathbf{\Phi}_n$ is the n-particle Lorentz-invariant phase space, and $\mathrm{d}\mathbf{\Phi}_n$ a differential element of this phase space. The Lorentz-invariant phase space is dependent on the final state particle momenta. If the incoming particles have momenta p_a and p_b and the final state particles have momenta p_f for $f \in \{1, \ldots, n\}$, we may express the differential Lorentz-invariant phase element as:

$$\mathrm{d}\mathbf{\Phi}_n = \left[\prod_{f=1}^{n} \frac{\mathrm{d}^3\mathbf{p}_f}{(2\pi)^3} \frac{1}{2E_f} \right] (2\pi)^4 \delta^{(4)} \left(p_a + p_b - \sum_{f=1}^{n} p_f \right). \tag{1.3.8}$$

In perturbation theory we assume the interacting theory is a small perturbation around the free theory [25]. To expand our theory perturbatively, the coupling g_s must be small. We can then use the coupling as our expansion parameter to produce

the power series expansion for the cross section:

$$\hat{\sigma} = \alpha_s^k K^{\mathrm{LO}} + \alpha_s^{k+1} K^{\mathrm{NLO}} + \alpha_s^{k+2} K^{\mathrm{NNLO}} + \ldots + \alpha_s^{k+n} K^{\mathrm{N^nLO}} + \ldots, \tag{1.3.9}$$

where $\alpha_s \equiv g_s^2/4\pi$. One may then terminate the series at the required accuracy. LO signifies an expansion to the *leading order* of perturbation theory (i.e. the lowest order at which the process may occur), and the notation $\mathrm{N^nLO}$ denotes the expansion carried n powers above the leading order i.e. the *(next-to-)^{n}leading order* term. Thus the quantities $K^{\mathrm{N^nLO}}$ represent the $\mathrm{N^nLO}$ correction (factorised of the appropriate power of α_s) to the cross section, with K^{LO} the LO cross section (factorised of α_s^k).

An expansion up to a finite order in perturbation theory is referred to as a *fixed-order* (FO) expansion, where we expand to finite power n above the leading order. LO and NLO predictions are readily available for most Standard Model processes with the frontier at $\mathrm{N^3LO}$ in, for example, low-multiplicity QCD processes [28]. Higher orders are notoriously difficult to calculate, and we discuss these complications in more detail in Sec. 1.3.2. Further, we have only thus far discussed partonic cross sections, we expand on the connection to the non-perturbative theory in Sec. 1.3.3.

Feynman diagrams and kinematics

To calculate a cross section to a given perturbative accuracy, all amplitudes contributing to the process up to that order must be calculated. A useful framework for evaluating these amplitudes is with *Feynman diagrams*. These are constructed from the *Feynman rules* for the theory, which can be derived from the terms in the Lagrangian. We interpret each interaction as a *vertex* that connects the interacting particles present. Initial and final state particles are referred to as *external* particles (which are physical and on-shell[1]). For most processes at LO (and all at higher orders) *internal* particles referred to as *propagators* (*virtual*, off-shell particles that propagate internally and do not feature in initial/final states) are required to con-

[1] *On-shell* signifies a particle for which the square of the four-momentum is equal to the (square of the) rest mass. For virtual/off-shell particles, the *virtuality* is the difference between the invariant mass and the rest mass of the particle.

nect the external particles corresponding to the initial and final states. For a FO expansion, all diagrams contributing up to that order are required.

The Feynman rules allow us to derive a mathematical expression corresponding to each diagram, these can then be summed to give the amplitudes at the required order. These diagrams quickly become involved to calculate and can feature (at higher orders) intricate and complex symmetries and structures such as internal loops.

For $2 \to 2$ scatterings, we can define the Mandelstam variables in terms of the momenta of the incoming and outgoing particles. For scatterings of the form $p_a, p_b \to p_1, p_2$ these are defined by:

$$\begin{aligned} \hat{s} &= (p_a + p_b)^2 = (p_1 + p_2)^2 \quad \xrightarrow{m\to 0} \quad 2p_a \cdot p_b = 2p_1 \cdot p_2, \\ \hat{t} &= (p_a - p_1)^2 = (p_b - p_2)^2 \quad \xrightarrow{m\to 0} \quad -2p_a \cdot p_1 = -2p_b \cdot p_2, \\ \hat{u} &= (p_a - p_2)^2 = (p_b - p_1)^2 \quad \xrightarrow{m\to 0} \quad -2p_a \cdot p_2 = -2p_b \cdot p_1. \end{aligned} \tag{1.3.10}$$

The hat notation denotes — as for the partonic cross section in Eq. (1.3.7) — quantities relating to partonic interactions. The Mandelstam variables represent the invariant mass of the exchanged particle in the relevant *channel*. For example, we refer to a diagram as an s-channel diagram if the exchanged gluon has (squared) invariant mass $\hat{s}$ and momentum $q = p_a + p_b$. The limits as the mass tends to zero are shown in Eq. (1.3.10), which will become relevant for partonic processes that typically occur at large energies compared to the on-shell quark masses in the SM (excluding the top quark).

In Fig. 1.2, three LO diagrams contributing to $gg \to gg$ scattering at the parton level are shown. Highlighted in each diagram is the momentum of each external gluon, and the momentum (q) of the exchanged virtual gluon, as well as adjoint colour indices (Latin letters), and Lorentz vector indices (Greek letters). We have excluded an additional LO diagram (arising from the four-gluon vertex) which also contributes, since we focus the discussion on Mandelstam variables.

Amplitudes can be expressed in terms of the Mandelstam variables, and their

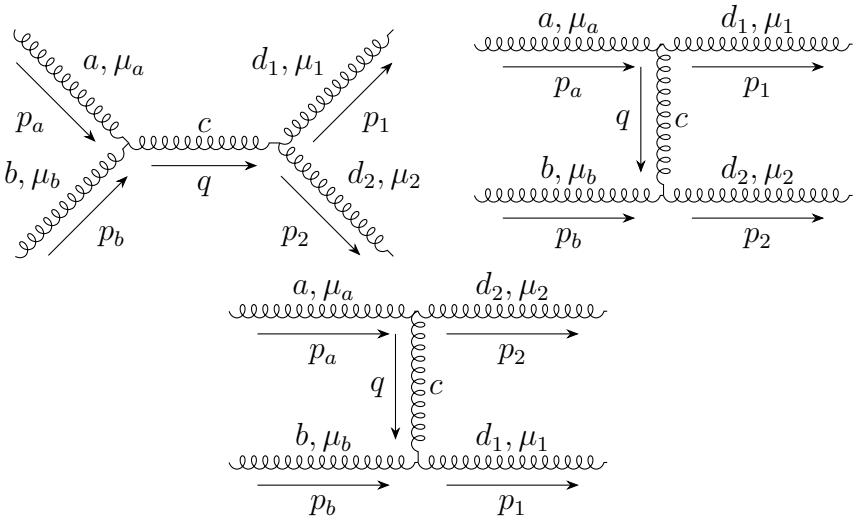

Figure 1.2: Three Feynman diagrams contributing at LO to $gg \to gg$ scattering for momenta $p_a p_b \to p_1 p_2$. The top-left, top-right, and bottom diagrams are mediated by gluon exchange in the s-, t-, and u-channels respectively.

inclusion makes clearer the dependence of an amplitude on the kinematics. Further, for interactions with more particles, one may define the invariant mass of any two momenta by a generalised Mandelstam-$\hat{s}$ variable:

$$\hat{s}_{ij} = (p_i + p_j)^2 \quad \xrightarrow{m \to 0} \quad 2p_i \cdot p_j = 2p_j \cdot p_i. \tag{1.3.11}$$

This will become useful when we outline the *High Energy Jets* framework in Sec. 2.2, where other kinematic variables are used.

Feynman diagrams impose momentum conservation at every vertex, meaning that momentum is conserved across the diagram. Sec. 4.6-4.7 of ref. [25] contains in-depth discussion of how the Feynman rules may be derived for a theory in full detail, while a list of Feynman rules for the Standard Model may be found in Appendix A.1 of ref. [25] and throughout ref. [24] as well as many other prominent QFT textbooks including (and not limited to) ref. [21]. The rules for QCD specifically are summarised in the Appendix of ref. [29] and Sec. 1.4 (p. 10) of ref. [30].

Spinor-helicity formalism and amplitudes

Feynman diagrams are not the only framework within which perturbative calculations can be made. We consider the spinor-helicity formalism and how it may be applied to calculate amplitudes in this section.

Returning to the γ matrices of Dirac theory, we note that the Clifford algebra of Eq. (1.1.6) does not define them uniquely, and they can be written in different bases. In this thesis we use the *Weyl basis* in four-dimensional spinor space:

$$\gamma^\mu = \begin{pmatrix} 0 & \sigma^\mu \\ \overline{\sigma}^\mu & 0 \end{pmatrix}, \tag{1.3.12}$$

where σ^μ is the Lorentz four-vector extension of the Pauli matrices σ^i and is given by $\sigma^\mu = (\mathbf{1}_2, \vec{\sigma})^\mu$ and $\overline{\sigma}^\mu = (\mathbf{1}_2, -\vec{\sigma})^\mu$. It can be verified that Eq. (1.3.12) satisfies the Clifford algebra Eq. (1.1.6).

The left-right projection operators, respectively P_L, P_R, are defined by:

$$P_{\frac{L}{R}} = \frac{\mathbf{1} \mp \gamma^5}{2}, \qquad \gamma^5 \equiv i\gamma^0\gamma^1\gamma^2\gamma^3. \tag{1.3.13}$$

Here P_L corresponds to the minus solution and P_R to the plus solution. Writing a Dirac spinor $u = (u_-, u_+)$ where $u_\pm$ are the two-component *Weyl spinors*, we may use the projection operators of Eq. (1.3.13) to arrive at:

$$P_L u = (u_-, \mathbf{0}), \qquad P_R u = (\mathbf{0}, u_+). \tag{1.3.14}$$

Fermion spinors can be related directly to helicity states. In the limit of massless fermions, we make the following definitions [31, 32]:

$$\begin{aligned} u_\pm(p_i) = v_\mp(p_i) \equiv |i^\pm\rangle \equiv |p_i^\pm\rangle\,, \\ \overline{u}_\pm(p_i) = \overline{v}_\mp(p_i) \equiv \langle i^\pm| \equiv \langle p_i^\pm|\,. \end{aligned} \tag{1.3.15}$$

We will use the notation:

$$\begin{aligned} |k^+\rangle \equiv |k], \quad |k^-\rangle \equiv |k\rangle\,, \\ \langle k^+| \equiv \langle k|\,, \quad \langle k^-| \equiv \langle k|\,, \end{aligned} \tag{1.3.16}$$

throughout this thesis, and define the spinor products by:

$$\begin{aligned} \langle ij\rangle &= \overline{u}_+(p_i)u_-(p_j), \quad [ij] = \overline{u}_-(p_i)u_+(p_j), \\ \langle ij] &= \overline{u}_+(p_i)u_+(p_j), \quad [ij\rangle = \overline{u}_-(p_i)u_-(p_j). \end{aligned} \tag{1.3.17}$$

Operators (such as the γ^μ matrices) can also be placed between helicity states in spinor products. Products of helicity states are also related to momenta and the Mandelstam variables e.g.:

$$(p_i + p_j)^2 = \langle ij\rangle\,[ji] \equiv \hat{s}_{ij}. \tag{1.3.18}$$

In this formalism, gluon polarisation vectors can be expressed as:

$$\varepsilon_-^\mu(k) = \frac{\langle q|\,\gamma^\mu|k]}{\sqrt{2}\langle qk\rangle}, \quad \varepsilon_+^\mu(k) = -\frac{[q|\gamma^\mu\,|k\rangle}{\sqrt{2}[qk]}, \tag{1.3.19}$$

with q a massless reference vector not collinear with the gluon momentum k.

Amplitudes evaluated in the spinor-helicity formalism separate the kinematics of a matrix element from the colour structure in QCD. For instance, the LO scattering of n gluons with momenta $\{p_i\}$ and helicities $\{\lambda_i\}$ takes a simple form [32]:

$$\mathcal{M}_{ng}^{\mathrm{LO}} \propto \sum_{\sigma\in S_n/Z_n} \mathrm{Tr}[t^{a_{\sigma(1)}}\cdot\cdots\cdot t^{a_{\sigma(n)}}]M(\sigma(1^{\lambda_1}),\ldots,\sigma(n^{\lambda_n})), \tag{1.3.20}$$

where t^a are the generators of QCD in the fundamental representation of the gauge group and σ is an arbitrary non-cyclical permutation of the indices. We recommend the reader ref. [32] for a comprehensive overview of this formalism, indeed we will make use of relations listed in this review and the references therein when deriving the amplitudes of *High Energy Jets* in Sec. 2.2.

1.3.2 Higher Orders and Divergences

The majority of processes in the SM have relatively simple leading-order amplitudes, with few diagrams contributing and no loops present in any of the Feynman dia-

grams[1], these are often referred to as *tree-level* or *Born-level* amplitudes. As noted in the previous section, this picture swiftly gains in complexity above the leading order. Truncating Eq. (1.3.9) at the NLO term, we obtain the NLO cross section:

$$\hat{\sigma}^{\mathrm{NLO}} = \alpha_s^k K^{\mathrm{LO}} + \alpha_s^{k+1} K^{\mathrm{NLO}}. \tag{1.3.21}$$

In terms of amplitudes, those contributing to the NLO cross section include the LO as well as amplitudes containing *real* and *virtual* emission corrections. Real emission amplitudes (at NLO) contain one more external particle than the LO. Virtual emission amplitudes contain one additional internal particle, forming a loop. This makes the expression for the NLO cross section more complex as the virtual- and real-emission amplitudes live in different phase spaces. The NLO partonic cross section is given in terms of these amplitudes as:

$$\hat{\sigma}^{\mathrm{NLO}} = \int \mathrm{d}\mathbf{\Phi}_0 \frac{1}{\mathcal{F}} \left(\overline{|\mathcal{M}^{\mathrm{LO}}|^2} + 2\,\mathrm{Re}\,\overline{\mathcal{M}^{\mathrm{LO}} \left(\mathcal{M}^{\mathrm{virtual}}\right)^*} + \int \mathrm{d}\mathbf{\Phi}_1 \overline{|\mathcal{M}^{\mathrm{real}}|^2} \right), \tag{1.3.22}$$

with $\mathbf{\Phi}_1$ the Lorentz-invariant phase space[2] over the additional real emission above LO ($\mathbf{\Phi}_0$), and the superscripts of the amplitudes indicate which parts of the process they correspond to. For compactness, Eq. (1.3.22) can be summarised as:

$$\hat{\sigma}^{\mathrm{NLO}} = \int \mathrm{d}\mathbf{\Phi}_0 \left(B(\mathbf{\Phi}_0) + \alpha_s V(\mathbf{\Phi}_0) + \int \mathrm{d}\mathbf{\Phi}_1 \alpha_s R(\mathbf{\Phi}_1) \right), \tag{1.3.23}$$

where B is the LO term, V is the term for the virtual corrections (with identical phase space to the LO), and R the real-correction term. This notation will become useful when we discuss matching and merging to parton showers in Sec. 2.3.3, and when we discuss NLO calculations in Monte Carlo event generation (Sec. 1.5.2).

[1] A notable exception is Higgs production through the gluon-gluon fusion mechanism, whose interaction is mediated by a massive quark loop at leading order.

[2] The notation here differs slightly from Eq. (1.3.8) where the subscript indicates the multiplicity. Here $\mathbf{\Phi}_n$ denotes the additional phase space with n emissions above LO.

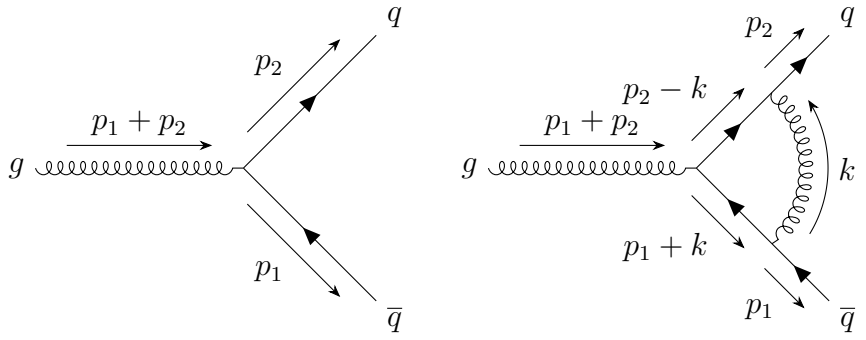

(a) LO (b) virtual correction

Figure 1.3: The gluon-quark-antiquark ($gq\overline{q}$) vertex in QCD at LO (a) and an example of a virtual loop correction (b). The momentum $p_1 + p_2$ of the gluon is incoming while p_1 and p_2 are both outgoing.

Loops and Renormalisation

Loops at higher orders induce corrections to the Feynman rules. The LO vertex term between a gluon and a quark and antiquark is shown in Fig. 1.3(a) and has Feynman rule $ig_s\gamma^\mu t^{a,ij}$, where the antiquark has colour index i and the quark has colour j in the fundamental representation, and the gluon has colour index a in the adjoint. Denoting the general vertex rule by $ig_s\Gamma^{\mu,a,ij}$, we can evaluate the vertex at different orders in perturbation theory. The virtual correction Fig. 1.3(b) contains a loop, formed by connecting a gluon propagator to the outgoing quarks. There is an unconstrained momentum k that runs through the loop which introduces a loop integral. The NLO part of the vertex is given by the loop integral:

$$\Gamma^{\mu,a,ij}_{\text{NLO}}(p_1,p_2,m) := 4\pi\alpha_s \cdot t^{b,ik} \cdot t^{a,kl} \cdot t^{b,lj} \int \frac{\mathrm{d}^4k}{(2\pi)^4} \frac{\gamma_\nu(\gamma\cdot p_2 - \gamma\cdot k + m)\cdot\gamma^\mu\cdot(\gamma\cdot p_1 + \gamma\cdot k + m)\gamma^\nu}{\left[(p_2-k)^2 - m^2\right]\cdot k^2 \cdot \left[(p_1+k)^2 - m^2\right]}. \tag{1.3.24}$$

This integral over the loop momentum is logarithmically divergent since the limits are unbounded from above. We refer to a divergence due to large loop momentum as an *ultraviolet* (UV) divergence [25], since in QED this would correspond to photons of large energy.

The integrals of this form arising in perturbation theory are *regularisable* i.e. we

can decompose them into their finite and divergent parts. We summarise broadly the procedure of *dimensional regularisation* most commonly used to regularise loop integrals in perturbation theory. This method is often seen as most suitable as the results it yields are both Lorentz- and gauge-invariant [25].

In dimensional regularisation (often abbreviated to dim. reg.) we work in $d := 4-2\epsilon$ space-time dimensions for some small $\epsilon > 0$ and *analytically continue* the integrals such that we may obtain analytic expressions of their divergent (in $d = 4$) parts. We can recover the original integral at any stage by taking $\epsilon \to 0$. To maintain dimensionality we introduce a scale of mass dimension +1 called the *renormalisation scale* μ_R, which transforms our integration measure:

$$\frac{\mathrm{d}^4 k}{(2\pi)^4} \to \mu_R^{2\epsilon} \frac{\mathrm{d}^{4-2\epsilon} k}{(2\pi)^{4-2\epsilon}}. \tag{1.3.25}$$

We may then follow the stages in Ch. 7 of ref. [25] (which focuses on QED though the discussion generalises) to work through the integration and obtain a Laurent series expansion for the integrals. Referring to an arbitrary integral $\mathcal{I}$ we may write:

$$\mathcal{I} = \frac{C_{-2}}{\epsilon^2} + \frac{C_{-1}}{\epsilon} + C_0 + \mathcal{O}(\epsilon), \tag{1.3.26}$$

where the divergent part is contained in the poles in ϵ, ϵ^2 and the rest of the integral is finite.

With regularisation we can calculate the finite parts of the integrals, however all we have done so far is express the (UV-)divergent parts in terms of unphysical poles. We know that the final result must be free of divergences as these are not observed in nature, thus we include the poles in the definitions of the *bare* quantities entering our theory (i.e. the fields, couplings and masses). This is the process of *renormalisation* and elegantly ensures that calculable quantities from our theory are free of UV divergences [25].

Instead of using the interaction term of the QCD Lagrangian at LO, we can represent the term for the vertex as a perturbative expansion in the strong coupling:

$$\Gamma^{\mu} = \Gamma^{\mu,a,ij}_{\mathrm{LO}} + \Gamma^{\mu,a,ij}_{\mathrm{NLO}} + ..., \tag{1.3.27}$$

where $\Gamma^{\mu,a,ij}_{\text{LO}} = \gamma^\mu t^{a,ij}$. Each subsequent term contributes an additional power of $4\pi\alpha_s$. One can use the vertex term expanded to the relevant accuracy for the perturbative expansion.

To ensure we can perform calculations this way we need to redefine the *bare* parameters in the Lagrangian to *physical* quantities with divergences absorbed into the normalisation [25]. We write:

$$\mathcal{L} = \mathcal{L}_{\text{renormalised}} + \mathcal{L}_{\text{counter-terms}}, \tag{1.3.28}$$

where the terms in $\mathcal{L}_{\text{renormalised}}$ are formed from the physical renormalised quantities of our theory. The fields, for example, are rescaled from their bare formulation to the physical:

$$\begin{aligned} \psi_{n,\text{bare}} &:= \sqrt{Z_2}\psi_n, \\ A^{a,\mu}_{\text{bare}} &:= \sqrt{Z_3}A^{a,\mu}, \\ c^a_{\text{bare}} &:= \sqrt{Z_2}c^a, \end{aligned} \tag{1.3.29}$$

where we use the expansion of the vertex $\Gamma^{\mu,a,ij}$ (as well as the *self-energies* of the particles and the other vertices) to absorb the poles in ϵ into their definition[1]. Since this does not produce an identical Lagrangian to the bare Lagrangian we started with, we need to add counter-terms containing just the unphysical, divergent parts. We express the coefficients Z_j as:

$$Z_j = 1 + \delta_j, \tag{1.3.30}$$

with δ_j containing the divergence (as well as part of the finite expression as we will see with renormalisation schemes). The coefficients of each field in the counter-term Lagrangian is thus δ_j so that the bare field is reconstructed by the sum.

Thus when we calculate a diagram above LO, we use the Feynman rules obtained at the order at which the diagram manifests, knowing that the UV divergences cancel in all of our final expressions. This is because they have been absorbed into the

[1]We have shown the renormalisation factor for ghosts c^a, however if we work in a gauge that does not introduce ghosts to the theory, this term is not needed.

definition of our physical fields, masses and couplings [25]. The UV divergences then cancel exactly in the limit $\epsilon \to 0$ as required for calculations in our theory.

Running coupling

The renormalisation scale μ_R was introduced in Eq. (1.3.25) to retain dimensionality of the integral measure and is not a physical feature of our theory, thus a physical quantity observable in experiment must be independent of this scale. Denoting an arbitrary observable quantity by $\mathcal{R}(\{p_j\}, \alpha_s, \{m_j\})$ where the outgoing momenta are indexed by p_j and the participating fields in the interaction have masses m_j, we can express this invariance requirement as [30]:

$$\mu_R \frac{\mathrm{d}}{\mathrm{d}\mu_R}\mathcal{R} \equiv \left[\mu_R \frac{\partial}{\partial \mu_R} + \mu_R \frac{\mathrm{d}\alpha_s}{\mathrm{d}\mu_R}\frac{\partial}{\partial \alpha_s} + \mu_R \sum_j \frac{\mathrm{d}m_j}{\mathrm{d}\mu_R}\frac{\partial}{\partial m_j}\right]\mathcal{R} = 0. \tag{1.3.31}$$

Here we have removed the arguments of $\mathcal{R}$ for concision. We may define the *β-function* for the coupling α_s and the *anomalous mass dimensions* γ for the masses m_j as:

$$\begin{aligned} \beta(\alpha_s) &:= \mu_R \frac{\mathrm{d}\alpha_s}{\mathrm{d}\mu_R}, \\ \gamma(m_j) &:= \frac{\mu_R}{m_j}\frac{\mathrm{d}m_j}{\mathrm{d}\mu_R}. \end{aligned} \tag{1.3.32}$$

This allows us to rewrite Eq. (1.3.31) as:

$$\mu_R \frac{\mathrm{d}}{\mathrm{d}\mu_R}\mathcal{R} \equiv \left[\mu_R \frac{\partial}{\partial \mu_R} + \beta(\alpha_s)\frac{\partial}{\partial \alpha_s} + \sum_j m_j \gamma(m_j)\frac{\partial}{\partial m_j}\right]\mathcal{R} = 0, \tag{1.3.33}$$

which is the *renormalisation group equation* in QCD for the observable $\mathcal{R}$. Similar relations may be obtained by analysing the correlation functions or n-point *Greens functions* of a theory. We point the reader to Ch. 12 of ref. [25] and Ch. 28 of ref. [24] for detailed derivations from the correlation functions.

The implications of scale-independence of observables are that the renormalised couplings and masses in the theory *run*, i.e. they depend on μ_R non-trivially. The quantities defined in Eq. (1.3.32) have expansions in α_s which means they can be expanded to orders in α_s not unlike the cross section and other observable quantities.

Renormalisation does not imply that we may only absorb infinities into the defini-

tions of fields and quantities entering our theory. Indeed, we may carry finite parts of the loop integrals in our renormalisation. Different prescriptions for expressing the renormalised quantities are referred to as *renormalisation schemes*. The minimal subtraction (MS) scheme subtracts only the poles as they appear in Eq. (1.3.26) while the $\overline{\text{MS}}$ (MS-bar) scheme absorbs also the constant term: $-\gamma^E + \log(4\pi)$ (with $\gamma^E = 0.57721...$ the Euler-Mascheroni constant) to the counter-terms, since this generally appears with the poles in loop integrals as part of the finite C_0 term in the expansion [25]. Choosing a different renormalisation scheme will produce different running of the coupling and of the masses i.e. $\alpha_s^{\overline{\text{MS}}}(\mu_R) \neq \alpha_s^{\text{MS}}(\mu_R)$.

The QCD β functions are power series in α_s:

$$\beta(\alpha_s) = -\alpha_s \sum_{n=0}^{\infty} \beta_n \left(\frac{\alpha_s}{4\pi}\right)^{n+1}, \tag{1.3.34}$$

where terms β_n may be calculated by renormalising the theory to $n+1$ loops. The one-loop correction coefficient β_0 is given by [30]:

$$\beta_0 = \frac{11}{3} C_A - \frac{4}{3} n_f T_R, \tag{1.3.35}$$

For QCD with $N_c = 3$ and quarks transforming in the fundamental representation (with $T_R = 1/2$) we can express the one-loop β-function as $\beta_0 = 11 - \frac{2}{3} n_f$. We often assume the quarks in the theory are massless and thus the number of fermions we choose to include in the theory can vary depending on the application. While there are six distinct Standard Model quarks charged under the strong force, many often work in schemes assuming a smaller number of massless quarks — at the scales of hadron collider experiments, this is a solid approximation. Five flavour schemes (excluding the top quark) are most often used since the top mass is so large that it is only produced at extremely large centre-of-mass (CoM) energy.

The result up to three loops is quoted in Ch. 2 of ref. [30] while the most recent calculations of the running of α_s are five-loop accurate. We direct the reader to ref. [33] for explicit expressions of the SU(3) QCD β-functions up to this accuracy and note that the normalisation Baikov and collaborators use in this study differs

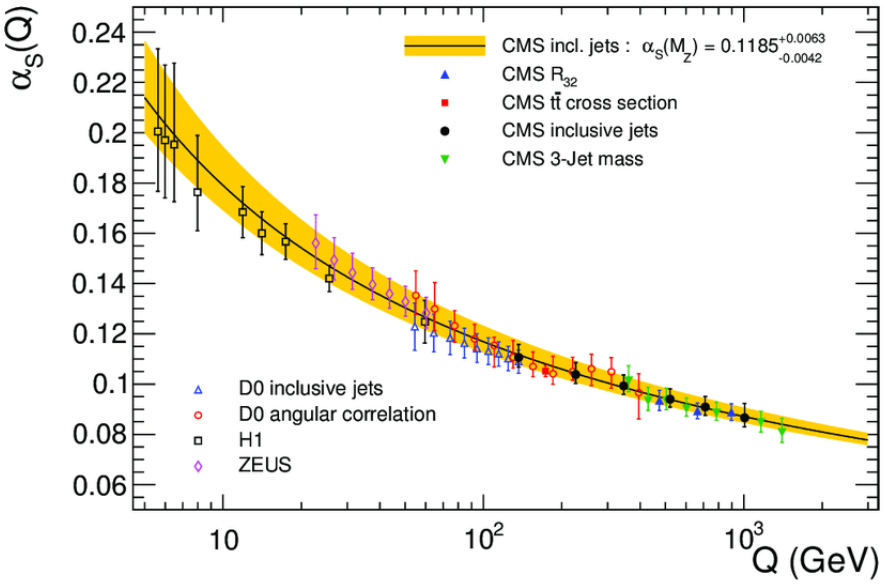

Figure 1.4: The running of α_s as compiled from several different experimental results. The figure is from the proceedings of the 2015 workshop *High precision measurements of α_s: From LHC to FCC-ee* at CERN [2]

slightly from the convention used by Ellis and collaborators in ref. [30], though the results are equivalent. The higher-order terms are naturally dependent on the renormalisation scheme used.

QCD is an *asymptotically free* theory. This means that the strength of the coupling diminishes with increasing energy scale as can be seen in Fig. 1.4 which displays this running. As QCD approaches the non-perturbative limit, confinement is observed and the free particles of the theory form *hadrons*. Thus to probe the perturbative theory, we need to examine the structure of the hadrons we observe in nature at significantly higher energy scales.

We may solve the equation for the running coupling by expanding the β-function to the required order in α_s, to one loop we arrive at:

$$\alpha_s(\mu) = \frac{\alpha_s(\mu_0)}{1 + \frac{\alpha_s(\mu_0)}{4\pi}\beta_0 \log \frac{\mu^2}{\mu_0^2}}, \tag{1.3.36}$$

where we have used the definition of ref. [30] for the β_n coefficients. Plain in this expression is the region for which the theory is perturbative. We may calculate the scale for which $\alpha_s(\mu)$ diverges to see where perturbativity breaks down, given the

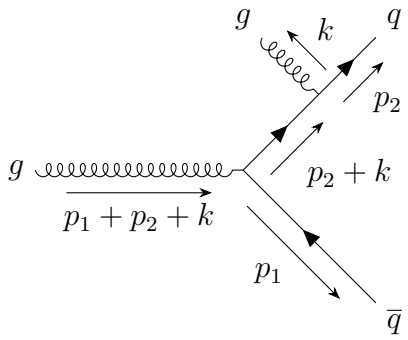

Figure 1.5: A real emission correction to the QCD gluon-quark-antiquark vertex of Fig. 1.3(a)

value of α_s at a certain reference scale. Generally, the mass of the Standard Model Z boson is used for this scale as experimental data gives robust constraints on this value. Results from CMS in 2020 [34] give $\alpha_s(m_Z) = 0.1175^{+0.0025}_{-0.0028}$, which means we can calculate the scale at which perturbative QCD breaks down ()Λ_{QCD}) and find it to be at the scale $\Lambda_{\text{QCD}} = \mathcal{O}(200)$ MeV (dependent on the renormalisation scheme), though this is only a LO-accurate statement since we used the one-loop running to determine the scale.

Infrared divergences and the KLN theorem

Returning to the loop integral for the vertex correction Eq. (1.3.24) corresponding to the vertex shown in Fig. 1.3(b), we can observe that the integrand diverges in the limit of $k^2 \to 0$, i.e. when the internal gluon becomes on-shell. In this case, the momentum of the gluon is small (or *soft*). We refer to this as an *infrared* (IR) divergence (again naming the regime by analogy to QED — where this would correspond to a soft photon). These are treated differently than UV divergences — which we had to renormalise our theory to accommodate.

This is where the role of the real emission corrections, $\mathcal{M}^{\text{real}}$ from Eq. (1.3.22), enters. Referring to Fig. 1.5, we can see an example of the real emission corrections, where an on-shell gluon is emitted from a final state quark.

If this configuration manifests in an amplitude (assuming the gluon with mo-

mentum $p_1 + p_2 + k$ is connected to some hard process), it contributes a factor:

$$\overline{u}_i(p_2)\varepsilon^*_{b,\mu}(k) \cdot (ig_s)^2 \cdot t^{a,ik} \cdot t^{b,kj} \cdot \gamma^\mu \frac{i\left(\gamma \cdot p_2 + \gamma \cdot k - m\right)}{\left(p_2 + k\right)^2 - m^2} \gamma^\nu \cdot v_j(p_1), \tag{1.3.37}$$

to the amplitude for that diagram, where b is the adjoint colour index of the gluon real emission with momentum k. This is divergent when the internal quark with momentum $p_2 + k$ becomes on-shell. The divergence is associated to the limit of $k \to 0$ since the on-shell external leg has mass m and momentum p_2 which implies $(p_2)^2 = m^2$. The amplitude contains an extra final state particle, the emitted gluon, which means the contribution to the cross section has to be integrated over the larger Lorentz-invariant phase space $\mathbf{\Phi}_1$.

In the limit that the emitted gluon is soft, and the quark leg is massless, we may make the *eikonal approximation* [35]:

$$\frac{i\left(\gamma \cdot p_2 + \gamma \cdot k\right)}{\left(p_2 + k\right)^2} \to \frac{i\gamma \cdot p_2}{2p_2 \cdot k}, \tag{1.3.38}$$

by assuming that the the energy of p_2 is much larger than that of k. This approximation is commonly taken and can simplify calculations greatly for matrix elements, especially for higher-order virtual corrections [36].

Examining the denominator of Eq. (1.3.37) more closely we may simplify the square of the momentum and express it as:

$$\left(p_2 + k\right)^2 - m^2 = 2p_2 \cdot k = E_2 E_k \left(1 - \sqrt{1 + \frac{m^2}{E_2^2}} \cos\vartheta\right), \tag{1.3.39}$$

where E_2 (E_k) corresponds to the energy of p_2 (k), and we have denoted by ϑ the angle (in 3-dimensional Euclidean space) between $\mathbf{p_2}$ and $\mathbf{k}$. We can see here that there is a *soft* divergence when either $\mathbf{k}$ or $\mathbf{p_2}$ approach $\mathbf{0}$. Similarly, approximating the fermion mass as zero[1] introduces a *collinear* divergence when the angle between the two momenta approaches 0 or 2π. All of these are part of the infrared-divergent structure of the theory.

[1]This is a generally taken approximation at hadron collider experiments where the energies probed are several orders of magnitude larger than the light quark and lepton masses.

After integration over $\mathbf{\Phi}_1$, these divergences manifest as poles with opposite signs between the real and virtual corrections[1], meaning they cancel exactly order-by-order in perturbation theory. This is shown by the KLN (named for the study of Kinoshita [37], and of Lee and Nauenberg [38] which explore independently the divergent structure of Feynman amplitudes focusing on QED) theorem, which demonstrates that loops with soft momenta and soft real emissions are *degenerate*, meaning that the divergence cancels for any inclusive infrared-safe observable (we discuss observables and infrared safety in Sec. 1.4).

The notion of inclusive and exclusive quantities is hugely relevant to the subject matter of this thesis. A quantity is described as *inclusive* if part of the contribution has been left unspecified and the associated degrees of freedom integrated over. Inclusivity must always be referred to in relation to some quantity, e.g. for jet production at hadron colliders, inclusive generally refers to the jet multiplicity since jets are produced from many different sources that cannot all be taken into account in a single calculation (see Sec. 1.4 for discussions of jets). When we discuss inclusivity in the context of `HEJ` resummation when considering the`HEJ`+Pythia merging of Ch. 3, the meaning is analogous, namely that there are regions of phase space not targeted by the resummation, thus the resummed cross section must be inclusive in those regions.

Exclusivity refers to the opposite situation, namely that the phase space configuration under consideration is fully determined in terms of particles, their quantum numbers, and their momenta. Differential observables (which we discuss in Sec. 1.4) are exclusive quantities in this regard. Similarly, for theoretical predictions, the exclusive regions of phase space are those where all degrees of freedom are explicitly calculated.

In summary, we have a fully regularised, renormalised expression for the cross section at NLO of Eq. (1.3.21). We may generalise this to higher orders, considering

[1]Dimensional regularisation can be used to show this, and is normally performed in $d = 4 + 2\epsilon$ dimensions for $\epsilon > 0$ to reflect that the integral diverges for $d \leq 4$ in the IR regime.

all combinations of real and virtual corrections that appear at required order in perturbation theory. Since the theory is UV-renormalised, we know that the high energy behaviour of our theory is accounted for. As a consequence of the KLN theorem, the infrared behaviour cancels providing all contributions are appropriately evaluated and integrated over their respective phase spaces. This becomes increasingly difficult above NLO. For example, at NNLO one needs to consider diagrams containing real-real, real-virtual and virtual-virtual corrections.

All-orders approaches

While fixed-order perturbation theory is a useful tool, expanding to low orders in the coupling can be a limiting approximation. Often the couplings α_i are not the parts of the amplitude which lead to divergences or slow convergence in an amplitude, but large logarithms L of widely differing scales can arise which make the product $\alpha_i^m L^m$ divergent or slowly convergent [30].

In some cases, these logarithms may be analytically *resummed* to *all orders*. Examples of these include resummation of large logarithms of $\hat{s}/\hat{t}$ in QCD [39] which gives rise the the BFKL formalism [40–44], and which inspires the approach of *High Energy Jets* we expand on in Sec. 2.2. The soft-collinear regime discussed here also gives rise to large logarithms in QCD [30, 39], and these are resummed by *parton showers*, which we discuss in Sec. 2.3. Resummation is a central component of the work presented in this thesis and we expand on it in greater detail, focusing on developments and applications of these formalisms, in Ch. 2. Ch. 3 presents a method of merging *High Energy Jets* resummation with a parton shower, and Ch. 4 presents resummed *High Energy Jets* predictions for inclusive $pp \to H + 1j$ at the LHC.

1.3.3 Factorisation in QCD

QCD, as it manifests in nature, is non-perturbative and only bound states are observable at macroscopic scales. To connect the perturbative theory probed at hadron collider experiments to this reality, we need to account for the non-perturbative

aspects of the theory. The cross section of Eq. (1.3.7) thus corresponds to the *hard* interaction i.e. the interaction at perturbative scales.

An important result for the case of QCD is that the non-perturbative and perturbative regimes *factorise*, i.e. we can consider them independently of each other. Thus we need integrate the hard cross section over the momentum distribution of quarks inside their parent hadrons and apply *hadronisation* corrections to the final states of our hard predictions to account for the observation of bound states in the detector.

Parton distribution functions

The *parton distribution functions* (PDFs) $f_{i/A}(x_i)$ in QCD express the probability of observing a parton i from the parent hadron A carrying fraction x_i of the parent hadron energy [39, 45]. However, when calculating these objects perturbatively we quickly encounter divergences in the infrared region as the PDF carries no scale dependence.

We may resolve this issue in a manner analogous to our treatment of UV divergences in the previous section, namely we define a non-physical *bare* PDF $f_{i/A}(x_i)$ and introduce a hardness scale μ_F — the *factorisation scale* which separates the soft from the hard region [30]. We can then observe the *physical* PDFs $f_{i/A}(x_i, \mu_F^2)$ which carry a scale dependence and have the divergences absorbed into their definition. The *factorisation scheme* is then the counterpart of the renormalisation scheme and prescribes which finite parts to carry in the counter-terms added to cancel the divergence.

The evolution of the PDFs is governed by the DGLAP equations [30]:

$$\begin{aligned} t\frac{\partial}{\partial t}\begin{pmatrix} q_i(x,t) \\ g(x,t) \end{pmatrix} &= \frac{\alpha_s(t)}{2\pi}\sum_{q_j,\bar{q}_j}\int_x^1 \frac{\mathrm{d}\xi}{\xi} \\ &\times \begin{pmatrix} P_{q_iq_j}\left(\frac{x}{\xi},\alpha_s(t)\right) & P_{q_ig}\left(\frac{x}{\xi},\alpha_s(t)\right) \\ P_{gq_j}\left(\frac{x}{\xi},\alpha_s(t)\right) & P_{gg}\left(\frac{x}{\xi},\alpha_s(t)\right) \end{pmatrix} \begin{pmatrix} q_j(\xi,t) \\ g(\xi,t) \end{pmatrix}, \end{aligned} \tag{1.3.40}$$

where we have defined $t = \mu_F^2$ and denoted the PDF for the gluon by $g(x,t)$ and for

quark i by $q_i(x,t)$. This equation applies itself in the $(2n_f+1)$-dimensional space spanned by the gluon, the quarks and antiquarks.

The functions $P_{ab}(z,\alpha_s(t))$ are the DGLAP *splitting functions*[1]. These functions have perturbative expansions e.g.:

$$P(z,\alpha_s) = P^{(0)}(z) + \frac{\alpha_s}{2\pi}P^{(1)}(z) + ..., \tag{1.3.41}$$

with each subsequent term a higher-order correction. The DGLAP evolution equation resums (see Ch. 2) large logarithms of the factorisation scale and thus controls the divergences similar to the running of the strong coupling [45].

These splitting functions may be calculated in perturbation theory and carry a satisfying physical interpretation as they manifest. We consider a n-parton process with matrix element $\mathcal{M}_n$ and *split* one of the external partons a to a collinear pair b,c. The $n+1$ matrix element in the limit that the intermediate parton a has much larger virtuality than the collinear partons b and c, is related to the lower multiplicity matrix element by [30]:

$$\mathrm{d}t\mathrm{d}z\int \mathrm{d}\phi \frac{1}{16\pi^2}\frac{\overline{|\mathcal{M}_{n+1}|^2}}{\overline{|\mathcal{M}_n|^2}} \sim \frac{\mathrm{d}t}{t}\mathrm{d}z\frac{\alpha_s}{2\pi}P_{ba}(z). \tag{1.3.42}$$

Here $P_{ba}(z)$ is the appropriate splitting function for the $a \to bc$ splitting [30] at energy fraction z. The quantity t now is referred to as the *evolution variable* or *ordering variable*. As an example, we illustrate the (leading order) splitting of $q \to qg$ in Fig. 1.6 and display the corresponding splitting function below [30]:

$$\overline{|\mathcal{M}_{n+1}|^2} \sim \frac{4g_s^2}{t}\overline{|\mathcal{M}_n|^2}P_{qq}(z), \tag{1.3.43}$$

with

$$P_{qq}(z) = C_F\frac{1+z^2}{1-z}. \tag{1.3.44}$$

This is the LO term in the expansion of Eq. (1.3.41). The leading-order splitting functions are listed in Ch. 4 of ref. [30] (where they are shown with their divergences

[1]We have previously used the scale as the argument of α_s rather than the square, the two notations refer in either case to the same evolution and different sources use different conventions.

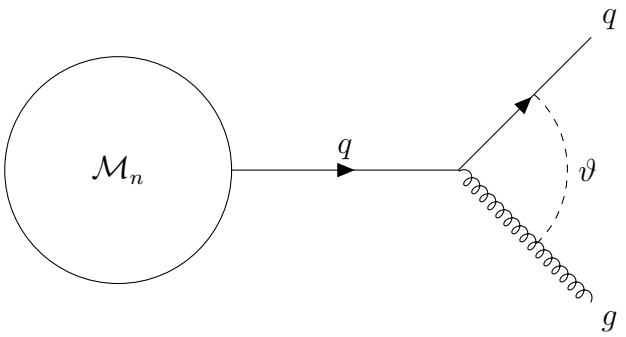

Figure 1.6: Schematic of the splitting $q \to gq$ with opening angle ϑ at LO in QCD.

unregulated) as well as several higher order corrections. We explore the application of these splitting functions in Sec. 2.3 and explore how they are used in resummation of soft and collinear logarithms arising to all orders in perturbation theory with parton showers [39].

QCD factorisation theorem

The final building block for the treatment of QCD we discuss is *factorisation*, where we may schematically separate the perturbative and non-perturbative regions and treat each independently. This is expressed most eloquently by the QCD factorisation theorem for hadron collisions [45]:

$$\sigma_{AB\to\Omega} = \sum_{a,b} \int \mathrm{d}x_a \mathrm{d}x_b \cdot f_{a/A}\left(x_a, \mu_F^2\right) \cdot f_{b/B}\left(x_b, \mu_F^2\right) \cdot \hat{\sigma}_{ab\to\hat{\Omega}}(x_a p_A, x_b p_B, \mu_R^2, \mu_F^2). \tag{1.3.45}$$

which expresses the hadronic cross section for a process involving a scattering between parent hadrons A, B to the final state Ω (corresponding to a partonic final state $\hat{\Omega}$) we wish to observe. Importantly, this is an *inclusive* quantity since we cannot observe the states we require in isolation due to hadronisation that takes place at lower energies/later times to the hard interaction. The non-perturbative nature of the initial state is encoded in the convolution with the PDFs. The perturbative part is described by the *partonic cross section* $\hat{\sigma}$ which is calculated using the Feynman rules of the theory (or with any other valid perturbative framework) as described in Sec. 1.3. The form of this partonic cross section for the hard, perturbative process is

given in Eq. (1.3.7). The energy fractions x_a and x_b relate the partonic centre-of-mass energy of interaction $\hat{s}$ to the hadronic centre-of-mass energy s by:

$$\sqrt{\hat{s}} = x_a x_b \sqrt{s}, \tag{1.3.46}$$

Just as we measure the total cross section, we may measure *distributions* of observable quantities $\mathcal{O}$. These are differential cross sections $\mathrm{d}\sigma/\mathrm{d}\mathcal{O}$. We describe observables and how these are constructed and calculated in Sec. 1.4.

The partonic cross section must also be supplemented with further non-perturbative corrections to account for hadronisation, for which there are only phenomenological descriptions (rather than descriptions one may derive explicitly from the theory). As with the PDFs, we may factorise the non-perturbative hadronisation corrections from the perturbative partonic cross section. When we discuss general purpose Monte Carlo (GPMC) event generators in Sec. 1.5.2 we briefly discuss the computational implementation of hadronisation models, focusing on the method of *string hadronisation* in Pythia [46, 47].

It is important to mention that other methods of working with QCD (or QFT in general) have been developed that do not make use of the factorisation of the theory into a perturbative and non-perturbative region. The most famous example of such a method is *lattice QCD* which calculates correlation functions in a finite, discretised space-time. This allows for calculations of non-perturbative quantities in QCD from first principles of the theory, though perturbative scattering amplitudes cannot be calculated with lattice QCD. The *Particle Data Group* (PDG) [48] review of lattice QCD provides a robust overview of this formalism and lists several core achievements of the theory.

Estimating theoretical uncertainty

The missing higher orders from theoretical predictions are the major source of theoretical uncertainty. Since the cross sections carry dependence on the factorisation and renormalisation scales, uncertainties can be estimated on predictions by varying

these scales independently (often by factors of 2 and 0.5) to produce an envelope around the central theoretical prediction. Since the difference between $\alpha_s(\mu_R)$ and $\alpha_s(\mu'_R)$ is $\mathcal{O}(\alpha_s^2(\mu'_R))$, this procedure gives an estimate of how the missing higher orders resummed in the running of the strong coupling would impact the matrix elements. Similarly, altering the factorisation scale accounts for missing higher orders in DGLAP evolution.

It is important to stress that the scale variation calculations can not account comprehensively for all missing higher-order effects since these are not treated completely by the running of α_s or by DGLAP evolution. Scales are chosen in perturbative calculations to be characteristic of the events in consideration. No standard framework is established to determine the meaning of "characteristic" in scale assignment and as such different functional forms of the scale can yield differing results. The most commonly accepted definition of "characteristic" is to choose a scale that minimises the size of logarithms of ratios of scales that can arise in the calculation — most typically the ratios are between process invariants and the chosen renormalisation scale. for multi-scale processes this becomes increasingly difficult to define so the scale-setting will aim to achieve a "middle-ground" between the logarithms that emerge.

An example of a commonly used dynamic scale in jet[1] studies is $H_T/2$, where H_T is the scalar sum of observed jet transverse momenta. One can see from this that events with high multiplicities and large transverse momenta will produce cross sections evaluated with smaller α_s if $H_T/2$ is chosen as the renormalisation scale.

In the next section we lay the groundwork to connect the theoretical formalism we have discussed to the practical considerations of constructing experiments and observables at hadron collider experiments.

[1]We formally define jets in the next section, Sec. 1.4.

1.4 Experimental Observables at Hadron Colliders

The hadronic cross section in Eq. (1.3.45) is a fully inclusive quantity, meaning that all degrees of freedom have been fully integrated over. This quantity is of limited use for comparisons to theoretical predictions, so instead we construct observables from the observed final states at detectors in hadron collider experiments. This allows us to produce differential cross sections or *distributions* for these observables, since they are dependent on the kinematical phase space. Given an observable quantity which is a function of the observed final state $\mathcal{O}(\Omega)$ we write:

$$\begin{aligned}\sigma_{AB\to\Omega}[\mathcal{O}] = &\sum_{a,b}\int \mathrm{d}x_a \mathrm{d}x_b \cdot f_{a/A}\left(x_a, \mu_F^2\right) \cdot f_{b/B}\left(x_b, \mu_F^2\right) \\ &\cdot \mathcal{O}(\Omega) \\ &\cdot \hat{\sigma}_{ab\to\hat{\Omega}}(x_a p_A, x_b p_B, \mu_R^2, \mu_F^2).\end{aligned} \tag{1.4.1}$$

Interpreting the squared amplitude as a probability, we see that this is similar in structure to an expectation value for the observable. The observable itself must depend on the final state kinematics as this is the information that would be detected at experiments. Histograms are constructed for such observables by splitting them into bins e.g.

$$\mathcal{O}(\Omega) = \prod_k \mathcal{O}^{(k)} \Theta\left(\mathcal{O} - \mathcal{O}^{(k)}_{\text{low}}\right) \Theta\left(\mathcal{O}^{(k)}_{\text{high}} - \mathcal{O}\right), \tag{1.4.2}$$

with $\mathcal{O}$ in the arguments of the Heaviside Θ functions being the value of the observable given the kinematic configuration. We may also apply *cuts* on the available phase space depending on the geometric constraints of the detector, or the objectives of a specific analysis.

With QCD final states, the unconfined products of the hard partonic process may not be observed in the detector since only colour-confined states occur at observable scales. Indeed detectors at the LHC such as ATLAS [49] and CMS [50] observe the hadronised products of parton evolution as they enter and decay in the hadronic calorimeters. Thus, if we restrict ourselves for the moment to the hard partonic

region, we require observables to be *infrared-safe* if we are to meaningfully compare predictions to experimental data [30]. This means that performing calculations for observables with partonic final states should not change in the limit of soft and collinear emissions. More precisely formulated:

$$\begin{aligned} &\mathcal{O}_{n+1}\left(p_1, ..., p_i, ..., p_n\right) \xrightarrow{p_i \to 0} \mathcal{O}_n\left(p_1, ..., p_{i-1}, p_{i+1}, ..., p_n\right), \\ &\mathcal{O}_{n+1}\left(p_1, ..., p_i, p_j, ..., p_n\right) \xrightarrow{\mathbf{p_i} \| \mathbf{p_j}} \mathcal{O}_n\left(p_1, ..., p_i + p_j, ..., p_n\right). \end{aligned} \tag{1.4.3}$$

In the top line we require that our observable for $n+1$ final state particles tends to the n-particle observable in the limit that one of the emissions is soft. The second line requires that for p_i and p_j collinear, the observable for $n+1$ final state particles tends to the n-particle observable with e.g. p_j removed and p_i replaced with the sum $p_i + p_j$ (or vice versa).

Four-momenta of particles incident on the calorimeters in a detector are not directly measurable and must be deduced from the available information. The detectors at the LHC are cylindrically symmetric and thus experimenters work in a coordinate system with the z-axis running along the beam pipe. This means the polar angle θ and the azimuthal angle ϕ with respect to the beam axis are readily available from the location of energy deposits in the calorimeters[1].

In Fig. 1.7 we display a transverse slice of the CMS detector, and discuss how particles are observed in collider experiments. The silicon tracker tracks the paths of particles produced in the interaction that are incident on the calorimeters which record the presence of electrons and hadrons. The superconducting solenoid is used to bend particle tracks in such a way that their momenta may be determined.

The calorimeters record the energy deposits of the particles produced in an interaction and as such, one can directly measure the *transverse momentum* $p_\perp$ (also often written as p_T, and in bold-face when we discuss it as a two-dimensional vector).

Since the LHC collides hadrons[2] along the z axis, the centre of mass of the hard

[1] This is true given the polar angle is measured from an axis running vertically through the interaction point

[2] We chiefly consider proton-proton collisions in this thesis, though make reference to heavy ion collisions when we discuss general purpose Monte Carlo event generation in Sec. 1.5.2.

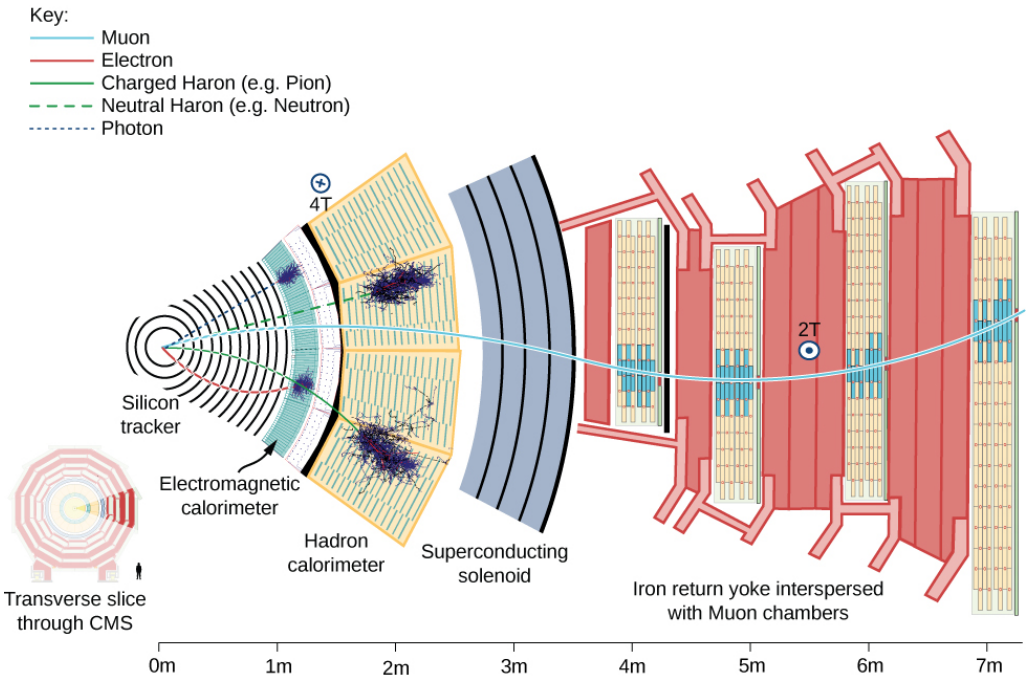

Figure 1.7: Transverse slice of the CMS detector with the z-axis pointing out of the page and the sequenced calorimeters in the plane of the page. Figure from ref. [3].

collision is not known exactly (unlike at a lepton-lepton collider) since it is the perturbative free quarks and gluons that interact rather than the hadrons.

Due to the azimuthal symmetry of the detector, we search for quantities Lorentz-invariant under boosts along the z-axis to reconstruct the four-momenta of produced particles in the lab frame. The azimuthal angle ϕ is by definition invariant for such boosts, however differences in the polar angle θ are not and as such we define the *pseudorapidity* η:

$$\eta = -\log\left[\tan\left(\frac{\theta}{2}\right)\right] \equiv \frac{1}{2}\log\frac{|\mathbf{p}| + p_z}{|\mathbf{p}| - p_z} \equiv \operatorname{arctanh}\left(\frac{p_z}{|\mathbf{p}|}\right). \tag{1.4.4}$$

This coincides with the *beam rapidity* (which we henceforth refer to just as the *rapidity* unless explicitly stated otherwise) in the limit that the particle is massless [30]. The rapidity y is given by:

$$y = \frac{1}{2}\log\frac{E + p_z}{E - p_z}. \tag{1.4.5}$$

While rapidities are not Lorentz-invariant for z-boosts, differences between two rapidities are (as are differences in η). From the azimuthal angle and the measured

polar angle (which gives us the rapidity) we can reconstruct four-momenta of particles incident on the detector as:

$$\begin{aligned}(E, p_x, p_y, p_z) &= (m_\perp \cosh y, p_\perp \cos\phi, p_\perp \sin\phi, m_\perp \sinh y),\\ m_\perp &:= \sqrt{m^2 + p_\perp^2}.\end{aligned} \tag{1.4.6}$$

Here $m_\perp$ is referred to as the *transverse mass*.

With these quantities defined we may return to the question of infrared safety and note again that partonic final states are not observable in the hadronic calorimeters. Thus we define *jets* as the IR-safe generalisations of the products of the hard interaction [30, 45, 51], following the observation that strong final state particles are detected in the calorimeters strongly correlated in narrow collimated beams rather than in isolation [25].

To formalise the definition of jets from this qualitative description we introduce *jet reconstruction algorithms* (or just jet algorithms) which recombine the energy deposits in the calorimeters as distributed in $y - \phi$ space [51]. The most widely used of these are the $k_\perp$-type (or k_T-type) algorithms which cluster particles according to the distance measure:

$$d_{ij} = \frac{\Delta R_{ij}^2}{R^2} \min\left\{p_{\perp i}^q, p_{\perp j}^q\right\}, \quad d_{iB} = p_{\perp i}^q, \tag{1.4.7}$$

with R the jet radius parameter, d_{iB} the generalised beam distance, and q an integer that defines the order of the clustering. We define the distance between particles i, j in $y - \phi$ space as:

$$\Delta R_{ij} = \sqrt{(y_i - y_j)^2 + (\phi_i - \phi_j)^2}. \tag{1.4.8}$$

The jet reconstruction process can be summarised as follows:

1. Find the minimum across all $\{d_{ij}, d_{iB}\}$.

2. If d_{ij} is the minimum, combine the particles i and j into one particle and return to step. 1.

3. If d_{iB} is the minimum, label particle i as a final state jet and remove particle

i from the list, return to step 1.

4. Continue until either the required number of jets have been identified (exclusive clustering) or until all particles have been clustered into jets (inclusive clustering) depending on what is required.

Provided the perturbative description is sufficiently comprehensive, the jets in an event should correspond to the jets resulting from clustering the final state partons with the same algorithms.

The choice $q = 2$ yields the $k_\perp$ algorithm, while $q = 0$ gives the Cambridge-Aachen (CA) algorithm [51]. A more recent jet algorithm favoured by experimenters at the LHC is the anti-$k_\perp$ (or $\overline{k_\perp}$) algorithm [52] which takes $q = -2$. From Eq. (1.4.7) we can see that this algorithm will cluster the harder partons first.

With the jets defined, forming infrared-safe observables from which to calculate distributions becomes straightforward. Rather than constructing observables from individual particles charged under QCD, we construct them for jet momenta and can calculate quantities in the differential phase space of the system i.e. pertaining to the momenta accessible from measurements of the final state. Using the phase space of the jets thus means the observables will be infrared-safe.

Such quantities include the $p_\perp$ of the jets in an event or the difference in $y - \phi$ space (ΔR) between any two jets (as well as myriad other quantities such as the invariant mass between any two jets). Jets in events are often indexed according to some order. The two most common forms of ordering are in hardness (i.e. jet 1 indexing the jet with the largest transverse momentum, 2 with the second largest, etc.) or in rapidity. In the case of rapidity ordering we refer to the jet with the smallest rapidity in an event as the most *backward* and that with the largest as the most *forward* (respectively denoted b and f). These ordering schemes can be used to define *dijet* systems, where two jets define much of the physics observed in the final state. Often the most forward and backward jets are chosen, or the two hardest jets, as the pair that forms the dijet.

Events containing electroweak boson decays e.g. $Z \to \nu\overline{\nu}$ or $W \to l\nu$ may be iden-

tified by *missing transverse momentum*. Since neutrinos are too weakly interacting to be directly detected at hadron colliders, events which produce them are easily identifiable since they appear to violate momentum conservation in the transverse plane. Measurements of the missing transverse momentum (often written as $p_{\perp,\text{miss}}$) are invaluable for identifying neutrino-producing weak decays at hadron colliders and constraining W and Z (and H) physics.

Next, we discuss how theoretical predictions can be obtained within perturbative frameworks. We introduce the Monte Carlo method of numerical integration, and discuss how it can be applied to produce theoretical predictions, including the widespread use of general purpose Monte Carlo event generators.

1.5 Monte Carlo Event Generation

Our treatment of the background behind producing predictions in perturbative QCD in the previous section has thus far been somewhat abstract with little explicit connection to how such calculations are performed. With descriptions of matrix elements evaluated in certain perturbative frameworks one still finds themselves far removed from the differential cross sections that may be produced from experiments. We have seen in Eq. (1.4.1) that differential cross sections are related to the matrix elements by a phase space integral. These integrals quickly climb in dimensionality for more complex on-shell final states and become (in the majority of cases) impossible to analytically evaluate. Experimental analyses also apply constraints to collect data which may complicate the phase space with cuts on certain observables and differing requirements for the observed jets in an event. Our theoretical formalism contains divergent quantities which cannot be evaluated numerically by their nature.

The most common methods for numerical integration in one dimension split the integration region into bins and interpolate the integrand as a polynomial in each bin [53]. Such methods include the trapezium rule (which interpolates linearly) and Simpson's rule (which interpolates to a quadratic polynomial). Such methods scale

poorly in computational time cost in higher dimensions. If, in one dimension, M function evaluations are required per bin, and we split the region into B bins, the computational cost scales as $\mathcal{O}(MB)$. In d dimensions, this scales exponentially as d increases, leading to costs of the order $\mathcal{O}((MB)^d)$. These methods quickly become infeasible for the high-dimensional phase spaces encountered in even the most simple cross sections at low perturbative orders and final state multiplicities.

The *Monte Carlo* (MC) method [53] is a simpler method of producing such integrals which randomly samples points in the region of integration. Thus the scaling of the time complexity for convergence does not depend on the dimensions integrated over. This means that Monte Carlo integration is the most suitable method of numerically integrating the high-dimensional phase spaces we encounter in cross section calculations. We summarise this method in this section, and examine how different parts of the calculation of hadron-hadron collisions are implemented in GPMC event generation frameworks.

1.5.1 The Monte Carlo Method

We address the generic problem of integrating a real-valued function $f(\mathbf{x})$ over the n-dimensional region Ω. We denote such an integral by:

$$I[f] := \int_\Omega f(\mathbf{x})\mathrm{d}\mathbf{x}. \tag{1.5.1}$$

The Monte Carlo method [53] selects N points $\mathbf{x}_i$ in Ω at random and calculates the average of the function evaluated at these points; this average is then related to the integral by:

$$I[f] = \overline{f_N}V; \qquad V \equiv \int_\Omega \mathrm{d}\mathbf{x}, \qquad \overline{f_N} \equiv \frac{1}{N}\sum_{i=1}^{n} f(\mathbf{x}_i). \tag{1.5.2}$$

The weak law of large numbers [54] ensures that, as N approaches infinity, the quantity $I_N \equiv \overline{f_N}V$ approaches I. The variance of the Monte Carlo approximation to the integral with N points, I_N is given by:

$$\mathrm{Var}(I_N) = \frac{V^2}{N^2}\sum_{i=1}^{n}\mathrm{Var}(f) = \frac{V^2}{N}\mathrm{Var}(f), \tag{1.5.3}$$

where we have denoted the limit of $\overline{f_N}$ as $\overline{f}$ and used:

$$\mathrm{Var}(f) = \frac{1}{N-1}\sum_{i=1}^{n}\left[f(\mathbf{x}_i) - \overline{f}\right]^2. \tag{1.5.4}$$

An estimate of the standard error on the Monte Carlo value (i.e. the expected deviation from the true value of I) may be calculated via [55]:

$$\delta I_N \simeq \frac{V}{\sqrt{N}}\sqrt{\mathrm{Var}(f)}. \tag{1.5.5}$$

Thus for a sufficiently "well-behaved" function f with small variance, the error associated to a Monte Carlo estimator for the integral decreases as $1/\sqrt{N}$ as N increases. Despite scaling well with the number of dimensions, the fact that the Monte Carlo error depends on the variance of f is crucial and cannot be neglected. We know that matrix elements alone peak strongly and diverge in different regions of the integration phase space and simply selecting points uniformly across Ω will lead to slow convergence of the Monte Carlo estimator, with large variances even for large values of N.

Importance sampling

We can address the inefficiency of sampling randomly in phase space by sampling points selected according to a probability density g which captures the behaviour of the integrand f. This procedure is referred to as *importance sampling* and transforms the integral of Eq. (1.5.1) to [56]:

$$I[f] = \int_\Omega \frac{f(\mathbf{x})}{g(\mathbf{x})} g(\mathbf{x})\mathrm{d}\mathbf{x} \equiv \int_{\Omega'} h(\mathbf{y})\mathrm{d}\mathbf{y}, \tag{1.5.6}$$

with $h = f/g$ and $\mathbf{y} = \mathbf{G}(\mathbf{x})$ for some transformation $\mathbf{G}$ satisfying:

$$\mathcal{J}[\mathbf{G}](\mathbf{x}) \equiv \det\left(\frac{\partial \mathbf{y}}{\partial \mathbf{x}}\right) = g(\mathbf{x}). \tag{1.5.7}$$

This formulation enables — for suitable choice of density g — us to calculate the integral in a region Ω' where the integrand varies more slowly than the uniform-sampling case. However in MC calculations for HEP we are rarely interested just in

the value of the integrated cross section but more often in distributed cross sections with respect to observables in the differential phase space. Thus it becomes more convenient to evaluate the integral in $\mathbf{x}$ and write:

$$I[f] = \int_{\Omega'} \det\left(\frac{\partial \mathbf{G}^{-1}}{\partial \mathbf{y}}\right)(\mathbf{y})\, f(\mathbf{G}^{-1}(\mathbf{y}))\, \mathrm{d}\mathbf{y}, \tag{1.5.8}$$

for the inverse $\mathbf{G}^{-1}$ of our coordinate transformation $\mathbf{y} = \mathbf{G}(\mathbf{x})$.

The corresponding Monte Carlo estimator for an importance-sampled integral thus carries *weights* w_i to ensure the proper convergence:

$$I_N[f] = \frac{V'}{N} \sum_{i=1}^{n} w_i f(\mathbf{G}^{-1}(\mathbf{y}_i)), \tag{1.5.9}$$

with:

$$w_i = \det\left(\frac{\partial \mathbf{G}^{-1}}{\partial \mathbf{y}}\right)(\mathbf{y}), \tag{1.5.10}$$

which allows us to select points uniformly in the transformed phase space Ω' with volume V'.

From our discussion of the cross section in Ch. 1, one may see immediately the probability distribution to use in importance sampling must reflect the behaviour of the integrand, namely the behaviour of the distribution must be similar to:

$$\mathcal{J}(\mathbf{x}_i) f(x_1(\mathbf{x_i}), \mu_F^2(\mathbf{x}_i)) f(x_2(\mathbf{x_i}), \mu_F^2(\mathbf{x}_i)) |\mathcal{M}|^2(\mathbf{x}_i), \tag{1.5.11}$$

to ensure that regions of phase space where the flux and matrix elements are peaked are sampled more frequently [8, 51].

Many methods have been developed for importance sampling, one of the most widely-used of which is the VEGAS method [57] which calculates $g(x_1, x_2, \dots)$ by assuming the density is separable i.e. $g(\mathbf{x}) = g_1(x_1) g_2(x_2) \cdots$. The algorithm populates histograms across the integration region Ω with values of the integrand f, and calculates the separated distributions g_i according to these.

We make note also that a bad choice of sampling density g can produce worse convergence than not performing any importance sampling. This is clear from considering $h = f/g$, it may be possible to introduce problematic behaviour in

regions where both f and g were slowly varying with f large and g small. This would artificially inflate the variance of h and lead to an oversampling in these regions and an under-sampling (for fixed N) in other regions where convergence is slow. One must take great care in producing such density functions to ensure the density g shares much behaviour with f.

Pseudorandom number generation

In computational applications of the Monte Carlo method, pseudorandom number generators (pRNGs) are used to produce sequences of numbers that appear statistically random, and allow for the probabilistic sampling of the integration phase space required. The sequences provided by pseudorandom number generators are produced by a completely deterministic process, which takes in (normally) a single integer parameter referred to as a *seed*. If the same seed is used with the same pRNG then the same sequence of numbers is produced. While not truly random, pRNGs are required to give sequences that are statistically indistinguishable from sequences produced by sampling a uniform distribution [53]. These allow for the results of any computational Monte Carlo integration to be reproduced, and for the statistical independence of different Monte Carlo integrations to be guaranteed (by changing the seed).

Existing pRNGs can differ greatly in their implementation. This means some pRNGs can produce problematic sequences of (pseudo-)random numbers which pass statistical tests in low dimensions but that produce correlated results for high dimensions. The most famous example of such are the linear congruential generators such as MIXMAX [58] which pass statistical independence tests in low dimensions, but produce points in parallel hyperplanes in higher dimensions [59, 60]. In *High Energy Jets* — which we introduce in Sec. 2.2 — the option is provided to use MIXMAX for random number generation, but by default the RANLUX [61] generator is used which improves on MIXMAX in this regard. High dimensions are a particularly important consideration for HEP as Monte Carlo integration phase spaces quickly

become large with increasing multiplicity in the final state as discussed earlier, and as such the statistical independence of individual runs must be assured with a robust pRNG.

1.5.2 General Purpose Monte Carlo Event Generators

General purpose Monte Carlo event generators are some of the most versatile tools in high energy physics, able to model all stages of a collider process in and beyond the Standard Model. The main three in use in the HEP community are `Sherpa` [62], Pythia [47,63] and `HERWIG` [64,65] as we discuss in Sec. 2.3. Focusing on the specific implementation of processes at hadron colliders we may schematically extend the inclusive cross section of Eq. (1.3.45) to include descriptions of the missing physical effects:

$$\begin{aligned}\sigma_{AB\to\Omega}[\mathcal{O}] = &\sum_{a,b}\int \mathrm{d}x_a \mathrm{d}x_b \cdot f_{a/A}\left(x_a, \mu_F^2\right)\cdot f_{b/B}\left(x_b,\mu_F^2\right)\\ &\cdot \mathcal{O}(\Omega)\\ &\cdot \hat{\sigma}_{ab\to\hat{\Omega}}(x_a p_A, x_b p_B, \mu_R^2, \mu_F^2)\\ &\cdot \mathrm{d\,P.S.}\cdot \mathrm{d\,Had.}\end{aligned} \tag{1.5.12}$$

where d P.S. represents parton shower evolution (including multiple parton interactions from the underlying event) and d Had. the hadronisation of partons at soft, non-perturbative energy scales. We illustrate the different contributions in a schematic from ref. [4] in Fig. 1.8. The dark green ellipses incoming along the horizontal axes represent the incoming hadron beams, the dark blue radiation from these are the incoming particles which enter the principal hard interaction indicated by the red circle and the red outgoing particles. Parton shower evolution is shown at all stages by the splitting partons e.g. leaving or entering the hard process. This connects the hard process matrix element with the hadronisation stage, and resums the soft-collinear logarithms arising in QCD. We review parton shower resummation in detail in Sec. 2.3.

Secondary scatterings from the other partons in the incoming beams may take place

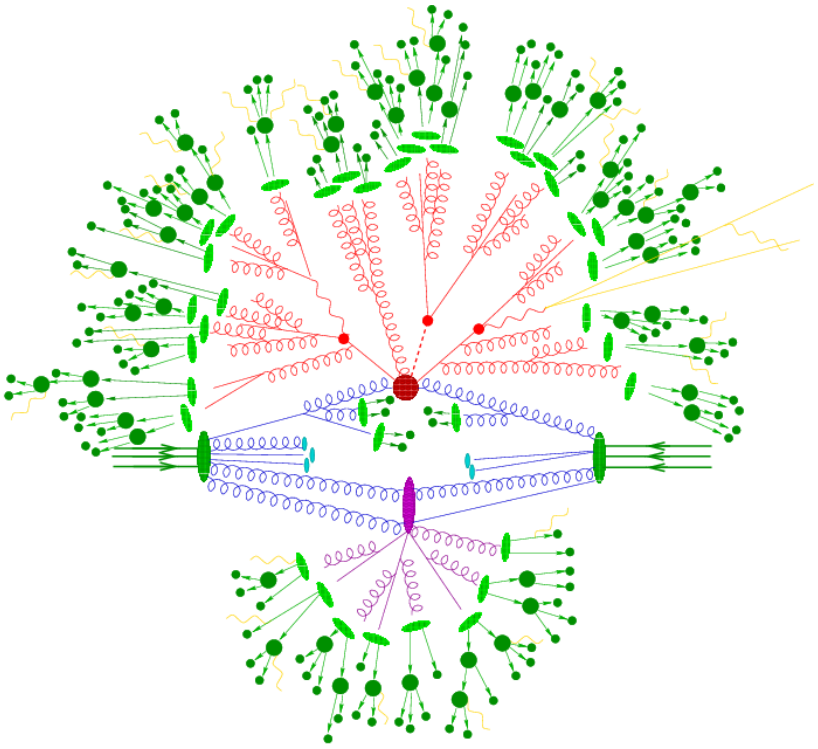

Figure 1.8: Schematic of the evolution of a scattering event at a hadron-hadron collider. See text for discussion. Figure from ref. [4].

(the purple interaction) and partons outside the hard process may interact with each other in soft sub-collisions — the underlying event contributions. The remnants of the incoming beams are in turquoise and the hadronisation of the outgoing partons is shown in light green. Leptons and photons produced outside of the hard interaction are shown in yellow.

To each of these parts of the process significant theoretical and computational challenges impose themselves which we explore in this section. We summarise how these are handled in modern GPMC frameworks.

Hard process generation

The construction of the hard process matrix elements and phase space in GPMC frameworks, while seemingly straightforward given our introduction in Sec. 1.3.2, imposes significant challenges on the calculation. In Fig. 1.8 the hard process is indicated by the red circle and red outgoing particles.

We continue the discussion for a NLO calculation for which the theoretical ground-

work was laid in Sec. 1.3.2. We noted that the UV divergence associated to the loop corrections could be regularised and renormalised, however the treatment of the IR divergences required invoking the KLN theorem to demonstrate the cancellation of poles in the real and virtual components. Borrowing the notation of Catani and Seymour [66] we may express the NLO cross section for a $2 \to n$ process as:

$$\mathrm{d}\sigma_{\mathrm{NLO}} = \int_{\Omega_n} \mathrm{d}\sigma_B + \int_{\Omega_n} \mathrm{d}\sigma_V + \int_{\Omega_{n+1}} \mathrm{d}\sigma_R, \tag{1.5.13}$$

where $\mathrm{d}\sigma_B$ is the LO or *Born-level* cross section, $\mathrm{d}\sigma_V$ are the regularised NLO virtual corrections, $d\sigma_R$ are the NLO real emission corrections, and Ω_n is the Lorentz-invariant phase space for n particles. The quantities $\mathrm{d}\sigma_V$ and $\mathrm{d}\sigma_R$ are individually divergent and the divergences only cancel after each has been integrated over its phase space.

A commonly adopted solution is to modify Eq. (1.5.13) to include additional subtraction terms, considering only the NLO parts we may write:

$$\int_{\Omega_n} \mathrm{d}\sigma_B + \int_{\Omega_n} \mathrm{d}\sigma_V + \int_{\Omega_{n+1}} \mathrm{d}\sigma_R = \int_{\Omega_n} \mathrm{d}\sigma_B + \int_{\Omega_n} (\mathrm{d}\sigma_V + \mathrm{d}\sigma_I) + \int_{\Omega_{n+1}} (\mathrm{d}\sigma_R - \mathrm{d}\sigma_S)\,, \tag{1.5.14}$$

where:

$$\mathrm{d}\sigma_I = \int_{\Omega_1} \mathrm{d}\sigma_S. \tag{1.5.15}$$

This means we have introduced a *subtraction* term $\mathrm{d}\sigma_S$ and an *integrated subtraction* term $d\sigma_I$ equal to the integral of the former over the one particle emission phase space. We choose a subtraction term to differ from the real emission term by a finite amount but to carry the same point-wise divergent structure. Importantly, this means that events can arise in the Monte Carlo generation with negative weights depending on the subtraction scheme since the finite parts in the integrated subtraction term can exceed the other positive-definite contributions [8].

There are many methods in use for construction of such counter-terms including FKS subtraction [67], antenna subtraction [68], and Catani-Seymour dipole subtraction [66]. The default in `Sherpa` — the main generator we use in this thesis for

producing fixed-order perturbative predictions — is the Catani-Seymour method.

GPMC event generators are well-equipped to produce matrix elements at tree-level for many processes, with options to configure and import libraries to construct more complex processes or consider higher perturbative orders. `Sherpa` uses two main matrix element generators, AMEGIC++ [69] and COMIX [70], between which many experimental processes of interest at particle colliders are readily calculable. For NLO processes, OpenLoops [71, 72] may be used in `Sherpa` on-the-fly to calculate loop integrals, though other libraries are available. PYTHIA may be interfaced to MADGRAPH5_aMC@NLO [5] to provide a larger set of hard process matrix elements than it has natively available. These efforts and more have yielded that NLO is now the standard for most processes and can be automated with reasonable efficiency, leaving NNLO and further now the frontier for many processes [8]. For even higher orders the calculations climb quickly in complexity and thus are generally treated analytically or case-by-case with dedicated calculations per process.

Parton shower evolution

Parton shower evolution may be applied on matrix element states though this is more complex than it may seem. Since the parton shower resums higher-order effects, one needs to ensure that double-counting does not occur between the matrix element (which could be evaluated to NLO or higher) and the shower evolution. Generally parton showers are *matched* or *merged* (or both) to fixed-order predictions. We dedicate Sec. 2.3 to discussing the parton shower formalism in detail, and Sec. 2.3.3 therein to matching and merging methods as these will be relevant to our discussion of the novel prescription for merging *High Energy Jets* resummation with a parton shower in Ch. 3.

In Fig. 1.8 the final state parton shower is shown by the red partons 'splitting' as they enter the final state. The initial state shower is shown by the additional blue radiation from the partons entering the hard interaction. The parton shower will evolve states hard in the evolution scale t (see Sec. 2.3 for details) down to the scales

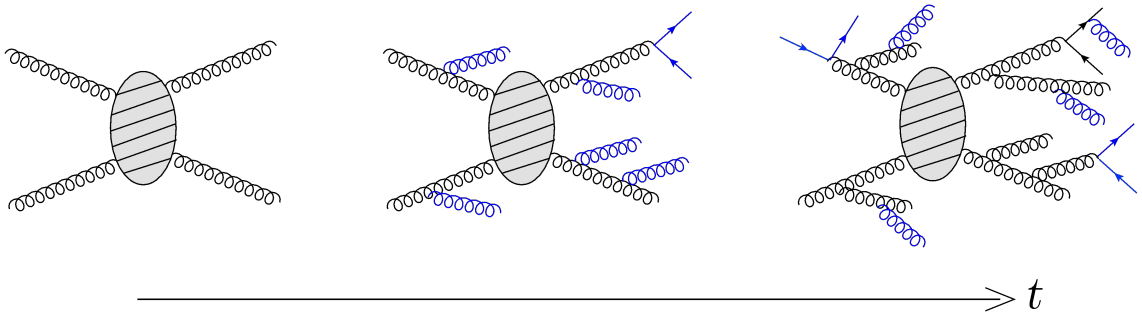

Figure 1.9: Schematic of the evolution of a hard $gg \to gg$ scattering under a parton shower with evolution variable t. As t decreases (to the right) further radiation is added to the matrix element configuration. At each stage the additional emissions enter the final state and thus can themselves undergo splitting. Both initial state and final state splittings are shown.

at which the showered partons can hadronise. This is illustrated schematically in Fig. 1.9, where we simplify the discussion by assuming we start with a LO $pp \to 2j$ matrix element state.

This follows the same basic procedure that we outline in Sec. 2.3. Soft and collinear radiation is applied to the process configuration, with emissions added according to the prescription we present in Sec. 2.3 with the Sudakov veto algorithm at successively lower scales, until hadronisation.

Underlying event and multiple parton interactions

An observed experimental result for the scaling of $2 \to 2$ differential cross section at hadron colliders, shows that the cross sections fall as $dp_\perp^2/p_\perp^4$. This means that the inclusive dijet cross section would exceed the total proton-proton inelastic scattering cross section (imposing some minimum transverse momentum cut $p_{\perp,\text{min}}$) [73]. This effect can be explained by including contributions from multiple hard scatterings involving multiple partons from the incoming hadrons as displayed by the red and purple hard interactions of Fig. 1.8. Collectively, such processes are referred to as *multiple parton interactions* or MPI. Translating such effects to a Monte Carlo framework poses much difficulty as MPI can occur at scales typically softer than the principal hard interaction of interest meaning that they can coincide with ordering of the parton shower. The approach of Pythia is to treat such interactions as

interleaved with the parton shower [74]. Together, such contributions are referred to as the *underlying event* [8].

MPI typically occur at much softer scales than hard starting scales for the shower, and are governed by many phenomenological parameters that form part of *tunes* for GPMC event generators [8]. These govern how MPI are produced and at which scales they are observed as well as their internal kinematics. The Monash 2013 tune [10] in PYTHIA compared to data obtained by the TOTEM collaboration [75] of the total proton-proton cross section at the LHC at $\sqrt{s} = 8$ TeV [76] to find that (at this CoM energy of interaction) $n_{\text{MPI}} \sim 1$ at scales of roughly $p_{\perp,\text{min}} \sim 5$ GeV. The full list of parameters used to obtain this tune is available in the same publication, ref. [10].

Hadronisation

There remains the treatment of hadronisation, in green from Fig. 1.8, of all final state partons for which several phenomenological models exist. Hadronisation occurs at non-perturbative energy scales. The form of the parton shower evolution and the multiple parton interactions that precede this stage can greatly alter the spectrum of observed hadrons in non-trivial ways [8]. The empirical nature of hadronisation models means that small differences in models can yield strongly differing theoretical predictions, even for identical hard process and parton shower evolution.

There are two main methods in use for GPMC generators, cluster hadronisation [77] and string hadronisation [78]. `Sherpa` and `HERWIG` use cluster hadronisation while PYTHIA uses a string hadronisation method called *Lund string hadronisation*.

The Lund string model treats colour-connected quark pairs in the showered final state as mesons connected by massless "strings" which *fragment* by radiating additional mesons ($q\overline{q}$ pairs) until the energy scales match those appropriate for hadrons. The radiation of additional $q\overline{q}$ pairs would be mediated by gluons during the parton showering stage but the gluons are treated as *topological defects* referred to as *kinks* in the string potential [63].

As with MPI, models of hadronisation are phenomenological and contain many parameters which are also absorbed into GPMC tunes. Often, when one references a parton-showered prediction, the presence of MPI and hadronisation can be implied. As such, we will later be explicit as to when we do and do not consider these effects in the HEJ+Pythia merging algorithm in Ch. 3.

Other Uses

GPMC event generators are not just tools for producing robust theoretical predictions but are also used to describe experimental data. Experimental studies will often precede the comparisons of event generators and theoretical predictions to data with details on how event generators were used to calibrate the data selection by comparing to known distributions [8].

A prominent example of where Monte Carlo predictions are useful for experiments is in experiment design; detectors are built based partly on which regions of phase space are likely to receive significant enough statistics to draw valid conclusions from. This process is instructed in parts by detector-level GPMC predictions which can inform on the size of the cross section across the available phase space. Detector-level simulations are also often applied to calibration distributions from GPMC event generators to better reflect the experimental data as observed.

For a review of these procedures in great detail, we recommend Chapters 16 and 17 of ref. [8] which provide a pedagogical overview of the many uses of GPMC event generators beyond producing theoretical predictions.

Having drawn the connection between the theoretical and the physical, and prescribed how theoretical predictions are produced in computational frameworks throughout this section, we occupy ourselves in the subsequent chapters with delving into the specifics of resummation in perturbation theory. We detail *High Energy Jets* and parton shower resummation in Ch. 2. We present developments to these resummation schemes that form the research basis of this thesis in Ch. 3-5.

Chapter 2

Frameworks for Perturbative Calculations in QCD

As we have made reference to throughout Ch. 1, the perturbative formulation of QCD requires a wide array of frameworks to calculate cross sections and distributions of observable quantities within different approximations that work to varying accuracies across phase space. We have discussed in Sec. 1.3.1 and Sec. 1.3.2 that cross sections can be calculated to fixed orders in the coupling and dedicate this section to exploring the behaviour of matrix elements in regions of phase space that receive logarithmic enhancement when the ratio between kinematic scales becomes large. In many cases, the logarithms are large enough to compensate for the smallness of the coupling in these regions of phase space. This poses issues for a perturbative description in such regions as the higher-order terms in the coupling would not produce successively smaller contributions (or at least contributions that would converge more slowly).

As alluded to in Sec. 1.3.2, in many cases it is possible to demonstrate that the the higher-order corrections in such regions of phase space are dominated by terms that are logarithmically enhanced:

$$\begin{aligned}\hat{\sigma} = \alpha_s^k \cdot \sum_{n=0}^{\infty} \sum_{m=0}^{n} \alpha_s^n L^m c_{n,m} = \alpha_s^k \cdot \Big[c_{0,0} + \alpha_s \left(c_{1,1} L + c_{1,0} \right) \\ + \alpha_s^2 \left(c_{2,2} L^2 + c_{2,1} L + c_{2,0} \right) + ... \Big].\end{aligned} \tag{2.0.1}$$

Here k is the minimum power of α_s at which the process occurs (i.e. the LO), and L is a logarithm of the scales[1] that becomes divergent/slowly convergent in the kinematic limit that populates the problematic region of phase space. The coefficients $c_{n,m}$ may then be calculated exactly how FO cross sections are calculated, except that the accuracy is determined not by which power of the coupling they are attached to. Rather we work to *logarithmic* accuracies, where the leading-logarithmic (LL) accuracy means the leading terms $\alpha_s^{n+k}L^n$ are accounted for to all orders of perturbation theory. Similarly, the (next-to)^l-leading-logarithmic (N^{l}LL) accuracies signify that we account for all the subleading terms up to $\alpha_s^{n+k}L^{n-l}$. Instead of including all amplitudes to a FO accuracy in the coupling, all amplitudes to the required logarithmic accuracy are included.

The process of calculating terms to all orders is called *resummation* and forms the basis of what we will explore in this chapter. Examples of such schemes include the analytic Balitsky-Fadin-Kuraev-Lipatov (BFKL) resummation [40–44] of large logarithms in $\hat{s}/p_\perp^2$, which the resummation of *High Energy Jets* is inspired by. Parton showers are also an example of widely-used resummation schemes, resumming the soft-collinear logarithms of QCD [30].

In this chapter, we outline the theoretical framework behind resummation in *High Energy Jets* which develops the ideas of the BFKL formalism and applies them to produce perturbative hard process-level predictions with Monte Carlo event generation (see Sec. 1.5). We conclude this chapter by exploring the resummation of soft-collinear logarithms in QCD with parton showers and link this to the DGLAP evolution of the PDFs discussed in Sec. 1.3.3.

2.1 Regge Scaling and the High Energy Limit

The study of processes with large centre-of-mass energies is of immense phenomenological and experimental interest. An important consideration for the research

[1] Often this is a ratio of two scales, and the logarithm itself may be a double or triple logarithm depending on the divergent structures that arise.

presented in this thesis is the separation of the strong- and electroweak-initiated production of a Higgs boson at hadron colliders, since we present developments to the *High Energy Jets* framework for the strong-initiated production of a Higgs boson with at least one jet in Ch. 4.

The distribution of the cross section for the production of a Higgs boson with (at least) two jets has long been known to be dominated by the QCD-initiated gluon fusion mechanism at small invariant masses of the two hardest (or the most forward and the most backward) jets [79, 80] with multiple studies corroborating these results theoretically following the discovery of the Higgs [81]. However, for large dijet invariant mass and rapidity separation ($m_{jj} \gtrsim 400$ GeV, $\Delta y_{jj} \gtrsim 2.8$), the spectrum is dominated by the weak fusion of two Z or W bosons. Thus precise modelling of the gluon-gluon fusion component in this region of phase space allows for precision studies of the weak initiated vector boson fusion process, since the QCD background will be readily removable in such studies of the Higgs-weak boson couplings.

For large dijet invariant masses, the correlations between the dijets in azimuthal angle ϕ are characteristic probes of the effective Higgs-gluon-gluon coupling (which approximates the interaction between the Higgs and two gluons mediated by a massive fermion loop in the Standard Model) [79, 82], for which precise descriptions are crucial to determine the CP structure of this coupling.

2.1.1 Multi-Regge Kinematics

The *high energy limit* for a $2 \to n$ scattering with momenta $p_a, p_b \to p_1, \ldots, p_n$ is defined by:

$$y_1 \ll y_2 \ll \cdots \ll y_{n-1} \ll y_n, \quad p_{\perp i} \approx k_\perp \quad \forall i \in \{1, 2, \cdots, n-1, n\}. \tag{2.1.1}$$

Here, y_i is the rapidity of momentum p_i, and $k_\perp$ is some momentum scale. This means the high energy limit applies for phase space configurations with final state particles widely separated in rapidity, with similar transverse momenta.

This limit is also known as the limit of *multi-Regge kinematics* (the MRK limit), and is equivalent to requiring [83]:

$$\hat{s} \gg \hat{s}_{ij} \gg k_\perp, \quad p_{\perp i} \approx k_\perp \quad \forall i,j \in \{1,2,\cdots,n-1,n\}, \quad i \neq j. \tag{2.1.2}$$

This expresses the limit in terms of the large invariant masses required between final state particles, where $\hat{s} = (p_a + p_b)^2$ is the partonic CoM energy of interaction. From the parametrisation of the four-momentum in Eq. (1.4.6), we can obtain the scaling of the Mandelstam variable $\hat{s}$ and $\hat{s}_{ij}$ in the MRK limit, again where all particles are massless:

$$\begin{aligned} \hat{s} = (p_a + p_b)^2 &\to p_{\perp 1}\, p_{\perp n} e^{y_n - y_1}, \\ \hat{s}_{ij} = 2p_i \cdot p_j &\to p_{\perp i}\, p_{\perp j} e^{|y_i - y_j|}. \end{aligned} \tag{2.1.3}$$

We can define a generalised Mandelstam $\hat{t}$:

$$\hat{t}_i \equiv \left(p_a - \sum_{l=1}^{i} p_l\right)^2 \to -p_{\perp i}^2. \tag{2.1.4}$$

For the case of a $2 \to 2$, scattering $p_a, p_b \to p_1, p_2$, the Mandelstam variables scale as:

$$\begin{aligned} \hat{s} &\to k_\perp^2 e^{\Delta y}, \\ \hat{t} &\to -k_\perp^2, \\ \hat{u} &\to -k_\perp^2 e^{\Delta y}, \end{aligned} \tag{2.1.5}$$

where $\mathbf{p}_{1\perp} = -\mathbf{p}_{2\perp} = \mathbf{k}_\perp$ (with $k_\perp = |\mathbf{k}_\perp|$), and we have chosen the origin of the rapidity axis without loss of generality to be the midpoint of y_1 and y_2, denoting $y_2 - y_1 = \Delta y$. From this, we can clearly see that any observable depending on the rapidity difference gives rise to large logarithms in $\hat{s}/k_\perp^2$, in the MRK limit:

$$\log\left(\frac{\hat{s}}{-\hat{t}}\right) \to \log\left(\frac{\hat{s}}{k_\perp^2}\right) = \Delta y. \tag{2.1.6}$$

This generalises for the n-particle scattering, and we can see that large logarithms in $\hat{s}_{ij}/p_{\perp i}p_{\perp j}$ arise wherever we have an observable depending on $\Delta y_{i,j} \equiv |y_i - y_j|$.

2.1.2 Regge Scaling of Amplitudes

The study of amplitudes in the limit of large invariant masses between final state particles pre-dates QCD. *Regge theory*, one of the original treatments of the $\mathrm{SU}(3)_c$ symmetry in nature from before QCD, predicts that amplitudes for $2 \to n$ scatterings scale in the MRK limit as [83]:

$$\mathcal{M}_{2\to n} \sim s_{12}^{J_{12}} \cdot s_{23}^{J_{23}} \cdot s_{34}^{J_{34}} \cdots s_{n-1,n}^{J_{n-1,n}}, \tag{2.1.7}$$

with J_{ij} the spin of the t-channel exchanged particle between emissions i and j — the *reggeon*. This inspires denoting the high energy limit by the MRK limit, as it was originally known.

This amplitude also applies to QCD [84, 85], with *reggeised gluons* exchanged in the t-channel. The consequence of reggeisation is that the exponents J_{ij} now depend on the (square of the) momentum exchanged in the t-channel, since their exchange gives rise to an additional intrinsic angular momentum [29, 84]. In the limit $\hat{t}_i \to 0$, the exponents tend to unity, indicating that the exchanges are spin-1 particles, as required for gluons. The difference from unity is referred to as $\alpha(\hat{t}_i)$. We say that the reggeised gluons exchanged follow the *Regge trajectory* $J = 1 + \alpha(\hat{t}_i)$.

If the outgoing momenta satisfy Eq. (2.1.1), with all outgoing partons emitted between 1 and n being gluons — provided the flavour of parton a (b) is the same as parton 1 (2) — the phase space configuration is referred to as a *Fadin-Kuraev-Lipatov* (FKL) state. These are enhanced with leading logarithms in $\hat{s}/p_\perp^2$ which can be resummed by solving the BFKL equation with the LL evolution kernel and impact factors [40–44].

This instructs our consideration of subleading logarithmic terms, as so far we have considered only configurations that give rise to leading-logarithmic evolution in the language of BFKL. We can also consider non-FKL states which tend to the same limit of Eq. (2.1.7) in the limit of large $\hat{s}/p_\perp^2$, though slower. The most obvious such correction contributing a next-to-leading-logarithmic effect would be suppression by removing exactly one factor of $\hat{s}_{ij}$ in the MRK limit. This may be achieved

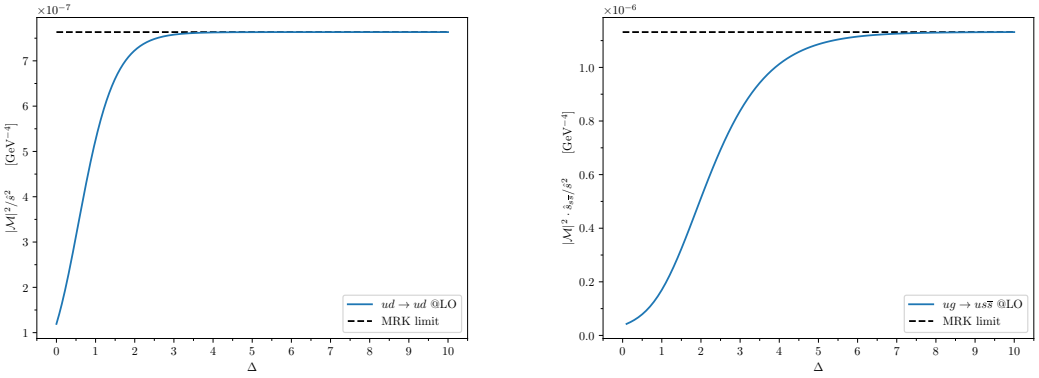

Figure 2.1: The form of the LO matrix elements for $ud \to ud$ (left) and $ug \to us\bar{s}$ (right) against half the rapidity separation between the forward and backward parton, evaluated for the phase space slices described in the text. LO matrix elements provided by MadGraph5_aMC@NLO [5].

by e.g. relaxing the requirement of strict rapidity ordering for exactly one pair of partons in the rapidity interval bounded by the extremal partons. This is often referred to as the *quasi-MRK (qMRK) limit*. The emission of one $q\bar{q}$ pair in lieu of a gluon in between y_1 and y_n is also a subleading correction. These contribute to the NLL evolution in the language of BFKL [86, 87].

In Fig. 2.1 we plot the evolution of matrix elements at leading order along a specific slice of phase space to highlight where the MRK limit provides a useful approximation to the amplitude. In the left plot we show both the full partonic LO amplitude for $ud \to ud$ with massless quarks, and the MRK-limit approximation of Eq. (2.1.7). The transverse momenta in the final state are both set as $p_{\perp u} = p_{\perp d} = 40$ GeV with the final state u (d) quark produced with $\phi = \pi$ (0) and rapidity Δ ($-\Delta$), the latter of which is varied in the plot. This configuration would be leading-logarithmic in the MRK limit, yet we can see that for rapidity differences $2\Delta \lesssim 6$ the MRK scaling does not produce a good approximation of the amplitude even to LO.

Connecting the theoretical background to the physical configurations at experiments highlights the problems of using the MRK limit for the full phase space. The ATLAS detector can observe particles with rapidities of up to $|\eta| \lesssim 4.9$ [49]. This implies that the largest observable rapidity differences are ~ 10 with the understanding that statistics for collisions with jets observed at such wide separations will be

low as their production is suppressed in the region between $2\Delta \sim 6$ and 10. For this LL configuration, the majority of the reliably sampled experimental phase space is not well-described by approximating the MRK limit everywhere, though the forward region is very well-described.

The subleading configurations enter into prominence for larger rapidity differences, thus the MRK limit provides a much weaker description for a larger region of phase space. This is best illustrated by the LO matrix element for $ug \to us\bar{s}$ — which contributes at NLL — plotted in the right of Fig. 2.1. The notation $ab \to f_1 f_2 \ldots$ implies, when we discuss high-energy logarithms or the `HEJ` framework, that the final state is listed in order of ascending rapidity. Final state partons were examined again along a specific slice of phase space where they are equidistant in ϕ and y with equal transverse momenta of 40 GeV. Again, Δ signifies half the difference in rapidity between the most forward and backward partons. It is only at $\Delta \sim 7$ that the MRK limit yields a solid approximation to the LO amplitude.

Dominant colour connections in the high energy limit

When considering amplitudes in QCD, the concept of *colour flow* is useful to consider when stripping the kinematics of an amplitude from the colour structure. With the products of QCD generator elements in amplitudes, one can trace the indices and connect the partons in a diagram with lines signifying the flow of colour in the diagram. A particular configuration of flow lines in colour space is referred to as a colour *connection*. Since gluons carry two colour indices, they can be connected in colour on either "side" in a diagram. Quarks, by contrast, may only be connected on one "side".

The study of ref. [88] found that in the limit of wide-angle hard radiation, $gg \to g \ldots g$ amplitudes in QCD were dominated in colour space by configurations that resemble rapidity-ordered "ladders". We show in Fig. 2.2 two examples of colour configurations, one dominant in the high energy limit, and another sub-dominant, for $gg \to gggg$, with final state partons ordered in rapidity. In the left plot, a

dominant high energy configuration is shown with the colour flow between gluons able to be arranged in a "ladder" without compromising the rapidity ordering of the final state. One can imagine "pinching" the colour vertex at gluon 2 in this leading contribution, and unravelling it to the left to create a rapidity-ordered "ladder" with the colour flow lines. These configurations (along with the planar configurations where no unfolding is required) are leading in the MRK limit.

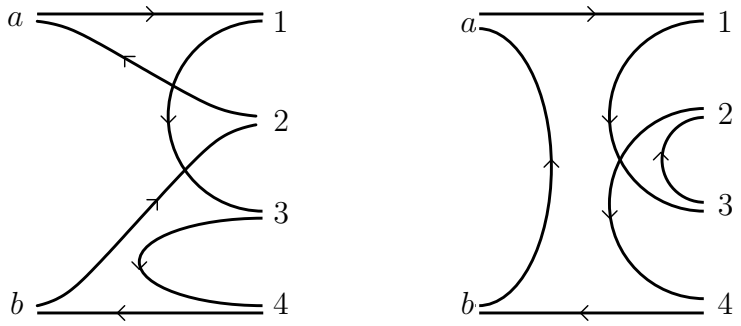

Figure 2.2: A colour flow contributing to the limit of widely-separated (in rapidity) hard radiation (left) and one not contributing in the same limit (right). The outgoing particles are ordered in rapidity. Reproduced from ref. [6].

The connection displayed in Fig. 2.2 (right) is sub-dominant, since the colour flow can not be rearranged into a non-crossing ladder without swapping the rapidity ordering of gluons 2 and 3. For processes involving quarks, the colour connections are analogous, with breaks in the colour flow line around the quarks. Introducing corrections that contribute at NLL, such as central $q\bar{q}$ pairs, introduces more breaks in the colour flow lines around additional quarks, or allows for the swapping of one pair of particles in rapidity ordering (corresponding to the qMRK limit). At LL, the reversed colour connection to a leading configuration (which can be found by e.g. reversing the colour flow in the left diagram of Fig. 2.2) contributes equally to the amplitude as the non-reversed configuration [88]. We use this result when considering the colour configurations of events in merging the high energy resummation of *High Energy Jets* with the Pythia parton shower in Ch. 3.

While the full framework of BFKL outlined in this section provides an invaluable prescription for accounting for large logarithms in the MRK limit, the matrix ele-

ments in Fig. 2.1 show that these effects are not sufficient to ensure an accurate description across the phase space. Inspired by this, the *High Energy Jets* framework builds on the BFKL formalism and implements LL and subleading corrections to all orders in perturbation theory, while matching to LO to retain fixed-order accuracy of matrix elements.

2.2 The *High Energy Jets* Framework

Following our brief overview of perturbative QCD in the high energy limit, we pause to note again that amplitudes calculated in the pure MRK limit are not well-suited to providing physical descriptions of matrix elements across phase space, though the corrections in the high energy limit are essential to a stable description of the large invariant mass region of phase space. Indeed, we have made note of studies for which this forward region is of immense interest, notably for the precise modelling of GF Higgs production in the region of VBF dominance where large dijet invariant masses $m_{jj} \gtrsim 400$ GeV are observed [81], though a precise modelling of such effects should not come at the expense of the perturbative description across phase space. This is precisely the motivation for the *High Energy Jets* (`HEJ`) formalism [23, 89–91] which builds on the amplitudes discussed in the previous section.

The `HEJ` framework is inspired by the BFKL formalism and the observation of t-channel pole factorisation in partonic matrix elements for jets produced in the MRK limit [92]. The `HEJ` framework combines the ideas we have introduced in the previous section to produce fully regularised, high energy-resummed, LO-matched Monte Carlo generated theoretical predictions in a fully differential phase space for direct comparison to experimental studies.

2.2.1 Currents and $2 \to 2$ Amplitudes in `HEJ`

We start by considering the full $2 \to 2$ case, focusing on the hard scattering of distinct quarks $qQ \to qQ$, where the LO contribution is illustrated in Fig. 2.3. We

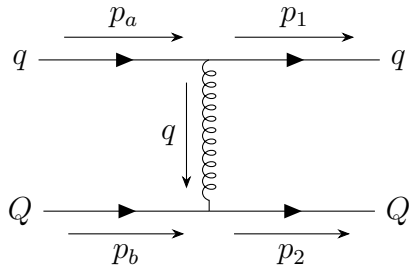

Figure 2.3: The LO scattering of distinct quarks $qQ \to qQ$.

decompose momenta into *lightcone coordinates*, defining:

$$p^{\pm} = E \pm p_z, \tag{2.2.1}$$

and generalising the transverse momentum to a complex representation $p_\perp \equiv p_x + ip_y$. We denote by p_a (p_b) the initial state parton incoming along the positive (negative) z-axis and denote the final state momenta by p_j for $j \in \{1, \ldots, n\}$ — in this starting case $n = 2$. The helicities are denoted in the same way i.e. h_a, h_b for the initial state and h_j for the final.

We revisit the spinor-helicity formalism outlined Sec. 1.3.1 to calculate this matrix element and use results of ref. [32] throughout our derivation in this section. Configurations with either $h_1 \neq h_a$ or $h_2 \neq h_b$ are suppressed in the MRK limit, and we only need evaluate the $q^{\pm}Q^{\pm} \to q^{\pm}Q^{\pm}$ and $q^{\pm}Q^{\mp} \to q^{\pm}Q^{\mp}$ amplitudes. The superscripts denote helicities. Using the definition of $\hat{t}$ in Eq. (1.3.10), we can write for the (colour- and coupling-stripped) amplitudes M with pairwise differing helicities:

$$\begin{aligned} M_{q^+Q^-\to q^+Q^-} &\equiv M^*_{q^-Q^+\to q^-Q^+} \\ &= \frac{1}{\hat{t}}[1|\gamma^\mu|a\rangle\,\langle 2|\,\gamma_\mu|b] = \frac{2}{\hat{t}}\langle a2\rangle[b1], \end{aligned} \tag{2.2.2}$$

and for the contribution with pairwise similar helicities:

$$\begin{aligned} M_{q^-Q^-\to q^-Q^-} &\equiv M^*_{q^+Q^+\to q^+Q^+} \\ &= \frac{1}{\hat{t}}\,\langle 1|\,\gamma^\mu|a]\,\langle 2|\,\gamma_\mu|b] = \frac{2}{\hat{t}}\langle 12\rangle[ba]. \end{aligned} \tag{2.2.3}$$

In both cases we have used the *Fierz identity* $\langle i|\,\gamma^\mu|j]\,\langle r|\,\gamma_\mu|s] \equiv 2\langle ir\rangle[sj]$ to produce the last equality [32].

We may concisely summarise these contributions by defining the spinor string:

$$\begin{aligned} S_{qQ\to qQ}^{h_a h_b \to h_1 h_2} &= \langle 1^{h_1}| \gamma^\mu |a^{h_a}\rangle \, g_{\mu\nu} \, \langle 2^{h_2}| \gamma^\nu |b^{h_b}\rangle \\ &= j_\mu^{h_1}(p_a, p_1) j^{h_2,\mu}(p_b, p_2). \end{aligned} \tag{2.2.4}$$

Here we have defined the currents for the helicity-conserving *impact factors* on the top and bottom legs of Fig. 2.3 by:

$$j_\mu^-(p,k) \equiv \langle p| \gamma_\mu |k] \equiv j_\mu^+(k,p). \tag{2.2.5}$$

We can then write for the summed, averaged square matrix element:

$$\overline{|\mathcal{M}_{qQ\to qQ}|^2} = \frac{1}{4}\frac{1}{N_c^2-1} ||S_{qQ\to qQ}||^2 \left(g_s^2 C_F \frac{1}{\hat{t}_1}\right)\left(g_s^2 C_F \frac{1}{\hat{t}_2}\right), \tag{2.2.6}$$

by defining:

$$||S_{qQ\to qQ}||^2 = \sum_{h_{a,1}, h_{b,2} \in \{+,-\}} S_{qQ\to qQ}^{h_a h_b \to h_1 h_2} \delta_{h_a h_1} \delta_{h_b h_2}. \tag{2.2.7}$$

In Eq. (2.2.6) we have — suggestively to our generalisation — absorbed a factor of $\hat{t}$ to each vertex and displayed them with their colour factors. Here we used $\hat{t}_1 = (p_a - p_1)^2$ and $\hat{t}_2 = (p_b - p_2)^2$, which are equal to each other in the $2 \to 2$ scattering.

All helicity-conserving $qg \to qg$ amplitudes may be obtained exactly in their t-channel factorised form by replacing the colour factor in the corresponding impact factor with the *colour acceleration multiplier* [93]:

$$C_F \to K_g(p_2^-, p_b^-) \equiv \frac{1}{2}\left(C_A - \frac{1}{C_A}\right)\left(\frac{p_2^-}{p_b^-} + \frac{p_b^-}{p_2^-}\right) + \frac{1}{C_A}, \tag{2.2.8}$$

where we have assumed that the backward parton is the gluon, though the form is the same for the case of the forward parton being the gluon instead. This displays the correct behaviour in the MRK limit as $p_b^- \to p_2^-$ gives the expected factor of C_A per gluon.

The helicity-violating amplitudes (for both $qg \to qg$ and $gg \to gg$) receive contributions from s- and u-channel mediated diagrams which are suppressed at high energies. Despite this, we retain the exact form of the gluon currents, for which

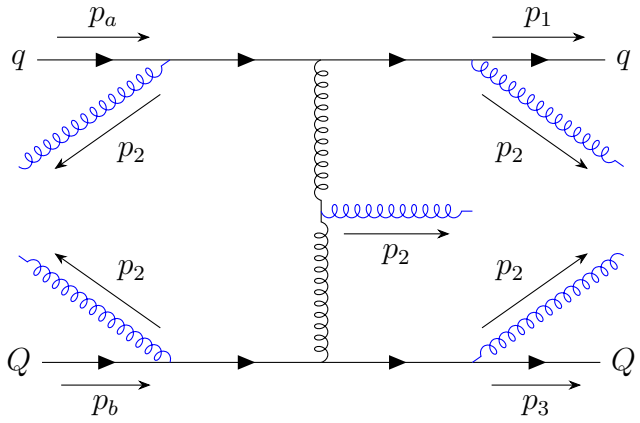

Figure 2.4: All possible LO $qQ \to qgQ$ diagrams with the emitted final state gluon with momentum p_2 highlighted in blue from each available vertex.

complete expressions may be found in ref. [93]. Though we still make arguments to suppress non-t-channel factorised contributions, the HEJ framework significantly improves the description of the pure BFKL formalism. In HEJ, more of the LO structure of the matrix elements is retained in the construction of the currents and the spinor strings than in the MRK limit.

2.2.2 Effective Emission Vertices in HEJ

Emissions in the BFKL formalism and the HEJ framework are implemented with effective vertices. Continuing from the $qQ \to qQ$ example, we derive the effective vertex for gluon emission by considering a real emission correction, $qQ \to qgQ$ i.e. the amplitude for a gluon emission inside the rapidity interval bounded by the two quarks. We consider the contributions to the amplitude from a gluon emission attached to each incoming and outgoing leg as well as the t-channel exchanged gluon. This is displayed in Fig. 2.4 where the partons have momenta $p_a, p_b \to p_1, p_2, p_3$ with p_2 the momentum of the gluon.

In QCD, we can write for the t-channel contribution:

$$\begin{aligned}\mathcal{M}_{t\text{-channel}} = &- f^{abc} t^{c,i_1 i_a} t^{b,i_3 i_b} \frac{g_s^3}{\hat{t}_1 \hat{t}_2} j_\mu(p_a^{h_a}, p_1^{h_1}) j_\nu(p_b^{h_b}, p_3^{h_3}) \varepsilon_\rho^{\lambda,*}(p_2) \\ &\times \left[(q_1+q_2)^\rho g^{\mu\nu} + (p_2-q_2)^\mu g^{\nu\rho} - (q_1+p_2)^\nu g^{\mu\rho}\right],\end{aligned} \tag{2.2.9}$$

where $t^{a,ij}$ is the i,j element of the fundamental $\mathrm{SU}(3)_c$ generator t^a, $q_i := p_a - \sum_{j<i} p_j$ such that $q_i^2 = \hat{t}_i$, and we have used the currents which retain more of the LO structure of the amplitude. This simplifies in the MRK limit:

$$\begin{aligned}\mathcal{M}_{t-\text{channel}} \to & f^{abc} t^{c,i_1 i_a} t^{b,i_3 i_b} \frac{-g_s^3}{\hat{t}_1 \hat{t}_2} \times S^{h_a,h_b\to h_1,h_2}_{qQ\to qQ} \times \varepsilon^{\lambda,*}_\mu(p_2) \\ & \times \left[2p_a^\mu \frac{\hat{s}_{23}}{\hat{s}} - 2p_b^\mu \frac{\hat{s}_{12}}{\hat{s}} - (q_1+q_2)^\mu \right].\end{aligned} \tag{2.2.10}$$

For the other four diagrams, we may use the eikonal approximation of Eq. (1.3.38) by assuming the gluon is soft and produce [92]:

$$\begin{aligned}\mathcal{M}_{q-\text{leg}} = & i g_s^3 \times S^{h_a,h_b\to h_1,h_2}_{qQ\to qQ} \times \varepsilon^{\lambda,*}_\mu(p_2) \\ & \times \left(t^{a,i_1 k} t^{b,k i_a} t^{b,i_3 i_b} \frac{p_1^\mu}{p_1\cdot p_2} \frac{1}{\hat{t}_{b3}} - t^{b,i_1 k} t^{a,k i_a} t^{b,i_3 i_b} \frac{p_a^\mu}{p_a \cdot p_2} \frac{1}{\hat{t}_{b3}} \right. \\ & \left. + t^{b,i_1 i_a} t^{a,i_3 k} t^{b,k i_b} \frac{p_3^\mu}{p_3\cdot p_2} \frac{1}{\hat{t}_{b3}} - t^{b,i_1 i_a} t^{b,i_3 k} t^{a,k i_b} \frac{p_b^\mu}{p_b \cdot p_2} \frac{1}{\hat{t}_{a1}} \right).\end{aligned} \tag{2.2.11}$$

This exhibits again an apparent t-channel pole structure despite that the emission was not mediated by a t-channel gluon. Retaining the full kinematic structure of Eq. (2.2.11) rather than approximating in the MRK limit (which we had to do for the t-channel contribution), we can combine this equation with Eq. (2.2.10) to produce [92]:

$$\begin{aligned}\overline{\left|\mathcal{M}_{qQ\to qgQ}\right|^2} = & \frac{1}{4\left(N_C^2-1\right)} \left\| S_{qQ\to qQ} \right\|^2 \\ & \cdot \left(g_s^2 C_F \frac{1}{\hat{t}_1} \right) \cdot \left(g_s^2 C_F \frac{1}{\hat{t}_2} \right) \\ & \cdot \left(\frac{-g_s^2 C_A}{\hat{t}_1 \hat{t}_2} V^\mu(q_1,q_2)\, V_\mu(q_1,q_2) \right).\end{aligned} \tag{2.2.12}$$

Here V^μ is the generalisation of the *Lipatov effective vertex* of the BFKL formalism to the `HEJ` framework, retaining the MRK limit results but accounting for the LO kinematics at greater accuracy. This is given by (generalising to momenta

q_i, q_{i+1}, p_{i+1}):

$$\begin{aligned} V^{\mu}\left(q_i, q_{i+1}\right) = & -\left(q_i + q_{i+1}\right)^{\mu} \\ & + \frac{p_a^{\mu}}{2}\left(\frac{q_i^2}{p_{i+1}\cdot p_a} + \frac{p_{i+1}\cdot p_b}{p_a\cdot p_b} + \frac{p_{i+1}\cdot p_n}{p_a\cdot p_n}\right) + p_a \leftrightarrow p_1 \\ & - \frac{p_b^{\mu}}{2}\left(\frac{q_{i+1}^2}{p_{i+1}\cdot p_b} + \frac{p_{i+1}\cdot p_a}{p_b\cdot p_a} + \frac{p_{i+1}\cdot p_1}{p_b\cdot p_1}\right) - p_b \leftrightarrow p_n. \end{aligned} \tag{2.2.13}$$

The Lipatov vertex carries a full dependence of the form $V^{\mu}(p_a, p_b, p_1, p_n, q_i, q_{i+1})$, however we often omit the momenta of the incoming partons (p_a, p_b) and the extremal partons in the final state (p_1, p_n) for concision. The retention of the MRK limit of this vertex can be demonstrated by showing:

$$|V(q_1, q_2)\cdot V(q_1, q_2)| \to \frac{4q_{\perp 1}^2 q_{\perp 2}^2}{p_{\perp 2}^2}, \tag{2.2.14}$$

in the MRK limit. Gauge invariance can be shown again by checking the *Ward identity*[1], $p_2 \cdot V(q_1, q_2) = 0$. As is evident from Eq. (2.2.14), the squared matrix element is divergent in the limit that the central gluon becomes soft, since $|V\cdot V|/\hat{t}_1\hat{t}_2$ behaves as $1/p_{\perp 2}^2$. This divergence will cancel with the all-order virtual corrections that we consider after generalising this to the full $2 \to n$ amplitude. We express here a $2 \to n$ scattering $f_1 f_2 \to f_1, g, \ldots, g, f_2$:

$$\begin{aligned} \overline{\left|\mathcal{M}^{\texttt{HEJ},\text{tree}-\text{level}}_{f_1 f_2 \to f_1 g \ldots g f_2}\right|^2} = & \frac{1}{4\left(N_C^2 - 1\right)}\left\|S_{f_1 f_2 \to f_1 f_2}\right\|^2 \\ & \cdot \left(g_s^2 K_{f_1}\frac{1}{\hat{t}_1}\right)\cdot\left(g_s^2 K_{f_2}\frac{1}{\hat{t}_{n-1}}\right) \\ & \cdot \prod_{i=1}^{n-2}\left(\frac{-g_s^2 C_A}{\hat{t}_i\hat{t}_{i+1}} V^{\mu}\left(q_i, q_{i+1}\right) V_{\mu}\left(q_i, q_{i+1}\right)\right), \end{aligned} \tag{2.2.15}$$

with K_{f_1} and K_{f_2} the colour factors corresponding to respectively f_1 and f_2, recalling the colour acceleration multiplier of Eq. (2.2.8) must be used for gluons. Manifest in this expression is the IR divergence appearing in the soft limit for each gluon inside the rapidity interval bounded by f_1 and f_2.

[1]For a process with one outgoing vector boson we define $\mathcal{M} = \varepsilon_{\mu}(p)M^{\mu}$. The *Ward-Takahashi*, or just *Ward* identity is then: $p_{\mu}M^{\mu} = 0$ as a consequence of gauge invariance [25, 39].

2.2.3 All-Orders with HEJ — The Lipatov Ansatz

The HEJ treatment of all-order corrections is to apply the *Lipatov ansatz* of the BFKL formalism, which is known to resum the corresponding leading logarithms from the BFKL evolution [84]:

$$\frac{1}{\hat{t}_i} \to \frac{1}{\hat{t}_i}\left(\frac{\hat{s}_{i-1,i}}{\hat{t}_i}\right)^{\alpha(\hat{t}_i)} \approx \frac{1}{\hat{t}_i}\exp\left[\alpha(\hat{t}_i)(y_{i-1}-y_i)\right]. \tag{2.2.16}$$

The cancellation between the soft real and virtual divergences can be organised by regularising the difference of the Regge trajectory α from unity. Regularising α in $4+2\epsilon$ dimensions (and introducing a regularising scale μ of mass dimension $+1$) gives [29, 92]:

$$\alpha(q_i) = \alpha_s C_A q_{\perp i}^2 \mu^{-2\epsilon}\int_0^{q_{\perp i}} \frac{\mathrm{d}^{2+2\epsilon}k_\perp}{(2\pi)^{2+2\epsilon}}\frac{1}{k_\perp^2(k_\perp - q_{\perp i})^2} = \frac{-2C_A}{(4\pi)^{1+\epsilon}}\frac{\Gamma(1-\epsilon)}{\epsilon}\alpha_s\left(\frac{q_{\perp i}^2}{\mu^2}\right)^\epsilon, \tag{2.2.17}$$

to leading-logarithmic accuracy. We have used the momentum q_i in the t-channel rather than the square $\hat{t}_i$ as the argument.

From the divergent behaviour of the real corrections in the soft limit for p_i, we can show the following:

$$\overline{|\mathcal{M}_{n+1}|^2} \to \left(\frac{4g_s C_A}{p_{\perp i}^2}\right)\overline{|\mathcal{M}_n|^2}, \tag{2.2.18}$$

where the n amplitude corresponds to the $n+1$ with the external leg of momentum p_i removed. The diligent reader may have noticed a connection with our definition of the QCD splitting functions in Eq. (1.3.43) and, for example, Eq. (1.3.42). These limits are not only relevant for organising the cancellation of soft divergences in HEJ amplitudes, but also when we consider matching HEJ with a parton shower in Ch. 3.

We can integrate the factor $\left(\frac{4g_s^2 C_A}{p_{\perp i}^2}\right)$ beneath an IR cutoff λ and dimensionally regularise the phase space integral, yielding:

$$\begin{aligned}\mu^{-2\epsilon}\int_{|\mathbf{p}_\perp|<\lambda}\frac{\mathrm{d}^{3+2\epsilon}\mathbf{p}_i}{(2\pi)^{3+2\epsilon}2E_i}\frac{4g_s^2C_A}{p_{\perp i}^2} &= \mu^{-2\epsilon}\int_{y_{i-1}}^{y_{i+1}}\frac{\mathrm{d}y_i}{4\pi}\int_0^\lambda\frac{\mathrm{d}^{2+2\epsilon}p_{\perp i}}{(2\pi)^{2+2\epsilon}}\frac{4g_s^2C_A}{p_{\perp i}^2}\\ &= \frac{4C_A}{(4\pi)^{1+\epsilon}}\Delta y_{i-1,i+1}\frac{1}{\epsilon\Gamma(1+\epsilon)}\alpha_s\left(\frac{\lambda^2}{\mu^2}\right)^\epsilon.\end{aligned} \tag{2.2.19}$$

Here the difference $\Delta y_{i-1,i+1}$ arises since the rapidity sampling at LL for p_i is flat in

the interval between y_{i-1} and y_{i+1}. Comparing Eq (2.2.17) to Eq. (2.2.19), we see that, order by order, the soft divergences between the virtual and real corrections cancel[1], leaving behind only the finite remainder:

$$\omega^0(q_i;\lambda^2)\Delta y_{i-1,i+1} := -\frac{\alpha_s C_A}{\pi}\log\left(\frac{q_{\perp i}^2}{\lambda^2}\right)\Delta y_{i-1,i+1}. \tag{2.2.20}$$

This a regularised analogue of the Regge trajectory. Noting that there is now a term to be subtracted for the soft divergence with $|\mathbf{p}_{\perp i}| < \lambda$, we can write the fully regularised HEJ matrix element with resummed high energy real and virtual corrections to all orders as [7, 92]:

$$\begin{aligned}
\overline{\left|\mathcal{M}^{\texttt{HEJ},\text{reg.}}_{f_1f_2\to f_1g\ldots gf_2}\right|^2} =& \frac{1}{4\left(N_C^2-1\right)}\left\|S_{f_1f_2\to f_1f_2}\right\|^2 \\
&\cdot\left(g_s^2K_{f_1}\frac{1}{\hat{t}_1}\right)\cdot\left(g_s^2K_{f_2}\frac{1}{\hat{t}_{n-1}}\right) \\
&\cdot\prod_{i=1}^{n-2}\left(g_s^2C_A\left(\frac{-1}{\hat{t}_i\hat{t}_{i+1}}V^\mu\left(q_i,q_{i+1}\right)V_\mu\left(q_i,q_{i+1}\right)-\frac{4}{\mathbf{p}_{\perp i}^2}\Theta\left(-\mathbf{p}_{\perp i}^2+\lambda^2\right)\right)\right) \\
&\cdot\prod_{j=1}^{n-1}\exp\left[\omega^0\left(q_j;\lambda^2\right)\left(y_{j+1}-y_j\right)\right], \\
\omega^0\left(q_j;\lambda^2\right) =& -\frac{\alpha_s C_A}{\pi}\log\frac{q_{\perp j}^2}{\lambda^2}.
\end{aligned} \tag{2.2.21}$$

This current-current scattering may be schematically represented in Fig. 2.5 where the t-channel reggeised gluon exchanges are shown as zig-zagged lines and the Lipatov effective emission vertices by the shaded boxes. The final state is ordered in rapidity. Importantly, this is **not** a Feynman diagram and only represents the structure of a HEJ amplitude calculation. These configurations are the FKL or LL configurations we referred to in Sec. 2.1. They are characterised by the rapidity interval bound by the partons with flavour f_1 and f_2 and that only gluons are emitted between them. Configurations such as those contributing to the matrix element plotted in the right of Fig. 2.1 are subleading — in particular the considered configuration is an extremal (in rapidity) $q\overline{q}$ pair production.

The subleading configurations to which HEJ can apply the leading logarithmic all-

[1] To LL, there is no collinear divergence, since all particles are strongly ordered in rapidity.

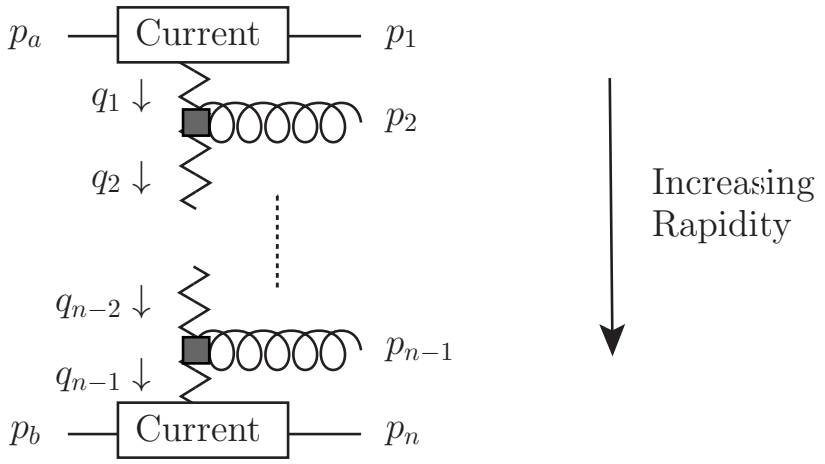

Figure 2.5: Schematic of a HEJ amplitude, showing the scattering of currents as mediated by t-channel *reggeised*-gluon exchanges. Emissions from HEJ-generalised effective vertices are ordered in rapidity on the right. From ref. [7].

order resummed corrections include, at the time of writing this thesis, the *unordered* emissions: those with a gluon or $q\overline{q}$ pair produced outside the rapidity interval formed by y_1 and y_n [7] (these are extremal $q\overline{q}$ configurations). LL resummation may be applied to configurations with a $q\overline{q}$ pair produced inside the rapidity interval; these are referred to as central $q\overline{q}$ production [87]. The states which HEJ can apply LL resummation to are referred to as (HEJ-)*resummable*, and the rest are classified as non-resummable. If we produce a HEJ prediction to LL accuracy only, then we imply that the subleading configurations have been treated as non-resummable for that prediction. Otherwise, for a full HEJ prediction including the LL resummation on LL and subleading configurations, the subleading configurations are treated as resummable.

The subleading corrections are implemented by making modifications to the currents in Eq. (2.2.5) to accommodate these processes. We examine the role of subleading corrections in greater detail in Ch. 3 when we discuss the classification of HEJ-resummable states in the HEJ+Pythia scheme for merging HEJ resummation with the parton shower of Pythia8 [47].

To draw from the resummed, regularised matrix elements in HEJ to cross sections,

one needs only integrate Eq. (2.2.21) over the Lorentz-invariant phase space:

$$\begin{aligned}\sigma_{2j}^{\text{resum}} = \sum_{f_1,f_2} \sum_m \prod_{j=1}^{m} \left(\int_{p_{\perp j}=0}^{p_{\perp j}=\infty} \frac{\mathrm{d}^2\mathbf{p}_{\perp j}}{(2\pi)^3} \int \frac{\mathrm{d}y_j}{2} \right) (2\pi)^4 \, \delta^{(2)}\left(\sum_{k=1}^{m} \mathbf{p}_{\perp k} \right) \\ \times \; x_a \, f_{a/f_1}(x_a, (\mu_a)^2) \; x_b \, f_{b/f_2}(x_b, (\mu_b)^2) \; \frac{\overline{\left|\mathcal{M}^{\texttt{HEJ,reg.}}_{f_1 f_2 \to f_1 g \ldots g f_2}\right|^2}}{\hat{s}^2} \mathcal{O}_{2j}(\{p_i\}).\end{aligned} \tag{2.2.22}$$

The x_a, x_b values are fixed by performing the integrals over these — as per the QCD factorisation formula of Eq. (1.3.45) — and using two of the δ-functions from the Lorentz-invariant phase space to use the final state to generate the required values. This is why the Lorentz-invariant phase space in Eq. (2.2.22) carries only two dimensions in the momentum-conserving δ-function. The inclusive two jet measure $\mathcal{O}_{2j}(\{p_i\})$ returns 1 if at least two jets are observed in the final state with momenta $\{p_i\}$ and 0 otherwise.

We have centred the discussion around inclusive dijet production in QCD however the HEJ framework has been applied to calculate such matrix elements for dijet production with $W^\pm$ [94], H [7], Z/γ^* [95] and same-sign $W^\pm W^\pm$ [96] bosons. For these states, the currents of Eq. (2.2.5) are modified to accommodate the boson emission. We detail the calculation for a Higgs boson current in Ch. 4 where we explore the behaviour of HEJ amplitudes for the production of a Higgs boson with at least one jet.

2.2.4 Event Generation in HEJ

High Energy Jets, while not a general purpose event generator, provides a Monte Carlo framework for evaluating the fully differential cross sections from the resummed matrix elements. Many of the considerations that feature in the general purpose framework feature also in our discussion of HEJ event generation and their generalisation is far from trivial, including LO matching. While the form of the purely HEJ-resummed cross section in Eq. (2.2.22) is simple, including LO matching requires much development.

We start by considering LL HEJ configurations (FKL configurations), i.e. events

which are $2 \to n$ scatterings of the form $f_1 f_2 \to f_1 g \cdots g f_2$ with the final state ordered in rapidity and f_1 (f_2) entering the initial state along the positive (negative) z axis. The HEJ cross section for the LL-resummed, LO-matched inclusive two jet scattering is given by [97]:

$$
\begin{aligned}
\sigma_{2j}^{\text{resum,match}} = & \sum_{f_1,f_2} \sum_m \prod_{j=1}^{m} \left(\int_{p_{\perp j}^B = p_{\perp,\min}^{J,B}}^{p_{\perp j}^B = \infty} \frac{\mathrm{d}^2 \mathbf{p}_{\perp j}^B}{(2\pi)^3} \int \frac{\mathrm{d}y_j^B}{2} \right) (2\pi)^4 \, \delta^{(2)}\left(\sum_{k=1}^{m} \mathbf{p}_{\perp k}^B \right) \\
& \times x_a^B \, f_{a/f_1}(x_a^B, (\mu_a^B)^2) \, x_b^B \, f_{b/f_2}(x_b^B, (\mu_b^B)^2) \, \frac{\overline{\left| \mathcal{M}_{\text{LO}}^{f_1 f_2 \to f_1 g \cdots g f_2}\left(\left\{ p_j^B \right\} \right) \right|^2}}{(\hat{s}^B)^2} \\
& \times \frac{w_{m-\text{jet}}}{\left| \mathcal{M}_{f_1 f_2 \to f_1 g \cdots g f_2}^{\text{LO}}\left(\left\{ p_j^B \right\} \right) \right|^2} \times (2\pi)^{-4+3m} \, 2^m \\
& \times \sum_{n=2}^{\infty} \int_{p_{\perp 1} = p_{\perp,\min}^J}^{p_{\perp 1} = \infty} \frac{\mathrm{d}^2 \mathbf{p}_{\perp 1}}{(2\pi)^3} \int_{p_{\perp n} = p_{\perp,\min}^J}^{p_{\perp n} = \infty} \frac{\mathrm{d}^2 \mathbf{p}_{\perp n}}{(2\pi)^3} \prod_{i=2}^{n-1} \int_{p_{\perp i} = \lambda}^{p_{\perp i} = \infty} \frac{\mathrm{d}^2 \mathbf{p}_{\perp i}}{(2\pi)^3} \, (2\pi)^4 \, \delta^{(2)}\left(\sum_{k=1}^{n} \mathbf{p}_{\perp k} \right) \\
& \times \mathbf{T}_y \prod_{i=1}^{n} \left(\int \frac{\mathrm{d}y_i}{2} \right) \mathcal{O}_{mj}^e \left(\prod_{l=1}^{m-1} \delta^{(2)}(\mathbf{p}_{\mathcal{J}_l \perp}^B - \mathbf{j}_{l\perp}) \right) \left(\prod_{l=1}^{m} \delta(y_{\mathcal{J}_l}^B - y_{\mathcal{J}_l}) \right) \\
& \times x_a f_{a/f_1}(x_a, \mu_a^2) \, x_b f_{b/f_2}(x_b, \mu_b^2) \, \frac{\overline{\left| \mathcal{M}_{f_1 f_2 \to f_1 g \cdots g f_2}^{\text{HEJ,reg.}}(\{p_i\}) \right|^2}}{\hat{s}^2} \, \mathcal{O}_{2j}(\{p_i\}) \\
& \times \frac{(\hat{s}^B)^2}{x_a^B \, f_{a/f_1}(x_a^B, (\mu_a^B)^2) \, x_b^B \, f_{b/f_2}(x_b^B, (\mu_b^B)^2)}.
\end{aligned}
\tag{2.2.23}
$$

We have highlighted different parts of the formula to refer to different stages of the calculation. Focusing first on the top two lines, highlighted in blue, we note that these are just LO cross sections for m jets (with the phase space integral on the first line and the flux and squared matrix element on the second line), summed over multiplicity. If we terminate the sum on the first line at $m = 2$ then these two lines are just the inclusive dijet cross section at LO. In each case LO quantities are indicated with a B superscipt (or LO superscript to indicate the matrix elements).

The third line, highlighted in orange encodes the matching procedure to ensure LO accuracy across phase space is guaranteed. The term $w_{m-\text{jet}}$ is given per LO phase space point by:

$$
w_{m-\text{jet}} \equiv \frac{\overline{\left| \mathcal{M}_{f_1 f_2 \to f_1 g \cdots g f_2}^{\text{LO}}\left(\left\{ p_j^B \right\} \right) \right|^2}}{\left| \mathcal{M}_{f_1 f_2 \to f_1 g \cdots g f_2}^{\text{LO, HEJ}}\left(\left\{ p_j^B \right\} \right) \right|^2}, \tag{2.2.24}
$$

which depends only on the corresponding HEJ LO approximation. Since the LO

approximation is used for HEJ in the matching term, the emission phase space is identical to the LO term and thus the same phase space point may be used to obtain the matching term as was used in the LO generation.

The last four lines of Eq. (2.2.23) encode the HEJ resummation as described in Sec. 2.2. The first line of this block (immediately following the matching term in orange) is the phase space integration of the transverse momenta of the event after emissions are added by HEJ. The sum at the start of this term simply ensures the all possible n-particle states are produced. This includes soft emissions beneath the minimum jet transverse momentum scale $p^J_{\perp,\min}$ (above which all fixed-order jets are generated). The soft emissions generated by HEJ are produced above a minimum soft transverse scale λ.

In the next line (line 5) we see the rest of the phase space integral measure and δ-functionals which ensure that — for a given m-jet phase space point at LO — the resummed HEJ event with additional soft radiation still contains m jets with transverse momenta exceeding $p^J_{\perp,\min}$. More specifically, a map is used to project an n particle phase space point onto the m particle LO phase space (for $n > m$). This map is given by:

$$\mathbf{p}^B_{\mathcal{J}_l\perp} = \mathbf{j}_{l\perp} + \mathbf{q}_\perp \frac{|\mathbf{p}_{\mathcal{J}_l\perp}|}{\sum |\mathbf{p}_\perp|}, \tag{2.2.25}$$

where $\mathbf{p}_{\mathcal{J}_l\perp}$ is the transverse momentum of the jet after resummation, $\mathbf{q}_\perp$ is the vector sum of non-jet transverse momenta in the event after resummation, $\mathbf{j}_{l\perp}$ is the vector transverse momentum of the LO jets. The sum in the denominator of the fraction on the right hand side is the scalar sum of all transverse momenta in the final state. The initial state momenta need to be reassigned after the momentum mapping is applied to the final state, this is done by summing the positive and negative lightcone-momentum components $p^\pm = E \pm p_z$ in the final state and setting the momentum of the partons incoming along the z-axis to:

$$p'_a = \left(\frac{P^+}{2}, 0, 0, \frac{P^+}{2}\right), \qquad p'_b = \left(\frac{P^-}{2}, 0, 0, \frac{-P^-}{2}\right), \tag{2.2.26}$$

with $P^\pm = \sum_f p_f^\pm$, where p_f are the momenta of the final state particles.

The exclusive jet observable measure:

$$\mathcal{O}^e_{mj}\left(\prod_{l=1}^{m-1}\delta^{(2)}(\mathbf{p}^B_{\mathcal{J}_l\perp}-\mathbf{j}_{l\perp})\right), \tag{2.2.27}$$

ensures that the projection of the resummation phase space point onto the Born/LO phase space produces the same jets as observed in the Born configuration. The jet rapidities are also required to be unchanged by the resummation and the whole final state is premultiplied by the rapidity-ordering operator $\mathbf{T}_y$.

The bottom two lines of Eq. (2.2.23) compute the integrand of the resummed expression, including the HEJ-resummed matrix elements of Eq. (2.2.21) and the PDFs re-evaluated at the resummation scales and x values corresponding to the resummation event. This requires reweighting the original Born integrand with the new values as done in the bottommost line.

Making predictions with HEJ

As well as neatly packaging the HEJ framework into one formula, Eq. (2.2.23) illustrates how this is implemented in HEJ (v2.0+) [98]. One requires a Born-level event generator (in practice Sherpa is most-often used) to produce the blue LO terms for each jet multiplicity until a maximum multiplicity, this corresponds to setting an upper limit in the sum over m in Eq. (2.2.23). This is mostly due to the computational cost of computing high multiplicity multi-leg matrix elements, which increases rapidly for increasing multiplicities. In cases where higher multiplicities are further required, HEJ (v2.0+) comes with a fixed-order generator that produces multi-jet matrix element states for very high multiplicities at low computational cost, but only using the HEJ approximation at LO.

The leading order sample is passed through HEJ which will then construct resummation *trials* for each LO input event, reweighting those that are successful by the phase space integral and resummation matrix element and flux in the four bottom lines of the equation. The end result is that all m-jet LO input is supplemented with HEJ resummation for the resummable configurations.

We noted in Sec. 1.5.1 that the errors in Monte Carlo integration can be calculated as per Eq. (1.5.5), thus one may naïvely conclude that the error in the Monte Carlo implementation of Eq. (2.2.23) can be calculated by the total number of events generated i.e. the total number of (successful) HEJ trials for each input LO event, summed. This is not the case as the integral in the top two lines of Eq. (2.2.23) is performed over a different phase space to the bottom four lines. This latter integral is performed over the resummation phase space for the current input fixed-order phase space point. The number of (successful) trials for an individual input LO event can only be used to derive the error on the integration for that event. The true Monte Carlo error in the HEJ prediction depends chiefly on how well-sampled the LO phase space is by the generator used to produce the LO events. Only the uncertainty on the resummation phase space is controlled by the number of resummation trials in HEJ.

To retain full LO matching, the non-resummable cross section must be included in the HEJ description. This takes a simpler form than the resummed:

$$\begin{aligned}\sigma_{2j}^{\text{non-resum}} = \sum_{f_1,f_2}\sum_m \prod_{j=1}^{m}\left(\int_{p_{\perp j}^B=0}^{p_{\perp j}^B=\infty}\frac{\mathrm{d}^2\mathbf{p}_{\perp j}^B}{(2\pi)^3}\int\frac{\mathrm{d}y_j^B}{2}\right)(2\pi)^4\,\delta^{(2)}\left(\sum_{k=1}^{m}\mathbf{p}_{\perp k}^B\right)\\ \times\; x_a^B\; f_{a/f_1}(x_a^B,(\mu_a^B)^2)\; x_b^B\; f_{b/f_2}(x_b^B,(\mu_b^B)^2)\;\frac{\overline{\left|\mathcal{M}_{\text{LO}}^{\text{non-resum}}\left(\left\{p_j^B\right\}\right)\right|^2}}{(\hat{s}^B)^2},\end{aligned} \tag{2.2.28}$$

i.e. the topmost two lines of Eq. (2.2.23) without any additional corrections. Since there is no probability of transitioning between resummable and non-resummable phase space in HEJ (unlike in the parton shower where all LO states could be produced by the shower, as we shall see in the next section), there is no risk of double-counting contributions in formulating the cross section this way. This means that for each phase space point read by HEJ, either the full LO matrix element is used, or the LO accuracy is bolstered with HEJ resummation, ensuring at least LO accuracy across phase space.

In addition to the FKL contributions explicitly formulated in Eq. (2.2.23), resummable configurations in HEJ (>v2.0) now include contributions to the subleading

processes in BFKL as mentioned in Sec. 2.2. The currents for these channels and for all mentioned processes are implemented in `HEJ`, and we discuss in Ch. 4 the development of `HEJ` matrix elements for the inclusive production of a Higgs boson with at least one jet. Ref. [87] provides a robust review of the subleading corrections to `HEJ` amplitudes for the inclusive production of a W boson with at least two jets, including how the subleading currents are implemented and discussions of NLO matching. We also discuss multiplicative NLO matching in Ch. 4 where we apply this concept to both inclusive $H + 1j$ production and $H + 2j$ production.

To conclude this chapter in the next section we lay out in detail the necessary theoretical groundwork behind the resummation of soft and collinear logarithms by parton showers.

2.3 Parton Showers and Soft-Collinear Logarithms

To illustrate the emergence of soft-collinear logarithms to all orders in perturbative QCD, we revisit the discussion of Sec. 1.3.2 on parton splittings. We sketched the derivation of the splitting functions in QCD and displayed an example for $q \to qg$ splitting in Fig. 1.6. We show again the spin- and azimuthal angle-averaged splitting function of Eq. (1.3.44) here:

$$P_{qq}(z) = C_F \frac{1+z^2}{1-z}.$$

We shall apply this for the moment to production of $q\overline{q}$ pairs from e^-e^+ scattering such that we only have to consider the probabilities of QCD splittings in the final state [45]. Assuming the quark q in the final state emits a gluon in much a similar manner to Fig. 1.6 we may use Eq. (1.3.42) to write for the cross section in the soft-collinear limit:

$$\mathrm{d}\hat{\sigma}(e^-e^+ \to qg\overline{q}) = \hat{\sigma}(e^-e^+ \to q\overline{q}) \frac{\mathrm{d}t}{t} \mathrm{d}z \mathrm{d}\phi \frac{\alpha_s}{2\pi} P_{qq}(z). \tag{2.3.1}$$

Since z is the energy fraction of the daughter[1] quark after it has emitted a gluon, the bounds of the integral over z are 0 and 1 — the latter being where the splitting function logarithmically diverges. We regulate this divergence by limiting the upper bound to $1-\epsilon$ ($0<\epsilon<1$) and calculate:

$$\begin{aligned}\int \mathrm{d}\phi \int_0^{1-\epsilon} \mathrm{d}z C_F \frac{\alpha_s}{2\pi}\frac{1+z^2}{1-z} &= C_F\alpha_s \int_0^{1-\epsilon}\mathrm{d}z \frac{1+z^2}{1-z} \\ &\approx C_F\alpha_s\int_0^{1-\epsilon}\mathrm{d}z\frac{2}{1-z} - C_F\alpha_s\int_0^1 \mathrm{d}z(1+z) \\ &= 2C_F\alpha_s\left[\log\left(\frac{1}{\epsilon}\right)-\frac{3}{4}\right],\end{aligned} \tag{2.3.2}$$

neglecting the running of α_s. Taking $\epsilon = t/t'$, with t the ordering variable (or the *scale* as it is often referred to), we can integrate over (the logarithmically divergent part of) Eq. (2.3.1) to give:

$$2C_F\int_{t_{\min}}^{t'}\frac{\mathrm{d}t}{t}\alpha_s\log\left(\frac{t'}{t}\right) = C_F\alpha_s\log^2\left(\frac{t'}{t_{\min}}\right)\propto\alpha_s L^2. \tag{2.3.3}$$

This is a leading-logarithmic correction to the LO process — a double logarithm of the ratio of scales widely separated in the soft and collinear limit [8]. We have introduced a resolution scale $t_{\min}$, which is the minimum scale of a parton shower emission (i.e. the scale beneath which emissions are no longer resolvable). The quantity t' represents the scale at which the Born process was produced, and there is a notion of ordering of soft emissions down to the minimum scale $t_{\min}$. Subleading single logarithms also contribute in the individual soft and collinear limits, giving rise to terms $\sim\alpha_s L$ rather than $\alpha_s L^2$.

Considering the n^{th} real emission correction to the LO $e^-e^+\to q\bar{q}$ cross section, the contribution from the splitting with the above kinematics is given by:

$$\frac{1}{n!}(-1)^{n+1}\left(\frac{\alpha_s C_F L^2}{2\pi}\right)^n, \tag{2.3.4}$$

to leading-logarithmic accuracy. We may thus *resum* these terms by multiplying the

[1]Typically, the parton pre-splitting is referred to as the *mother* and the splitting products the *daughters*.

LO cross section by [30, 39, 45]:

$$\Delta_{ab}(t', t_{\min}) := \exp\left\{-\int_{t_{\min}}^{t'} \frac{\mathrm{d}t}{t}\left(\frac{\alpha_s(t)}{2\pi}\int_{z_{\min}}^{z_{\max}} \mathrm{d}z P_{ab}(z)\right)\right\}. \tag{2.3.5}$$

This is the famous *Sudakov form factor* for a generic $a \to bc$ splitting, in the most general form with the running of α_s restored. We have left the limits on the z integration arbitrary for full generality, since this Sudakov form factor produces the no-emission probability for any two scales, i.e. $\Delta(t_j, t_k)$ gives the no-emission probability between scales t_j and t_k, with $t_j > t_k$. We arrive at the no-emission probability by imposing unitarity; the probability of observing n emissions is exactly the difference from unity of the corresponding probability of no-emission. A Taylor expansion of Eq. (2.3.5) verifies indeed that the all-orders double logarithms are resummed. Further logarithmic accuracy may be obtained (in a manner analogous to the treatment of subleading accuracies in the BFKL formalism of Sec. 2.1) by including the subleading terms to the kernel:

$$P_{ab}(t, z) := \frac{\alpha_s(t)}{2\pi}\frac{1}{t}P_{ab}(z). \tag{2.3.6}$$

If we consider QCD initial and final states (e.g. generalising from e^-e^+ scattering to $q\overline{q} \to q\overline{q}$), we note that there is a probability for initial state partons to emit QCD radiation that enters the final state. Convolving the partonic cross section of Eq. (2.3.1) with the PDFs to yield the hadronic cross-section of Eq. (1.3.45) will not produce the correct DGLAP evolution. The initial state radiation (ISR) splitting probabilities must be reweighted by a an additional factor compared to the final state radiation (FSR) probabilities. This is done to reproduce the correct *backward evolution* [30] for an initial state splitting with flavours $i \to jk$:

$$P_{ij}(t, z) \xrightarrow{\text{ISR}} \frac{x_j f_j(x_j, \mu_F^2)}{x_i f_i(x_i, \mu_F^2)} P_{ij}(t, z). \tag{2.3.7}$$

Interpreting the resummation beneath a more probabilistic lens, we note that the Sudakov form factor of Eq. (2.3.5) is nothing more than a probability of no emission between scales t' and $t_{\min}$. The review of ref. [39] draws an aesthetic parallel to the

decay constant in radioactive decay for which the no-emission probability between different times is also an exponentially distributed variable. Indeed, taking the derivative with respect to the ordering variable t of Eq. (2.3.5) yields:

$$\frac{\mathrm{d}\Delta_{ab}(t, t_{\min})}{\mathrm{d}t} = -\Delta_{ab}(t, t_{\min}) \int \mathrm{d}z P_{ab}(t, z). \tag{2.3.8}$$

We hence often refer to $P_{ab}(t, z)$ as displayed in Eq. (2.3.6) as the splitting *probability*.

The all-orders soft-collinear virtual corrections follow from unitarity; the addition of soft-collinear radiation does not alter integrated cross sections for hard processes since the probability for a resolvable emission and that for an unresolvable emission (i.e. the Sudakov form factor) must sum to one [39]. More formally:

$$P(\text{resolvable, real}) = 1 - P(\text{unresolvable, real + virtual}), \tag{2.3.9}$$

showing the separation of real and virtual corrections explicitly.

2.3.1 The Sudakov Veto Algorithm

The Monte Carlo tools used to numerically resum the soft-collinear logarithms arising from parton splittings are called *parton showers*. They proceed at their most simple by evolving a hard process (a $2 \to 2$ scattering for dijet production, for instance) down in evolution scale from an initial scale t_0, applying emissions down to the lowest scale $t_{\min}$ according to the following algorithm [30]:

1. Generate a random number r uniformly distributed in $[0, 1]$.

2. Solve $\Delta(t_i, t_{i+1}) = r$ for t_{i+1}, this is the scale of the splitting.

3. If $t_i > t_{\min}$ then set $i \to i + 1$ and return to step 1, otherwise terminate the evolution.

This dresses the $2 \to 2$ configuration with the appropriately constructed soft and collinear radiation resulting from parton splittings. This formulation is severely limited outside of the regions with soft-collinear enhancement — just as the MRK

limit produces weaker descriptions of the full phase space outside of the MRK-enhanced regions. Modern parton showers typically are packaged with fuller GPMC event generators which we discuss in Sec. 1.5.2. GPMC event generators come equipped with schemes for matching and merging high multiplicity fixed-order matrix elements with parton shower resummation and present the natural generalisation of these effects as `HEJ` was for the high-energy logarithms. We outline these procedures in Sec. 2.3.3.

Solving $\Delta(t,t') = r$ for generic $r \in [0,1]$ is complicated and computationally expensive. Instead, the *Sudakov veto algorithm* is used [51,63]. Noting that $\Delta(t,t) = 1$, our interpretation of the Sudakov factor as a no-emission probability allows us to write for the probability of an emission at scale $t' < t$:

$$\frac{\Delta(t,t')}{\Delta(t,t)} =: \frac{F(t')}{F(t)}, \tag{2.3.10}$$

where we have defined $F(t') := \Delta(t,t')$. If the primitive of F, f, is known then another monotonic positive-definite function G may be identified (with corresponding primitive g) satisfying:

$$\frac{f(t')}{F(t')} < \frac{g(t')}{G(t')}. \tag{2.3.11}$$

If the function G is simpler to work with than F then one may use it to generate the correct probability distribution by following the aforementioned Sudakov veto algorithm:

1. Start downward evolution from scale t_i ($i = 0$ from hard process).
2. Solve $G(t') = rG(t_i)$ for random r uniformly distributed in $[0,1]$
   (a) If $\frac{f(t')}{F(t')} > s\frac{g(t')}{G(t')}$ and $t' > t_{\min}$ for random s uniformly distributed in $[0,1]$, then keep the emission at scale t' by setting $i \to i+1$, $t_{i+1} = t'$ and returning to step 1.
   (b) Otherwise, if $\frac{f(t')}{F(t')} \leq s\frac{g(t')}{G(t')}$ and $t' > t_{\min}$, then *veto* the emission and set $t_i = t'$, then return to step 2 to find a new t' at a lower scale than the current value.

(c) Otherwise, if $t' < t_{\min}$ then no emission occurs, the shower can be terminated.

This procedure will produce and veto additional emissions in between each stage of the shower. Intuitively, one can see that this replicates the necessary probability distribution. A rigorous proof of this may be found in much of the supporting literature to this thesis, we recommend Sec. 4.2 of ref. [63], the original physics manual for the PYTHIA event generator (v6.4). We make use of this method of showering when producing a subtracted shower for merging with HEJ in Ch. 3.

Ordering variable

Our discussion of the ordering variable t has been rather general, we now explore the specifics. The factor $1/t$ arising in the splitting probability comes from the pole in the propagator that precedes the splitting. Returning to Eq. (1.3.39) and recasting in the limit of massless partons, we see that the divergence arises when partons are collinear or soft after a splitting. The ordering variable parametrises the transition to the infrared-divergent region of emission phase space such that, for large values of t, the splittings are less divergent. There is a significant freedom in the specific form of this ordering variable and there are implementations using the virtuality of the mother parton q^2, the transverse momentum of the emission $p_\perp^2$, and the opening angle ϑ as evolution variables [39]. To leading-logarithmic accuracy, these ordering variables produce equivalent results [39, 99]:

$$\frac{dp_\perp^2}{p_\perp^2} = \frac{d\vartheta}{\vartheta} = \frac{dq^2}{q^2}. \tag{2.3.12}$$

Angular ordering, available in HERWIG [64, 65] for example, uses the opening angle ϑ between the daughter partons as this evolution variable[1]. Emissions are produced initially at wide opening angles between the LO partons with these reducing until the minimum scale is reached.

[1] Specifically, the angular ordered shower of ref. [65] uses $\vartheta^2 E^2$ as the evolution variable, with E the energy of the mother parton.

2.3.2 Modern Parton Showers

The parton showers of PYTHIA [47, 63] and `Sherpa` [62] are transverse momentum-ordered. Here, the transverse momentum is understood to signify the momentum of the emission transverse to the mother parton. We focus on the implementation of PYTHIA as this will lend itself pertinently to our discussion of the `HEJ`+PYTHIA merging algorithm in Ch. 3. The PYTHIA evolution variable is given by:

$$p_\perp^2 = \begin{cases} z(1-z)q^2 & \text{FSR} \\ (1-z)q^2 & \text{ISR} \end{cases}, \qquad q^2 = \begin{cases} (p^2 - m_0^2) & \text{FSR} \\ (-p^2 + m_0^2) & \text{ISR} \end{cases}, \tag{2.3.13}$$

where q^2 is the (positive-definite) virtuality of the mother parton.

Some parton showers — including `Ariadne` [100] — resum these soft and collinear logarithms with *dipole showers*. In this picture, one may approximate (in the large-N_c limit [39]) colour-connected partons as colour-anticolour dipoles in an event configuration. This arises from the factorisation of colour structure from the kinematic parts of amplitudes [32], and allows us to draw these connections with the colour flow corresponding to products of the relevant colour factors. The dipoles formed by connecting partons in colour then produce splittings rather than the individual partons themselves [39].

We illustrate examples of dipoles in Fig. 2.6 for a diagram in LO $gg \to gg$ scattering, showing the two possible colour connections. There are four dipoles in each, since each gluon carries colour and anticolour charge. In the left diagram there are four FI/IF dipoles $a1$, $1b$, $b2$ and $2a$ which connect the initial (I) state quarks to the final (F) state. In the right, there is one FF dipole 12, an II dipole ba and two FI/IF dipoles $a1$ and $b2$.

When a colour dipole splits, the emitted parton has access to the momentum stored in the dipole and thus each splitting contains three particles — the emitter, the emission and the recoiler. Dipole showers were first suggested in ref. [101] and have since been implemented in the major GPMC event generators PYTHIA, `Sherpa`, and `HERWIG`.

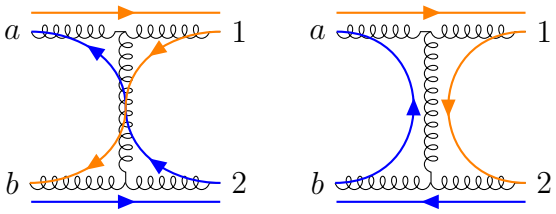

Figure 2.6: The two possible colour flows (up to direction swaps) for scattering of gluons at LO. The left colour flow can be summarised as $(a1b2a)$ and the right as $(a12ba)$. The colour flow is highlighted in blue and orange to not mix the pattern in the left diagram for a crossing.

In dipole showers, splittings are understood to occur between two connected partons $(ij), k$ and produce three connected particles i, j, k. We generalise the discussion from the above splitting kernels to generic dipole splitting kernels $\mathcal{K}^{(\mathrm{DD})}_{ij;k}(\mathbf{\Phi}_1)$, where D indexes the location of each dipole end (i.e. the initial state I or the final state F) and $\mathbf{\Phi}_1$ is the one-particle phase space measure for the emission [39]. The emitter corresponds to i, the emission to j, and the recoiler to k. There are different forms of these kernels as well as the ordering variable depending on the four dipole structures FF, IF, FI, II. To highlight the connections with the splitting kernels of Eq. (2.3.6), we list the FF dipole kernels $\mathcal{K}^{(FF)}$, as provided in ref. [39]:

$$\begin{aligned}
\mathcal{K}^{(FF)}_{qg,k} &= C_F \left[\frac{2}{1 - z_i \left(1 - y_{ij;k}\right)} - (1 + z_i) \right], \\
\mathcal{K}^{(FF)}_{gg,k} &= 2C_A \left[\frac{1}{1 - z_i \left(1 - y_{ij;k}\right)} + \frac{1}{1 - (1 - z_i) \left(1 + y_{ij;k}\right)} - 2 + z_i \left(1 - z_i\right) \right], \\
\mathcal{K}^{(FF)}_{q\bar{q},k} &= T_R \left[1 - 2 z_i \left(1 - z_i\right)\right],
\end{aligned} \tag{2.3.14}$$

where:

$$\begin{aligned}
y_{ij;k} &= \frac{p_i \cdot p_j}{p_i \cdot p_j + p_i \cdot p_k + p_j \cdot p_k}, \\
z_i &= \frac{p_i \cdot p_k}{(p_i + p_j) \cdot p_k} = 1 - z_j.
\end{aligned} \tag{2.3.15}$$

These kernels are produced by requiring that the behaviour in the soft-collinear limit(s) reproduces that of the parton splitting kernels. More formally [39]:

$$\mathcal{K}_{ij;k}\left(\mathbf{\Phi}_1\right) \longrightarrow \begin{cases} \frac{1}{p_i \cdot p_j} P_{(ij)i}\left(z\left(\mathbf{\Phi}_1\right)\right) & \text{(collinear)} \\ \frac{1}{p_i \cdot p_j} \cdot \frac{p_i \cdot p_k}{(p_i + p_j) \cdot p_k} & \text{(soft)} \end{cases} . \tag{2.3.16}$$

The collinear limit applies away from $z \to 1$ and the soft limit applies when $z \to 1$, since all IR limits arise in the limit of $(p_i + p_j) \cdot p_k \to 0$ in the dipole picture.

For a full list of the dipole splitting kernels, the corresponding evolution variables, and kinematics reconstruction, we refer the reader to Appendix C.2 of ref. [39].

The presence of the recoiler in the dipole formalism informs us of the conceptual problem of splitting the momenta of partons such that they remain on-shell. To overcome this, *recoil strategies* are used to reconstruct the kinematics of a splitting such that all participating partons retain their on-shell masses. Recoil strategies can be local — as is the case for dipole showers[1] — where one spectator/recoiler parton is used to reshuffle the momentum in a dipole such that masses are conserved for individual particles.

Pythia8 uses local recoil strategies in the final state dipole shower though the option is provided for *global* recoil strategies to be used [47]. These strategies distribute the additional momentum from adding partons to on-shell, momentum-balanced event configurations amongst all particles in the event.

In Pythia, where FSR is treated by the dipole shower, the (local) recoil strategy for a splitting can be summarised by boosting the particles to the CoM frame of the dipole and writing $(ij), k^0 \to (ij)^*, k \to i, j, k$, where $(ij)^*$ is the intermediate propagator of virtuality Q^2, and k^0 is the recoiler before the splitting. Firstly, the intermediate momenta are assigned:

$$\begin{aligned} p_{(ij)^*} &= p_{(ij)} + \frac{Q^2}{m^2_{(ij),k^0}} p_{k^0}, \\ p_k &= \left(1 - \frac{Q^2}{m^2_{(ij),k^0}}\right) p_{k^0}, \end{aligned} \tag{2.3.17}$$

with $m^2_{(ij),k^0}$ the invariant mass of the dipole before splitting (which is conserved) [104]. This ensures that on-shell momenta p_i, p_j may be added in the dipole CoM frame without violating momentum conservation. The momenta in the process CoM frame can then be obtained by boosting back from the dipole CoM frame. Unlike the

[1] There are modern dipole showers wherein global recoil strategies are used, including PanGlobal [102] and `Alaric` [103].

FSR shower, the kinematics reconstruction of the ISR shower in PYTHIA is handled completely by global recoil strategies since the initial state partons must remain collinear with the hadron beam axis.

Logarithmic accuracy of parton showers

Determining the logarithmic accuracy of parton showers beyond LL is a more involved undertaking than analytic resummation schemes. The question of logarithmic accuracy in the most simple form is simply the number of terms $\alpha_s^n L^{2n-m}$ that are resummed in the soft-collinear limit. However, parton showers provide fully differential descriptions of phase space for many processes meaning some observables may be well-described while others are less so. The resummation is not applied in isolation; recoil strategies and kinematics reconstruction are imposed on the resummed configurations in ways that are not always guaranteed to preserve claimed accuracies of the resummation [99]. Comparisons of early developments in showers with dipole-local recoil schemes identified a shortfall when results were compared to QCD matrix elements in the soft-collinear-enhanced regions of phase space [99].

The recent study of ref. [99] presents an analysis of the formal accuracy of two transverse momentum-ordered showers with dipole-local recoil in FSR — the PYTHIA shower [74], and the `Dire` shower [105] used in `Sherpa`. The criteria proposed by the study for the accuracy of parton showers are:

1. The shower must reproduce the behaviour of matrix elements in the limit of strong ordering between scales.

2. The shower must reproduce the results of analytic resummation of the soft-collinear logarithms to the claimed accuracy where such predictions are available.

The study found that both showers accounted for the leading logarithms to a suitable degree of accuracy by these criteria but that significant discrepancies arose for each at the subleading level, meaning full NLL accuracy for either shower could not be

claimed. Discrepancies were recorded especially when compared to two-emission matrix elements, indicating that the other factors entering a shower calculation (ordering, recoil, kinematics) aside from the resummation carry can alter the accuracy non-trivially. The subsequent study ref. [106] highlighted that modifications to the evolution variables and to the dipole partitions (retaining local, dipole-based recoil) would allow showers to achieve full NLL accuracy consistently for a wide range of observables. Considerations of shower accuracy will become important for this thesis when we produce our own recoil strategy for use in the HEJ+Pythia merging algorithm of Ch. 3.

2.3.3 Matching and Merging Hard Processes to Parton Showers

Since parton shower evolution resums an infinite tower of logarithms, combining fixed-order matrix elements with parton showers quickly becomes complex as the accuracy of ME configurations increases. We display in Fig. 2.7 a graphical representation of the terms present in a perturbative expansion (in $\alpha_s^n L^m$ for shower logarithms L), with shading to indicate the accuracy to which each term is described.

Solid filled terms represent a fully accurate accounting for the corresponding term while half-coloured terms represent only a real emission-accurate description of the term (i.e. excluding a description of the virtual corrections). It is assumed for the purpose of the demonstration that the shower is NLL-accurate. Simple "hardest-emission" LO matching is illustrated in Fig. 2.7(a) where LO ME configurations are matched to the parton shower with only the real emission correction accounted for in the $\mathcal{O}(\alpha_s)$ correction above LO. In Fig. 2.7(b) NLO matching is shown where full NLO ME accuracy is retained (subtracting shower double-counting) and full parton shower resummation is applied. Displayed in Fig. 2.7(c) is multi-jet merging, where the real emission corrections are provided exactly up to a higher perturbative order and systematically supplemented with shower resummation.

For a LO matrix element (where LO is understood to mean the lowest perturbative

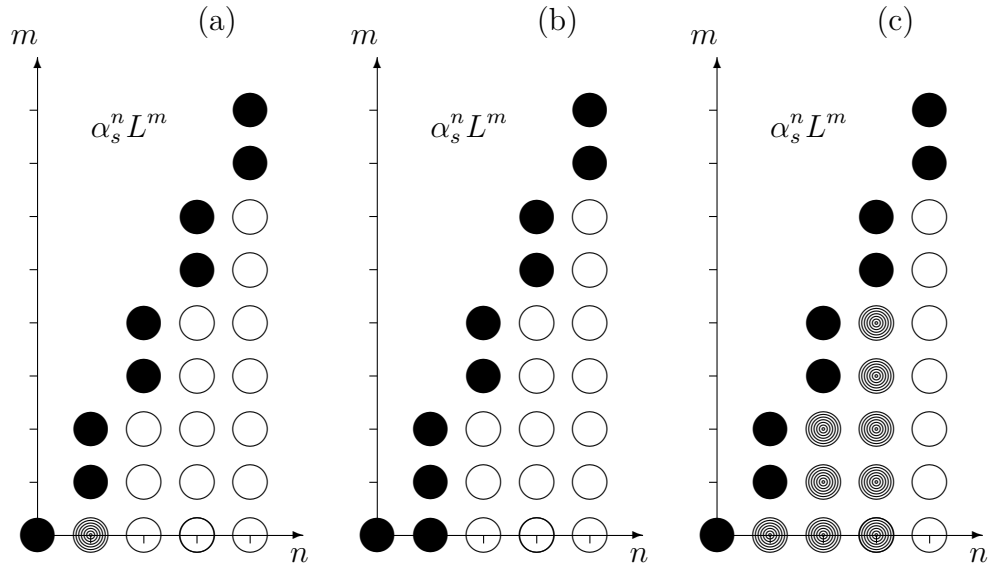

Figure 2.7: Schematic representation of terms featuring in the perturbative expansion for fixed-order frameworks and for parton shower resummation. The vertical axis plots orders in α_s while the horizontal plots powers of the shower logarithms L. Matrix element corrections are depicted in (a), full NLO matching in (b), and CKKW-L-style multi-jet merging in (c). See text for details. Figure reproduced from ref. [8].

order for the *inclusive* process), one needs not worry about ruining the convergence when adding a parton shower since the logarithms appear from the first emission above LO. This would be similar to the configuration in Fig. 2.7(a), except with the half-filled circle at NLO unfilled, as the LO ME would account for the bottom-left term and the shower would account for the rest.

To increase the formal accuracy of the LO+shower combination, the first developments of this procedure sought to map the LO phase space to the parton shower phase space, after the first emission supplied by the shower. This means that, after one emission, the parton shower phase space may be mapped directly onto the LO phase space. Thus ME "corrections" may be applied to the shower for the first emission, increasing the accuracy to include the real emission phase space for the $\mathcal{O}(\alpha_s)$ correction to the LO [8, 107, 108]. This ensures that observables related to the first emission of the shower (referred to often as the "hardest", due to the hardness interpretation of transverse momentum-based evolution variables) are correctly described in shape though not in normalisation, since the LO matrix element has

been used to construct the cross section [8]. These procedures are referred to as LO *matching*, since a LO matrix element is used to complement to first emission and since the full cross section retains LO accuracy.

The natural extension to LO matching is to match to NLO matrix elements. This presents significant problems as, considering the terms shaded in Fig. 2.7(b), both the shower and the matrix element provide descriptions in the top two terms in the column corresponding to the $\mathcal{O}(\alpha_s)$ correction to the LO. Thus, the first emission from the shower must be corrected to reflect the inclusion of those terms in the matrix element. An example of such a method include the *Positive Weight Hard(est) Emission Generator* (POWHEG) method [109], which separates the singular and non-singular parts of the real emission kernel of the NLO correction and produces events with positive weights. The `MC@NLO` method [110, 111] is another example, which adds shower emissions to NLO configurations without real emissions, and starts the shower from an appropriate (lower) scale if the NLO configurations do contain real emissions. For an in-depth comparison of these methods which casts both in the same notation, we recommend the comprehensive study of ref. [112]. Other methods and prescriptions exist for NLO matching and are widely used [8], though these are not the focus of this thesis.

The next advancement logically following NLO matching is to account for the real emission kernels for many multiplicities above the inclusive LO state. Such procedures are referred to as multi-jet *merging* procedures, since the emissions above the inclusive LO process are taken above some hardness scale — typically the minimum transverse momentum of jets in an analysis. The higher-order multiplicities are each calculated to LO (thus accounting only for the real emission corrections exactly above the inclusive LO) and showered with the double-counted contributions removed. This forms the basis of such algorithms as those developed independently by Catani, Kuhn, Krauss, and Webber — CKKW [113] — and by Lönnblad [114]. These methods are referred to collectively as CKKW-L *merging algorithms*.

Adopting the notation of ref. [8], wherein $B(\mathbf{\Phi}_0)$ represents the Born term, $\alpha_s R(\mathbf{\Phi}_1)$

the real emission kernel of the NLO correction and $\mathbf{\Phi}_n$ the phase space for n emissions above LO, we may decompose the real emission kernel (stripped of α_s) into a singular and non-singular part:

$$R(\mathbf{\Phi}_1) = R_s(\mathbf{\Phi}_1) + R_{ns}(\mathbf{\Phi}_1), \tag{2.3.18}$$

where R_s produces the divergences resummed by the shower and R_{ns} is required for full NLO accuracy of the kernel.

These multi-jet merging procedures start by introducing the merging scale cutoff t_{MS} for the R_s term in the expansion: $R_s(\mathbf{\Phi}_1) = R(\mathbf{\Phi}_1) \times \Theta(t_{\mathrm{MS}} - t(\mathbf{\Phi}_1))$. This means that the phase space can be split cleanly according to the scale t into a region covered by the ME generator (i.e. jet production *above* the merging scale) and one covered by the parton shower (jet evolution *below* the merging scale). Using this scale, we can express the CKKW-L-merged cross-section for correcting the n^{th} emission recursively by:

$$\begin{aligned}
\mathrm{d}\sigma_{n+1}^{\mathrm{CKKW-L}} = \mathrm{d}\mathbf{\Phi}_n \alpha_s R_n(\mathbf{\Phi}_n) \Theta(t_n - t_{\mathrm{MS}}) \Delta(t, t_n) \\
\Big[\Delta(t_n, t_0) \\
+ \mathrm{d}t_{n+1} \mathrm{d}z_{n+1} \alpha_s(t_{n+1}) P(t_{n+1}, z_{n+1}) \Theta(t_{\mathrm{MS}} - t_{n+1}) \Delta(t_n, t_{n+1}) \\
+ \mathrm{d}\mathbf{\Phi}_{n+1} \alpha_s(t_{n+1}) \frac{R_{n+1}(\mathbf{\Phi}_{n+1})}{R_n(\mathbf{\Phi}_n)} \Theta(t_{n+1} - t_{\mathrm{MS}}) \Delta(t_n, t_{n+1}) \Big], \\
R_0(\mathbf{\Phi}_0) \equiv B(\mathbf{\Phi}_0).
\end{aligned} \tag{2.3.19}$$

with the understanding that appropriately reweighted splitting probabilities (and the appropriate evolution variable) is used for ISR and FSR in the Sudakov factors. The α_s factors are highlighted in blue since we will discuss how coupling factors are treated later, the splitting function shown here is hence stripped of α_s as shown. We use the shorthand $t_n \equiv t(\mathbf{\Phi}_n)$. In Fig. 2.7(c), this arrangement is shown with the ME generator half-filling the perturbative series up to a maximum multiplicity N_{max}, with the shower describing exactly the resummed terms. This means summing the contribution for each emission up to a multiplicity N_{max}. Double-counting is removed in Eq. (2.3.19) since the phase space split ensures the probability of ME and

shower overlap is zero [8]. The form of Eq. (2.3.19) highlights how multi-jet merging can be implemented. One may produce first LO events generated with LO matrix elements up to a maximum multiplicity N_{max} and start applying shower emissions by sampling the phase space available at each stage.

In the CKKW approach [113], the Sudakov factors are calculated numerically at each stage and then used to multiply the event weights; this is the approach used in `Sherpa`. For PYTHIA, CKKW-L [114] is used wherein each intermediate state is produced for a ME event configuration in a sequence referred to as a parton shower *history*. These are ordered sequences of states $\mathcal{S}_i$ which have each i emissions above a Born-type configuration $\mathcal{S}_0$. We will use in this thesis the notation:

$$\mathcal{H} = \{\mathcal{S}_0, \mathcal{S}_1, \ldots, \mathcal{S}_{l-1}, \mathcal{S}_l\}, \tag{2.3.20}$$

to illustrate a history, with $\mathcal{S}_l$ the original event with l more emissions than the Born configuration $\mathcal{S}_0$. At each stage of the history $\mathcal{S}_i$ the shower adds emissions and vetoes the event if an emission occurs at evolution scale t larger than the scale t_i of the state in the history from which it originates. This reproduces the analytical form of Eq. (2.3.19) exactly due to the interpretation of the Sudakov form factor as an exponentially-distributed no-emission probability.

We have highlighted α_s in blue in Eq. (2.3.19) since the treatment of the running coupling requires some discussion. Convergence of the shower merging is better assured if the coupling is evaluated at the scales of the splittings [114]. Since the higher-multiplicity multi-jet states are initially produced by LO ME generators, they will be generated with couplings evaluated at some pre-determined renormalisation scale μ_R (often constant, or a function of the kinematics of the system). This means that at each stage of the shower the event weights will be multiplied by $\alpha_s(t_m)/\alpha_s(\mu_R^2)$, where t_m is the scale of the trial emission.

The generalisation to NLO multi-jet merging is again straightforward to consider. One of the first extensions to CKKW-L merging was the MENLOPS method of ref. [115] which formulates the merged cross section similarly to CKKW-L mer-

ging except with local K-factor reweighting and corrected Sudakov form factors. Matching and merging to parton showers remains an active field of study with many methods released and in development. Other notable approaches include truncated showers [116], Unitarised NLO+PS (UNLOPS) [117, 118], and many more. We have not mentioned all methods and formalisms here, intending only to give an overview of the motivation and approaches for reinforcing the accuracy of resummed logarithms with the accuracy of fixed-order matrix elements. The material in this section will lend itself to much use when we discuss the HEJ+Pythia merging algorithm in the next chapter.

Chapter 3

Merging High Energy and Soft Collinear Resummation

The robustness of fixed-order calculations in describing data has been demonstrated with numerous experimental studies. In particular, FO calculations provide solid descriptions of event kinematics and inclusive effects as mentioned in Ch. 2. With the frontier of FO calculations for most processes at NNLO (with some low-multiplicity processes boasting descriptions available at even N^3LO) [8], these predictions are due only to improve in the near future.

However, in our discussion of higher-order effects in Ch. 2, we found that there remains scope to account for missing higher orders in FO calculations perturbatively, by resumming dominant corrections to all orders. All-order approaches have demonstrated their strength in describing better the observables that receive significant contribution from such higher order effects that would normally be excluded by the truncation of the perturbative series in a fixed-order calculation. Parton showers have been applied with such success that it is now almost standard procedure to provide LO and NLO calculations merged with parton showers via the procedures we have made reference to in Sec. 2.3.3 [8].

However, many difficulties manifest when attempting to combine all-order approaches, e.g. `HEJ` with a parton shower. To obtain a description of both that retains

to each component the respective logarithmic accuracy across all of phase space, a subtle approach is required that accounts for the probability that the additional radiation supplied by the parton shower has not already been produced in HEJ.

The application of a parton shower to HEJ has been studied twice prior [6,119]. The study of ref. [119] applied the parton shower of Ariadne [100] to HEJ, and was used in studies of jet vetoes and azimuthal decorrelations [12], where the combination of the two resummation schemes produced a robust prediction in the regions of phase space targeted by the experimental study. However, the implementation provided an incomplete description as it excluded multiple parton interactions [119]. In the study, HEJ+Ariadne was compared to Pythia with and without MPI enabled. Both HEJ+Ariadne and Pythia without MPI enabled produced poor descriptions of jet profiles (which we define and expand on in Sec. 3.2). The MPI-enabled Pythia run predicted jet profiles more consistent with data. This shows that the MPI (along with models of hadronisation) are of immense importance in accounting for soft-collinear behaviour in the jet cone.

The study of ref. [6] combined HEJ with Pythia 8 [46], and is the study on which this chapter builds. In addition to including an intervleaved description of MPI with the evolution of the shower, Pythia can merge FO predictions with the CKKW-L merging algorithm discussed in Sec. 2.3.3, which was modified in the study to merge HEJ input states. This merging significantly improved on the description of HEJ+Ariadne for many observables, importantly providing highly detailed descriptions of jet substructure that the latter description lacked.

However, the method of ref. [6] was limited, since the subtraction of double-counted effects between HEJ and the parton shower was not applied for every emission from the shower. We explore the problems of such an approach in Sec. 3.1, and demonstrate how we are able to improve on these shortfalls significantly in the new HEJ+Pythia merging method. We discuss our method throughout the next section, and present results in Sec. 3.2, before concluding in Sec. 3.3.

3.1 The HEJ+Pythia All-Orders Merging Scheme

We aim to produce a method of merging the resummation of HEJ with the parton shower resummation of Pythia that retains the logarithmic accuracy of each prediction. Cross sections for QCD processes receive significant corrections from both resummations in regions of phase space that overlap in a non-trivial way. Removing the double-counted contributions with a merging scale, or with a phase space partition, will not be adequate to ensure retaining the logarithmic accuracy of each resummation. The overlap has to be calculated for every phase space point to ensure it can be physically subtracted. The procedure we outline in this section builds on the previous studies of adding a parton shower to HEJ [6, 119] and defines a subtraction term between the two resummations that is evaluated for every emission the shower adds.

HEJ and Pythia are both exclusive to their perturbative accuracy, meaning the usual CKKW-L-inspired multi-jet merging procedures for FO input can not be used, since FO calculations are inclusive. The approach of ref. [6] was to construct shower histories for HEJ-resummed events and subtract the HEJ probability of producing Pythia emissions in the intermediate stages by implementing a sophisticated veto on the Pythia splittings. As mentioned earlier, this approach was significantly limited, since it allowed at most one emission from Pythia to be accepted at an intermediate state in the history. The accepted state with the Pythia emission would then be showered freely in Pythia, without any more subtraction. This introduces double-counting from merged low-multiplicity states from HEJ as the higher-multiplicity emissions would not be subtracted despite that they could overlap with other HEJ events.

The procedure we describe in this section develops these concepts. We implement a merging procedure that navigates the complexities introduced in exclusive-exclusive merging by allowing an unlimited number of emissions from Pythia in and beyond the HEJ event history. We subtract the overlap probability for each emission with an analogous veto procedure to the method of ref. [6]. If a Pythia emission is kept

during the trial shower in the history, it is kept and added to the HEJ event input and the momentum recoiled appropriately. The result of this is that the all HEJ emissions are kept for every input phase space configuration, and dressed with the shower emissions PYTHIA would have added at all stages of the history.

Further to this, the subtraction is extended after the construction of the subtracted shower in the history, and PYTHIA does not shower freely after merging the event. This remedies the impact of double-counting from low-multiplicity HEJ events showered freely in PYTHIA.

We discuss in detail the classification of states and how this impacts the merging procedure. We take careful consideration of the regions of phase space in which HEJ resummation is inclusive and exclusive, in a way not accounted for previously, and use this to produce a robust and tailored procedure that ensures the logarithmic accuracy is retained.

To retain the full LO-matched accuracy of HEJ and the multi-jet merged accuracy of CKKW-L for inclusive LO states, we merge the non-resummable LO events contributing to the inclusive dijet cross section with the CKKW-L merging algorithm, and combine this with the HEJ-resummable states merged with our new all-orders merging scheme. We refer to this component as the *CKKW-L complement* prediction to the merged HEJ-resummed component in a full HEJ+PYTHIA prediction.

3.1.1 The All-Orders Subtracted Trial Shower

The core principle behind combining the high-energy resummation of HEJ with a parton shower remains the same as in the previous studies [6, 119] exploring merging the two resummation schemes — that we can subtract the HEJ contribution from the shower contribution for any point in phase space. We thus cover phase space twice, once with each HEJ and PYTHIA, and subtract exactly the overcounted contributions. We accomplish this by expressing the resummation of HEJ in the language of the parton shower and define HEJ analogues for the QCD splitting kernels of Eq. (1.3.42). We may calculate the analogue of the splitting kernel in HEJ by substituting the

pure QCD matrix elements with the HEJ matrix elements discussed in Sec. 2.2:

$$P^{\texttt{HEJ}} = \frac{1}{2}\frac{1}{16\pi^2}\frac{\left|\mathcal{M}^{\texttt{HEJ}}_{n+1}\right|^2}{\left|\mathcal{M}^{\texttt{HEJ}}_{n}\right|^2}, \tag{3.1.1}$$

where $P^{\texttt{HEJ}}$ corresponds to the splitting kernel in Eq. (2.3.6). The extra factor of 1/2 in the HEJ splitting kernel arises when we consider the colour configurations discussed in Sec. 2.1.2, each of the two leading contributions to the colour configurations is weighted equally in our treatment.

From this, the HEJ cross section can be expressed in a form reminiscent of the parton shower. The n-parton HEJ-resummed cross section is given by:

$$\mathrm{d}\sigma^H_n = \mathrm{d}\sigma^*_2 \left(\prod_{i=1}^{n-2} P^H_i(t_i)\Delta^H_{i-1}(t_{i-1},t_i)\mathrm{d}t_i\Theta(t_{i-1}-t_i)\right). \tag{3.1.2}$$

Here, we use the superscript H as a shorthand for the HEJ splitting kernels of Eq. (3.1.1), and have suppressed the dependence on z in the splitting kernels and the z integral measures. The Sudakov form factors Δ^H denote the usual form factors with the HEJ splitting kernel in the exponent, rather than the QCD splitting kernels used in PYTHIA.

We centre this discussion around inclusive dijet production. We discuss the potential challenges of using this framework to produce shower-merged predictions for HEJ-resummable processes involving a W, Z/γ, or H boson when we conclude in Sec. 3.3, and relegate exploration of these processes to future studies.

Manifest in Eq. (3.1.2) is the formulation of a parton shower history for a HEJ event; this is no more than an ordered sequence of states separated by scales t_i which trace back the $2 \to n$ parton event to a LO $2 \to 2$ configuration. We use the notation of Eq. (2.3.20) to denote an event history, with $\mathcal{S}_0$ the most clustered state and $\mathcal{S}_l$ the original event.

The merging algorithm of ref. [6] introduced a subtracted Sudakov form factor,

given by:

$$\Delta^S(t_{i-1},t_i) = \exp\left\{-\int_{t_i}^{t_{i-1}} \mathrm{d}t \int \mathrm{d}z \underbrace{\Theta(P^P(t,z)-P^H(t,z))\left[P^P(t,z)-P^H(t,z)\right]}_{\text{Subtracted splitting probability: } P^S(t,z)}\right\}, \tag{3.1.3}$$

which subtracts systematically the contribution of HEJ from that of Pythia across phase space. The z-dependence is restored for full clarity in the integral, though the arguments of P^H are schematic, and no analytical dependence on t and z is needed. We express the subtraction between HEJ and Pythia in exactly the same way and implement it with the same veto procedure as ref. [6], i.e. vetoing each emission from Pythia with probability:

$$\mathcal{P}^{\text{veto}} = \frac{P^H}{P^P}\cdot\Theta(P^P-P^H)+1\cdot\Theta(-P^P+P^H). \tag{3.1.4}$$

The difference with our implementation is that we apply this subtraction for every emission from Pythia, regardless of whether or not a Pythia emission has been accepted previously. This presents complications to the classification of events which we discuss in Sec. 3.1.4. For now, we display the contribution to the HEJ+Pythia-merged cross section with n partons due to HEJ-resummable input states with $m<n$ partons below:

$$\mathrm{d}\sigma_{m,n}^{\text{HEJ+Pythia}} = \mathrm{d}\sigma_2^* \underbrace{\prod_{i=1}^{m-2} P_i^H \Delta_{i-1,i}^H}_{\text{HEJ event history}} \cdot \underbrace{\left[\prod_{\lambda=1}^{\lambda_i} P_{i_\lambda}^S \Delta_{i_{\lambda-1},i_\lambda}^S\right]}_{\text{Trial shower in history}} \underbrace{\cdot \prod_{j=m-1}^{n-\mathcal{N}-2}\left(P_j^S\Delta_{j-1,j}^S\right)}_{\text{Shower after history}}. \tag{3.1.5}$$

Here we have adopted a more compact notation relative to Eq. (3.1.2), defining:

$$P_i \equiv P(t_i)\equiv P(t_i,z_i), \quad \Delta_{i,j}\equiv\Delta(t_i,t_j), \quad i_0\equiv i-1. \tag{3.1.6}$$

In Eq. (3.1.5), we have additionally suppressed the Heaviside Θ functions as well as the z and t_i integral measures. We have also implied that the scales t_i are ordered. In blue, the HEJ event history is shown explicitly, with the products of the HEJ splitting kernels and Sudakov form factors that denote emission and no-emission between the scales that separate the states.

Between states $\mathcal{S}_{i-1}$, $\mathcal{S}_i$ in the history, λ_i emissions are added from PYTHIA with the subtracted splitting kernel and Sudakov factor of Eq. (3.1.3), shown in orange. Within our method, this means that the emissions were not vetoed during the trial shower; here we understand vetoing to mean that the emission generated by PYTHIA at scale t is **not** added to the event record, and the shower continues evolving below scale t without the added particle. Others trialled by PYTHIA could have been vetoed. The end result is that the original HEJ event is kept, but the phase space in between the states $\mathcal{S}_i$ of the history is filled by the subtracted shower. The additional emissions are appended to the HEJ event within a suitable scheme for recoiling the additional momentum that we outline in Sec. 3.1.2. In total, $\mathcal{N} \equiv \sum_i \lambda_i$ emissions from PYTHIA are added in this stage. We note that MPI are not counted and are treated unaltered by the PYTHIA shower since there is no description of MPI in HEJ.

We have omitted a Sudakov form factor from the orange term, which is implied since the phase space between scales $t_{i_{\lambda_i}}$ and t_i is sampled by PYTHIA, but no emissions are added (we detail the implementation of this in Sec. 3.1.2). This means that the emissions from the subtracted trial shower in the event history should be written with an additional Sudakov factor $\Delta^S(t_{i_{\lambda_i}}, t_i) \equiv \Delta^S_{i_{\lambda_i},i}$, i.e.

$$\left[\prod_{\lambda=1}^{\lambda_i} P^S_{i_\lambda} \Delta^S_{i_{\lambda-1},i_\lambda}\right] \to \left[\prod_{\lambda=1}^{\lambda_i} P^S_{i_\lambda} \Delta^S_{i_{\lambda-1},i_\lambda}\right] \Delta^S_{i_{\lambda_i},i}. \tag{3.1.7}$$

We have suppressed the additional Sudakov to clearly isolate the contribution from each emission, though it is important to emphasise the implicit presence of this factor since it ensures the full phase space is covered by the subtracted shower.

Finally, the black term on the far-right of Eq. (3.1.5) encodes the PYTHIA shower after progressing through the history. The subtracted splitting kernels and Sudakov factors are used for the rest of the evolution until hadronisation. We have implied a subtracted Sudakov form factor of $\Delta^S_{n,\min}$ between the state with scale t_n and the hadronisation scale $t_{\min}$ after this stage of the shower.

By summing over the contribution from m-parton HEJ-resummable events, and

over all multiplicities n in the shower, we obtain the following:

$$\mathrm{d}\sigma^{\texttt{HEJ+PYTHIA}}_{\text{resummable}} = \sum_{n=2}^{\infty} \mathrm{d}\sigma_2^* \sum_{m=2,\, m\leq n}^{n} \prod_{i=1}^{m-2} P_i^H \Delta^H_{i-1,i} \cdot \left[\prod_{\lambda=1}^{\lambda_i} P^S_{i_\lambda} \Delta^S_{i_{\lambda-1},i_\lambda} \right] \cdot \prod_{j=m-1}^{n-\mathcal{N}-2} \left(P_j^S \Delta^S_{j-1,j} \right). \tag{3.1.8}$$

We account for the non-HEJ-resummable events that contribute to LO m-jet cross sections, and merge these configurations with the CKKW-L merging algorithm. This procedure removes the double-counting between FO and the parton shower, and is all that needs to be considered for non-resummable events as there is no HEJ description for such states. As mentioned earlier, this is referred to in this thesis as the CKKW-L complement prediction. For LL-resummed HEJ merged with HEJ+Pythia, the complement consists of the HEJ-subleading configurations, and the non-HEJ-resummable configurations, merged at LO accuracy with CKKW-L. For HEJ-resummed LL and subleading configurations, the complement consists only of merging the non-resummable states at LO accuracy with CKKW-L.

This method has been implemented in the HEJ+Pythia C++ software, which is based on the Pythia (v8.309) code [47], and uses Pythia-derived classes for the merging and construction of histories. Combining Eq. (3.1.8) with the CKKW-L merging for the non-HEJ-resummable states, we display the program flow for HEJ+Pythia in Fig. 3.1. The colour coding for the generation of histories and the subtracted trial shower in the event history is the same as in Eq. (3.1.5). The algorithm is shown for one input event from HEJ, and is understood to be the same for the ensemble.

In the next section we discuss in further detail how we are able to append Pythia emissions to the HEJ event record when clustering back in the history. This is the most significant development that allows us to incorporate the subtraction between HEJ and Pythia on a systematic level to all orders.

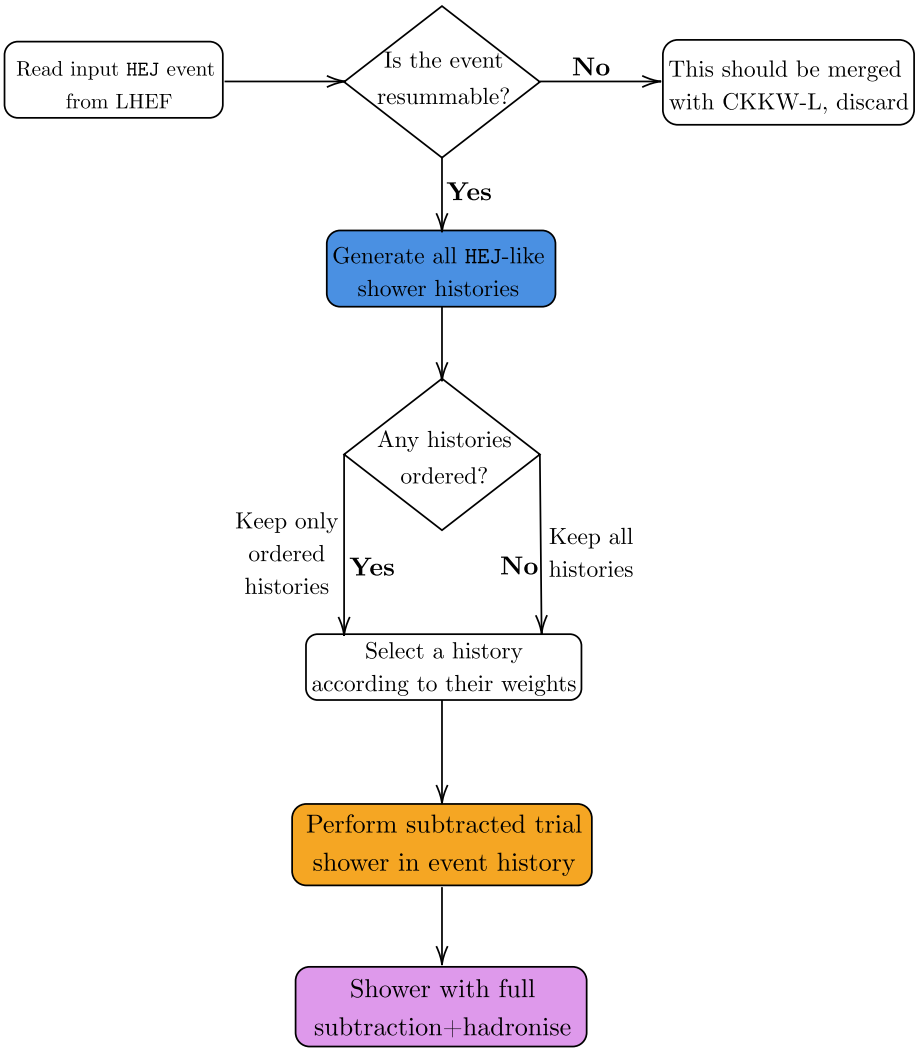

Figure 3.1: Schematic overview of the HEJ+PYTHIA merging algorithm for each input HEJ configuration. The blocks are colour-coded for ease of reference.

3.1.2 Constructing Subtracted Trial Showers for HEJ Event Histories

The native Pythia machinery is used to construct (and select from) all possible event histories, with minimal modification to ensure that the chosen history is a sequence of HEJ-resummable states (see Sec. 3.1.4) as required by Eq. (3.1.2). The construction of histories corresponds to the blue block in Fig. 3.1, and likewise the blue term (for an individual event) from Eq. (3.1.5). The construction of ordered histories is handled completely as Pythia would normally construct such histories for e.g. CKKW-L merging and are generated with Pythia splitting probabilities. The one difference with the selection of histories is that the history is selected in HEJ+Pythia by a weight given by the product of the HEJ splitting probabilities of the intermediate state, rather than the regular product of the Pythia splitting probabilities. The appending of non-vetoed Pythia emissions in the event histories is encapsulated in the orange block from Fig. 3.1, and the additional emissions are shown precisely in the orange term in Eq. (3.1.5).

We display in full these stages of the algorithm (the subtracted trial shower in the HEJ event history) in Fig. 3.2. This flowchart makes clear that we progress through the states (or *nodes*) $\mathcal{S}_i \in \mathcal{H}$, and allow the Pythia shower to populate the phase space in between each. The veto probability means that we can use the Pythia shower unaltered and still produce results that have been produced with a subtracted splitting kernel and Sudakov form factor.

To implement the veto we generate a random number, uniformly distributed in the interval $(0, 1)$, and compare it to the veto probability of Eq. (3.1.4) as evaluated for the phase space configurations in consideration (i.e. the *process* event prior to the splitting, and the *trial* event just after the splitting). The classification of states again becomes relevant here as we consider that, as the shower progresses, the events quickly become non-resummable as would be classified by HEJ. We discuss how the interpretation of HEJ and parton shower *exclusive* and *inclusive* regions of phase

space allows us to make the subtraction reflect the physical application of each resummation in Sec. 3.1.4.

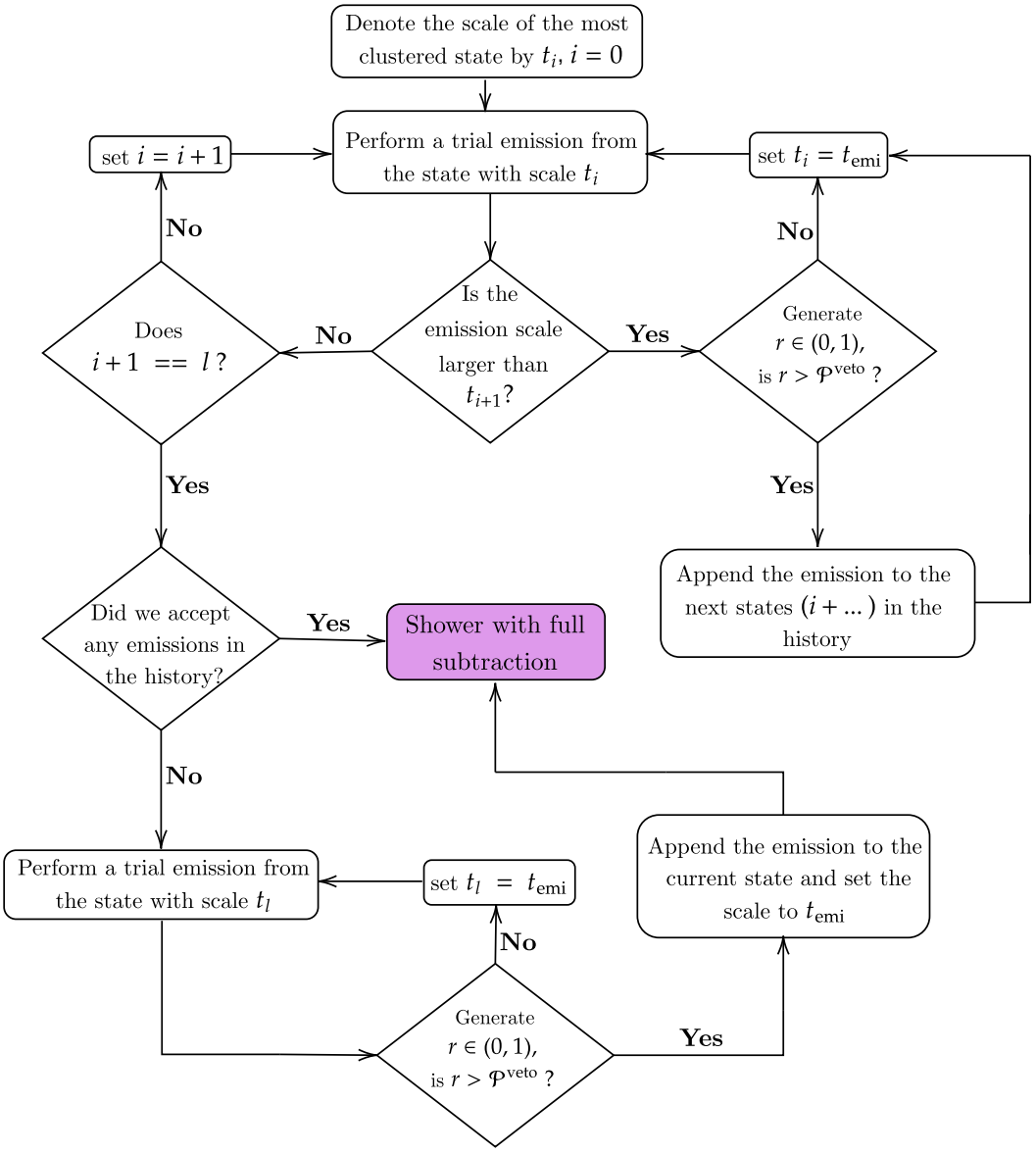

Figure 3.2: All stages of the subtracted trial shower in the HEJ event history. For concision, we may refer to this also as the "merging" stage despite that the full procedure in Fig. 3.1 is the all-orders merging procedure.

The end result of this stage of the algorithm is that the input HEJ event will have the chosen history dressed fully with the emissions the shower would have added in between, produced with a reduced probability having taken into account the HEJ probability of generating them.

Recoiling excess momentum

When appending emissions from a trial event in the history to all subsequent nodes, a global prescription for recoiling the excess momentum is used to produce physical states with additional emissions. Importantly, this is *not* a recoil strategy as would be understood in the regular parton shower interpretation — rather this strategy *reinterprets* later nodes in the history with the emission from a larger scale present.

Using local shower recoil strategies, such as the Pythia dipole-local recoil scheme (for FSR), can produce sequences of states that violate the shower ordering for this application. For example, splitting a dipole between two gluons in a trial emission that occurs before the same dipole splits later in the history can reduce the momentum available in that dipole and make the splitting in that node no longer possible at the same scale. With high-multiplicity final states this effect worsens rapidly due to the connections between dipoles. This means emissions can alter the kinematics of the surrounding dipoles significantly if recoiled locally — later nodes in the history could become kinematically viable only at larger scales which may exceed the scale of the trial emission. The impact of using such a strategy in this application is to violate the shower ordering in such a way that the logarithmic accuracy of the shower resummation is no longer assured.

Before recoiling the excess momentum and appending the emission, we first have to identify the parton in the later node which serves as the *mother* (see Sec. 2.3) of the splitting. There is, in general, an ambiguity as to which parton we may choose, since the kinematics and colour connections may differ significantly in the subsequent nodes. To resolve this ambiguity (for final state emissions) we iterate over the partons of eligible flavour in the final state[1] to produce the splitting, and choose from these *candidate* partons that which minimises the distance measure:

$$\Delta R_{\text{extended}}(p_m, p_c) = \sqrt{(y_c - y_m)^2 + (\phi_c - \phi_m)^2 + \left(\frac{p_{\perp c} - p_{\perp m}}{p_{\perp m}}\right)^2}, \tag{3.1.9}$$

[1]For example, if the trial emission was a final state $g \to q\bar{q}$ splitting, we would only consider gluons when searching for the mother in a later node.

with p_m and p_c the four-momentum of the mother (from the trial event) and the candidate (from the node) respectively. Quantities related to the four-momenta are indexed by m and c to indicate whether they belong to the mother or candidate parton respectively.

For initial state radiation, the ambiguity no longer features as there are exactly two partons to choose from, one incoming along the positive and the other along the negative z-axis. Thus the same parton can be chosen as in the trial emission.

There is a possibility of flavour conflicts from the trial emissions relative to later nodes in the history. The simplest example is for an initial state gluon that splits into a $q\overline{q}$ pair in a trial emission, but which would have split in a later node to a different quark-antiquark pair $Q\overline{Q}$. We thus check for each trial emission that there are no flavour conflicts from the splitting before appending the emission to *any* state in the history. If a conflict is found, then the emission is vetoed. Crucially, this does not mean we effectively exclude flavour-changing splittings and therefore restrict to gluon-gluon splittings. We allow flavour-changing shower splittings while performing the trial shower between states in the history **provided** that there exists in the subsequent states in the history a parton which can split in the same way. This includes emissions which have already been recoiled and appended from the trial shower to the later states meaning the incidence of such flavour conflicts is rare. Testing on large samples of low- and high-multiplicity events, we find the occurrence of such conflicts is vanishingly small.

The global strategy used in the HEJ+PYTHIA algorithm induces small modifications to all particles present to ensure changes to the scales of nodes in the history, relative to trial emissions at larger scales, are small. The strategy is as follows:

1. Reshuffle the excess transverse momentum across the final state partons, conserving the mass and rapidity of each.

2. Rescale all transverse momenta by a constant factor λ such that the invariant mass of the initial state $\sqrt{\hat{s}}$ is conserved. Then, reassign the E and p_z components of each final state particle such that the rapidities and masses of each

are conserved.

3. Sum over positive and negative lightcone components of the final state momenta to find physical analogues for the momenta of the initial state partons.

4. Boost along the z-axis such that that the initial state momenta are the same as they were in the original state, using the momenta in step 3 to derive the boost parameter ψ required.

We illustrate step 1, the reshuffling, by appending to state $\mathcal{S}_k$ in the history (with m partons in the final state) a splitting with momentum p_{emi} (for the emission) and p_{rad} (for the mother post emission). When we identify the mother parton in the state $\mathcal{S}_k$ — particle i for some $i < m$ — we replace this parton momentum p_i with p_{rad} and append the parton with momentum p_{emi} from the trial to the event. Referring to the overall excess in momentum in the node as $p_{m+1} \equiv p_{\text{emi}} + p_{\text{rad}} - p_i$, we may define:

$$\text{norm} \equiv \sum_{j=1}^{m+1} |\mathbf{p}_{\perp j}|, \qquad y_j = \frac{1}{2}\log\frac{E_j + p_{z,j}}{E_j - p_{z,j}} \quad \forall j \in \{1, ..., m+1\}, \tag{3.1.10}$$

where y_j is the rapidity of particle j. We reassign the momenta according to:

$$\begin{aligned} \mathbf{p}_{\perp j} &\to \mathbf{p}_{\perp j} - \mathbf{p}_{\perp m+1} \cdot \frac{\left|\mathbf{p}_{\perp j}\right|}{\text{norm}} \equiv \mathbf{p}'_{\perp j}, \\ E_j &\to m'_{\perp j} \cosh\left(y_j\right) \equiv E'_j, \\ p_{z,j} &\to m'_{\perp j} \sinh\left(y_j\right) \equiv p'_{z,j}, \end{aligned} \tag{3.1.11}$$

where

$$m_{\perp j} \equiv \sqrt{m_j^2 + p_{\perp j}^2}, \tag{3.1.12}$$

is the transverse mass. Following through with these definitions, the reassignment of the four-momenta after reshuffling the excess transverse momentum clearly conserves the masses and rapidities of all the final state particles.

In step 2, we rescale all transverse momenta in the event to ensure that adding many emissions does not lead to problematic excesses in energy. To calculate the

scaling factor, we express the product of four-momenta p_i, p_j as:

$$p_i \cdot p_j = m_{\perp i} m_{\perp j} \cosh\left(\Delta y_{i,j}\right) - p_{\perp i} p_{\perp j} \cos\left(\Delta\phi_{i,j}\right), \tag{3.1.13}$$

which allows us to calculate the factor we require to preserve the centre-of-mass energy of the interaction (and not lead to excesses in energy). The centre-of-mass energy can be calculated from the final state momenta p_i by:

$$\hat{s} = \left(\sum_i p_i\right)^2 = \sum_{i\neq j} p_i \cdot p_j + \sum_i p_i^2 = \sum_{i\neq j} p_i \cdot p_j + \sum_i m_i^2. \tag{3.1.14}$$

We can use Eq. (3.1.13) to simplify the sum over products of non-alike four-momenta. If we define:

$$\begin{aligned} f(\lambda^2;\hat{s}) = &\sum_{i\neq j}\left[\sqrt{m_i^2+\lambda^2 p_{\perp i}}\sqrt{m_j^2+\lambda^2 p_{\perp j}}\cosh\left(\Delta y_{i,j}\right) - \lambda^2 p_{\perp i} p_{\perp j}\cos\left(\Delta\phi_{i,j}\right)\right] \\ &+ \sum_i m_i^2 - \hat{s}, \end{aligned} \tag{3.1.15}$$

then finding the roots of f will allow us to find the factor λ which would produce the required centre-of-mass energy after rescaling the transverse momenta in the final state. With massless particles, the roots of f are analytically calculable. However, final state quarks in PYTHIA are required to be massive for physical treatment of the beam remnants after the hadronisation stage [47]. Thus, we solve $f(\lambda^2;\hat{s}) = 0$ numerically. Then, all final state transverse momenta are rescaled by a factor λ (taking the positive root).

To account for the rescaling, we treat the initial state and produce physical momenta as in step 3. We denote the sum of the lightcone momenta (as defined in Eq. (2.2.1)) in the final state as $P^{\pm}$ for each the positive and negative components. We then choose the physical configuration for the four-momenta in the initial state:

$$p_a' = \left(\frac{P^+}{2}, 0, 0, \frac{P^+}{2}\right), \qquad p_b' = \left(\frac{P^-}{2}, 0, 0, \frac{-P^-}{2}\right), \tag{3.1.16}$$

where a (b) is the initial state parton entering the hard interaction along the positive (negative) z-axis. Importantly, these are the momenta for the initial state required

to produce the final state after rescaling the final state transverse momenta.

In step 4 we use the physical configuration identified in step 3, and the conservation of $\sqrt{\hat{s}}$ to construct a boost to the reference frame in which the initial state momenta are the same as they were before the reshuffling. Denoting the original momenta by:

$$p_a = (E_a, 0, 0, E_a)\,, \qquad p_b = (E_b, 0, 0, -E_b)\,, \tag{3.1.17}$$

we may find a boost along the z-axis that takes the reference frame of Eq. (3.1.16) to Eq. (3.1.17). The boost parameter ψ may be found by conserving e.g. p_a,

$$E_a = \frac{P^+}{2}(\cosh(\psi) - \sinh(\psi)) = \frac{P^+}{2}\exp(-\psi). \tag{3.1.18}$$

Then we can maintain p_a, p_b in their original form by boosting the final state particles (after having been recoiled) along the z-axis:

$$\begin{aligned} E_j &\to E_j\cosh(\psi) - p_{z,j}\sinh(\psi), \\ p_{z,j} &\to -E_j\sinh(\psi) + p_{z,j}\cosh(\psi). \end{aligned} \tag{3.1.19}$$

This step is required to maintain the dynamics of the initial state, while ensuring that the momenta remain physical and are minimally modified. Boost parameters, and the transverse momentum rescaling factors λ, were found to differ from 0 and 1 respectively by small amounts as would be expected. In the case of FSR, rescaling factors λ are always slightly smaller than unity, while the rescaling is slightly larger than unity for ISR[1] which adds energy to the event. The method we show here ensures that such a boost may always be performed, and that the same boost is obtained by conserving either of p_a or p_b. The combined recoiled, boosted final state momenta and the original initial state momenta produce a physical state that corresponds to a global reinterpretation of a node in the history after the inclusion of an earlier trial emission.

[1]This is because "original", as to be understood for the momenta in Eq. (3.1.17), refers to the momenta of the initial state in the *trial* event for ISR, as otherwise ISR would not be recoiled with this strategy.

3.1.3 Full Subtraction in the PYTHIA Shower

The final stage of the algorithm displayed in Fig. 3.1 is to continue the PYTHIA shower after the HEJ event history has been fully dressed with parton shower emissions produced with the subtracted splitting kernel and Sudakov form factor of Eq. (3.1.3). Adding shower emissions in the HEJ event histories is a major development over the previous HEJ+PYTHIA merging algorithm of ref. [6]. However, since there is no limit[1] on the parton multiplicity of HEJ-resummed final states, the dressing of HEJ histories with subtracted shower emissions is not sufficient to account for all double counting.

To this end, we restrict the PYTHIA shower to veto emissions with the same probability of Eq. (3.1.4) until hadronisation, meaning that all HEJ-like emissions are subtracted for the full parton-level evolution. This is represented by the magenta stage at the bottom of Fig. 3.1, and is expanded on in Fig. 3.3.

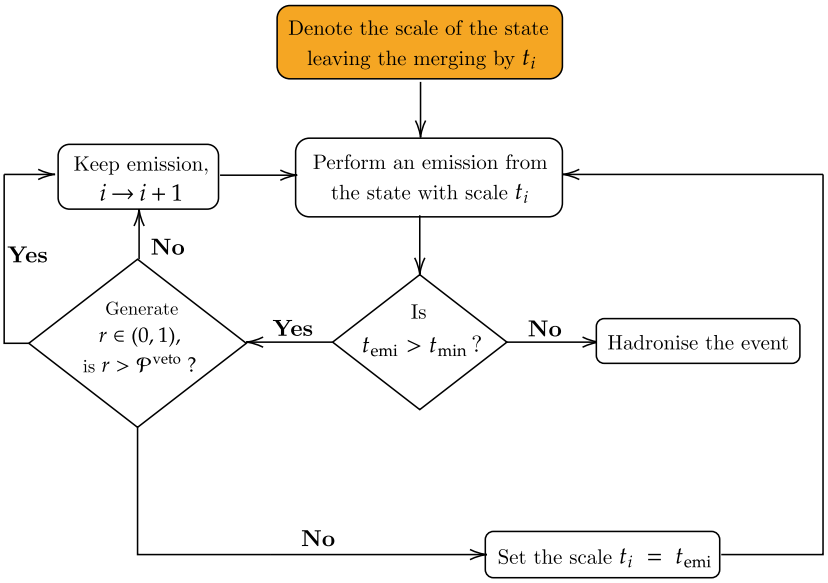

Figure 3.3: Flow diagram charting the full subtraction in the shower evolution on the HEJ-resummed input states, after constructing the histories.

[1]Though there is no theoretical cap on the number of soft gluons that can be added by HEJ, the software implementation does impose an upper limit of 1000 gluons. In practice, this limit is never reached.

In Fig. 3.3, the scale of hadronisation is denoted by t_{min}, and the implementation of the veto procedure is simpler than in the history. Since there are no emissions remaining from the original HEJ event in this part of the evolution, the native recoil strategies of PYTHIA are used as normal when adding emisions.

This extension of the subtraction procedure ensures that there is no need to introduce a merging scale or impose a maximum multiplicity of final states in HEJ as was required previously [6]. The subtraction is encoded in the veto procedure for every point in phase space, to all orders in perturbation theory, and for all shower evolution scales until hadronisation in a way that cannot be accounted for by introducing a merging scale.

3.1.4 Classification of HEJ-Resummable States

To extend the subtraction to all orders, a sophisticated development to the classification of HEJ-resummable states is used compared to previous methods of merging HEJ with a parton shower. The major complications with using the basic classification procedures based on hard process (i.e. pre-shower) final states at parton-level are that these quickly become non-resummable as interpreted by HEJ after few shower emissions — even with the inclusion of subleading corrections in HEJ. For example, a jet containing a single gluon splitting to a collinear $q\overline{q}$ pair would, in HEJ, render the entire event non-resummable[1].

Inclusive and exclusive regions of phase space

The classification of events used in the subtraction procedure builds on an understanding of the *inclusive* and *exclusive* regions of phase space in HEJ. From the example we describe earlier, of the hard gluon splitting into a collinear $q\overline{q}$ pair, the ordering of the shower means that this non-resummable emision could have been added by the shower before several emissions that would have made for HEJ-

[1]There is ongoing work to attain full NLL accuracy in HEJ. When this is achieved, such a splitting would no longer be necessarily non-resummable.

resummable events had they occurred first. In HEJ, the ordering in shower evolution scale is not part of the resummation, as such the other emissions should have a HEJ contribution subtracted. However, the ratio of matrix elements required to produce a HEJ splitting probability can not be calculated, as the presence of the non-HEJ emission in the event means the event is classified as non-resummable.

We illustrate this point schematically in Fig. 3.4, where we show two possible sequences of evolution for a $2 \to 2$ HEJ state showered with PYTHIA after several emissions, with the shower emissions ordered in decreasing evolution scale. In the leftmost diagram, the non-HEJ emission is added first, meaning the other HEJ-like emissions receive no subtraction. In the rightmost diagram, the order of these emissions is flipped. This means the same kinematic configuration could have evolved under a subtracted splitting kernel only partially if the events are classified naïvely.

Figure 3.4: Schematic diagrams for the possible shower evolution for a (e.g.) $2 \to 2$ HEJ state (indicated by the black lines) showered with PYTHIA. Orange (solid, double-barred) lines represent shower emissions for which HEJ could produce a splitting kernel, while blue (dotted, double-barred) lines represent non-HEJ splittings. The shower emissions are ordered in decreasing evolution scale t.

The non-HEJ emissions are inclusive corrections to the HEJ description, since there is no description of them in HEJ. The classification procedure we use in HEJ+PYTHIA thus examines the events by considering them stripped of the HEJ-inclusive corrections of the parton shower. The procedure we use follows the stages outlined below:

1. Cluster the event into hard jets using the parameters set in the HEJ configuration.

2. To each jet assign a flavour equal to the sum of the flavours of the parton content of the jet, modulo the gluon particle ID.

3. Balance the momentum in the clustered event, assigning initial state momenta according to the sum of lightcone-decomposed momentum in the clustered final state.

This procedure removes the impact of collinear $q\bar{q}$ emissions inside the jet cone from the classification, as well as other HEJ-inclusive corrections. This allows us to connect the evolved event to a Born-like input configuration, and considers the emission relative to this configuration. We refer to this as constructing the exclusive configuration in HEJ for a showered event. This event can be examined by the HEJ parton-level classifier and will be classified as resummable or non-resummable appropriately, having stripped the impact of the inclusive shower corrections that do not alter the underlying high-energy structure of the event.

Classification in the veto procedure

This classification allows us to separate the resummable and non-resummable phase space in HEJ through the parton shower merging, and justifies our inclusion of the CKKW-L-merged non-HEJ-resummable states. When we refer to vetoing with probability $\mathcal{P}^{\text{veto}}$ as given in Eq. (3.1.4) earlier, the procedure for calculating the probability involves application of the above jet clustering procedure for the trial and process event. This ensures the treatment of emissions is consistent in both the HEJ and Pythia/parton shower framework across all of phase space. We decide whether a Pythia emission should be vetoed in the following way:

1. If the process event (the event before the trial emission) is an exclusive HEJ event and the trial is also, then veto the emission with probability $\mathcal{P}^{\text{veto}}$, and go to step 4.

2. If the process event is an exclusive HEJ event and the trial is not, then keep the emission, and go to step 4.

3. If the process event is non-HEJ-exclusive, construct the exclusive configuration for the process with the jet clustering procedure.

   (a) If this clustered process is not HEJ-resummable then never veto, go to step 4.

   (b) If this clustered process is HEJ-resummable, identify the last splitting from the trial event:

      i. Construct the exclusive configuration for the trial event with the jet clustering procedure.

      ii. If this state is HEJ-resummable then veto the emission with probability $\mathcal{P}^{\text{veto}}$ as calculated with the exclusive configuration for the process and trial. Otherwise, never veto. Go to step 4.

4. If we vetoed, discard the emission but continue the evolution from the scale of the vetoed emission. Otherwise, keep the emission and continue the evolution from the scale of the trial event.

This ensures that the correct treatment is used when the events are still HEJ-resummable at the parton level, early in shower evolution, and when the parton-level configurations are not HEJ-resummable due to the addition of inclusive shower emissions, later in the evolution.

When the classification of the event in terms of the corresponding HEJ-exclusive configuration is non-resummable, we can safely conclude that the phase space configuration corresponding to the evolved HEJ input event has been sufficiently modified by the shower that the overlap between HEJ and PYTHIA for subsequent emissions is zero. Without this method, or a similar accounting of inclusive effects, one would not be able to draw the same conclusion from a naïve classification based solely on the parton content of events.

The procedures outlined throughout this section make clear that we systematically account for all sources of double-counting in the all-orders combination of the HEJ and PYTHIA resummation.

Filling the HEJ-exclusive phase space

We have discussed that both the parton shower and HEJ resummation are each exclusive to their respective logarithmic accuracies, and that the HEJ-exclusive region is defined by the rapidities of the extremal jets in an event. Specifically, HEJ adds soft gluons inside the rapidity interval bounded by the extremal jets, and can only add soft emissions outside this region if they are within the jet cone of either external jet. The exclusive resummation of Pythia is unrestricted in this way, and when considered in the context of e.g. CKKW-L merging, the exclusive and inclusive phase space is defined by the merging scale t_{MS}.

Precise control over the inclusive and exclusive regions for the shower is required for accurate predictions for differing analyses. Often this means altering the merging scale (in CKKW-L merging) for different analyses such that the regions covered by the hard matrix element generator (i.e. the shower-inclusive parts) and those covered by the shower (the shower-exclusive parts) are altered to widen the inclusive region [113]. There is no general prescription for choosing the optimal merging scale for an analysis, though ($p_\perp$-based) merging scales must be softer than or equal to the hard jet scale of an analysis — since the inclusive hard jet cross sections are produced initially by the matrix element generator. Often merging scales of half the analysis jet $p_\perp$ cutoff are used, dependent on the phase space in which the predictions are analysed.

We encounter a similar subtlety in HEJ+Pythia, namely that the disparity in the exclusive regions between the HEJ and shower resummation can lead to showered configurations being treated as HEJ-inclusive when the dynamics of the event are fully HEJ-exclusive. In Fig. 3.5, we show an example HEJ event with three jets, and several soft gluons, using the same colour-coding as Fig. 3.4 for emissions to indicate that they are HEJ-exclusive emissions for which HEJ splitting kernels can be derived. The Born partons form hard jets, and the orange emisisons added from HEJ form soft jets.

We consider the possible evolution of such an event in Pythia, inspecting the

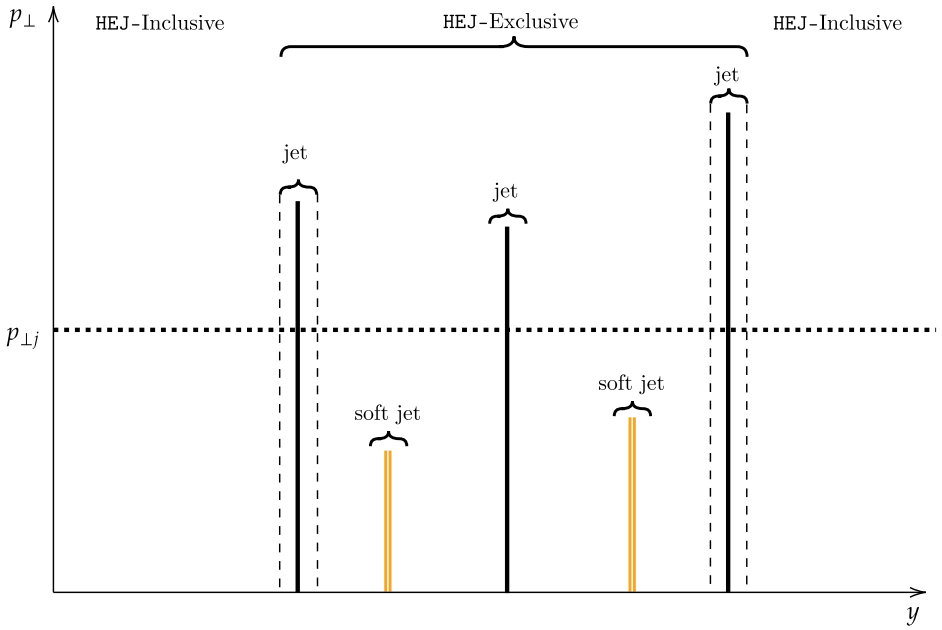

Figure 3.5: An example schematic three-jet event from HEJ, displayed in the $y - p_\perp$ plane with the hard Born jet transverse momentum cut $p_{\perp j}$ indicated. The Born partons (forming the Born jets) are indicated by the black lines. As in Fig. 3.4, orange (solid, double-barred) lines represent emissions for which HEJ could produce a splitting kernel, in this case added by HEJ.

evolution after several stages of showering. We present a possible configuration in Fig. 3.6 for the event shown in Fig. 3.5 after showering under the subtracted splitting kernel, with states classified as we discuss earlier in this section. Importantly, the parton shower has added soft emissions outside the rapidity interval bounded by the forward and backward hard jets, among other emissions that HEJ would not have added for Born-level input generated with all jets above $p_{\perp j}$.

Upon closer inspection, the event shown in Fig. 3.6 exhibits a widening of the exclusive HEJ region if the cut for the jet transverse momentum is reduced slightly. Indeed, if one allows the extremal jets to be counted above a lower transverse momentum cut than the rest of the HEJ jets, more of the emissions that in Fig. 3.6 were HEJ-inclusive become HEJ-exclusive, and can be produced with a HEJ splitting kernel. We display exactly the same configuration as Fig. 3.6 in Fig. 3.7, except labelling a lower transverse momentum cut for the extremal jets $p_\perp^{\text{ext}}$ and relabelling the emissions to show the widening of the exclusive HEJ phase space.

In practice, widening the HEJ exclusive region means producing LO input events

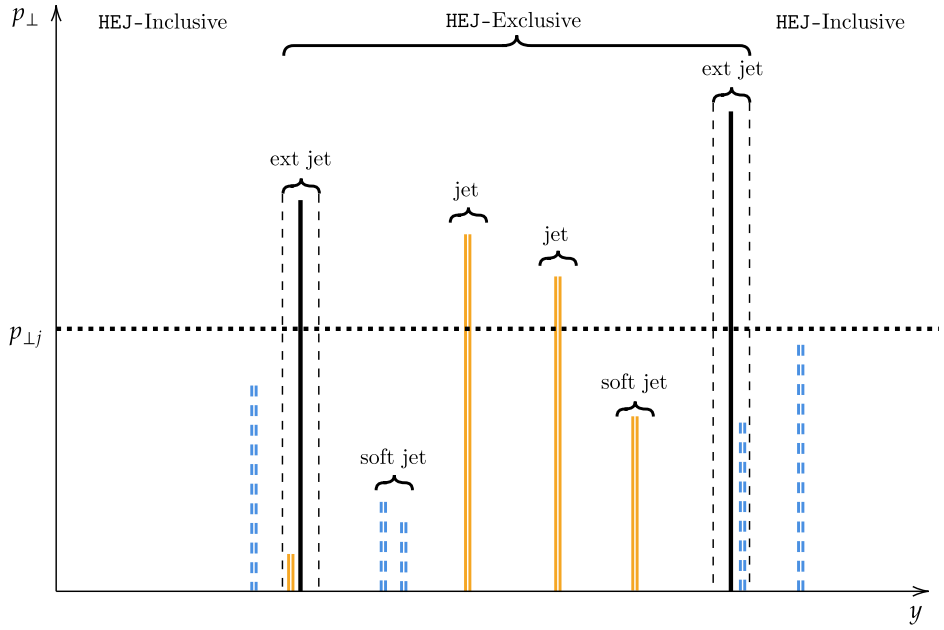

Figure 3.6: A possible configuration for the shower evolution of the schematic three-jet event from HEJ shown in Fig. 3.5. The partons at the centres of the extremal jets are coloured black to draw the connection with the Born partons. As in Fig. 3.4, orange (solid, double-barred) lines represent emissions for which HEJ could produce a splitting kernel, and blue (dashed, double-barred) lines indicate PYTHIA emissions for which HEJ can not produce a splitting kernel.

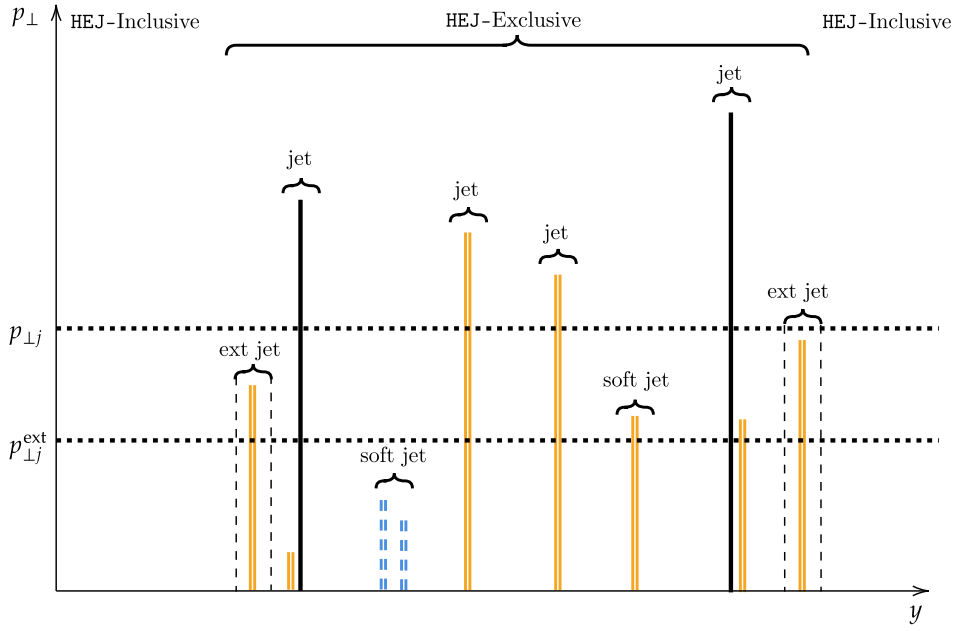

Figure 3.7: The evolution shown in Fig. 3.6 interpreted with a lower extremal transverse momentum cut for the jets, with the same colour/texture coding of emissions. By allowing the extremal jets to be counted above a softer transverse momentum cut, the HEJ-exclusive phase space is widened.

for HEJ at a lower transverse momentum cut, requiring that that at least two jets are harder than than the desired analysis jet transverse momentum cut. This will extend the region sampled by HEJ such that the configurations that can receive subtraction from such sequences of evolution in HEJ+Pythia are provided as input. Importantly, producing HEJ events this way will give suitable input to the HEJ+Pythia merging scheme but will not produce a physical HEJ prediction for the required analysis. For such a prediction (to which HEJ+Pythia can be compared), the generation must follow the method outlined in Sec. 2.2.4. To claim LO accuracy to n-jets above $p_{\perp j}$, higher multiplicities must be generated with the lower transverse momentum cut $p_\perp^{\text{ext}}$ in this prescription, since the resummation phase space integration in HEJ is filled by soft emissions that can now be added at FO.

Following this intensive overview of the HEJ+Pythia all-orders method for merging high energy and soft-collinear resummation, we proceed to show predictions obtained with this method, including comparisons to experimental data, in the next section. We conclude in Sec. 3.3, as well as discussing the future of the work.

3.2 Predictions and Comparisons to Data

We demonstrate the predictive capabilities of the merging algorithm outlined in this section. Comparisons are made to LHC data for a variety of observables and distributions, highlighting studies which are sensitive to higher-order effects in the soft-collinear and high-energy limits, as well as more complex observables where higher-order effects from both limits contribute in a non-straightforward manner. Analyses in this section are implemented in Rivet [120]. All showered productions include MPI and hadronisation unless otherwise stated.

3.2.1 Differential and Integrated Jet Profiles

To show that the HEJ+Pythia merging algorithm preserves the logarithmic accuracy of the parton shower, we consider first an observable for which the contribution is

dominated by soft-collinear corrections. The jet profiles (or jet shapes) are normalised measures of the transverse momentum distribution inside the cone of a jet, as such they are well-described by parton showers which are equipped to populate jet cones with the soft-collinear emissions required [9]. The study of ref. [119] showed that the parton shower alone was not sufficient to produce an accurate description of jet profiles, and that MPI and hadron-level corrections were crucial for correctly predicting the distribution of transverse momentum in a jet. We consider the observables from the inclusive jets study of ref. [9] in this section.

The differential jet profile is defined by the normalised sum of transverse momenta in an annulus (in y—ϕ space) of width Δr inside a jet with cone radius parameter R:

$$\rho(r) = \frac{1}{\Delta r}\frac{1}{N_{\text{jet}}}\sum_{\text{jets}}\frac{p_\perp(r-\Delta r/2, r+\Delta r/2)}{p_\perp(0,R)}, \tag{3.2.1}$$

where:

$$p_\perp(r_A, r_B) = \sum_{i\in\text{jet}} p_{\perp i}\Theta(\Delta R(i,0) - r_A)\Theta(r_B - \Delta R(i,0)). \tag{3.2.2}$$

The integrated jet profile is defined as the definite integral of ρ up to a radius $r \leq R$:

$$\Psi(r) = \frac{1}{N_{\text{jet}}}\sum_{\text{jets}}\frac{p_\perp(0,r)}{p_\perp(0,R)}, \tag{3.2.3}$$

which thus measures the total transverse momentum in a disc of radius $r < R$. The jet profiles are visualised in Fig. 3.8, where the left figure shows the annuli within which the differential profiles are calculated, and the right figure shows the definite integral from the centre of the jet to some radius $r < R$.

In Fig. 3.9, we compare HEJ+Pythia to experimental data from ATLAS at $\sqrt{s} =$ 7 TeV [9]. Two parton-showered predictions are also shown: a CKKW-L-merged LO prediction, and a prediction using just the shower of Pythia on LO $pp \to 2j$ input states (i.e. with no matching or merging). For all three showered predictions, the Monash 2013 tune [10] was used, and interleaved MPI were included as well as hadron-level corrections. For the original LO input events entering the merged predictions, the NLO QCD PDF set `NNPDF31_nlo_as_0118` [121] was used, while

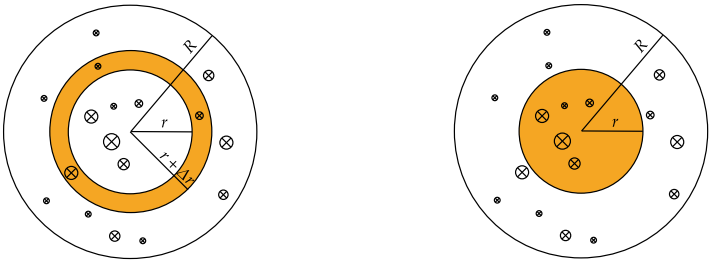

Figure 3.8: Visualisation of the differential (left) and integrated (right) jet profiles, showing the distribution of transverse momentum inside the jet cone.

the LO (QCD+QED) PDF set `NNPDF23_lo_as_0130_qed` [122] was used for the "pure" Pythia prediction, which is the default PDF of the Monash 2013 tune. Both PDFs were interfaced to the MC predictions with LHAPDF [123]. LO events were generated with `Sherpa` [62], using the Comix [70] ME generator.

For the `HEJ`+Pythia prediction, no difference was observed between using `HEJ` LL-resummed events as input and `HEJ` LL- and subleading-resummed events (i.e. the inclusion of subleading channels in the resummable part of the `HEJ` prediction has no impact on the jet profiles). Thus, we show the `HEJ`+Pythia prediction for LL+subleading-resummed `HEJ` (with the complement prediction included comprising non-resummable LO events, merged with CKKW-L).

The experimental study of ref. [119] showed that MPI are crucial for for a robust description of jet profiles. As such, theoretical predictions for the jet profiles are more strongly dependent on tune parameters than "harder" multi-jet observables. All three predictions shown in Fig. 3.9 describe well the differential distribution of transverse momentum inside jets, with the Pythia prediction closest to data throughout.

The differences between all three predictions are small and we motivate these as tune effects rather than improvements in the perturbative description from each. The `HEJ`+Pythia description in, for instance, the $160 \leq p_{\perp j} < 210$ GeV bin exhibits a smaller discrepancy with data than the CKKW-L-merged prediction, however

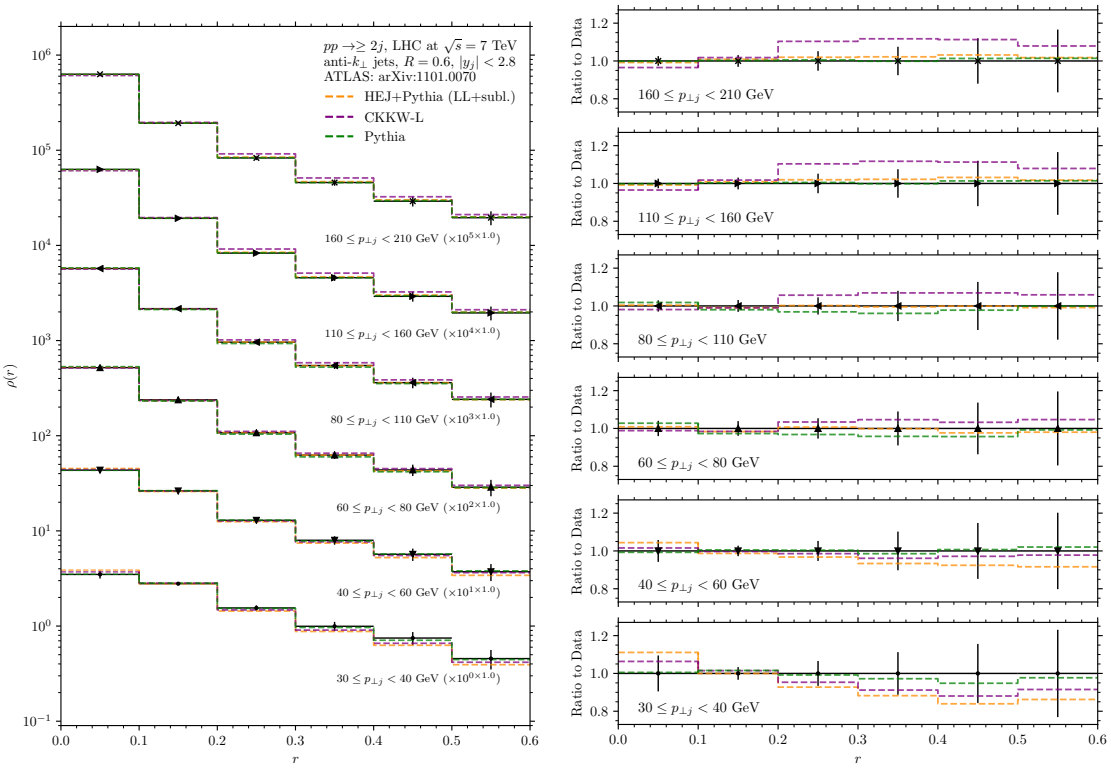

Figure 3.9: HEJ+Pythia, CKKW-L-merged, and Pythia predictions for the differential jet profile $\rho(r)$, split into $p_{\perp j}$ bins, and the ratio of these predictions to data from ATLAS [9]. All showered predictions use the Monash 2013 tune [10]. Analysis cuts displayed on the figure.

HEJ+Pythia owes the description of thet jet profiles entirely to the Pythia shower, thus this does not reflect an "improvement" over CKKW-L for this observable.

Since the tune parameters are phenomenologically determined, subleading differences can be incurred between different shower predictions (using e.g. different PDFs and matching/merging schemes). The broad trend shown allows us to conclude that HEJ+Pythia can be used to produce complete pictures of jet profiles.

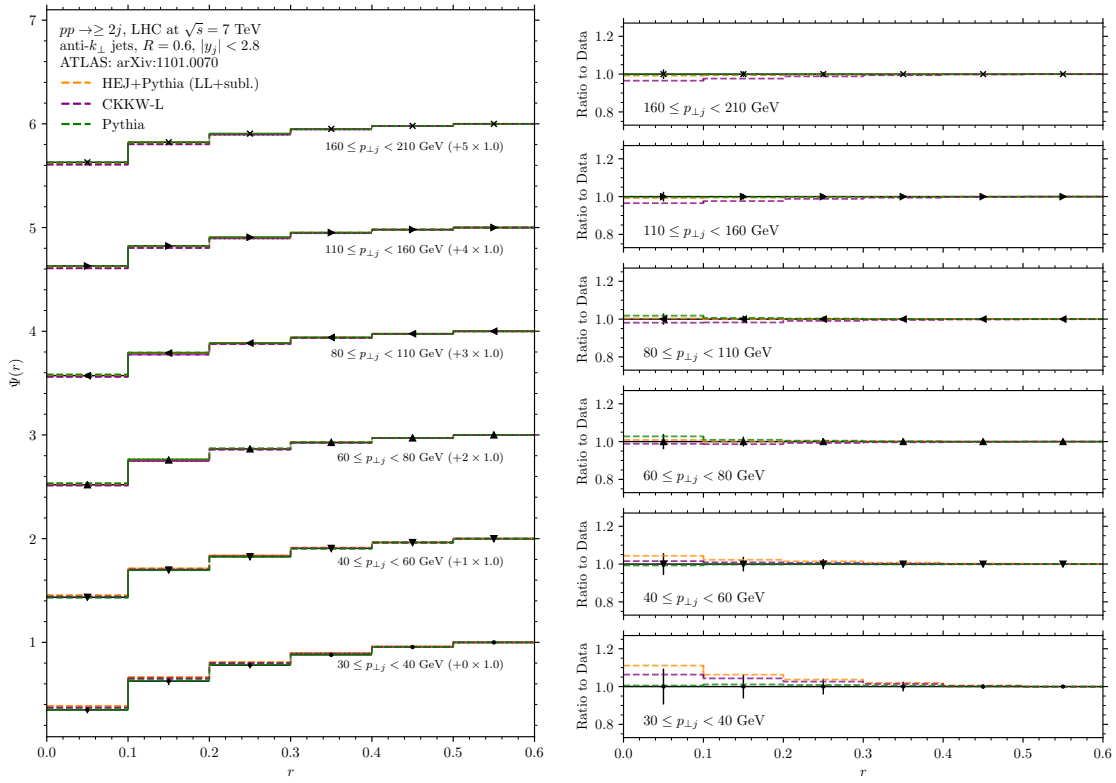

Figure 3.10: HEJ+Pythia, CKKW-L-merged, and Pythia predictions for the integrated jet profile $\Psi(r)$, split into $p_{\perp j}$ bins, and the ratio of these predictions to data from ATLAS [9]. All showered predictions use the Monash 2013 tune [10]. Analysis cuts displayed on the figure.

For completeness, we display also the integrated jet profiles in Fig. 3.10 for the same jet transverse momentum bins. Consistently with the differential profiles, these figures display solid agreement between HEJ+Pythia, the other showered predictions, and the experimental data. Generally, HEJ+Pythia predicts narrower jets — especially for softer jet transverse momenta — than the other showered predictions, however we attribute these differences to tune effects as we motivated for the differential profiles of Fig. 3.9.

3.2.2 Multi-Jet Cross Sections

We demonstrate further the developments of our all-orders merged description by examining differential distributions for inclusive dijet production. We compare to experimental data from the ATLAS collaboration, and examine the sensitivity of the merged prediction on the inclusion of subleading-logarithmic effects in HEJ.

The analysis we consider in this section is ref. [11], which considered inclusive central dijet production. Jets were clustered with the anti-$k_\perp$ algorithm using jet radius $R = 0.4$, and requiring $p_{\perp j} > 60$ GeV, $|y_j| < 2.8$. The hardest jet in an event was required to have transverse momentum $p_{\perp j_1} > 80$ GeV.

In Sec. 3.1.4, we observe that HEJ+Pythia predictions should be produced with the correct physical input to reflect the phase space probed in an analysis. While this was not observed to pose issues for the jet profiles in Sec. 3.2.1, for multi-jet differential observables the phase space sampled over has a significant impact on the merged description. The HEJ+Pythia predictions we display in this section were produced as the result of an in-depth analysis of how to construct this phase space with appropriate generation cuts. LO input was generated for $pp \to 2-6j$ (to claim LO accuracy for $pp \to 2-5j$), with a minimum transverse momentum cut of 40 GeV on each jet (requiring, as per Sec. 3.1.4, two jets with transverse momentum larger than the analysis cut of 60 GeV). The PDF set used was the NLO QCD set `NNPDF31_nlo_as_0118`, as for the jet profiles. The CKKW-L-merged complement prediction, forming part of the full HEJ+Pythia prediction, was produced with the same PDF set, and with the the merging scale defined by the same jet transverse momentum generation cut, $t_{\text{MS}} = (40 \text{ GeV})^2$.

The physical HEJ predictions we compare to were produced with the same PDF as the HEJ+Pythia prediction, only with a minimum jet transverse momentum of 60 GeV in line with the analysis jet cut. All jet multiplicities for $pp \to 2-5j$ are generated and LO-matched. This is not the HEJ prediction used as input for HEJ+Pythia, which is instead generated according to the prescription above.

We compare not only to HEJ and experimental data in this section, but also to a

CKKW-L-merged LO prediction for $pp \to 2-5j$. This prediction was produced with several choices of PDF and merging scale, and a thorough analysis of the output from this showed that the LO (QCD+QED) PDF set `NNPDF23_lo_as_0130_qed`, and a merging scale $t_{\text{MS}} = (30\text{ GeV})^2$, gave the most promising prediction. We did not use the same PDF set for the CKKW-L complements to the HEJ+Pythia prediction since this would produce erroneous DGLAP evolution for the PDFs when Pythia adds initial state radiation. LO events were again generated with `Sherpa`, using Comix as ME generator, for all predictions in this section. The renormalisation and factorisation scales for all predictions were given dynamically by $H_T/2$, with H_T the scalar sum of jet transverse momenta in an event. All showered predictions again used the Monash 2013 tune.

Sensitivity of merged prediction on HEJ subleading logarithms

When introducing the subleading corrections for inclusive $W + 2j$ production in HEJ in ref. [87], the sensitivity of the high-energy resummed predictions on the new subleading components was analysed to highlight the stability of the HEJ prediction, and to demonstrate where the subleading corrections enter into prominence. Since we consider inclusive dijet production in this chapter, the cross sections are dominated by different partonic hard processes than for inclusive $W + 2j$. Particularly, the $gg \to gg$ hard process dominates the inclusive dijet cross section at the LHC [45], meaning a larger proportion of the cross section is HEJ-resummable for the fully inclusive LO prediction than for $W + 2j$ production.

We analyse in this section the impact of these subleading corrections on the merged HEJ+Pythia prediction — specifically on the inclusion of the subleading HEJ-resummable states in the resummed part of the cross section, and the CKKW-L-merged complement. In other words, we show that our classification of states in HEJ+Pythia, and the split of the cross section, are insensitive to which part of the cross section the subleading states are chosen to belong. Thereby we show that HEJ+Pythia is similarly stable to HEJ in the inclusion of subleading effects.

In Fig. 3.11, the inclusive dijet cross sections are analysed for full LO-matched HEJ predictions including and exclusing resummation for subleading states, and the corresponding HEJ+Pythia predictions. Theoretical uncertainties are estimated for HEJ by varying the renormalisation and factorisation scales independently as described in Sec. 1.3.3. Theoretical uncertainties in shower-merged predictions are more difficult to consider since the values of α_s are reweighted for e.g. ISR emissions, and in CKKW-L merging meaning there is no straightforward generalisation of the scale variation estimator for HEJ+Pythia. We use "LL+subl." to indicate LL and subleading states resummed, with the rest of the cross section retained at LO accuracy for HEJ and merged via CKKW-L in HEJ+Pythia. Similarly "LL" denotes full LL resummation in HEJ with subleading and non-resummable states kept to LO, and merged via CKKW-L in HEJ+Pythia.

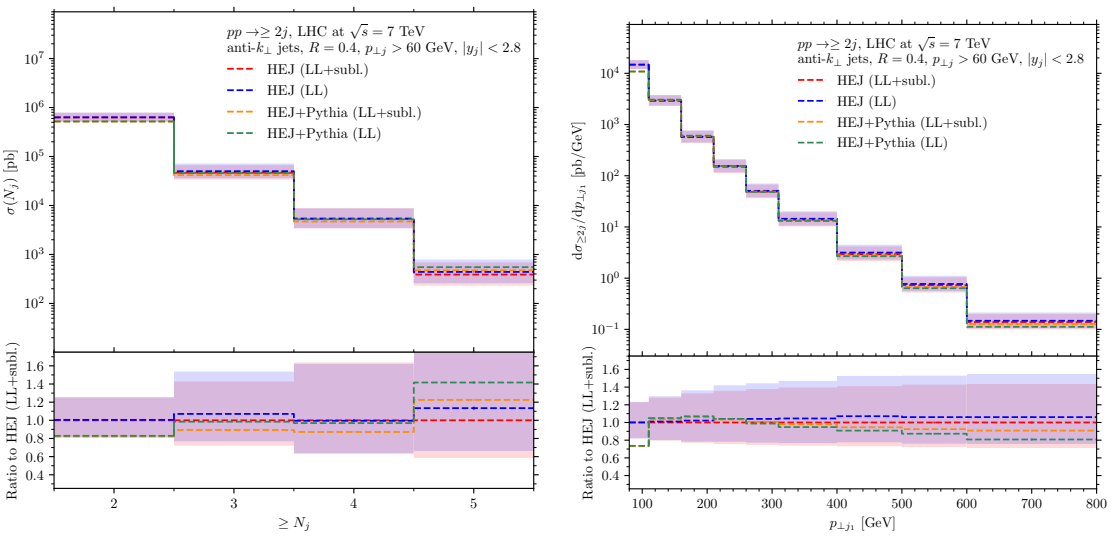

Figure 3.11: HEJ+Pythia and HEJ predictions for the inclusive jet cross sections (left) and the distribution of the transverse momentum of the hardest jet for inclusive dijet events (right). The analysis matches the described cuts from ATLAS [11], which are displayed on the figures.

The inclusive dijet integrated cross sections show that the configuration we have described earlier places the HEJ+Pythia predictions within the theoretical uncertainty estimate of the corresponding HEJ predictions — which was not observed to be the case if the same generation cuts are used on both. The inclusive dijet cross section is lower for HEJ+Pythia than for HEJ, though this effect is mitigated by the

generation prescription enough to ensure agreement within theoretical uncertainty. The variation in the HEJ+Pythia predictions is not only within the uncertainty for each prediction, but also resembles the variation in HEJ in magnitude throughout.

From the hardest jet transverse momentum spectrum we can infer that the reduction in the inclusive dijet rate between HEJ and HEJ+Pythia is dominated by contributions at the peak of the distribution for low transverse momenta. The distributions are similarly insensitive between including and excluding the subleading components from the HEJ-resummed component of the cross section.

In more detail, we inspect the difference in composition of the HEJ+Pythia-merged prediction between the HEJ-resummed and CKKW-L-merged parts, and the impact on the full prediction in Fig. 3.12. We plot the full HEJ+Pythia distribution of the hardest jet transverse momentum (as shown in Fig. 3.11), for each the full "LL" and "LL+subl." predictions. We then calculate the relative difference in each component by subtracting the "LL+subl." component from the "LL" and dividing by the "LL" component to gauge the variation of the component based on the classification.

We note the expected dominance of the HEJ+Pythia-merged resummed component in both cases, with the subleading configurations contributing significantly when included in this part of the cross section. For the HEJ predictions, two-jet observables would observe smaller contributions from subleading processes, since the LO $2 \to 2$ process is either a LL state (a FKL configuration as discussed in Sec. 2.1.2), or non-resummable. However, since we allow jets with lower transverse momentum to contribute in HEJ+Pythia — as deemed necessary in our generation framework — subleading $2 \to 3, 4, 5j$ processes have a larger contribution once showered in inclusive two-jet distributions. This motivates the $\sim 10\%$ effect we note between Figs. 3.12(a) and (b), exchanged between the resummed component and the CKKW-L-merged complement.

The variation in the full prediction (i.e. HEJ+Pythia-merged resummed and CKKW-L-merged complement) is remarkably stable to the split in classification. The full HEJ+Pythia prediction does not vary by more than $\sim 10\%$ throughout the

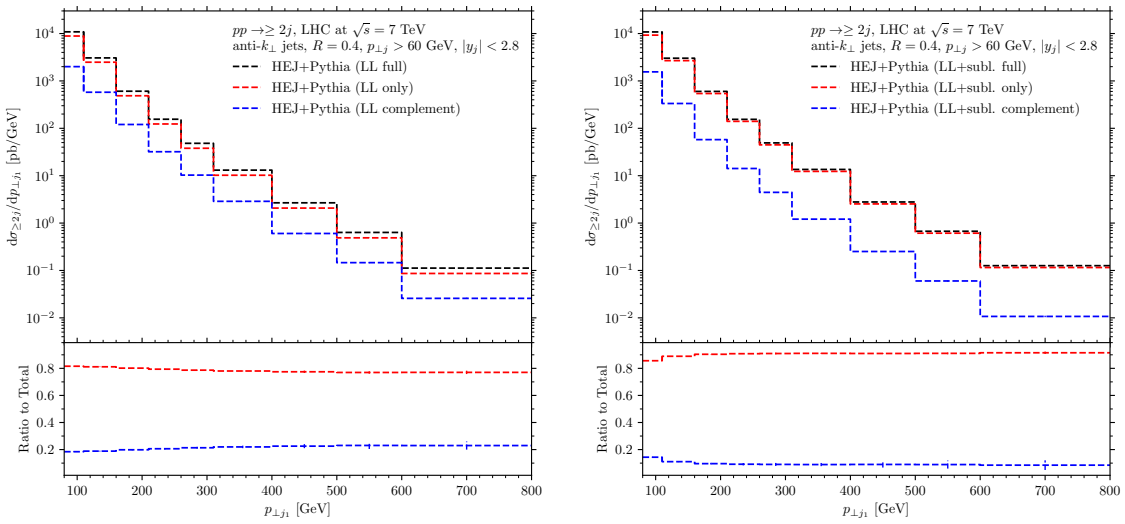

(a) (b)

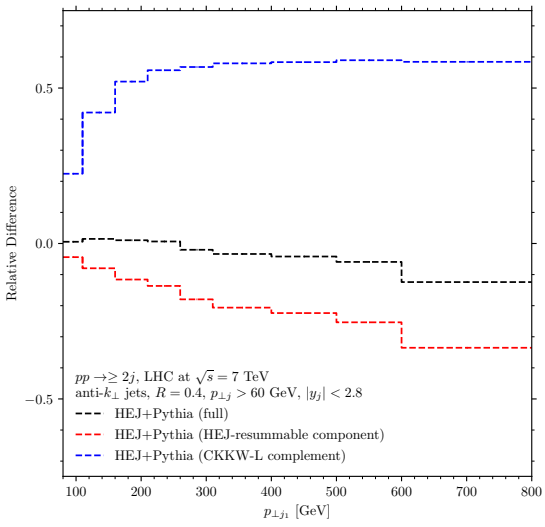

(c)

Figure 3.12: The decomposition of HEJ+Pythia into the full prediction, the resummable part merged with the algorithm we present in this chapter, and the CKKW-L-merged complement, for the hardest-jet transverse momentum distribution. In (a) this decomposition is plotted for the "LL" prediction, while (b) plots the decomposition for the "LL+subl." prediction. The relative difference — calculated as described in the text — is plotted in (c). Analysis cuts from ATLAS [11] are displayed on the figures.

distribution, despite the change in treatment. This is similar to the results observed for HEJ subleading effects as displayed for $W + 2j$ production in ref. [87] — wherein the total HEJ prediction demonstrates similar stability in a similar decomposition.

To demonstrate that this stability generalises for higher jet multiplicities — where the subleading HEJ logarithms become more important — we produce a similar decomposition for the distribution of the scalar sum of transverse momenta H_T in inclusive $pp \to 4j$ events, shown in Fig. 3.13.

The same stability can be noted for this inclusive four-jet distribution, with the full prediction varying throughout by between $\sim 5\%$ and $\sim 15\%$. The importance of the subleading corrections is again clearly demonstrated by the expected increase in the "LL+subl. only" line relative to "LL only". Furthermore, the relative differences calculated are more flat than for the decomposition in Fig. 3.12(c), where the importance of the subleading resummation in HEJ manifests through the shower merging and increases uniformly with transverse momentum. For the four-jet inclusive distribution in Fig. 3.13, the relative difference shows that the subleading effects are important throught the distribution, but that our description is stable to their inclusion as required.

Comparison to data

We compare the HEJ+Pythia prediction to experimental data from ATLAS [11] and to the HEJ and CKKW-L-merged predictions we have described at the start of this section. The analysis of ref. [11] focused on multi-jet cross sections and transverse momentum-based distributions, providing a robust testing ground for the HEJ+Pythia merging since both high-energy and soft-collinear effects overlap in a non-straightforward way. Furthermore, the experimental analysis of ref. [11] presented with the data Monte Carlo predictions from Sherpa, Pythia, Herwig, and ALPGEN [124]. These included predictions obtained just with the parton shower, and with matching and merging. In all cases, predictions were rescaled by a constant factor that matched the predicted inclusive dijet cross section to the experimental

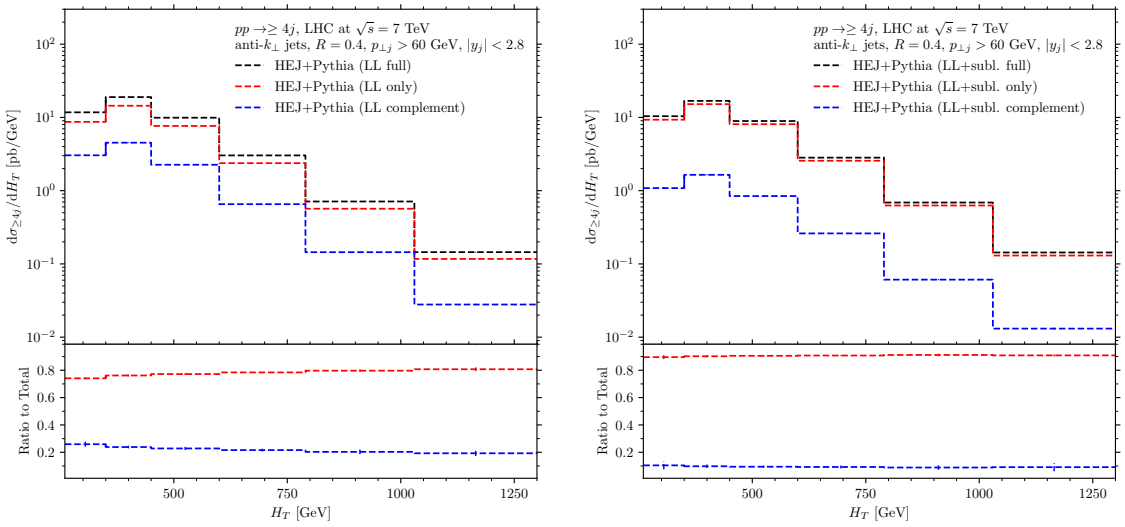

Figure 3.13: The decomposition of HEJ+Pythia into the full prediction, the resummable part merged with the algorithm we present in this chapter, and the CKKW-L-merged complement, for the H_T distribution for inclusive $pp \to 4j$ events. In (a) this decomposition is plotted for the "LL" prediction, while (b) plots the decomposition for the "LL+subl." prediction. The relative difference — calculated as described in the text — is plotted in (c). Analysis cuts from ATLAS [11] are displayed on the figures.

data. These factors ranged from 0.65-1.22, showing that a large variation in inclusive dijet cross section was observed in the MC predictions.

We present our predictions in this section **without** rescaling the observed cross sections, thus a larger discrepancy with data than for predictions presented in the experimental study may be observed for inclusive dijet distributions.

In Fig. 3.14, we show the inclusive N_j cross sections and the differential inclusive dijet cross section in the transverse momentum of the hardest jet. The HEJ and HEJ+Pythia predictions shown are for the "LL+subl." (including non-resummable states kept at LO and merged with CKKW-L respectively) configuration. Just with HEJ, a respectable description of both the integrated jet inclusive jet cross sections and the hardest jet transverse momentum is readily obtained. CKKW-L merging and the full HEJ+Pythia prediction produce similarly strong descriptions of these observables, though the inclusive dijet cross section is $\sim$ 15% beneath data for HEJ+Pythia and just outside the experimental uncertainty bars.

Examining the peak of the distribution in hardest jet transverse momentum in Fig. 3.14 (right), we see that a significant contribution is missing for momenta between 80-100 GeV for HEJ+Pythia. The rest of the distribution is described similarly as well by HEJ+Pythia as by HEJ and with CKKW-L. This suggests that the framework we have introduced to widen the HEJ-inclusive region in the input to HEJ+Pythia may require a slight adjustment for the hardest jet in this analysis, since the hardest jet is required to have $p_{\perp j_1} > 80$ GeV. A more complex generation framework may be required to adequately populate the region of phase space required for this emission (e.g. requiring one jet harder than 80 GeV in $p_\perp$ and another harder than 60 GeV, rather than uniformly using 60 GeV), without increasing significantly the tail of the distribution.

In Fig. 3.15, we compare the second- and third-hardest jet transverse momentum distribution as predicted by the HEJ, HEJ+Pythia, and CKKW-L setup outlined with experimental data. though we observe a similar reduction in the second-hardest jet distribution, for low transverse momenta, HEJ+Pythia provides a strong descrip-

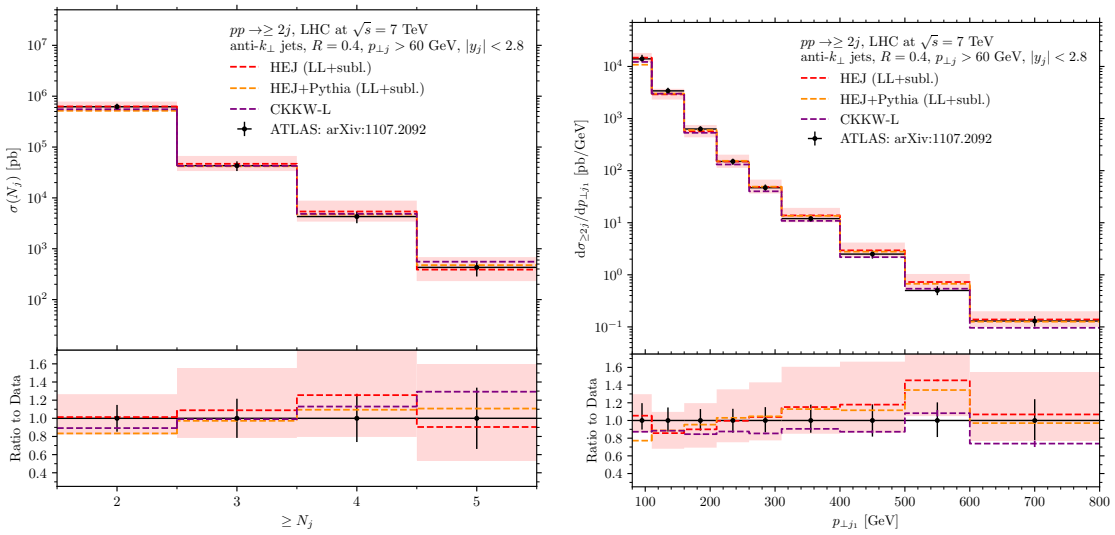

Figure 3.14: HEJ, HEJ+Pythia, and CKKW-L predictions for the inclusive jet cross sections (left) and the distribution of the transverse momentum of the hardest jet for inclusive dijet events (right). Data and analysis cuts from ATLAS [11], which are displayed on the figures.

tion of the spectrum. The deficit in the low-$p_{\perp j_2}$ bins is again due to the missing configurations highlighed above, though this effect is smaller and similar to the CKKW-L prediction in this region. The description of the full distribution makes clear that HEJ+Pythia works as intended, improving the description over HEJ and surpassing the CKKW-L merged description in the large-$p_\perp$ tail.

The distribution of the inclusive three-jet cross section on the third-hardest jet transverse momentum in Fig. 3.15 (right) demonstrates the strength of the HEJ+Pythia prediction in clearer terms, where the discrepancy with data is small throughout. The strength of the CKKW-L prediction in this distribution highlights the importance of the LO accuracy on correctly describing jet multiplicities, and showcases that this is translated through to HEJ+Pythia in our procedure.

In Fig. 3.16, we examine higher multiplicity cross sections as distributed in H_T. The left and right figures respectively show the inclusive three- and four-jet cross section. All three theoretical predictions provide robust descriptions of the differential cross sections when compared to data which makes evident that the HEJ+Pythia framework correctly accounts for the overlap between HEJ and the parton shower, and conserves the in-built LO accuracy of the cross sections.

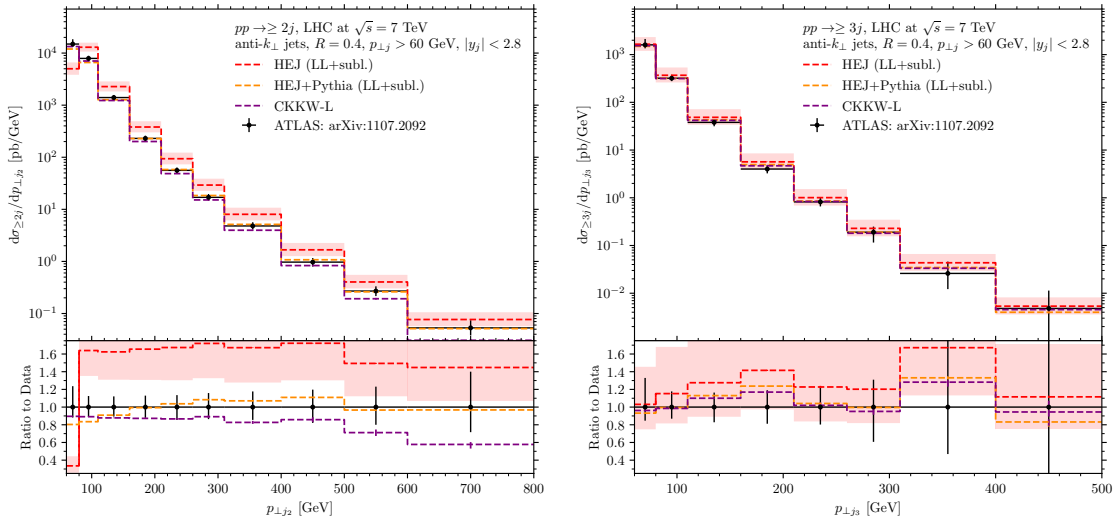

Figure 3.15: HEJ, HEJ+Pythia, and CKKW-L predictions for the distribution of the transverse momentum of the second-hardest (left) and third-hardest jet (right) for inclusive dijet and three-jet events respectively. Data and analysis cuts from ATLAS [11], which are displayed on the figures.

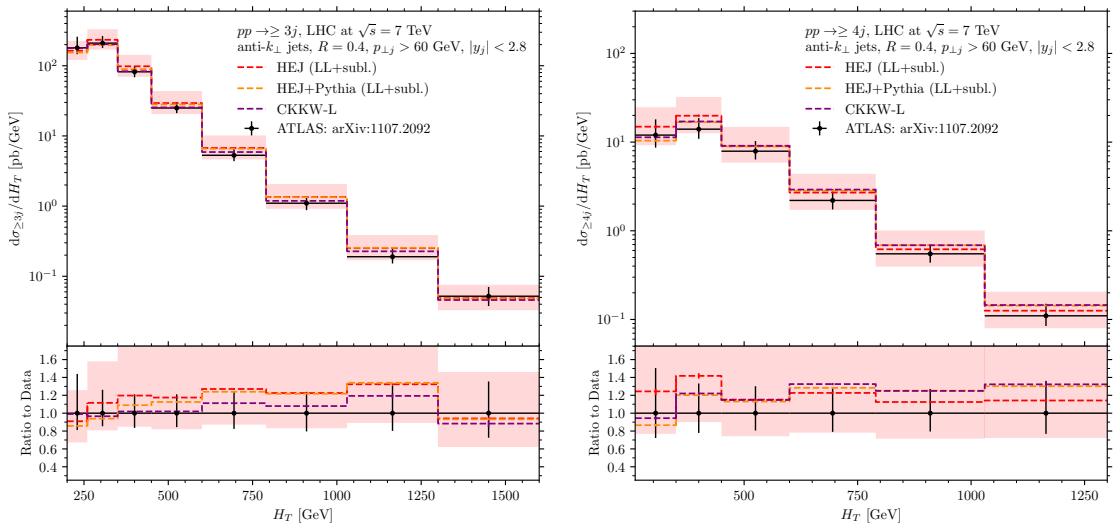

Figure 3.16: HEJ, HEJ+Pythia, and CKKW-L predictions for the distribution of the inclusive three-jet (left) and inclusive four-jet (right) cross sections in H_T. Data and analysis cuts from ATLAS [11], which are displayed on the figures.

3.2.3 Predictions for the Average Number of Jets

We compare HEJ+Pythia in this section to an experimental analysis focusing on the radiation in the rapidity interval spanned by dijet systems, and on the ensuing azimuthal decorrelations of the jets. The observable we are chiefly concerned with predicting is the average number of jets, as distributed in the rapidity difference between the hardest jets.

The experimental analysis we compare to is the ATLAS analysis ref. [12], which presents data for jets clustered with the anti-$k_\perp$ algorithm, using $R = 0.6$, and requiring $p_{\perp j} > 20$ GeV, with rapidities for jets allowed in the region $|y_j| < 4.4$. The hardest two jets were required to satisfy $p_{\perp j_1} > 60$ GeV, $p_{\perp j_2} > 50$ GeV. Since the rapidity interval sampled by the analysis phase space covers the full extent of the ATLAS detector in rapidity, and since the events analysed observe a hierarchy in transverse momentum, a multiplicity-sensitive observable in this region would provide a significant opportunity to test the HEJ+Pythia method. The region sampled is one where both high-energy and soft-collinear effects are essential for full, precise description of the QCD process.

The HEJ and HEJ+Pythia predictions use Sherpa-generated LO input, with the PDF set NNPDF31_nlo_as_0118 as used earlier, and the central scale choice of $H_T/2$ for both the renormalisation and factorisation scales. LO input was generated in line with the analysis cuts outlined, since the hierarchy imposed in transverse momentum was found to provide the appropriate configurations for HEJ+Pythia to account for the difference in interpretation of inclusive corrections between HEJ and HEJ+Pythia. Events were generated for $pp \to 2-5j$ to claim five-jet LO accuracy[1]. CKKW-L-merged LO predictions are also generated with the same jet multiplicities, scale choice, and cuts as HEJ and HEJ+Pythia.

The dependence of the average number of jets in the rapidity interval formed by the dijets on the magnitude of this rapidity difference is plotted in Fig. 3.17. For

[1]Since the analysis and generation cuts are aligned, there is no need to generate higher-multiplicity input to claim five-jet LO accuracy.

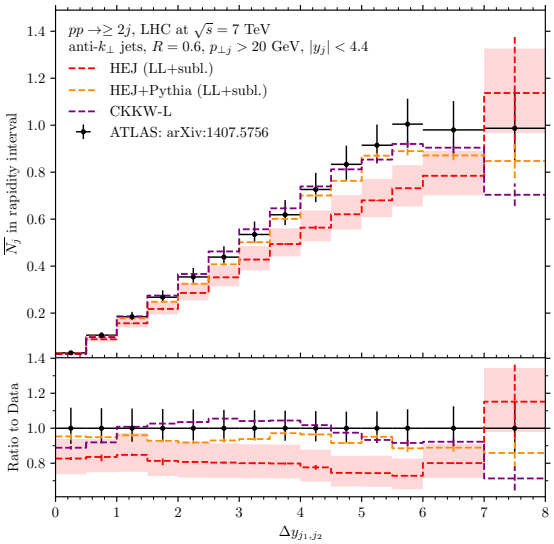

Figure 3.17: HEJ, HEJ+Pythia, and CKKW-L predictions for the average number of jets in the rapidity interval between the two hardest jets, distributed in the size of this interval $\Delta y_{j_1,j_2}$. Data and analysis cuts from ATLAS [12], which are displayed on the figures.

HEJ and HEJ+Pythia, the full "LL" and "LL+subl." predictions differed minimally, and as such we display only the "LL+subl." lines. The choice of analysis cuts highlights that both the high-energy and the soft-collinear corrections are important to consider, emphasised by the fact that the HEJ prediction alone does not describe the data well. This is a feature consistent with the HEJ and HEJ+Ariadne predictions presented in the original experimental study [12], where the shower corrections added by Ariadne (limited though the implementation was) produced a better description than HEJ alone. Statistical uncertainties are large for this distribution since the average number of jets is formed by calculating ratios. The uncertainties for each sample were propagated appropriately for the numerators and denominators, however this can lead to amplifications as observed. The error bars shown should be treated as an overestimate of the statistical uncertainty.

The prediction shown here with HEJ+Pythia surpasses all predictions from the original study, differing from data by less than one standard deviation for much of the distribution, and never (where statistics are reliable enough to draw valid conclusions from) by more than $\sim 15\%$. The description obtained from CKKW-L highlights the importance of both the LO accuracy of the jet rates and the shower

corrections for this analysis, demonstrating that the HEJ+Pythia method accounts for these effects, and incorporates the HEJ description of physics at large rapidity differences.

Further exploratory analyses

To complement the discussion in this section, we display HEJ+Pythia predictions for an analysis matching the cuts investigated in a joint theoretical study of high-energy and soft-collinear effects, ref. [13]. We require jets to be clustered with the anti-$k_\perp$ algorithm, using $R = 0.5$ and requiring $p_{\perp j_1} > 45$ GeV, $p_{\perp j} > 35$ GeV, $|y_j| < 4.7$. The process analysed is inclusive $pp \to jj$ at $\sqrt{s} = 7$ TeV. Comparisons in the study were made between HEJ, NLO, and with several parton shower predictions including Powheg+Pythia.

Compared to the experimental study of ref. [12], it was found that these cuts sampled regions of phase space wherein both parton shower and high-energy effects were important. We therefore produced HEJ and HEJ+Pythia predictions suitable for the analysis. HEJ was generated from Sherpa LO input, with all jets above 35 GeV in transverse momentum, and $\mu_R = \mu_F = H_T/2$, with the NNPDF31_nlo_as_0118 PDF set for $pp \to 2 - 5j$. All components of the HEJ+Pythia prediction were generated with transverse momentum above 25 GeV (the square of this was used as the merging scale in the complement prediction) for $pp \to 2 - 6j$ in the resummable component, and $pp \to 2 - 5j$ in the non-resummable. Two jets, in the resummable component, were required to be harder than the analysis jet cut of 35 GeV in transverse momentum in order with our generation framework such that $pp \to 2-5j$ accuracy can be claimed. The same PDF set and scale choice was used in the base LO prediction as HEJ. For both predictions, the full "LL+subl." configuration was used in the resummation, with non-resummable states retained at LO for HEJ and merged in the CKKW-L complement for HEJ+Pythia. CKKW-L and pure Pythia predictions were not produced as the analysis in ref. [13] provided predictions from parton showers which demonstrate the soft-collinear behaviour.

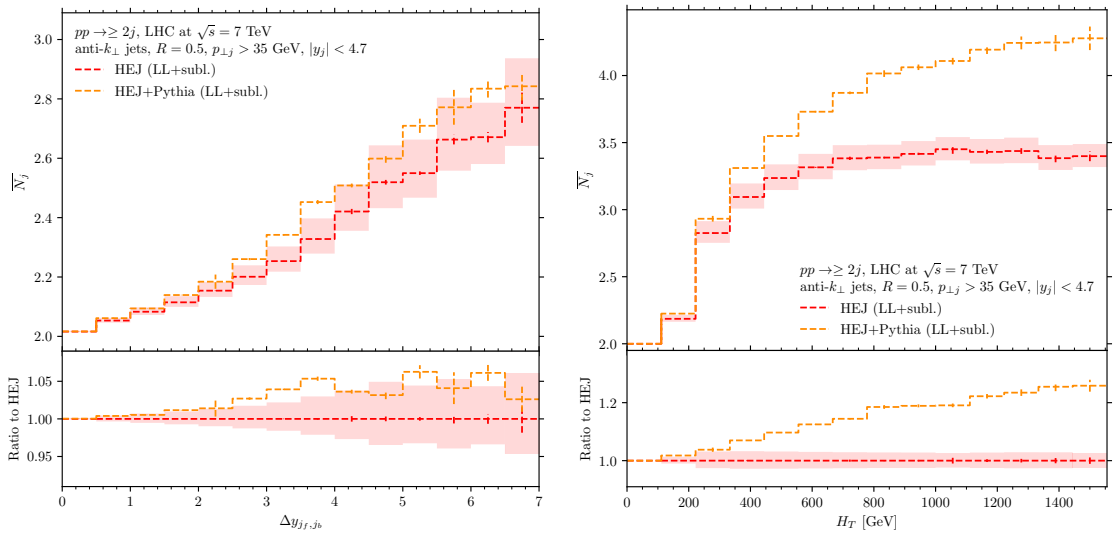

Figure 3.18: HEJ and HEJ+Pythia predictions for average number of jets against the rapidity difference of the forward and backward jets $\Delta y_{j_f,j_b}$ (left), and against H_T (right). Analysis cuts match those of ref. [13], and are displayed on the figures.

In Fig. 3.18, we plot the average number of jets (including the dijet pair) against the rapidity difference between the forward and backward jets $\Delta y_{j_f,j_b}$ (left) and against H_T (right). The distribution in $\Delta y_{j_f,j_b}$ is a direct probe of the HEJ corrections in the limit this quantity becomes large, however for small values the shower corrections were found to be important in the study ref. [13] (Fig. 6, top-left in the publication). The distribution we show reflects this picture exactly, with HEJ+Pythia within or close to HEJ theoretical uncertainty throughout. The excesses between roughly 2.5 and 4 units of rapidity reflect that the shower corrections are additionally important in describing the jet spectrum for such a distribution, but the broad trend shows a systematic agreement with HEJ within statistical uncertainty[1]. The HEJ prediction here produces slightly different results than from the study ref. [13], this is due to differing scale choices and that the subleading corrections were not included in the prediction shown in ref. [13].

The H_T distribution of the average number of jets in Fig. 3.18 (right) is similar in form to the analogous distribution in ref. [13] (Fig. 6, bottom-left in the publication),

[1]As with the distribution in Fig. 3.17, error propagation in ratio predictions is prone to amplifications in statistical error, thus staistical error bars here are to be seen as overestimates.

showing that this distribution is not sensitive to subleading high-energy effects. While the HEJ prediction is similar to that in the publication, the HEJ+Pythia prediction no longer resembles the HEJ prediction for this observable which has already been established in Sec. 3.2.2 as a characteristic indicator of parton shower logarithms. For large H_T, configurations with hierarchies in transverse momentum dominate the cross section since the jet threshold cuts are far softer than the values of H_T for which the distributions plateau. This means that parton showers will provide the most accurate description of the radiation spectrum as distributed in H_T and similar observables. The HEJ+Pythia prediction shown reaches a plateau at $\overline{N_j} \sim 4.25$ for large H_T, which is similar to the plateau observed for Powheg+Pythia in the study. This is, once again, a clear demonstration that the HEJ+Pythia description produces the required distributions according to the logarithms resummed by each component prediction without double counting.

3.3 Conclusions and Future Work

Througout this chapter we have introduced a sophisticated novel framework for merging the exclusive high-energy resummation of HEJ with the soft-collinear parton shower resummation of Pythia that has been demonstrated to systematically account for the double counted contributions between each description to all orders. The description we obtain has been shown to be precise and stable, rendering it an invaluable tool to retain when considering the missing higher-order effects from FO predictions in perturbative QCD.

This study has been a proof-of-concept and rigorous testing for the new framework. We envisage that the tool we have developed will be invaluable for comparisons to data from the high-luminosity era of the LHC, where analyses could obtain larger datasets for regions receiving significant contributions from high-energy and soft-collinear effects. In particular, harder dijet cuts may be imposed on HL-LHC data, and larger transverse momentum hierarchies can be explored by extending the range

of H_T distributions to several TeV (and imposing stricter requirements on H_T, as well as the jet transverse momenta). HL-LHC [26] data will be more precise for large rapidity differences between dijets than in the data we have compared to in Fig. 3.17, meaning a reliable isolation of high-energy effects can be explored. Other high-energy distributions of interest could be probed at larger scales, such as the dijet invariant mass which may also be extended to several TeV in range.

Such analyses would demonstrate the predictive power of the HEJ+Pythia method, showing that both high-energy and soft-collinear effects require precise understanding and accounting for in a complete perturbative prediction. This is a core feature of the future prospects of the work, that a precise and stable accounting for these higher order effects can be used where needed for precise data sets in new experiments.

3.3.1 Future Work in HEJ and HEJ+Pythia

Here we outline several developments in HEJ and HEJ+Pythia that will impact the description we obtain with this method. These developments are ongoing and are relegated to future studies of merging HEJ resummation with a parton shower.

Developments in HEJ perturbative accuracy

There is an ongoing initiative in the HEJ collaboration to attain full NLL accuracy in the HEJ description of high-energy logarithms $\log \hat{s}/p_\perp^2$, the inclusion of the subleading corrections described in e.g. ref. [87] is a significant step forward in this direction. To reach this milestone, the one-loop corrections to HEJ impact factors, as well as the one-loop corrections to the HEJ Lipatov vertices and the two-loop corrections to the Regge trajectory, will be required [125]. This means that the resummation in HEJ will not only just be able to resum NLL configurations at LO (where all partons form distinct, hard jets) to LL accuracy. The regularisation of collinear divergences at NLL accuracy would allow HEJ to produce e.g. central $q\bar{q}$ pairs in LL configurations without requiring that each quark forms a distinct hard jet.

The implications of such developments on HEJ+Pythia are significant. With

greater HEJ accuracy the demand for a physical shower-merged prediction will grow to ensure precision modelling of higher-order high-energy and soft-collinear effects with a rigorous treatment of the overlap.

The classification procedure we have introduced in Sec. 3.1.4 does not translate to the framework of fully NLL-accurate HEJ base predictions, and the definition of inclusive and exclusive regions for HEJ resummation will change accordingly. In particular, the collinear splitting of a (hard) gluon into a collinear $q\bar{q}$ pair is currently treated as HEJ-inclusive evolution in HEJ+Pythia since the current accuracy of HEJ is not equipped to calculate the necessary matrix elements to derive the corresponding splitting probability. This aspect of the classification would need to be altered to widen the HEJ-exclusive region in the shower to align with the HEJ accuracy. However, the flexibility of the framework we have introduced ensures that such modifications would be simple to implement when NLL accuracy in HEJ is achieved. The algorithm for merging LO-matched, HEJ-resummed events will not need to be changed as it has been in the past.

Processes with decaying W, Z/γ, H bosons

HEJ can produce resummed event output for jet production with decaying W, Z/γ, and H bosons. The framework we have presented at the start of this section can not be easily translated to such events since the inclusive Born-level prediction starts at jet multiplicities for which HEJ can not produce resummable events. This means that the construction of histories in Pythia presents significant complications to the interpretation of HEJ-resummable events in the shower language for such processes.

Concentrating on the example of W production, a $pp \to W + 2j$ event is treated as a QCD $2 \to 2$ process, with the W emission an electroweak correction. This means that the lowest possible jet multiplicity for a resummable state in HEJ with a W boson is two, i.e. the event history starts from a Born configuration for $pp \to W + 2j$.

In the parton shower, a $pp \to W + 2j$ scattering (indeed a $pp \to W + nj$ scattering) is inclusive QCD evolution to Drell-Yan production of a W boson: $pp \to W$. Thus

the event history for a $pp \to W + 2j$ configuration starts from a Born configuration with jet multiplicity zero. The original configuration is connected to the Born by two QCD emissions.

This difference means that constructing histories for HEJ-resummable events is not possible to the lowest-order Born-level process in the shower. When we produce histories for HEJ events, we can only cluster back to the HEJ-resummable Born configurations, i.e. the histories for HEJ events will start from states $\mathcal{S}_0$ corresponding to $W + 2j$ final states. Then, a $W + 4j$ HEJ-resummed event (with no additional soft gluons) would be separated from the Born configuration by two shower emissions, rather than four. Yet, the CKKW-L complement to the resummable part is not restricted in this way, and can be clustered back to the $W + 0j$ state to retain full LO accuracy.

To work around these restrictions, we could consider relaxing the requirement that the history for a HEJ event must be a sequence of HEJ-resummable states for states with e.g. a W boson, and fewer than two jets. Considering the trial shower in the event history of Eq. (3.1.5), we may write:

$$\begin{aligned} \mathrm{d}\sigma_{m,n}^{W,\,\texttt{HEJ+Pythia}} = \mathrm{d}\sigma_0^* \cdot P_1^P \Delta_{0,1}^P \cdot P_2^P \Delta_{1,2}^P \cdot \prod_{i=3}^{m} P_i^H \Delta_{i-1,i}^H \\ \cdot \left[\prod_{\lambda=1}^{\lambda_i} P_{i_\lambda}^S \Delta_{i_{\lambda-1},i_\lambda}^S \right] \cdot \prod_{j=m}^{n-\mathcal{N}} \left(P_j^S \Delta_{j-1,j}^S \right), \end{aligned} \tag{3.3.1}$$

such that the HEJ-resummable part of the cross section is clustered back to a $W + 0j$ configuration with Pythia splitting probabilities and Sudakov form factors. When the evolution reaches the scales at which the event becomes HEJ-resummable, emissions from Pythia are subject to the subtraction required for removal of double-counted effects.

However, this method poses issues to our interpretation of the emission with splitting kernel P_2^P, since this emission evolves a non-HEJ-resummable state to a HEJ-resummable state. In the ensemble of events from HEJ used as input to HEJ+Pythia, such a state will have been already provided meaning the probability of the state having been produced in HEJ must be subtracted. The definition of the HEJ splitting

kernel in Eq. (3.1.1) is calculated by a ratio of (square) HEJ matrix elements, for which there would only exist an expression of the numerator and not the denominator.

This issue would also feature in the CKKW-L complement prediction since the classification procedure for states (which we discuss in Sec. 3.1.4) respects that the treatment is consistent between HEJ-resummable and non-resummable states for the full evolution, since no subtraction is applied on the CKKW-L-merged complement. However, for (e.g.) $W + 0, 1j$ states merged via CKKW-L, HEJ-resummable configurations can arise early in the evolution and the subtraction for such emissions is similarly ill-defined.

One may naïvely consider artificially imposing a limit on the clustering in the history for all input events, only producing histories for inclusive dijet processes, however this method does not respect the logarithmic accuracy of the parton shower or the LO accuracy of the base prediction. This is due to the effect of low-parton-multiplicity input evolving to a higher-multiplicity state in the shower i.e. the shower may not only decrease the jet count in an event, but also increase it (e.g. by splitting a hard jet at large scales into two softer jets still above the analysis jet transverse momentum cut). Thus perturbative accuracy can not be retained to the accuracy required since there will contributions from showered $W + 0, 1j$ events that produce $W + 2j$ (and higher) final states.

This discussion shows that adapting the framework presented in this chapter to consider different processes than inclusive dijet production is a complex and subtle undertaking. A significant reorganisation of the classification procedure and on the interpretation of double counting in events at large scales is required. However, we are confident that a method can be developed for producing HEJ-resummed, parton-showered predictions for such processes by applying the core principles that have guided the development of the HEJ+Pythia method.

3.3.2 Final Comments

The framework and results that we have presented in this chapter demonstrate that the HEJ+Pythia method is a robust and potent method for producing precise, stable predictions for perturbative QCD processes at hadron colliders. The retention of HEJ and Pythia logarithmic accuracies has been shown for a diverse range of results and observables including differential cross sections and jet profiles. The flexibility and comprehensiveness of the framework ensure that minimal developments are required to the classification to accommodate future accuracies in HEJ, and that the algorithm itself is "future-proof" from the point of view of advances in HEJ.

Consistently with the previous studies refs. [6, 119], this work shows that comprehensive decomposition of the HEJ and the parton shower resummation is required for physical results. The benefits of such considerations cannot be overstated, and we are confident that HEJ+Pythia will assume a prominent role in the theoretical and experimental analyses of the future.

Chapter 4

Inclusive Production of a Higgs Boson with at Least One Jet in *High Energy Jets*

We have discussed in Sec. 1 that detailed precision analysis of the Higgs sector is among the forefront of the objectives of the LHC. Experiments aim for accurate measurements of processes where Higgs bosons are produced, both inclusively or in association with other identified particles. Given the phenomenological importance of processes involving Higgs boson production, there are considerable efforts to provide high-precision theory predictions. Perturbative corrections are typically large, necessitating the inclusion of effects at higher orders. This endeavour faces a major challenge: in large regions of phase space, Higgs boson production is dominated by the gluon fusion mechanism, which is typically mediated by a virtual top quark loop. Inclusive gluon fusion Higgs boson production with full finite top mass contributions can currently be calculated at NNLO [126]. Including jets reduces the accuracy available for fixed-order perturbative expansions with full top mass effects. Exclusive Higgs boson plus jet production is only calculable at NLO [127, 128] with full top mass effects, and Higgs boson production with dijets can only be calculated currently to leading-order [79, 129] with finite top mass.

To facilitate calculations, the top quark mass is often assumed to be much larger than all other scales. Based on this approximation, the aforementioned processes have been computed to one higher order in perturbation theory [130–139]. However, one is often interested in observables where the assumption of a comparatively large top quark mass is invalid and the full mass dependence has to be accounted for. One example is the study of the high-energy tail in the Higgs boson transverse momentum distribution. When the Higgs boson is produced at large transverse momentum around and above $p_{\perp H} \sim 100$ GeV, the approximation that the top quark mass m_t is infinite becomes less accurate, since $m_t = 174$ GeV in the SM [48]. To produce reliable calculations in such regions of phase space requires the inclusion of finite quark mass effects. The inclusion of one jet allows for these effects to manifest with larger contributions than for Higgs production without jets since the recoil of a Higgs boson against a hard jet can allow it to attain large transverse momentum.

Another avenue towards better theory predictions consists of the all-order resummation of contributions that are enhanced in kinematic regions of interest. In our exploration of the high energy limit in Sec. 2.1, and the *High Energy Jets* framework in Sec. 2.2, we motivated the exploration of the high energy limit by considering the VBF- and GF-dominated regions of phase space. In the VBF-dominated region, the GF contribution for Higgs boson production with at least one jet is enhanced by large logarithms in $\hat{s}/|p_\perp|^2$, where $\sqrt{\hat{s}}$ is the square of the partonic CoM energy and $p_\perp$ a characteristic transverse momentum scale [140]. For the case of two or more jets, the resummation of these high energy logarithms has been shown to lead to significant corrections, especially after VBF cuts are applied [141]. This provides a strong motivation to extend the study of logarithmic enhancement to the inclusive production of a Higgs boson with a single jet.

We focus on the on-shell scattering involving two or more final state particles, which receives logarithmically enhanced perturbative corrections in the MRK limit. This is the limit we explored in Sec. 2.1, of large *partonic* CoM energy $\sqrt{\hat{s}}$, with all particles

produced with similar transverse momentum. As described, the BFKL formalism can predict the logarithmic corrections (in $\hat{s}/|p_\perp|^2$) to the on-shell scattering matrix elements [142], and has been used for inclusive calculations of Higgs boson production with jets [143, 144].

In contrast, our resummation of high-energy logarithms is based on the HEJ framework that we have outlined in Sec. 2.2. The calculation presented here is the first use of this approach for an inclusive single-jet process. As is necessary in the high-energy region, the all-order resummation includes the full effects of finite quark masses. We first review the formalism and derive the new building blocks required for leading-logarithmic resummation for Higgs boson plus jet production in Sec. 4.1. In Sec. 4.2, we compare our predictions to experimental measurements and propose observables tailored to the systematic analysis of high-energy corrections. We conclude in Sec. 4.3.

4.1 Higgs Boson plus Jets Production in the High Energy Limit

In the following, we discuss the general properties and structure of amplitudes in the high energy limit. We briefly summarise LL resummation in the HEJ framework and derive the new ingredients for the production of a Higgs boson together with a single jet by starting with a review of inclusive $H + 2j$ processes in HEJ.

4.1.1 $H+ \geq 2j$ Processes within HEJ

Generally, we are interested in the behaviour of amplitudes in the MRK limit, as defined in Eq. (2.1.1). We have explored in Sec. 2.2 the scaling of amplitudes in the MRK limit and plotted (squared) LO amplitudes for $ud \to ud$ and $ug \to us\overline{s}$ in Fig. 2.1 for specific phase space slices to explicitly demonstrate this scaling. The HEJ formalism has been used to describe inclusive $pp \to H + 2j$ production, and the construction of the LL calculation is well-documented [125, 141]. Here we summarise

the main points in order to frame the discussion of the new components calculated in the research presented in this thesis.

The LL configurations in pure QCD have the form $f_a f_b \to f_a \cdots f_b$, where f_a, f_b indicate the incoming parton flavours and the ellipsis denotes an arbitrary number of gluons. As in Sec. 2.2, the particles are written in order of increasing rapidity.

The production of an additional Higgs boson proceeds via an effective coupling to two or more gluons. Since invariant masses are large in the high-energy region, it is crucial that the exact dependence on the top quark mass is included in this effective coupling.

A final state Higgs boson with momentum $p_H = p_j$ at an intermediate rapidity y_j such that $y_{j-1} \ll y_j \ll y_{j+1}$ can then exchange t-channel gluons with the outgoing partons $j-1, j+1$. It was shown in ref. [125] that the scaling behaviour in Eq. (2.1.7) directly generalises when a Higgs boson is emitted in the middle of the quarks and gluons. Therefore, all configurations $f_a f_b \to f_a \cdots H \cdots f_b$ contribute at LL accuracy.

In the MRK limit the amplitudes are found to factorise into a neat product of simple functions. In the HEJ framework we cast these into the form:

$$\begin{aligned}\overline{\left|\mathcal{M}_{\texttt{HEJ}}^{f_a f_b \to f_a \cdots H \cdots f_b}\right|^2} = \mathcal{B}_{f_a,H,f_b}(p_a, p_b, p_1, p_n, q_j, q_{j+1}) \\ \cdot \prod_{\substack{i=1 \\ i\neq j}}^{n-2} \mathcal{V}(p_a, p_b, p_1, p_n, q_i, q_{i+1}) \\ \cdot \prod_{i=1}^{n-1} \mathcal{W}(q_i, y_i, y_{i+1}),\end{aligned} \tag{4.1.1}$$

for the modulus square of the matrix element, summed and averaged over helicities and colours. In this expression, p_a (p_b) is the incoming momentum along the positive (negative) z-direction and $p_1, \ldots, p_n$ are the outgoing momenta ordered in increasing rapidity. We illustrate this calculation in the schematic of Fig. 4.1. The t-channel momenta are given by:

$$q_1 = p_a - p_1, \qquad q_i = q_{i-1} - p_i \ \text{ for } i > 1. \tag{4.1.2}$$

At Born level, the right-hand side of Eq. (4.1.1) reduces to the function $\mathcal{B}_{f_a,H,f_b}$,

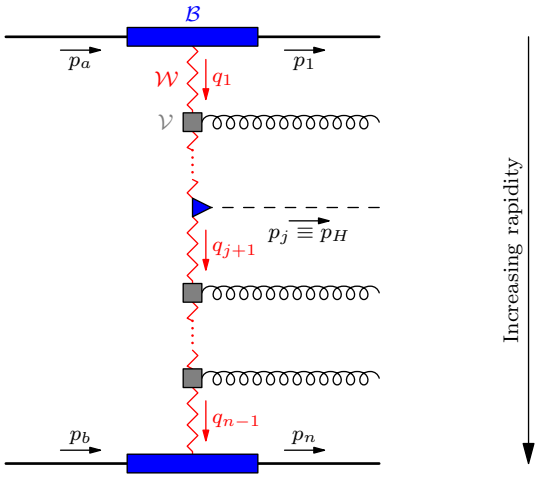

Figure 4.1: Structure of the matrix element for the process $f_a f_b \to f_a \cdots H \cdots f_b$, as obtained in the HEJ framework. This diagram is a representation of the calculation in Eq. (4.1.1).

described below. $\mathcal{V}$ comprises the real corrections due to the production of $n-3$ gluons in addition to f_a, f_b, and the Higgs boson. It is given by the contraction of two Lipatov vertices [125]:

$$\begin{aligned}\mathcal{V}(p_a,p_b,p_1,p_n,q_i,q_{i+1}) = &-\frac{C_A}{\hat{t}_i\hat{t}_{i+1}}V_\mu(p_a,p_b,p_1,p_n,q_i,q_{i+1})V^\mu(p_a,p_b,p_1,p_n,q_i,q_{i+1})\\ &-\frac{4C_A}{\mathbf{p}_{\perp i}^2}\Theta\left(-\mathbf{p}_{\perp i}^2+\lambda^2\right),\end{aligned} \tag{4.1.3}$$

where $V^\mu(p_a,p_b,p_1,p_n,q_i,q_{i+1})$ (with the full dependence restored) is given by Eq. (2.2.13), and $\hat{t}_i = q_i^2$. The second line of Eq. (4.1.3) includes the IR regularisation term that is added to the real corrections such that cancellation with IR divergences in the virtual corrections occurs at all orders. These all-order virtual corrections are encapsulated in the process-independent $\mathcal{W}$ functions, given by:

$$\begin{aligned}\mathcal{W}(q_i,y_i,y_{i+1}) &= \exp\left[\omega^0\left(q_i;\lambda^2\right)(y_{i+1}-y_i)\right],\\ \omega^0\left(q_i;\lambda^2\right) &= -\frac{\alpha_s C_A}{\pi}\log\left(\frac{q_{\perp i}^2}{\lambda^2}\right),\end{aligned} \tag{4.1.4}$$

as in the bottom two lines of the regularised, resummed HEJ amplitude of Eq. (2.2.21).

The process-dependent part of the amplitude is absorbed in the Born-level factor

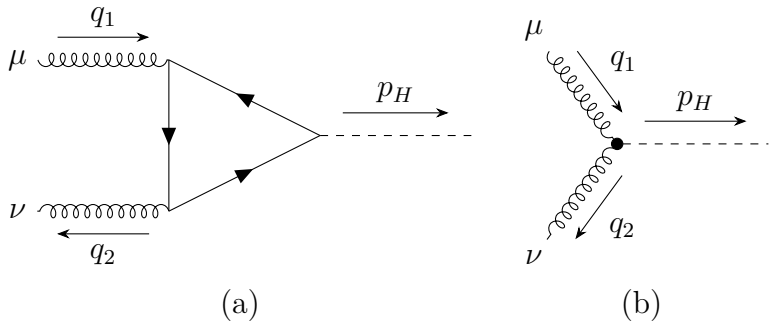

Figure 4.2: The GF interaction producing a Higgs boson as mediated by a massive quark loop (a) at high energies. At low energies/large distances, the assumption of infinite quark mass can be taken which produces the simpler effective vertex in (b).

given by:

$$\mathcal{B}_{f_a,H,f_b} = \frac{(4\pi\alpha_s)^{n-1}}{4(N_c^2-1)} \frac{K_{f_a}(p_1^-, p_a^-)}{\hat{t}_1} \frac{K_{f_b}(p_n^+, p_b^+)}{\hat{t}_{n-1}} \frac{\left\|S_{f_a f_b \to f_a H f_b}\right\|^2}{\hat{t}_j \hat{t}_{j+1}}. \tag{4.1.5}$$

Here, we use the colour acceleration multipliers K_f mentioned in Eq. (2.2.8), passing the lightcone components of the relevant momenta as arguments. The difference between incoming gluons and quarks/antiquarks is encoded completely in these multipliers. In general, these are given by:

$$K_g(x,y) = \frac{1}{2}\left(\frac{x}{y}+\frac{y}{x}\right)\left(C_A - \frac{1}{C_A}\right) + \frac{1}{C_A} \qquad f = g, \tag{4.1.6}$$

$$K_q(x,y) = C_F \qquad f \in \{q, \overline{q}\}. \tag{4.1.7}$$

Where we defined the sum over helicities of the contracted currents for $qQ \to qQ$ explicitly in Eq. (2.2.7), we now construct the analogous quantity for $f_a f_b \to f_a H f_b$:

$$\left\|S_{f_a f_b \to f_a H f_b}\right\|^2 = \sum_{\substack{\lambda_a=+,-\\ \lambda_b=+,-}} \left| j_\mu^{\lambda_a}(p_1,p_a) V_H^{\mu\nu}(q_j, q_{j+1}) j_\nu^{\lambda_b}(p_n, p_b)\right|^2. \tag{4.1.8}$$

Here, the vertex $V_H^{\mu\nu}$ is the Feynman rule for the coupling of two gluons to a single Higgs boson, mediated by a massive quark loop, as shown in Fig. 4.2. The full expression for this Feynman rule is listed in Appendix A, which borrows from the appendices of ref. [141]. The vertex rule can be evaluated with full quark mass dependence, and the contributions from all massive quarks summed. The

approximation that the top quark mass greatly exceeds all other scales gives rise to the effective vertex in Fig. 4.2(b), this is the *Higgs effective field theory* (HEFT). The inclusion of the full vertex in Eq. (4.1.1) then gives the correct finite quark mass contributions at LL for *any* number of final state partons/jets. Finally, the current j is given by:

$$j_\mu^\lambda(p,q) = \bar{u}^\lambda(p)\gamma_\mu u^\lambda(q). \tag{4.1.9}$$

In addition to the LL resummation discussed so far, gauge-invariant subsets of next-to-leading-logarithmic corrections originating from non-FKL configurations have also been included in `HEJ`. One source of NLL corrections are the configurations $qf_b \to Hq\cdots f_b$ and $f_aq \to f_a\cdots qH$, which only permit $n-2$ t-channel gluon exchanges instead of the $n-1$ exchanges found in LL configurations. In these cases, we adapt the matrix element for the corresponding LL configurations to a flipped rapidity order of outgoing quark/antiquark and Higgs boson. If the Higgs boson is emitted first (in rapidity ordering), we use Eq. (4.1.1) with $p_2 = p_H$ and exclude the virtual correction factor $\mathcal{W}$ for $i = 1$. In the other case of the Higgs boson being emitted last, we set $p_{n-1} = p_H$ and omit $\mathcal{W}$ for $i = n-1$.

A second class of non-FKL configurations arises for three or more produced jets, when the most backward or forward outgoing particle is a gluon, but the corresponding incoming parton is a quark or antiquark. These "unordered gluon" configurations, $qf_b \to gq\cdots H\cdots f_b$ and $f_aq \to f_a\cdots H\cdots qg$, allow one t-channel gluon exchange fewer than the corresponding FKL configurations in which the unordered gluon is swapped with the neighbouring quark/antiquark. Hence, they contribute at NLL accuracy. Without loss of generality, we consider the case where the unordered gluon is the most backward emitted particle. We denote the momentum of this gluon by p_g and the subsequent (in rapidity ordering) momenta by $p_1,\ldots,p_n$. The modulus square of the matrix element then has the same structure as in Eq. (4.1.1). The only differences are that the first t-channel momentum is now $q_1 = p_a - p_1 - p_g$ and that a different Born-level function $\mathcal{B}_{gq,H,f_b}$ (depending also on p_g) appears. For a derivation, and explicit expressions, see ref. [125].

4.1.2 Scaling of $H+ \geq 1j$ Amplitudes

To extend the formalism to the production of a Higgs boson with a single jet we first need to identify the LL configurations, and demonstrate the MRK scaling of amplitudes as in Fig. 2.1, and then derive the corresponding resummed matrix elements.

So far, we have only considered LL configurations in which both the most backward and the most forward outgoing particle is a parton. We can use Eq. (2.1.7) to explore the MRK limit of the amplitudes. The amplitude for the process $gq \to Hq$ should scale as $\mathcal{M} \sim \hat{s}_{Hq}$, as there is a gluon exchange (i.e. a spin-1 exchange) in the t-channel. Similarly, the process $gg \to Hg$ corresponds to $\mathcal{M} \sim \hat{s}_{Hg}$. For Higgs boson plus dijet production, the same argument allows us to establish that $gq \to Hgq$ scales as $\mathcal{M} \sim \hat{s}_{Hg}\hat{s}_{gq}$. All of these configurations therefore contribute at LL accuracy. This is no longer the case if, for example, outgoing parton flavours are rearranged: $gq \to Hqg$ scales as $\mathcal{M} \sim \hat{s}_{Hq}\hat{s}_{qg}^{1/2}$.

Note that these scalings are valid whether we consider the full LO amplitude (with the Higgs-gluon-gluon interaction mediated by massive quark loops) or in HEFT — with an infinite top mass m_t — as shown in Fig. 4.3. These plots were produced with LO amplitudes from MadGraph5_aMC@NLO [5] evaluated in a one-dimensional phase space slice. The remaining degree of freedom is the (equidistant) separation between all neighbouring pairs of particles in rapidity. For consistency, the scaling of the full LO result in the limit of large top mass is plotted against the HEFT result. We compare to the LO truncation of the all-order `HEJ` amplitudes, anticipating their derivation from the high energy scaling which we detail in Sec. 4.1.3.

The momentum configurations explored in Fig. 4.3 are summarised in Table 4.1. We emphasise that the behaviour shown is not dependent on specific values of azimuthal angle or transverse momentum, but only on the rapidity assignment of the particles, due to the fact we only explore the amplitudes in single-dimensional slices of phase space.

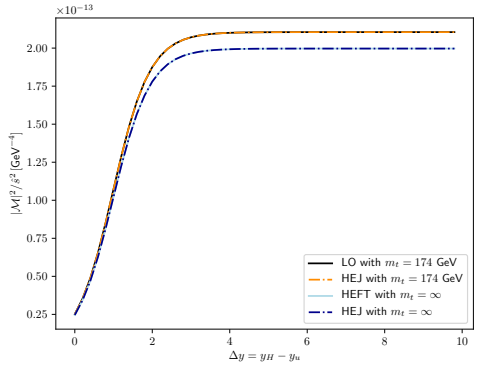

(a) $|\mathcal{M}|^2/\hat{s}^2$ for the process $gu \to Hu$

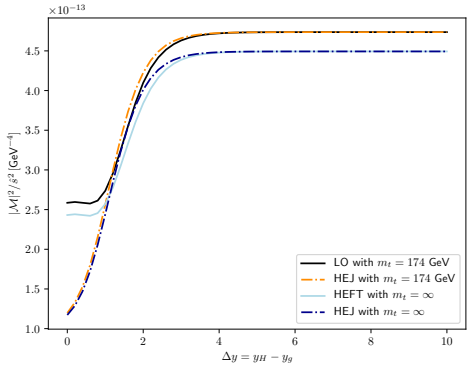

(b) $|\mathcal{M}|^2/\hat{s}^2$ for the process $gg \to Hg$

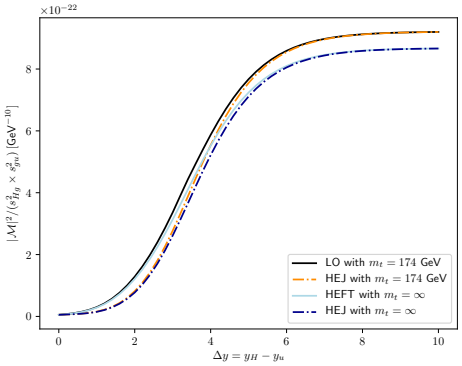

(c) $|\mathcal{M}|^2/(\hat{s}^2_{Hg} \times \hat{s}^2_{gu})$ for the process $gu \to Hgu$

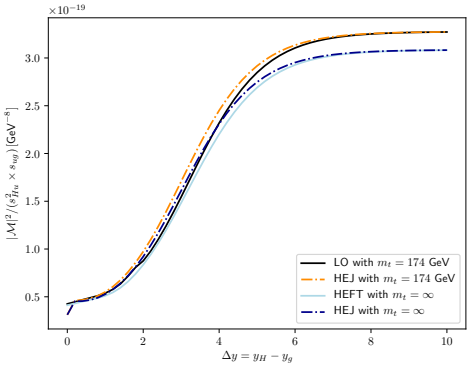

(d) $|\mathcal{M}|^2/(\hat{s}^2_{Hu} \times \hat{s}_{ug})$ for the process $gu \to Hug$

Figure 4.3: Verifying the Regge scaling of the squared LO matrix elements, as in Eq. (2.1.7), for four different processes, indicated in the subcaptions for each figure. The MRK limit is approached as Δy becomes large. Final states are understood to be ordered in rapidity as listed. The phase space configurations used in each plot are shown in Table 4.1.

4.1.3 New Components for $H+ \geq 1j$ and an Outer Higgs Boson

In Sec. 4.1.2 we discussed the factorisation of LL amplitudes for $f_a f_b \to f_a \cdots H \cdots f_b$ into a Born-level function $\mathcal{B}$, a product over real emission vertices $\mathcal{V}$, and a product of virtual corrections $\mathcal{W}$. The same type of factorisation holds for LL configurations with the Higgs boson as the most forward or backward outgoing particle. The virtual corrections are the same as given in Eq. (4.1.1) due to the process-independence of the Lipatov ansatz. To derive the remaining factors, we first analyse the Born-level process $g f_b \to H f_b$ and then consider real corrections.

Process	Phase space slice configuration
$gq \to Hq$	$\begin{cases} y_q = -\Delta \text{ and } y_H = \Delta \\ \phi_q = \frac{\pi}{4} \\ p_{\perp q} = 40\,\text{GeV} \end{cases}$
$gg \to Hg$	$\begin{cases} y_g = -\Delta \text{ and } y_H = \Delta \\ \phi_g = \frac{\pi}{4} \\ p_{\perp g} = 40\,\text{GeV} \end{cases}$
$gq \to Hgq$	$\begin{cases} y_q = -\Delta, y_g = 0 \text{ and } y_H = \Delta \\ \phi_g = \frac{\pi}{2} \text{ and } \phi_q = -\frac{\pi}{3} \\ p_{\perp g} = k_{\perp q} = 40\,\text{GeV} \end{cases}$
$gq \to Hqg$	$\begin{cases} y_g = -\Delta, y_q = 0 \text{ and } y_H = \Delta \\ \phi_g = -\frac{\pi}{2} \text{ and } \phi_q = \frac{\pi}{3} \\ p_{\perp g} = k_{\perp q} = 40\,\text{GeV} \end{cases}$

Table 4.1: The momentum configurations used to generate the phase space explorer plots in Fig. 4.3.

Higgs Current

The Born-level function $\mathcal{B}_{H,f_b}$ for the process $gf_b \to H \cdots f_b$ is obtained by deriving a t-channel factorised form analogous to Eq. (4.1.5) from the modulus square of the Born-level amplitude in the MRK limit. For $gq \to Hq$, the tree-level amplitude is determined by a single diagram, depicted in Fig. 4.4.

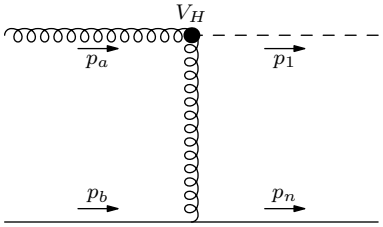

Figure 4.4: The tree-level diagram for the process $gq \to Hq$. The straight solid line denotes an arbitrary light quark or antiquark.

Without requiring any approximations we obtain the factorised expression:

$$\mathcal{B}_{H,f_b} = \frac{(4\pi\alpha_s)^{n-1}}{4(N_c^2-1)}\frac{1}{t_1}\frac{K_{f_b}(p_n^+, p_b^+)}{t_{n-1}}\left\|S_{gf_b\to Hf_b}\right\|^2, \tag{4.1.10}$$

$$\left\|S_{gf_b\to Hf_b}\right\|^2 = \sum_{\substack{\lambda_a=+,-\\ \lambda_b=+,-}} \left|\epsilon_\mu^{\lambda_a}(p_a)\; V_H^{\mu\nu}(p_a, p_a - p_1)\; j_\nu^{\lambda_b}(p_n, p_b)\right|^2, \tag{4.1.11}$$

for $f_b = q$, where $\epsilon^{\lambda_a}(p_a)$ is the polarisation vector of the incoming gluon. This

is plotted along with the exact LO results from MadGraph5_aMC@NLO [5] in Fig. 4.3(a), showing exact agreement between HEJ and LO for finite top quark mass and in HEFT. In the MRK limit, this formula also holds for $f_b = g$, which is shown in Fig. 4.3(b). In this case there is some approximation away from the limit, but very quickly the LO and HEJ lines converge as Δy increases.

Lipatov Vertex for Additional Gluon Emission

In Sec. 4.1.1, we described the simple factorised structure of amplitudes within the MRK limit and nearby limits. Not only are the different components independent of momenta in different parts of the chain, they are independent of the particle content of the rest of the chain. This should mean that the Lipatov vertex derived in pure QCD processes for additional gluons still applies. However, the Lorentz and colour structure of the "Higgs current" $j_H^\nu = \epsilon_\mu V_H^{\mu\nu}$ differ compared to pure QCD processes, therefore it is important to verify that this is indeed the case.

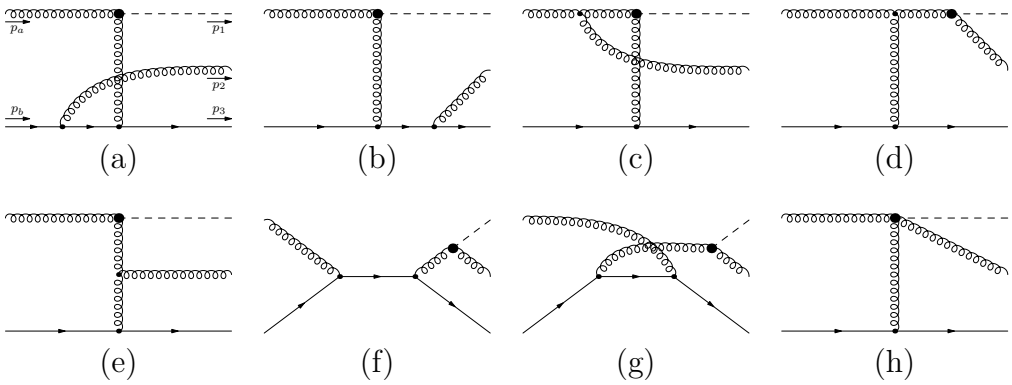

Figure 4.5: The eight LO diagrams which contribute to the process in Eq. (4.1.12).

We will consider the process:

$$g(p_a)q(p_b) \to H(p_1)g(p_2)q(p_3), \tag{4.1.12}$$

in the MRK limit $y_1 \ll y_2 \ll y_3$. There are eight LO diagrams, as shown in Fig. 4.5. Compact expressions for tree-level Higgs plus four-parton colour-ordered amplitudes appear in ref. [145, 146]. Setting $q_1 = p_a - p_1$ and $q_2 = p_3 - p_b$, the HEJ amplitude is

given by:

$$\mathcal{M}_{\texttt{HEJ}} = ig_s^2 f^{2ea} t^{e,3b} \frac{\bar{u}(p_3)\gamma^\nu u(p_b)}{q_1^2 q_2^2} V^\alpha(p_a, p_b, p_a, p_3, q_1, q_2) V_H^{\mu\nu}(p_a, q_1)\, \varepsilon_\mu(p_a)\varepsilon_\alpha(p_2)^*. \tag{4.1.13}$$

As the outer particle is no longer colour-charged, the third argument of the Lipatov vertex (with full dependence restored) entering in Eq. (4.1.3) is now p_a instead of p_1. The colour factor of the HEJ amplitude may be rewritten:

$$if^{2ea}t^{e,3b} = (t^a t^2)^{3b} - (t^2 t^a)^{3b}. \tag{4.1.14}$$

We can then directly compare Eq. (4.1.13) with the MRK limit of Eq. (26) and Eq. (27) in ref. [146], and we find agreement at LL up to an unphysical phase. Specifically, the LL term in the MRK and infinite top quark mass limit of Eq. (4.1.13) is given by:

$$g_s^2 \left(\frac{\alpha_s}{3\pi v}\right) if^{2ea}t^{e,3b} \frac{\langle 3a\rangle[ab]}{|p_{\perp 2}||p_{\perp 3}|} \to g_s^2 \left(\frac{\alpha_s}{3\pi v}\right) if^{2ea}t^{e,3b} \frac{\hat{s}}{|p_{\perp 2}||p_{\perp 3}|}, \tag{4.1.15}$$

where the angle and square brackets are Lorentz-invariant kinematic factors defined by:

$$\langle ij\rangle = \bar{u}(p_i)P_R u(p_j), \quad [ij] = \bar{u}(p_i)P_L u(p_j). \tag{4.1.16}$$

This resembles the form introduced in Eq. (1.3.17) with the left and right projection operators acting explicitly on the spinor states.

Matrix element including additional gluons

We can now use these results to form the analogue of Eq. (4.1.1) for the process $gf_b \to H \cdots f_b$

$$\begin{aligned}\overline{\left|\mathcal{M}_{\texttt{HEJ}}^{gf_b\to H\cdots f_b}\right|}^2 = {} & \mathcal{B}_{H,f_b}(p_a, p_b, p_1, p_n) \\ & \cdot \prod_{i=1}^{n-2} \mathcal{V}(p_a, p_b, p_a, p_n, q_i, q_{i+1}) \\ & \cdot \prod_{i=1}^{n-1} \mathcal{W}(q_i, y_i, y_{i+1}),\end{aligned} \tag{4.1.17}$$

where the only differences to Eq. (4.1.1) are the Born-level function $\mathcal{B}_{H,f_b}(p_a, p_b, p_1, p_n)$ given in Eq. (4.1.10) and the third argument of the real correction function $\mathcal{V}$. We illustrate that this gives the correct behaviour in the MRK limit in Fig. 4.3(c) for the processes $gu \to Hgu$, and in Fig. 4.3(d) we show that we obtain the correct limiting behaviour for the NLL configuration from a peripheral Higgs emission, $gu \to Hug$.

4.2 Predictions and Comparison to Data

In this section we compare predictions for Higgs boson production in association with one or more jets obtained with `HEJ` to those of fixed next-to-leading-order perturbation theory and to experimental analyses. The analyses are implemented in Rivet [120] and relate to data collected at the LHC operated at both 13 TeV [14, 15] and 8 TeV [16].

In our predictions, `Sherpa` [62] is used to generate leading-order events with the Comix [70] matrix element generator and OpenLoops [71, 147] (for evaluation of loop integrals) for $H + n$ jets, where $n = 1, \ldots, 5$. We include the exact dependence on the top quark mass where available (i.e. for $n = 1, 2$), and for higher multiplicities we use the simpler results valid for an infinite top mass. High energy resummation is then applied using the method of `HEJ`, described in detail in Sec. 2.2.4 and in ref. [97]. This takes the fixed-order events as input and then produces the all-order corrections (real and virtual) corresponding to each Born phase space point. The resulting resummation events are reweighted by:

$$\frac{|\mathcal{M}_{\texttt{HEJ}}(m_t, m_b)|^2}{|\mathcal{M}_{\text{LO, }\texttt{HEJ}}(m_t, 0)|^2} \qquad \leq 2 \text{ jets}, \tag{4.2.1}$$

$$\frac{|\mathcal{M}_{\texttt{HEJ}}(m_t, m_b)|^2}{|\mathcal{M}_{\text{LO, }\texttt{HEJ}}(\infty, 0)|^2} \qquad > 2 \text{ jets}. \tag{4.2.2}$$

$\mathcal{M}_{\texttt{HEJ}}(m_t, m_b)$ is the `HEJ` all-order matrix element discussed in Eq. (4.1.17), where we have indicated the dependence on the top quark mass m_t and the bottom quark mass m_b. Where these are not set to zero or infinity, the quantities indicate their Standard Model values, i.e. $m_t = 174$ GeV and $m_b = 4.7$ GeV. We denote the leading-

order truncation of the HEJ matrix element by $\mathcal{M}_{\text{LO, HEJ}}(m_t, m_b)$. The $p_\perp$-sampling for the LO events used for the matching extends slightly beyond the cuts used in the analysis, as required by the mapping between the high-multiplicity m-body resummation phase space point and the n-parton ($n < m$) phase space point of the matching. This ensures the full resummation phase space is properly explored, since the momentum reshuffling in HEJ (after soft gluon emissions are added) modifies the momenta relative to the LO input, meaning that Born jets softer than the analysis $p_\perp$ cutoff can map to resummation events with all jets harder than the cutoff. We discussed this effect in Sec. 2.2.4, when outlining the momentum reshuffling in Eq. (2.2.25).

Sherpa and OpenLoops are used to provide NLO 1-jet and 2-jet predictions in the infinite top quark mass limit without resummation, for comparisons with HEJ and the experimental data. The cross sections presented from HEJ are further matched to NLO by multiplying the inclusive 1-jet (2-jet) distributions by the ratio of the inclusive 1-jet (2-jet) cross section at NLO and the inclusive 1-jet (2-jet) cross section of HEJ expanded to NLO. Since the HEJ cross sections we discussed in Sec. 2.2 observe order-by-order cancellation of infrared divergences, we may truncate the HEJ all-orders expression at arbitrary order to obtain an approximation for the HEJ cross section at that order. Reweighting predictions in this way changes the normalisation of distributions, and reduces the width of the theoretical uncertainty estimates obtained by varying the renormalisation and factorisation scales. Differential cross sections for inclusive one- and two-jet observables $\mathcal{O}$ are reweighted according to:

$$\frac{\mathrm{d}\sigma_{\text{HEJ},nj}}{\mathrm{d}\mathcal{O}} \to \frac{\sigma_{\text{NLO},nj}}{\sigma_{\text{HEJ@NLO},nj}} \frac{\mathrm{d}\sigma_{\text{HEJ},nj}}{\mathrm{d}\mathcal{O}}, \tag{4.2.3}$$

where $\sigma_{\text{NLO},nj}$ ($n = 1, 2$) denotes the inclusive n-jet cross section at NLO, and $\sigma_{\text{HEJ@NLO},nj}$ the corresponding HEJ prediction (expanded to NLO) for the inclusive n-jet cross section. Note that the exclusive components of the cross section with three or more jets as predicted by HEJ are technically matched only at Born-level, but since they form part of the inclusive one and two-jet observables, their contribution

is scaled by the relevant ratio in Eq. (4.2.3).

For the analyses we consider in this section, the NLO matching factors used to rescale the HEJ predictions are shown in Table. 4.2.

Analysis	$\sqrt{s} = 8$ TeV			$\sqrt{s} = 13$ TeV		
Scale	μ_F, μ_R	$(\mu_F, \mu_R)/2$	$2(\mu_F, \mu_R)$	μ_F, μ_R	$(\mu_F, \mu_R)/2$	$2(\mu_F, \mu_R)$
1j factor	1.87	1.54	2.15	1.59	1.30	1.84
2j factor	1.98	1.48	2.40	1.62	1.19	2.00

Table 4.2: HEJ NLO Reweighting factors with $\mu_F = \mu_R = \max(m_{12}, m_H)$, calculated as given by Eq. (4.2.3).

We use the NNPDF30@NNLO [148] PDF set provided from the LHAPDF collaboration [123] for HEJ and NLO predictions, with the central scale choice $\mu_F = \mu_R = \max(m_{12}, m_H)$ (where m_{12} is the invariant mass between the two hardest jets, and set to $m_{12} = 0$ for 1-jet events). In order to gauge the scale dependence of the predictions the scales are varied independently by a factor of two, excluding combinations where μ_F and μ_R differ by a factor of more than two. This is the procedure described in Sec. 1.3. The shaded regions in the figures below indicate the theoretical uncertainty envelope formed by these scale variations.

We produced predictions with an alternative central scale choice $\mu_F = \mu_R = H_T/2$ to investigate the stability of the predictions at different scales and of the estimate of theoretical uncertainties. The predictions differ minimally with this scale compared to the custom scale choice above and so are not presented here.

4.2.1 Predictions for $\sqrt{s} = 13$ TeV and Comparison to Data

In this section we present predictions for a CMS analysis [14, 15] at CoM energy $\sqrt{s} = 13$ TeV, and for additional distributions showcasing differences between HEJ and fixed-order predictions at NLO. The CMS study explored distributions for Higgs boson production (and decay in the diphoton channel) both inclusively and in association with one jet.

The baseline cuts related to the photons and the jets are listed in Table 4.3 (see

refs. [14, 15] for a full discussion). The pseudorapidity jet cuts are specific to the observables studied and are listed in Table 4.4. Jets are reconstructed with the anti-$k_\perp$ [52] jet algorithm with $R = 0.4$.

Description	Baseline cuts
Leading photon transverse momentum	$p_{\perp\gamma_1} > 30$ GeV
Subleading photon transverse momentum	$p_{\perp\gamma_2} > 18$ GeV
Diphoton invariant mass	$m_{\gamma\gamma} > 90$ GeV
Pseudorapidity of the photons	$\lvert\eta_\gamma\rvert < 2.5$ excluding $1.4442 < \lvert\eta_\gamma\rvert < 1.566$
Ratio of harder photon $p_\perp$ to diphoton invariant mass	$p_{\perp\gamma_1}/m_{\gamma\gamma} > \frac{1}{3}$
Ratio of softer photon $p_\perp$ to diphoton invariant mass	$p_{\perp\gamma_2}/m_{\gamma\gamma} > \frac{1}{4}$
Photon isolation cut	$\mathrm{Iso}^{\gamma}_{\mathrm{gen}} < 10$ GeV
Jet transverse momentum	$p_{\perp j} > 30$ GeV

Table 4.3: Baseline photon and jet cuts of the 13 TeV analysis, following the CMS analysis of [14, 15]. $\mathrm{Iso}^{\gamma}_{\mathrm{gen}}$ denotes the sum of transverse energies of stable particles in a cone of radius $\Delta R = 0.3$ around each photon.

Observable	Pseudorapidity jet cut
Number of jets N_{jets}, Fig. 4.6, left	$\lvert\eta_j\rvert < 2.5$ (all jets)
$\lvert p_{\perp j_1}\rvert$, Fig. 4.6, right	$\lvert\eta_{j_1}\rvert < 2.5$ (hardest jet) and $\lvert\eta_j\rvert < 4.7$ (other jets)
$\min m_{ff}$, Fig. 4.7, left	$\lvert\eta_{j_1}\rvert < 2.5$ (hardest jet) and $\lvert\eta_j\rvert < 4.7$ (other jets)
$\max m_{ff}$, Fig. 4.7, right	$\lvert\eta_{j_1}\rvert < 2.5$ (hardest jet) and $\lvert\eta_j\rvert < 4.7$ (other jets)
$\max \Delta y_{ff}$, Fig. 4.8, left	$\lvert\eta_{j_1}\rvert < 2.5$ (hardest jet) and $\lvert\eta_j\rvert < 4.7$ (other jets)
$\max \Delta y(H, j)$, Fig. 4.8, right	$\lvert\eta_{j_1}\rvert < 2.5$ (hardest jet) and $\lvert\eta_j\rvert < 4.7$ (other jets)

Table 4.4: Pseudorapidity jet cuts used for the 13 TeV analysis observables presented in this section, following the CMS analysis of [14, 15].

The `HEJ` and NLO QCD predictions only describe $pp \to H + n$-jet processes via gluon fusion where the jets consist of light quarks and gluons. The data includes a non-GF contribution from electroweak VBF, VH and $t\bar{t}H$ processes, labelled together as HX in the experimental papers. We have extracted the value of this component from the experimental papers for the rest of this section, and added it to both the `HEJ` and NLO QCD predictions, where possible. This is indicated with "+HX" in the legend. Since `HEJ` does not include a description of these effects, there is no double-counting in adding the contributions to our predictions.

The left plot of Fig. 4.6 shows the exclusive n-jet cross sections, with the 1-jet and

2-jet HEJ predictions rescaled as described in Eq. (4.2.3). The fixed-order predictions are limited to 2 jets at NLO and 3 jets at LO, whereas HEJ allows us to make predictions for the $\geq$ 4-jet bin and reasonable agreement is achieved throughout.

In Fig. 4.6, the distribution of the cross section in the transverse momentum of the hardest jet is displayed in the right plot. We have compared to data from ref. [15] here rather than ref. [14] as the data in the former covers a wider range of transverse momenta. The discrepancy between NLO and HEJ predictions as the transverse momentum increases is due to high energy logarithms resummed by HEJ as well as the inclusion of finite mass effects. Similar differences between NLO and HEJ matched to NLO have also been observed for W+jets processes [87]. The effect is more pronounced for larger values of $p_\perp$, however the collected data does not probe these regions of phase space. In harder transverse momentum spectra, for $H+ \geq 2j$ processes in HEJ, a greater sensitivity to the effects of using finite top and bottom quark masses can be observed. This is most clearly demonstrated in ref. [141] for the transverse momentum distribution of the Higgs.

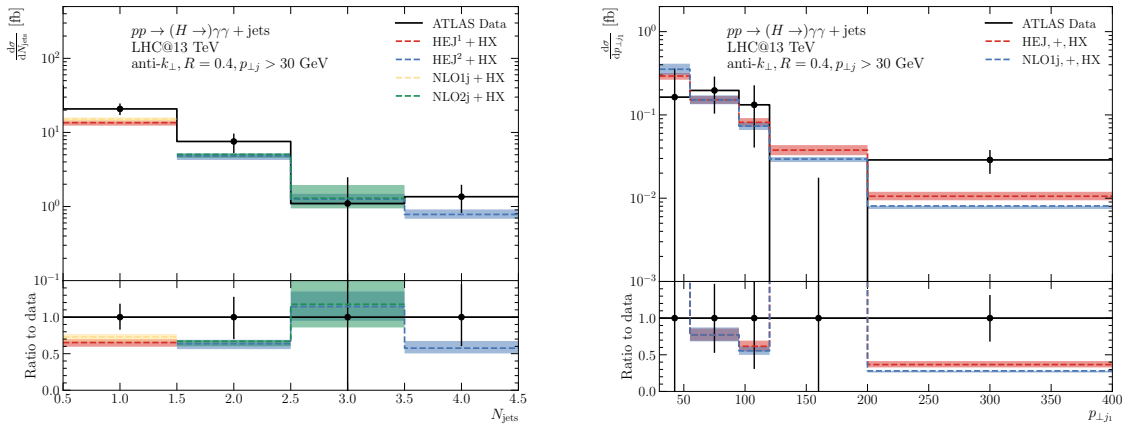

Figure 4.6: The integrated cross section distributed against exclusive jet count (left), compared to CMS data from ref. [14], and the distribution of leading jet transverse momentum (right), compared to CMS data [15]. Both analyses apply the cuts described in Table 4.3. The "HX" component is extracted from those publications.

The distribution of the cross section in the minimum rapidity separation between any two particles in the final state is shown in Fig. 4.7(a). As the Higgs boson forms

part of the final states, this is an inclusive one-jet observable, and the NLO one-jet predictions are shown for comparison and used to rescale the HEJ predictions. This observable is very sensitive to high-energy logarithmic corrections. As was observed in previous studies (see ref. [141]), the effect of the resummation is to reduce the HEJ prediction compared to fixed-order, by as much as 50% at large values. Figure 4.7(b) shows the distribution of the cross section in the maximum invariant mass between any two particles in the final state. This is related to the high energy limit where all pairwise invariant masses are taken to be large, but also includes configurations where two or more particles have a small invariant mass. The impact of the logarithmic corrections is not as strong here, and the fixed-order and resummed predictions agree within uncertainties. In both distributions displayed in Fig. 4.7, no "HX" component is added to the HEJ predictions or the NLO predictions.

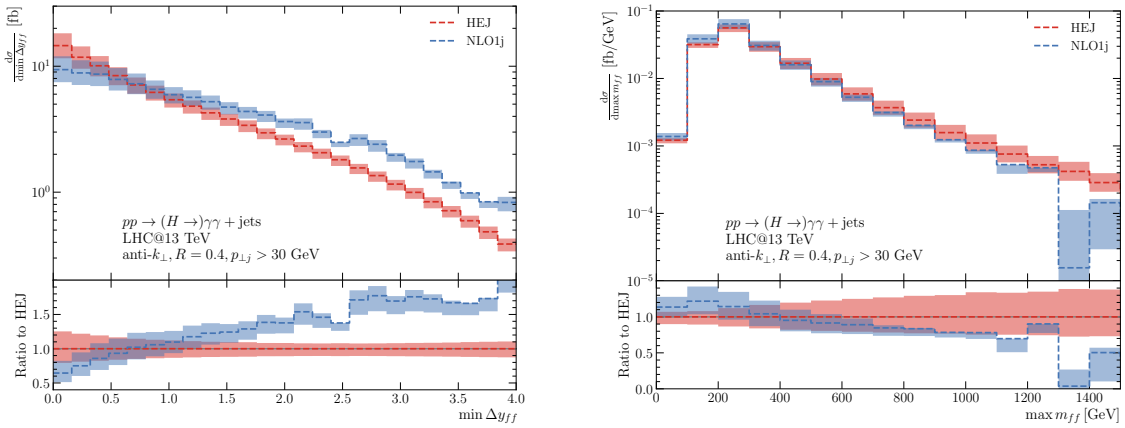

Figure 4.7: Distributions sensitive to high energy effects. In the left plot is plotted the minimum rapidity separation between any two outgoing particles (Higgs boson or jets) and in the right plot the maximum invariant mass between any two outgoing particles (Higgs or jets). Since these are inclusive single-jet observables, HEJ results are rescaled by the inclusive cross section ratio $\sigma_{\text{NLO},1j}/\sigma_{\texttt{HEJ@NLO},1j}$.

We further display the QCD component of the 13 TeV prediction in distributions that emphasise the high energy treatment of the Higgs boson analogously to a parton in the scaling of matrix elements (as in Fig. 4.3). In Fig. 4.8 are plotted the distribution of the cross section in the maximum rapidity difference between any final state particles, and between the Higgs boson and any jet, with predictions from

HEJ and NLO $H + 1j$. Only GF contributions are shown, with no "HX" component added.

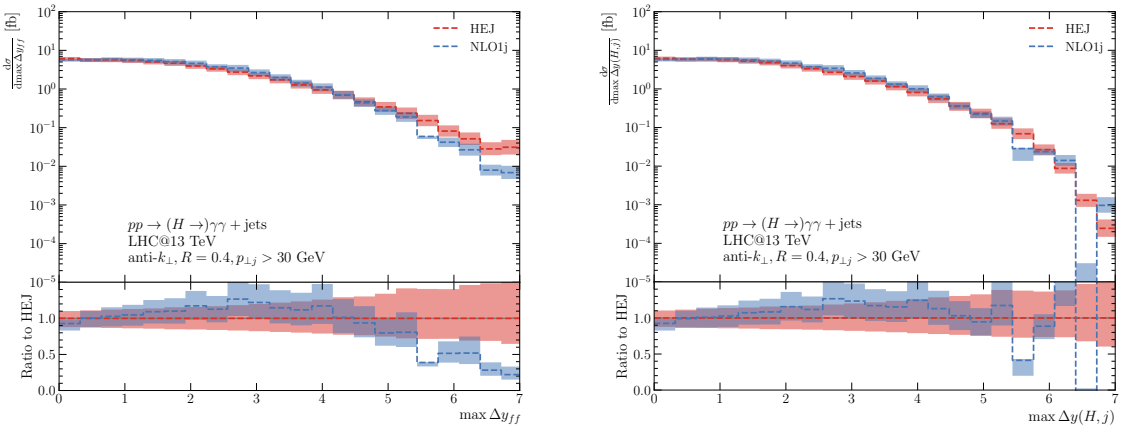

Figure 4.8: Distributions sensitive to high energy effects. In the left plot is plotted the maximum rapidity separation between any two outgoing particles (Higgs boson or jets) and in the right plot the maximum rapidity difference between the Higgs boson and any jet. Since these are inclusive single-jet observables, HEJ results are rescaled by the inclusive cross section ratio $\sigma_{\text{NLO},1j}/\sigma_{\texttt{HEJ@NLO},1j}$.

For rapidity differences of up to ~ 4.5, stellar agreement between the HEJ and NLO descriptions is demonstrated for both $\max \Delta y_{ff}$ and $\max \Delta y(H, j)$. Similarly, the distributions for both observables display similar forms across both theoretical predictions, motivating the treatment of the Higgs boson analogously to a parton in the high energy approach. For large $\max \Delta y(H, j)$, the differential cross section is reduced, compared to that at similar values of $\max \Delta y_{ff}$ as predicted by HEJ. This demonstrates that configurations with the Higgs boson extremal in rapidity are subleading in the high energy logarithms in this regime, at the distribution level. The treatment in HEJ produces a stable description of such observables and demonstrates the required precision for predictions of the GF background with a robust accounting of the high energy effects present.

4.2.2 Predictions for $\sqrt{s} = 8$ TeV and Comparison to Data

We now present predictions for the ATLAS analysis of inclusive Higgs production at CoM energy $\sqrt{s} = 8$ TeV of ref. [16], as implemented in Rivet [120]. We list the

relevant experimental cuts used in this analysis in Table 4.5, the complete list being available in the experimental publication. As with the experimental analysis, the jets are reconstructed with the anti-$k_\perp$ algorithm with a radius parameter of $R = 0.4$. The experimental study ref. [16] explored the inclusive and differential cross sections for Higgs boson production in the diphoton decay channel. For our purposes, we select the observables which correspond to Higgs boson production plus at least one jet, where our predictions are applicable.

Description	Baseline cuts
Photon transverse momentum	$p_{\perp\gamma} > 25$ GeV
Diphoton invariant mass	105 GeV $< m_{\gamma\gamma} <$ 160 GeV
Pseudorapidity of the photons	$\lvert\eta_\gamma\rvert < 2.37$ excluding $1.37 < \lvert\eta_\gamma\rvert < 1.56$
Ratio of harder photon $p_\perp$ to diphoton invariant mass	$p_{\perp\gamma_1}/m_{\gamma\gamma} > 0.35$
Ratio of softer photon $p_\perp$ to diphoton invariant mass	$p_{\perp\gamma_2}/m_{\gamma\gamma} > 0.25$
Photon isolation cut	$\mathrm{Iso}^{\gamma}_{\mathrm{gen}} < 14$ GeV
Jet transverse momentum	$p_{\perp j} > 30$ GeV
Jet rapidity	$\lvert y_j\rvert < 4.4$

Table 4.5: Baseline cuts of the 8 TeV inclusive Higgs production analysis, following the ATLAS cuts in ref. [16]. $\mathrm{Iso}^{\gamma}_{\mathrm{gen}}$ denotes the sum of transverse energies of stable particles in a cone of radius $\Delta R = 0.4$ around each photon.

We divide our results into 1-jet observables, i.e. containing at least one jet, where the new components of `HEJ` as detailed in Sec. 4.1.2 can be tested, and 2-jet observables. As for the 13 TeV results previously shown, the experimental data include a non-GF contribution. We have extracted this "HX" component from ref. [16] where available and added it to our GF predictions.

$H+ \geq 1j$ observables

In Fig. 4.9(a), we show the integrated cross section against the exclusive number of jets. As was evidenced from the 13 TeV analysis, the differences between fixed-order and resummed predictions are limited after the inclusive cross sections are rescaled. For the NLO and `HEJ` 1- and 2-jet rates the theoretical uncertainty estimate bands overlap with the experimental error on the data. The higher jet multiplicity

($\geq 3j$) cross sections are lower as predicted both with HEJ and at NLO than for the experimental data.

In Fig. 4.9(b), the distribution of the cross section in the rapidity of the leading jet is displayed. The discrepancy between the fixed-order and the resummed predictions increases as the rapidity of the jet increases. This is a high energy effect since the corrections in $\hat{s}/|p_\perp|^2$ are sizeable in this region of phase-space, and previous studies (e.g. ref [141]) showed little dependence on the inclusion of the finite quark mass effects on this observable. However, this is not the case for the transverse momentum of the Higgs boson, for which the distribution is plotted in Fig. 4.9(c). The finite quark mass effects and the resummation lead to a hardening of the large-$p_\perp$ tail of the Higgs boson. The difference would be yet more pronounced for larger transverse momentum. Since the phase space probed in the experimental analysis focuses around softer transverse momenta ($p_\perp < 140$ GeV), HEJ and fixed-order predictions for the hardest jet transverse momentum, whose distribution is plotted in Fig. 4.9(d), are difficult to discern from each other.

The high energy-sensitive observables plotted in Fig. 4.10 are similarly distributed to those at 13 TeV (Fig. 4.7) since the phase space explored in these regions includes regions where high energy and finite quark mass effects become important as we noted in Sec. 4.2.1. This is demonstrated by the wide discrepancy between HEJ and NLO, of roughly 50%, for large values of $\min \Delta y_{ff}$.

$H+ \geq 2j$ observables

We produce predictions now for $H+ \geq 2j$ observables, including comparisons to experimental data and explorations of observables sensitive to high energy perturbative effects. These are displayed in Figs. 4.11-4.12. The impact of the resummation on high energy-sensitive observables is to reduce the observed rates compared to fixed-order approaches, as can be seen for wide dijet rapidity separation in Fig. 4.11(a), large rapidity values of the second-hardest jet in Fig. 4.11(b) and for large dijet invariant mass in Fig. 4.11(c). As expected, the resummation has little impact on

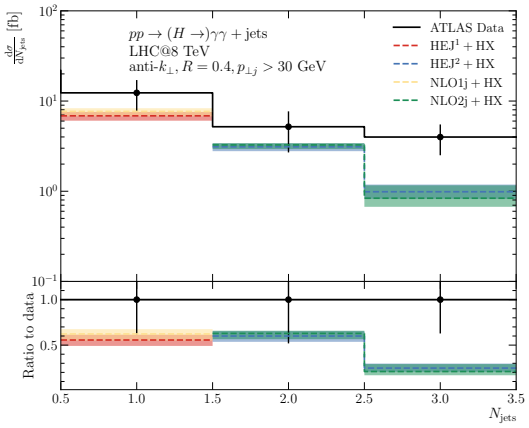

(a) Exclusive jet multiplicity.

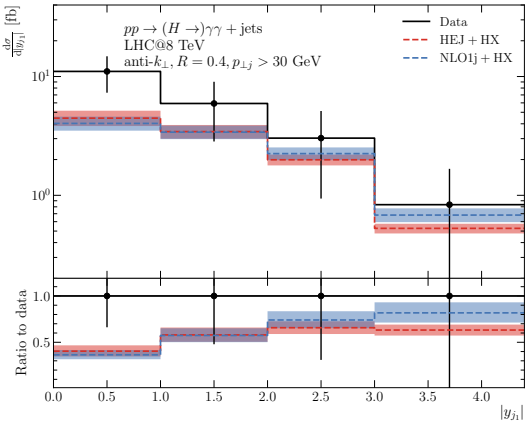

(b) Leading jet rapidity

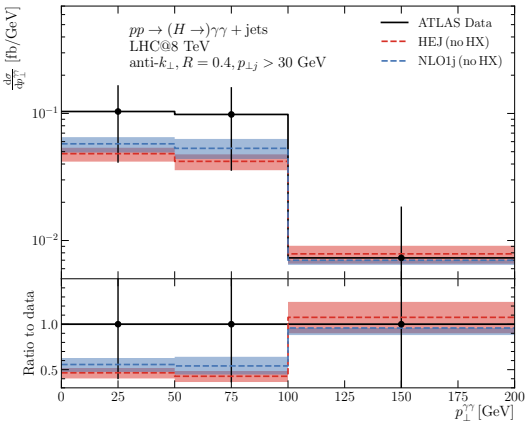

(c) $p_\perp$ of the Higgs boson, $N_{\text{jets}} = 1$

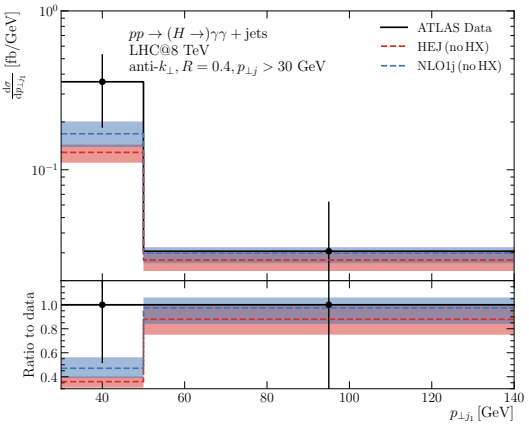

(d) Leading jet $p_\perp$, $N_{\text{jets}} = 1$

Figure 4.9: Integrated and differential cross sections against single- and multi-jet observables. The 1-jet HEJ predictions are rescaled by the inclusive cross section ratio $\sigma_{\text{NLO},1j}/\sigma_{\texttt{HEJ@NLO},1j}$ while the HEJ predictions of the 2- and 3-jet bins of (a) are rescaled by $\sigma_{\text{NLO},2j}/\sigma_{\texttt{HEJ@NLO},2j}$. In (a) and (b), the "HX" component is extracted from ref. [16]. The "HX" component was not available for (c) and (d).

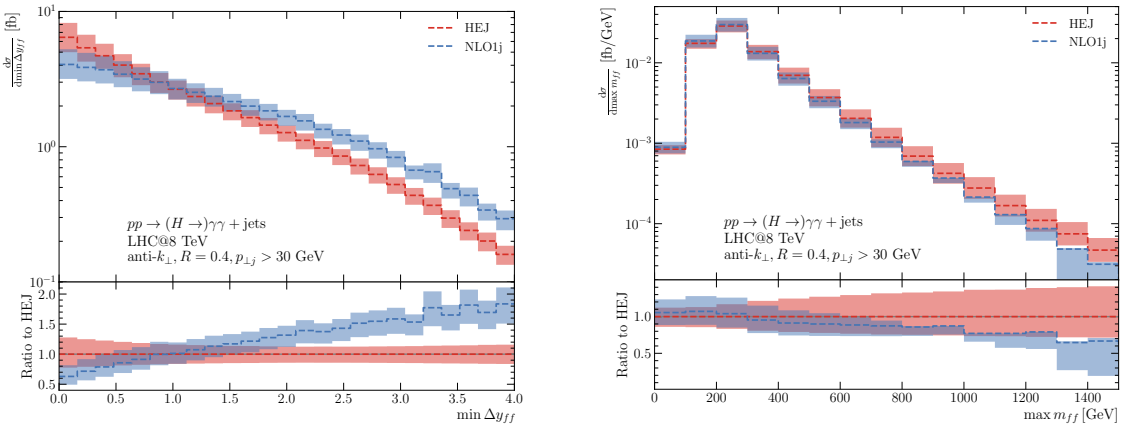

Figure 4.10: High energy-sensitive 1-jet distributions. (a): minimum rapidity separation between any two outgoing particles (Higgs boson or jets). (b): maximum invariant mass between any two outgoing particles (Higgs boson or jets). HEJ results are rescaled by the inclusive cross section ratio $\sigma_{\text{NLO},1j}/\sigma_{\texttt{HEJ@NLO},1j}$.

the observables dependent on the azimuthal degrees of freedom; the azimuthal angle difference between the leading two jets of Fig. 4.11(d) and the azimuthal angle difference between the diphoton system (produced by the Higgs decay) and the dijet formed by the two leading jets, as plotted in Fig. 4.12(a), though small differences manifest for small azimuthal decorrelations (i.e. $\Delta\phi \sim \pi$).

As previously observed, the combination of the resummation of large logarithms in $\hat{s}/|p_\perp|^2$ and the finite quark mass effects tend to increase the observed cross sections in the tail of transverse momentum distributions compared to FO predictions. This is apparent in the description of the third-leading jet transverse momentum of Fig. 4.12(b), and in the transverse momentum of the diphoton-dijet system of Fig. 4.12(c). Although the Higgs transverse momentum seems to be independent of the effect of the resummation, previous results give reason to suggest that, for $p_\perp^{\gamma\gamma}$ larger than 200 GeV, the disparity between the two approaches would become more pronounced. Though the momentum range is small in Fig. 4.12(d), we begin to note that the transverse momentum spectra of HEJ predictions is harder than those predicted at NLO for the diphoton-dijet composite system, a consistent feature arising from the inclusion of finite quark mass effects.

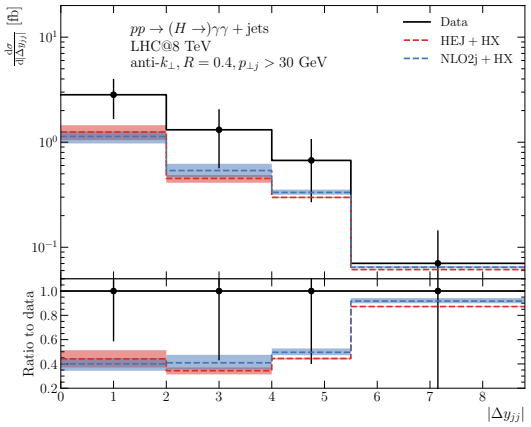

(a) Dijet rapidity separation

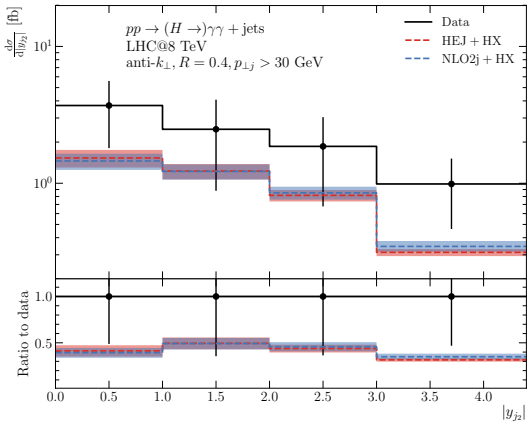

(b) Subleading jet rapidity

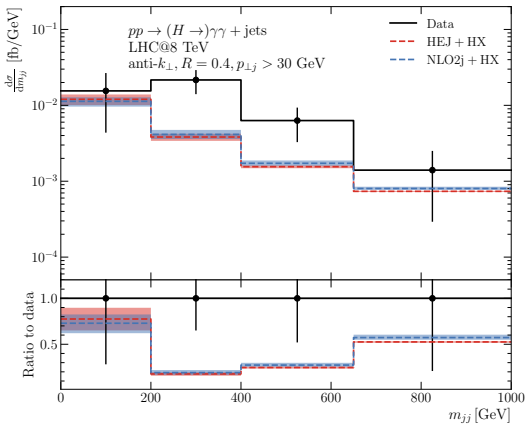

(c) Invariant dijet mass

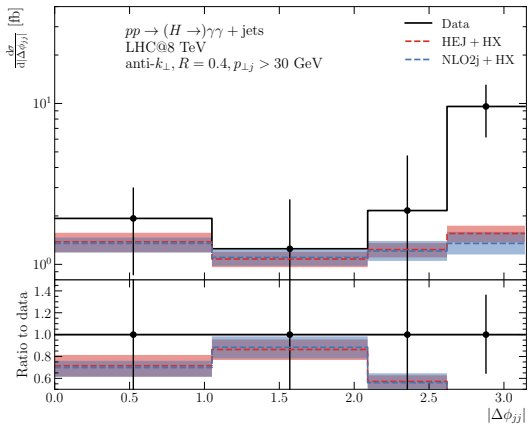

(d) $\Delta\phi$ between the leading 2 jets

Figure 4.11: Differential cross sections against inclusive $H+ \geq 2j$ observables. All 2-jet HEJ predictions are rescaled by the inclusive cross section ratio $\sigma_{\text{NLO,2J}}/\sigma_{\texttt{HEJ,2J}}$. The "HX" component is extracted from ref. [16] and added to the GF predictions.

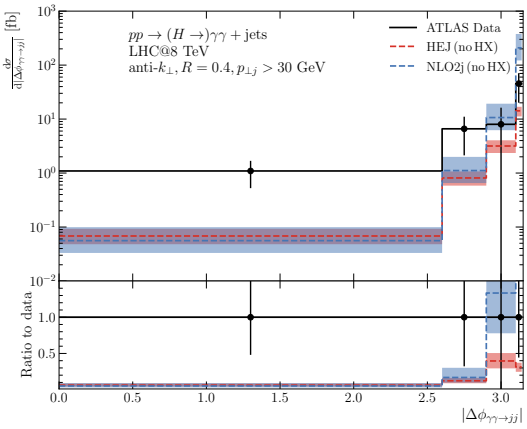

(a) $\Delta\phi$ between dijet and diphoton systems

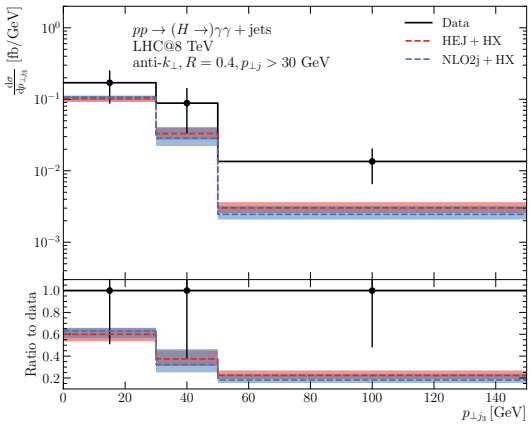

(b) Third-leading jet $p_\perp$

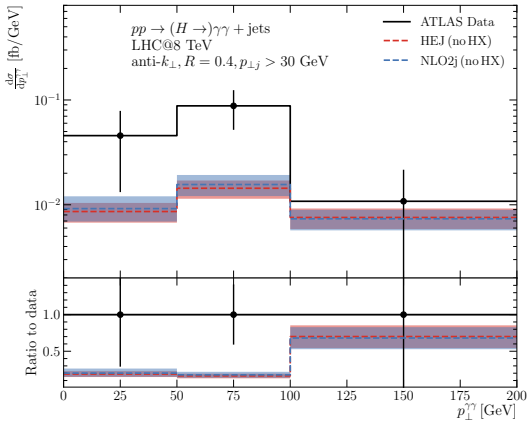

(c) Higgs $p_\perp$ with $N_{\text{jets}} = 2$

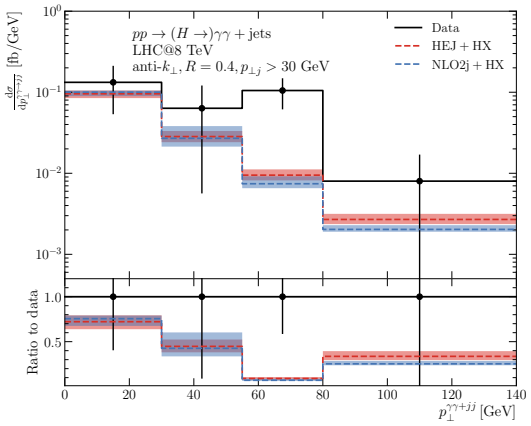

(d) $p_\perp$ of diphoton-dijet system

Figure 4.12: Differential cross sections against inclusive $H+ \geq 2j$ observables and inclusive $H+ \geq 3j$ observables. All 2- and 3-jet HEJ predictions are rescaled by the inclusive cross section ratio $\sigma_{\text{NLO},2j}/\sigma_{\texttt{HEJ@NLO},2j}$. In (a) and (d), the "HX" component was extracted from ref. [16]; this was not available for (b) and (c).

Similarly to our demonstration of the behaviour of high energy effects for the 13 TeV prediction in Fig. 4.8, we produce analogous distributions for 8 TeV and display these in Fig. 4.13. Again, only GF contributions are shown, with no "HX" component.

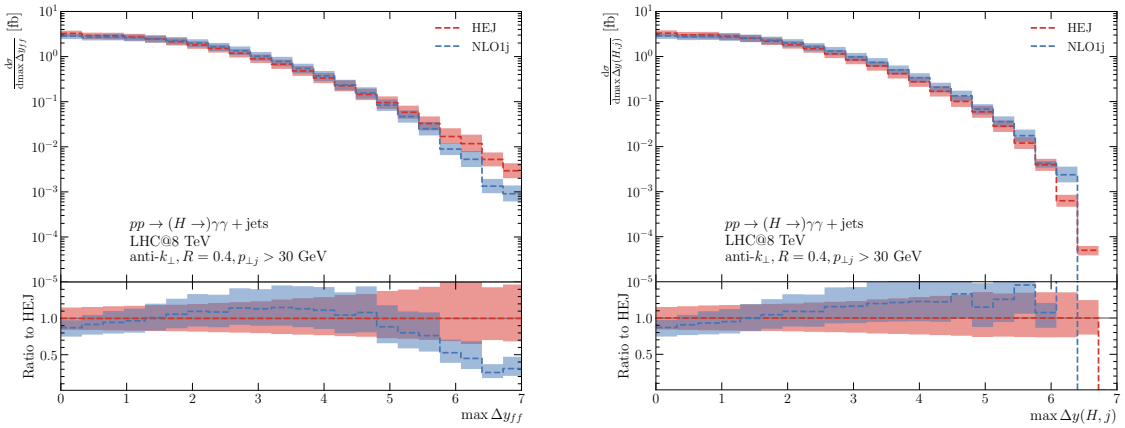

Figure 4.13: Distributions sensitive to high energy effects. In the left plot is plotted the maximum rapidity separation between any two outgoing particles (Higgs boson or jets) and in the right plot the maximum rapidity difference between the Higgs boson and any jet. Since these are inclusive single-jet observables, HEJ results are rescaled by the inclusive cross section ratio $\sigma_{\text{NLO},1j}/\sigma_{\texttt{HEJ@NLO},1j}$.

The conclusions from the distributions based on maximal rapidity differences are similar to those drawn from the 13 TeV plots in Fig. 4.8, namely that good agreement between HEJ and NLO is shown throughout, until the tail of each distribution (where the rapidity differences are large). Here the differential cross sections are small, but precise descriptions are important as this is the very region in which the high energy effects manifest with large logarithms, slowing the convergence of the perturbative expansion. The difference in the HEJ leading and subleading logarithms is again apparent from comparisons of the tail of each distribution, where the differential cross sections at similar max Δy_{ff} and max $\Delta y(H, j)$ are larger for the former than for the latter.

4.3 Conclusions

We have presented a method of resumming large logarithms in $\hat{s}/|p_\perp|^2$ for the inclusive production of $pp \to H+ \geq 1j$ within the HEJ framework. The method we have displayed is LL-accurate. The significant advantage of this approach is that full dependence on the finite top and bottom quark masses in the couplings of the Higgs boson to gluons is maintained for *any* number of jets, which quickly exceeds the multiplicities currently calculable with finite quark mass at even leading-order. This presents the LL resummation in $\hat{s}/|p_\perp|^2$ for an inclusive 1-jet process for the first time in the HEJ framework, allowing for robust comparison to other perturbative predictions and to a larger sample of experimental data.

Comparisons of these HEJ-resummed predictions to fixed-order predictions and to LHC data in Sec. 4.2 found that the impact of the resummation is greatest for large jet transverse momenta. The resummed results give a harder $p_\perp$-spectrum compared to NLO — for both the Higgs and jet transverse momenta. This demonstrates the significance of including finite quark mass effects in the coupling between the Higgs and two gluons. We also observe a large suppression of the cross section compared to NLO at large values of rapidity separation between all pairs of final state particles (i.e. jets or the Higgs boson). This suppression can be as high as 50% for wide minimum rapidity separations, well outside the theoretical uncertainty bands estimated by scale variations on both predictions. Other observables, e.g. azimuthal decorrelations between jets, or between jets and the Higgs boson, are less sensitive to these logarithmic corrections.

Looking forward to analyses of LHC Run 3 data, our results suggest that the inclusion of finite quark masses for higher jet multiplicities *and* of logarithmic corrections in $\hat{s}/|p_\perp|^2$ will be important when producing theoretical predictions for comparison. The thorough and stable accounting for high energy effects for inclusive $H + 1j$ final states will be an invaluable component of the precise modelling of the GF component of Higgs production in the era of the high-luminosity LHC.

Chapter 5

Conclusions and Outlook

We opened this thesis by motivating the necessity for comprehensive, precise, and stable predictions in perturbative QCD at hadron colliders to ensure that a rigorous understanding of Standard Model processes is achieved. Precision modelling is a crucial tool in the HL-LHC era, not just for pure QCD processes but importantly to model QCD background contributions to electroweak processes. The Higgs sector in particular is the least well-explored sector of the SM in experiments, owing to the relatively recent discovery in 2012, and requires increased theoretical precision to compare to new experimental data. Fixed-order calculations in perturbative QCD are described, and we note how such calculations predict inclusive quantities well. However, fixed-order calculations become extremely difficult to calculate for higher-order processes — especially for multi-scale processes — and the precision required for modelling of SM effects in extreme regions of phase space is not satisfied at fixed-orders.

In Ch. 2, we demonstrate that the omitted higher orders in a fixed-order calculation incur significant corrections in regions of phase space where the amplitudes are susceptible to logarithmic enhancement. These logarithms can spoil the convergence of the perturbative series in such regions, and a systematic all-orders treatment is required for comprehensive treatment of perturbative effects.

The framework of *High Energy Jets* is introduced and discussed in detail in Sec. 2.2,

as a resummation of high-energy logarithms of the form $\log \hat{s}/p_\perp^2$ in the limit of hard, wide-angle radiation at hadron collider experiments, motivating the necessity of such corrections as assuming a critical role in the description of large invariant mass regions where e.g. VBF Higgs production dominates in the SM. A QCD description of Higgs processes in such regions of phase space is incomplete without accounting for these corrections. HEJ builds on the BFKL formalism that preceded it by imposing approximations only at the amplitude level, and not on the phase space, as well as matching to the full LO cross section meaning a solid description of inclusive cross-sections is assured.

We also explore the widely-used resummation of soft-collinear effects with parton showers in Sec. 2.3, drawing the connection to our discussion of infrared divergences in Sec. 1.3.3. Parton showers dress inclusive Born configurations with soft and collinear radiation, resumming double logarithms of transverse scales that arise from the required ordering of emissions. Parton showers evolve hard ME configurations down in scale and set the stage for multi-parton interactions and hadronisation to be introduced to the final states — drawing closer the theoretical picture to the reality of experiments. The corrections applied in this regime are crucial for precise descriptions of QCD processes, and it is standard procedure to present fixed-order calculations in QCD matched and/or merged with parton showers. The field of matching and merging with parton showers is well-explored and fastly developing.

This discussion lends itself to motivate the research presented in Ch. 3, where we seek to combine the all-orders approaches of HEJ and of the Pythia parton shower. Such studies have been performed before with promising results. The framework we present in Ch. 3 builds significantly on the concepts explored in these earlier studies and provides a robust and in-depth novel method of combining the all-orders approaches of HEJ and Pythia that systematically removes double counting to all orders in perturbation theory. The LO accuracy of the base prediction is retained throughout, and the accuracy of the resummation of both HEJ and the shower are demonstrated to be conserved. A description of where each resummation should

be interpreted as inclusive and exclusive is found to be a crucial element of such a procedure, allowing for flexible development in the future when greater accuracies are achieved in HEJ and in the parton shower. The distributions analysed with the full HEJ+Pythia prediction for inclusive dijet production, as well as the comparisons to experimental data, show the predictive potential of HEJ+Pythia as a precision tool for modelling perturbative QCD processes. Development of the formalism is ongoing to ensure other HEJ-resummable processes can be predicted with the HEJ+Pythia method.

Finally, we extend the HEJ framework in the Higgs sector to produce the first predictions for inclusive $pp \to H + 1j$ processes at the LHC, presenting the theory and predictions for distributions in Ch. 4. The description we obtain includes full dependence on the top and bottom quark masses in the resummation, and is multiplicatively matched to NLO. Comparisons of the resummed predictions to experimental data from the LHC highlight that the HEJ resummation provides essential detail for distributions of significant theoretical and experimental interest. Precision modelling of the QCD-initiated process is demonstrated for inclusive $H+1j$ and $H + 2j$ distributions in high-energy observables such as the maximum invariant mass and rapidity difference between the Higgs boson and any jet (and others). Inclusive $H + 1j$ is another significant development in the HEJ framework that admits for detailed study of Higgs processes.

Reflecting on the research presented in this thesis, we see that we have motivated and demonstrated an in-depth exploration of higher-order high-energy and soft-collinear effects. We hope that the research may be applied to studies of new HL-LHC data, and that the precision modelling of QCD processes we have shown will prove invaluable in accounting for the SM background to LHC processes. The scope of the research presented is vast and rapidly evolving, and we anticipate that developments in the near future will bolster the predictive potential we have shown yet further to ensure stability and precision in perturbative QCD at hadron colliders.

Appendix A

The Higgs-Gluon-Gluon Coupling

We display in this section the coupling of a Higgs boson to two gluons via a massive quark loop, borrowing throughout from Appendix A in ref. [141].

In Fig. 4.2(a), this coupling is displayed, with momenta assigned to each external leg. The form factor $V_H^{\mu\nu}$ for this coupling, with one gluon incoming with momentum q_1 and Lorentz index μ, a gluon outgoing with momentum q_2 and Lorentz index ν, and a Higgs boson outgoing with momentum p_H, is given by:

$$V_H^{\mu\nu}(q_1,q_2) = \frac{\alpha_s m^2}{\pi v}\Big[g^{\mu\nu}T_1(q_1,q_2) - q_2^\mu q_1^\nu T_2(q_1,q_2)\Big]\,. \tag{A.0.1}$$

The outgoing momentum of the Higgs boson is $p_H = q_1 - q_2$. The form factors T_1 and T_2 are given by [140]

$$\begin{aligned}
T_1(q_1,q_2) = & -C_0(q_1,q_2)\left[2m^2 + \frac{1}{2}\left(q_1^2+q_2^2-p_H^2\right) + \frac{2q_1^2q_2^2p_H^2}{\lambda}\right] \\
& - \left[B_0(q_2) - B_0(p_H)\right]\frac{q_2^2}{\lambda}\left(q_2^2-q_1^2-p_H^2\right) \\
& - \left[B_0(q_1) - B_0(p_H)\right]\frac{q_1^2}{\lambda}\left(q_1^2-q_2^2-p_H^2\right) - 1\,, \qquad (A.0.2)\\
T_2(q_1,q_2) = & \, C_0(q_1,q_2)\left[\frac{4m^2}{\lambda}\left(p_H^2-q_1^2-q_2^2\right) - 1 - \frac{4q_1^2q_2^2}{\lambda} - \frac{12q_1^2q_2^2p_H^2}{\lambda^2}\left(q_1^2+q_2^2-p_H^2\right)\right] \\
& - \left[B_0(q_2) - B_0(p_H)\right]\left[\frac{2q_2^2}{\lambda} + \frac{12q_1^2q_2^2}{\lambda^2}\left(q_2^2-q_1^2+p_H^2\right)\right] \\
& - \left[B_0(q_1) - B_0(p_H)\right]\left[\frac{2q_1^2}{\lambda} + \frac{12q_1^2q_2^2}{\lambda^2}\left(q_1^2-q_2^2+p_H^2\right)\right]
\end{aligned}$$

$$- \frac{2}{\lambda}\left(q_1^2 + q_2^2 - p_H^2\right) , \tag{A.0.3}$$

where we have used the scalar bubble and triangle integrals

$$B_0\left(p\right) = \int \frac{d^d l}{i\pi^{\frac{d}{2}}} \frac{1}{\left(l^2 - m^2\right)\left((l+p)^2 - m^2\right)} , \tag{A.0.4}$$

$$C_0\left(p,q\right) = \int \frac{d^d l}{i\pi^{\frac{d}{2}}} \frac{1}{\left(l^2 - m^2\right)\left((l+p)^2 - m^2\right)\left((l+p-q)^2 - m^2\right)} , \tag{A.0.5}$$

and the Källén function

$$\lambda = q_1^4 + q_2^4 + p_H^4 - 2q_1^2 q_2^2 - 2q_1^2 p_H^2 - 2q_2^2 p_H^2 . \tag{A.0.6}$$

The relation to the form factors A_1, A_2 given in ref. [140] is

$$A_1(q_1, q_2) = \frac{i}{16\pi^2} T_2(-q_1, q_2) , \tag{A.0.7}$$

$$A_2(q_1, q_2) = -\frac{i}{16\pi^2} T_1(-q_1, q_2) . \tag{A.0.8}$$

Bibliography

[1] A. B. Arbuzov, *Quantum Field Theory and the Electroweak Standard Model*, 1801.05670.

[2] D. d'Enterria and P. Z. Skands, eds., *Proceedings, High-Precision α_s Measurements from LHC to FCC-ee: Geneva, Switzerland, October 2-13, 2015*, (Geneva), CERN, 12, 2015.

[3] CMS collaboration, G. Bayatian, S. Chatrchyan, G. Hmayakyan, A. Sirunyan, W. Adam, T. Bergauer et al., *CMS Physics Technical Design Report: Addendum on High Density QCD with Heavy Ions*, .

[4] S. Höche, *Introduction to parton-shower event generators*, in *Theoretical Advanced Study Institute in Elementary Particle Physics: Journeys Through the Precision Frontier: Amplitudes for Colliders*, pp. 235–295, 2015, 1411.4085, DOI.

[5] J. Alwall, R. Frederix, S. Frixione, V. Hirschi, F. Maltoni, O. Mattelaer et al., *The automated computation of tree-level and next-to-leading order differential cross sections, and their matching to parton shower simulations*, *JHEP* **07** (2014) 079, [1405.0301].

[6] J. R. Andersen, H. M. Brooks and L. Lönnblad, *Merging high energy with soft and collinear logarithms using HEJ and PYTHIA*, *Journal of High Energy Physics* **2018** (Sep, 2018) .

[7] J. R. Andersen, T. Hapola, A. Maier and J. M. Smillie, *Higgs boson plus dijets: higher order corrections*, *Journal of High Energy Physics* **2017** (sep, 2017) .

[8] A. Buckley et al., *General-purpose event generators for LHC physics*, *Phys. Rept.* **504** (2011) 145–233, [1101.2599].

[9] ATLAS collaboration, G. Aad et al., *Study of Jet Shapes in Inclusive Jet Production in pp Collisions at $\sqrt{s} = 7$ TeV using the ATLAS Detector*, *Phys. Rev. D* **83** (2011) 052003, [1101.0070].

[10] P. Skands, S. Carrazza and J. Rojo, *Tuning PYTHIA 8.1: the Monash 2013 Tune*, *Eur. Phys. J. C* **74** (2014) 3024, [1404.5630].

[11] ATLAS collaboration, G. Aad et al., *Measurement of multi-jet cross sections in proton-proton collisions at a 7 TeV center-of-mass energy*, *Eur. Phys. J. C* **71** (2011) 1763, [1107.2092].

[12] ATLAS collaboration, G. Aad et al., *Measurements of jet vetoes and azimuthal decorrelations in dijet events produced in pp collisions at $\sqrt{s} = 7\,\text{TeV}$ using the ATLAS detector*, *Eur. Phys. J. C* **74** (2014) 3117, [1407.5756].

[13] S. Alioli, J. R. Andersen, C. Oleari, E. Re and J. M. Smillie, *Probing higher-order corrections in dijet production at the LHC*, *Phys. Rev. D* **85** (2012) 114034, [1202.1475].

[14] CMS collaboration, *Measurement of the Higgs boson inclusive and differential fiducial production cross sections in the diphoton decay channel with pp collisions at $\sqrt{s}$ = 13 TeV*, 2208.12279.

[15] CMS collaboration, A. M. Sirunyan et al., *Measurement of inclusive and differential Higgs boson production cross sections in the diphoton decay*

channel in proton-proton collisions at $\sqrt{s}$ = 13 TeV, *JHEP* **01** (2019) 183, [1807.03825].

[16] ATLAS collaboration, G. Aad et al., *Measurements of fiducial and differential cross sections for Higgs boson production in the diphoton decay channel at $\sqrt{s} = 8$ TeV with ATLAS*, *JHEP* **09** (2014) 112, [1407.4222].

[17] J. R. Andersen, H. Hassan, A. Maier, J. Paltrinieri, A. Papaefstathiou and J. M. Smillie, *High energy resummed predictions for the production of a Higgs boson with at least one jet*, *JHEP* **03** (2023) 001, [2210.10671].

[18] ATLAS collaboration, *Observation of a new particle in the search for the standard model higgs boson with the ATLAS detector at the LHC*, *Physics Letters B* **716** (sep, 2012) 1–29.

[19] CMS collaboration, *Observation of a new boson at a mass of 125 gev with the cms experiment at the lhc*, *Physics Letters B* **716** (2012) 30–61.

[20] CDF collaboration, *High-precision measurement of the w boson mass with the cdf ii detector*, *Science* **376** (2022) 170–176, [https://www.science.org/doi/pdf/10.1126/science.abk1781].

[21] M. D. Schwartz, *Quantum Field Theory and the Standard Model*. Cambridge University Press, 3, 2014.

[22] J. M. Pendlebury, S. Afach, N. J. Ayres and e. a. Baker, *Revised experimental upper limit on the electric dipole moment of the neutron*, *Phys. Rev. D* **92** (Nov, 2015) 092003.

[23] J. R. Andersen, T. Hapola, M. Heil, A. Maier and J. M. Smillie, *Higgs-boson plus dijets: higher-order matching for high-energy predictions*, *Journal of High Energy Physics* **2018** (Aug, 2018) .

[24] M. Srednicki, *Quantum Field Theory*. Cambridge Univ. Press, Cambridge, U.K., 2007.

[25] M. E. Peskin and D. V. Schroeder, *An Introduction to Quantum Field Theory*. Addison-Wesley, Reading, U.S.A., 1995.

[26] M. Cepeda et al., *Report from Working Group 2: Higgs Physics at the HL-LHC and HE-LHC*, *CERN Yellow Rep. Monogr.* **7** (2019) 221–584, [1902.00134].

[27] Super-Kamiokande collaboration, Y. Fukuda, T. Hayakawa, E. Ichihara et al., *Evidence for oscillation of atmospheric neutrinos*, *Physical Review Letters* **81** (aug, 1998) 1562–1567.

[28] C. Duhr, *QCD at NNLO and beyond*, *Nuclear and Particle Physics Proceedings* **273-275** (2016) 2128 – 2135.

[29] J. R. Forshaw and D. A. Ross, *Quantum chromodynamics and the pomeron*, vol. 9. Cambridge University Press, 1, 2011.

[30] R. K. Ellis, W. J. Stirling and B. R. Webber, *QCD and Collider Physics*. Cambridge Monographs on Particle Physics, Nuclear Physics and Cosmology. Cambridge University Press, 1996, 10.1017/CBO9780511628788.

[31] P. De Causmaecker, R. Gastmans, W. Troost and T. T. Wu, *Multiple Bremsstrahlung in Gauge Theories at High-Energies. 1. General Formalism for Quantum Electrodynamics*, *Nucl. Phys. B* **206** (1982) 53–60.

[32] L. J. Dixon, *A brief introduction to modern amplitude methods*, in *Theoretical Advanced Study Institute in Elementary Particle Physics: Particle Physics: The Higgs Boson and Beyond*, pp. 31–67, 2014, 1310.5353, DOI.

[33] P. Baikov, K. G. Chetyrkin and J. H. Kühn, *Five-loop running of the qcd coupling constant*, *Physical Review Letters* **118** (feb, 2017) .

[34] ATLAS collaboration, *Determination of the strong coupling constant $\alpha_s(m_Z)$ from measurements of inclusive $w\pm$ and z boson production cross sections in*

proton-proton collisions at $\sqrt{s}$ = 7 and 8 tev, *Journal of High Energy Physics* **2020** (jun, 2020) .

[35] S. J. Wallace, *Eikonal expansion*, *Annals Phys.* **78** (1973) 190–257.

[36] K. Khelifa-Kerfa and Y. Delenda, *Eikonal gluon radiation at finite-Nc beyond 2 loops*, *PoS* **DIS2015** (2015) 143, [1507.01132].

[37] T. Kinoshita, *Mass singularities of feynman amplitudes*, *Journal of Mathematical Physics* **3** (1962) 650–677, [https://doi.org/10.1063/1.1724268].

[38] T. D. Lee and M. Nauenberg, *Degenerate Systems and Mass Singularities*, *Phys. Rev.* **133** (1964) B1549–B1562.

[39] J. Campbell, J. Huston and F. Krauss, *The Black Book of Quantum Chromodynamics: A Primer for the LHC Era.* Oxford University Press, 12, 2017, 10.1093/oso/9780199652747.001.0001.

[40] V. Fadin, E. Kuraev and L. Lipatov, *On the pomeranchuk singularity in asymptotically free theories*, *Physics Letters B* **60** (1975) 50–52.

[41] L. N. Lipatov, *Reggeization of the Vector Meson and the Vacuum Singularity in Nonabelian Gauge Theories*, *Sov. J. Nucl. Phys.* **23** (1976) 338–345.

[42] I. I. Balitsky and L. N. Lipatov, *The Pomeranchuk Singularity in Quantum Chromodynamics*, *Sov. J. Nucl. Phys.* **28** (1978) 822–829.

[43] E. A. Kuraev, L. N. Lipatov and V. S. Fadin, *The Pomeranchuk Singularity in Nonabelian Gauge Theories*, *Sov. Phys. JETP* **45** (1977) 199–204.

[44] E. A. Kuraev, L. N. Lipatov and V. S. Fadin, *Multi - Reggeon Processes in the Yang-Mills Theory*, *Sov. Phys. JETP* **44** (1976) 443–450.

[45] J. M. Campbell, J. W. Huston and W. J. Stirling, *Hard interactions of quarks and gluons: a primer for LHC physics*, *Reports on Progress in Physics* **70** (Dec, 2006) 89–193.

[46] T. Sjöstrand, S. Ask, J. R. Christiansen, R. Corke, N. Desai, P. Ilten et al., *An introduction to PYTHIA 8.2*, *Computer Physics Communications* **191** (jun, 2015) 159–177.

[47] C. Bierlich et al., *A comprehensive guide to the physics and usage of PYTHIA 8.3*, 2203.11601.

[48] Particle Data Group collaboration, R. L. Workman and Others, *Review of Particle Physics*, *PTEP* **2022** (2022) 083C01.

[49] ATLAS collaboration, *The ATLAS Experiment at the CERN Large Hadron Collider*, *JINST* **3** (2008) S08003.

[50] CMS collaboration, *The CMS Experiment at the CERN LHC*, *JINST* **3** (2008) S08004.

[51] T. Plehn, *Lectures on LHC Physics*, *Lecture Notes in Physics* (2012) .

[52] M. Cacciari, G. P. Salam and G. Soyez, *The anti-k_t jet clustering algorithm*, *JHEP* **04** (2008) 063, [0802.1189].

[53] H. V. Smith, *Numerical methods of integration*. Chartwell-Bratt, Bromley, 1993.

[54] F. Dekking, C. Kraaikamp, H. Lopuhaä and L. Meester, *A Modern Introduction to Probability and Statistics: Understanding Why and How*. Springer Texts in Statistics. Springer, 2005.

[55] I. Hughes and T. Hase, *Measurements and Their Uncertainties: A Practical Guide to Modern Error Analysis*. OUP Oxford, 2010.

[56] T. Kloek and H. K. van Dijk, *Bayesian estimates of equation system parameters: An application of integration by monte carlo*, *Econometrica* **46** (1978) 1–19.

[57] T. Ohl, *Vegas revisited: Adaptive Monte Carlo integration beyond factorization*, *Comput. Phys. Commun.* **120** (1999) 13–19, [hep-ph/9806432].

[58] K. G. Savvidy, *The MIXMAX random number generator*, *Comput. Phys. Commun.* **196** (2015) 161–165, [1403.5355].

[59] G. Marsaglia, *Random numbers fall mainly in the planes.*, *Proceedings of the National Academy of Sciences of the United States of America* **61 1** (1968) 25–8.

[60] K. Savvidy and G. Savvidy, *Spectrum and Entropy of C-systems. MIXMAX random number generator*, *Chaos Solitons Fractals* **91** (2016) 33–38, [1510.06274].

[61] M. Luscher, *A Portable high quality random number generator for lattice field theory simulations*, *Comput. Phys. Commun.* **79** (1994) 100–110, [hep-lat/9309020].

[62] Sherpa collaboration, E. Bothmann et al., *Event Generation with Sherpa 2.2*, *SciPost Phys.* **7** (2019) 034, [1905.09127].

[63] T. Sjostrand, S. Mrenna and P. Z. Skands, *PYTHIA 6.4 Physics and Manual*, *JHEP* **05** (2006) 026, [hep-ph/0603175].

[64] M. Bahr et al., *Herwig++ Physics and Manual*, *Eur. Phys. J. C* **58** (2008) 639–707, [0803.0883].

[65] S. Gieseke, P. Stephens and B. Webber, *New formalism for QCD parton showers*, *JHEP* **12** (2003) 045, [hep-ph/0310083].

[66] S. Catani and M. H. Seymour, *A General algorithm for calculating jet cross-sections in NLO QCD*, *Nucl. Phys. B* **485** (1997) 291–419, [hep-ph/9605323].

[67] S. Frixione, Z. Kunszt and A. Signer, *Three jet cross-sections to next-to-leading order*, *Nucl. Phys. B* **467** (1996) 399–442, [hep-ph/9512328].

[68] D. A. Kosower, *Antenna factorization of gauge theory amplitudes*, *Phys. Rev. D* **57** (1998) 5410–5416, [hep-ph/9710213].

[69] F. Krauss, R. Kuhn and G. Soff, *AMEGIC++ 1.0: A Matrix element generator in C++*, *JHEP* **02** (2002) 044, [hep-ph/0109036].

[70] T. Gleisberg and S. Hoeche, *Comix, a new matrix element generator*, *JHEP* **12** (2008) 039, [0808.3674].

[71] F. Buccioni, S. Pozzorini and M. Zoller, *On-the-fly reduction of open loops*, *Eur. Phys. J. C* **78** (2018) 70, [1710.11452].

[72] F. Cascioli, P. Maierhofer and S. Pozzorini, *Scattering Amplitudes with Open Loops*, *Phys. Rev. Lett.* **108** (2012) 111601, [1111.5206].

[73] T. Sjöstrand and M. van Zijl, *A multiple-interaction model for the event structure in hadron collisions*, *Phys. Rev. D* **36** (Oct, 1987) 2019–2041.

[74] T. Sjostrand and P. Z. Skands, *Transverse-momentum-ordered showers and interleaved multiple interactions*, *Eur. Phys. J. C* **39** (2005) 129–154, [hep-ph/0408302].

[75] TOTEM collaboration, G. Anelli et al., *The TOTEM experiment at the CERN Large Hadron Collider*, *JINST* **3** (2008) S08007.

[76] TOTEM collaboration, G. Antchev et al., *Luminosity-Independent Measurement of the Proton-Proton Total Cross Section at* $\sqrt{s} = 8$ *TeV*, *Phys. Rev. Lett.* **111** (2013) 012001.

[77] J.-C. Winter, F. Krauss and G. Soff, *A Modified cluster hadronization model*, *Eur. Phys. J. C* **36** (2004) 381–395, [hep-ph/0311085].

[78] B. Andersson, G. Gustafson, G. Ingelman and T. Sjostrand, *Parton Fragmentation and String Dynamics*, *Phys. Rept.* **97** (1983) 31–145.

[79] V. D. Duca, W. Kilgore, C. Oleari, C. Schmidt and D. Zeppenfeld, *Gluon-fusion contributions to h+2 jet production*, *Nuclear Physics B* **616** (nov, 2001) 367–399.

[80] G. Klämke and D. Zeppenfeld, *Higgs plus two jet production via gluon fusion as a signal at the CERN LHC*, *Journal of High Energy Physics* **2007** (apr, 2007) 052–052.

[81] J. Bendavid, F. Caola, V. Ciulli, R. Harlander, G. Heinrich, J. Huston et al., *Les Houches 2017: Physics at TeV Colliders Standard Model Working Group Report*, 2018.

[82] T. Plehn, D. Rainwater and D. Zeppenfeld, *Determining the structure of higgs couplings at the CERN large hadron collider*, *Physical Review Letters* **88** (jan, 2002) .

[83] R. Brower, C. DeTar and J. Weis, *Regge theory for multiparticle amplitudes*, *Physics Reports* **14** (1974) 257–367.

[84] V. Del Duca, *An introduction to the perturbative QCD pomeron and to jet physics at large rapidities*, hep-ph/9503226.

[85] G. Chachamis, *Bfkl phenomenology*, 2015. 10.48550/ARXIV.1512.04430.

[86] J. R. Andersen, *A closer look at the analysis of NLL BFKL*, in *AIP Conference Proceedings*, AIP, 2005, DOI.

[87] J. R. Andersen, J. A. Black, H. M. Brooks, E. P. Byrne, A. Maier and J. M. Smillie, *Combined subleading high-energy logarithms and NLO accuracy for*

W production in association with multiple jets, *JHEP* **04** (2021) 105, [2012.10310].

[88] V. Del Duca, *Equivalence of the Parke-Taylor and the Fadin-Kuraev-Lipatov amplitudes in the high-energy limit*, *Phys. Rev. D* **52** (1995) 1527–1534, [hep-ph/9503340].

[89] J. R. Andersen and J. M. Smillie, *Constructing All-Order Corrections to Multi-Jet Rates*, *JHEP* **1001** (2010) 039, [0908.2786].

[90] J. R. Andersen and J. M. Smillie, *The Factorisation of the t-channel Pole in Quark-Gluon Scattering*, *Phys.Rev.* **D81** (2010) 114021, [0910.5113].

[91] J. R. Andersen and J. M. Smillie, *Multiple jets at the LHC with high energy jets*, *Journal of High Energy Physics* **2011** (Jun, 2011) .

[92] J. R. Andersen and J. M. Smillie, *Constructing All-Order Corrections to Multi-Jet Rates*, *Journal of High Energy Physics* **2010** (Jan, 2010) .

[93] J. R. Andersen and J. M. Smillie, *The Factorization of the t-channel Pole in Quark-Gluon Scattering*, *Physical Review D* **81** (Jun, 2010) .

[94] J. R. Andersen, T. Hapola and J. M. Smillie, *W plus multiple jets at the LHC with high energy jets*, *Journal of High Energy Physics* **2012** (Sep, 2012) .

[95] J. R. Andersen, J. J. Medley and J. M. Smillie, *Z/γ^* plus multiple hard jets in high energy collisions*, *Journal of High Energy Physics* **2016** (may, 2016) .

[96] J. R. Andersen, B. Ducloué, C. Elrick, A. Maier, G. Nail and J. M. Smillie, *Logarithmic corrections to the QCD component of same-sign w-pair production for vector boson scattering studies*, *Physical Review D* **104** (dec, 2021) .

[97] J. R. Andersen, T. Hapola, M. Heil, A. Maier and J. M. Smillie, *Higgs-boson plus Dijets: Higher-Order Matching for High-Energy Predictions*, *JHEP* **08** (2018) 090, [1805.04446].

[98] J. R. Andersen, T. Hapola, M. Heil, A. Maier and J. Smillie, *HEJ 2: High Energy Resummation for Hadron Colliders*, 1902.08430.

[99] M. Dasgupta, F. A. Dreyer, K. Hamilton, P. F. Monni and G. P. Salam, *Logarithmic accuracy of parton showers: a fixed-order study*, *JHEP* **09** (2018) 033, [1805.09327].

[100] L. Lönnblad, *ARIADNE version 4: A Program for simulation of QCD cascades implementing the color dipole model*, *Comput. Phys. Commun.* **71** (1992) 15–31.

[101] Z. Nagy and D. E. Soper, *A New parton shower algorithm: Shower evolution, matching at leading and next-to-leading order level*, in *Ringberg Workshop on New Trends in HERA Physics 2005*, pp. 101–123, 1, 2006, hep-ph/0601021, DOI.

[102] M. van Beekveld, S. Ferrario Ravasio, G. P. Salam, A. Soto-Ontoso, G. Soyez and R. Verheyen, *PanScales parton showers for hadron collisions: formulation and fixed-order studies*, *JHEP* **11** (2022) 019, [2205.02237].

[103] F. Herren, S. Höche, F. Krauss, D. Reichelt and M. Schoenherr, *A new approach to color-coherent parton evolution*, 2208.06057.

[104] B. Cabouat and T. Sjöstrand, *Some Dipole Shower Studies*, *Eur. Phys. J. C* **78** (2018) 226, [1710.00391].

[105] S. Höche and S. Prestel, *The midpoint between dipole and parton showers*, *Eur. Phys. J. C* **75** (2015) 461, [1506.05057].

[106] M. Dasgupta, F. A. Dreyer, K. Hamilton, P. F. Monni, G. P. Salam and G. Soyez, *Parton showers beyond leading logarithmic accuracy*, *Phys. Rev. Lett.* **125** (2020) 052002, [2002.11114].

[107] M. H. Seymour, *Matrix element corrections to parton shower algorithms*, *Comput. Phys. Commun.* **90** (1995) 95–101, [hep-ph/9410414].

[108] M. Bengtsson and T. Sjostrand, *Coherent Parton Showers Versus Matrix Elements: Implications of PETRA - PEP Data*, *Phys. Lett. B* **185** (1987) 435.

[109] P. Nason, *A New method for combining NLO QCD with shower Monte Carlo algorithms*, *JHEP* **11** (2004) 040, [hep-ph/0409146].

[110] S. Frixione and B. R. Webber, *Matching NLO QCD computations and parton shower simulations*, *JHEP* **06** (2002) 029, [hep-ph/0204244].

[111] S. Frixione and B. R. Webber, *The MC@NLO 3.3 Event Generator*, hep-ph/0612272.

[112] S. Hoeche, F. Krauss, M. Schonherr and F. Siegert, *A critical appraisal of NLO+PS matching methods*, *JHEP* **09** (2012) 049, [1111.1220].

[113] S. Catani, F. Krauss, B. R. Webber and R. Kuhn, *QCD Matrix Elements + Parton Showers*, *Journal of High Energy Physics* **2001** (Nov, 2001) 063–063.

[114] L. Lönnblad, *Correcting the Colour-Dipole Cascade Model with Fixed Order Matrix Elements*, *Journal of High Energy Physics* **2002** (May, 2002) 046–046.

[115] K. Hamilton and P. Nason, *Improving NLO-parton shower matched simulations with higher order matrix elements*, *JHEP* **06** (2010) 039, [1004.1764].

[116] S. Höche, F. Krauss, S. Schumann and F. Siegert, *QCD matrix elements and truncated showers*, *Journal of High Energy Physics* **2009** (May, 2009) 053–053.

[117] L. Lönnblad and S. Prestel, *Merging Multi-leg NLO Matrix Elements with Parton Showers*, *JHEP* **03** (2013) 166, [1211.7278].

[118] J. Bellm, S. Gieseke and S. Plätzer, *Merging NLO Multi-jet Calculations with Improved Unitarization*, *Eur. Phys. J. C* **78** (2018) 244, [1705.06700].

[119] J. R. Andersen, L. Lonnblad and J. M. Smillie, *A Parton Shower for High Energy Jets*, *JHEP* **07** (2011) 110, [1104.1316].

[120] C. Bierlich et al., *Robust Independent Validation of Experiment and Theory: Rivet version 3*, *SciPost Phys.* **8** (2020) 026, [1912.05451].

[121] NNPDF collaboration, R. D. Ball et al., *Parton distributions from high-precision collider data*, *Eur. Phys. J. C* **77** (2017) 663, [1706.00428].

[122] R. D. Ball et al., *Parton distributions with LHC data*, *Nucl. Phys. B* **867** (2013) 244–289, [1207.1303].

[123] A. Buckley, J. Ferrando, S. Lloyd, K. Nordström, B. Page, M. Rüfenacht et al., *LHAPDF6: parton density access in the LHC precision era*, *Eur. Phys. J. C* **75** (2015) 132, [1412.7420].

[124] M. L. Mangano, M. Moretti, F. Piccinini, R. Pittau and A. D. Polosa, *ALPGEN, a generator for hard multiparton processes in hadronic collisions*, *JHEP* **07** (2003) 001, [hep-ph/0206293].

[125] J. R. Andersen, T. Hapola, A. Maier and J. M. Smillie, *Higgs Boson Plus Dijets: Higher Order Corrections*, *JHEP* **09** (2017) 065, [1706.01002].

[126] M. Czakon, R. V. Harlander, J. Klappert and M. Niggetiedt, *Exact Top-Quark Mass Dependence in Hadronic Higgs Production*, *Phys. Rev. Lett.* **127** (2021) 162002, [2105.04436].

[127] S. P. Jones, M. Kerner and G. Luisoni, *Next-to-Leading-Order QCD Corrections to Higgs Boson Plus Jet Production with Full Top-Quark Mass Dependence*, *Phys. Rev. Lett.* **120** (2018) 162001, [1802.00349].

[128] X. Chen, A. Huss, S. P. Jones, M. Kerner, J. N. Lang, J. M. Lindert et al., *Top-quark mass effects in H+jet and H+2 jets production*, *JHEP* **03** (2022) 096, [2110.06953].

[129] V. Del Duca, W. Kilgore, C. Oleari, C. Schmidt and D. Zeppenfeld, *Higgs + 2 jets via gluon fusion*, *Phys. Rev. Lett.* **87** (2001) 122001, [hep-ph/0105129].

[130] C. Anastasiou, C. Duhr, F. Dulat, F. Herzog and B. Mistlberger, *Higgs Boson Gluon-Fusion Production in QCD at Three Loops*, *Phys. Rev. Lett.* **114** (2015) 212001, [1503.06056].

[131] F. Dulat, B. Mistlberger and A. Pelloni, *Differential Higgs production at N^3LO beyond threshold*, *JHEP* **01** (2018) 145, [1710.03016].

[132] B. Mistlberger, *Higgs boson production at hadron colliders at N^3LO in QCD*, *JHEP* **05** (2018) 028, [1802.00833].

[133] L. Cieri, X. Chen, T. Gehrmann, E. W. N. Glover and A. Huss, *Higgs boson production at the LHC using the q_T subtraction formalism at N^3LO QCD*, *JHEP* **02** (2019) 096, [1807.11501].

[134] X. Chen, T. Gehrmann, E. W. N. Glover, A. Huss, B. Mistlberger and A. Pelloni, *Fully Differential Higgs Boson Production to Third Order in QCD*, *Phys. Rev. Lett.* **127** (2021) 072002, [2102.07607].

[135] R. Boughezal, F. Caola, K. Melnikov, F. Petriello and M. Schulze, *Higgs boson production in association with a jet at next-to-next-to-leading order in perturbative QCD*, *JHEP* **06** (2013) 072, [1302.6216].

[136] X. Chen, T. Gehrmann, E. W. N. Glover and M. Jaquier, *Precise QCD predictions for the production of Higgs + jet final states*, *Phys. Lett. B* **740** (2015) 147–150, [1408.5325].

[137] R. Boughezal, F. Caola, K. Melnikov, F. Petriello and M. Schulze, *Higgs boson production in association with a jet at next-to-next-to-leading order*, *Phys. Rev. Lett.* **115** (2015) 082003, [1504.07922].

[138] J. M. Campbell, R. K. Ellis and G. Zanderighi, *Next-to-Leading order Higgs + 2 jet production via gluon fusion*, *JHEP* **10** (2006) 028, [hep-ph/0608194].

[139] J. M. Campbell, R. K. Ellis and C. Williams, *Hadronic Production of a Higgs Boson and Two Jets at Next-to-Leading Order*, *Phys. Rev. D* **81** (2010) 074023, [1001.4495].

[140] V. Del Duca, W. Kilgore, C. Oleari, C. R. Schmidt and D. Zeppenfeld, *Kinematical limits on Higgs boson production via gluon fusion in association with jets*, *Phys. Rev. D* **67** (2003) 073003, [hep-ph/0301013].

[141] J. R. Andersen, J. D. Cockburn, M. Heil, A. Maier and J. M. Smillie, *Finite Quark-Mass Effects in Higgs Boson Production with Dijets at Large Energies*, *JHEP* **04** (2019) 127, [1812.08072].

[142] A. H. Mueller and H. Navelet, *An Inclusive Minijet Cross-Section and the Bare Pomeron in QCD*, *Nucl. Phys. B* **282** (1987) 727–744.

[143] B.-W. Xiao and F. Yuan, *BFKL and Sudakov Resummation in Higgs Boson Plus Jet Production with Large Rapidity Separation*, *Phys. Lett. B* **782** (2018) 28–33, [1801.05478].

[144] F. G. Celiberto, D. Y. Ivanov, M. M. A. Mohammed and A. Papa, *High-energy resummed distributions for the inclusive Higgs-plus-jet production at the LHC*, *Eur. Phys. J. C* **81** (2021) 293, [2008.00501].

[145] S. Dawson and R. P. Kauffman, *Higgs boson plus multi - jet rates at the SSC*, *Phys. Rev. Lett.* **68** (1992) 2273–2276.

[146] R. P. Kauffman, S. V. Desai and D. Risal, *Production of a Higgs boson plus two jets in hadronic collisions*, *Phys. Rev. D* **55** (1997) 4005–4015, [hep-ph/9610541].

[147] F. Buccioni, J.-N. Lang, J. M. Lindert, P. Maierhöfer, S. Pozzorini, H. Zhang et al., *OpenLoops 2*, *Eur. Phys. J. C* **79** (2019) 866, [1907.13071].

[148] NNPDF collaboration, R. D. Ball et al., *Parton distributions for the LHC Run II*, *JHEP* **04** (2015) 040, [1410.8849].